THESIS FOR THE DEGREE OF DOCTOR OF PHILOSOPHY

Dynamic Models of Wind Turbines

A Contribution towards the Establishment of Standardized Models of Wind Turbines for Power System Stability Studies

ABRAM PERDANA

Division of Electric Power Engineering
Department of Energy and Environment
CHALMERS UNIVERSITY OF TECHNOLOGY
Göteborg, Sweden 2008

Dynamic Models of Wind Turbines
A Contribution towards the Establishment of Standardized Models of Wind Turbines for Power System Stability Studies
ABRAM PERDANA
ISBN 978-91-7385-226-5

Doktorsavhandlingar vid Chalmers tekniska högskola
Ny serie nr. 2907
ISSN 0346-718X

Division of Electric Power Engineering
Department of Energy and Environment
Chalmers University of Technology
SE-412 96 Göteborg
Sweden
Telephone + 46 (0)31-772 1000

Chalmers Bibliotek, Reproservice
Göteborg, Sweden 2008

To the One
who gives me life

Dynamic Models of Wind Turbines
A Contribution towards the Establishment of Standardized Models of Wind Turbines for Power System Stability Studies
ABRAM PERDANA
Division of Electric Power Engineering
Department of Energy and Environment
Chalmers University of Technology

Abstract

The impact of wind power generation in the power system is no longer negligible. Therefore, there is an urgent need for wind turbine models that are capable of accurately simulating the interaction between wind turbines or wind farms and the power system. One problem is that no standardized model of wind turbines for power system stability studies is currently available. In response to this problem, generic dynamic models of wind turbines for stability studies are proposed in this thesis. Three wind turbine concepts are considered; fixed-speed wind turbines (FSWTs), doubly fed induction generator (DFIG) wind turbines and full converter wind turbines (FCWTs).

The proposed models are developed for positive-sequence phasor time-domain dynamic simulations and are implemented in the standard power system simulation tool PSS/E with a 10 ms time step. Response accuracy of the proposed models is validated against detailed models and, in some cases, against field measurement data. A direct solution method is proposed for initializing a DFIG wind turbine model. A model of a dc-link braking resistor with limited energy capacity is proposed, thus a unified model of an FCWT for a power system stability analysis can be obtained.

The results show that the proposed models are able to simulate wind turbine responses with sufficient accuracy. The generic models proposed in this thesis can be seen as a contribution to the ongoing discourse on standardized models of wind power generation for power system stability studies.

Aggregated models of wind farms are studied. A single equivalent unit representation of a wind farm is found to be sufficient for most short-term voltage stability investigations. The results show that non-linearities due to maximum power tracking characteristics and saturation of electrical controllers play no important role in characterizing wind farm responses. For a medium-term study, which may include wind transport phenomena, a cluster representation of a wind farm provides a more realistic prediction.

Different influencing factors in designing dynamic reactive power compensation for an offshore wind farm consisting of FSWTs are also investigated. The results show that fault ride-through capability of the individual turbines in the wind farm utilizing an active stall control significantly reduces the requirement for the dynamic reactive power compensation.

Keywords: wind turbine, modeling, validation, fixed-speed, variable-speed, power system stability, voltage stability, frequency stability, aggregated model.

Acknowledgements

This work has been carried out at the Division of Electric Power Engineering, Department of Energy and Environment at Chalmers University of Technology. The financial support by Nordic Energy Research, Svenska Kraftnät and Vattenfall is gratefully acknowledged.

First of all, I would like to express my deep and sincere gratitude to my supervisor Associate Professor Ola Carlson for his excellent supervision and helps during this work. I would like to express gratitude to my examiner Professor Tore Undeland for providing guidance and encouragement. I gratefully thank Professor Torbjörn Thiringer for his valuable suggestions and constructive advice on this thesis.

I really appreciate Jarle Eek for providing valuable comments and suggestions. I would also like to thank Sanna Uski and Dr. Torsten Lund for good collaboration. My gratitude also goes to all members of the Nordic Reference Group for their fruitful discussions during various meetings.

I would like to thank Dr. Nayeem Rahmat Ullah for his companionship and for proofreading parts of this manuscript. I also appreciate Marcia Martins for her friendly help and good cooperation throughout my research. I would also like to thank Dr. Massimo Bongiorno for helpful discussions. Thanks go to Dr. Ferry August Viawan for good companionship. I also thank all the people working at the Division of Electric Power Engineering and the Division of High Voltage Engineering for providing such a nice atmosphere.

My ultimate gratitude goes to my parents, Siti Zanah and Anwar Mursid, and my parents in law, Siti Maryam and Dr. Tedjo Yuwono. It is because of their endless pray, finally I can accomplish this work. My most heartfelt acknowledgement must go to my wife, Asri Kirana Astuti for her endless patient, love and support. Finally, to my sons Aufa, Ayaz and Abit, thank you for your love, which makes this work so joyful.

Table of Contents

Chapter 1

Introduction

1.1 Background and Motivations

By the end of 2007, the amount of installed wind power worldwide reached 93.8 GW, which is equal to 200 TWh of generated electricity. The growth in wind generation capacity during the past two years has been approximately 26% per year[1].

Wind power generation has traditionally been treated as distributed small generation or negative load. Wind turbines have been allowed to be disconnected when a fault is encountered in the power system. Such a perspective does not require wind turbines to participate in frequency control and the disconnection of wind turbines is considered as insignificant for loss of generation.

However, recently the penetration of wind power has been considerably high particularly in some countries such as Denmark (19.9%), Spain (9.8%), Portugal (8.1%), Ireland (6.9%) and Germany (6.4%) [2]. These figures are equivalent to the annual production of wind power over the total electricity demand. Consequently, the maximum penetration during peak hours may be 4-5 times these figures [3].

As the presence of wind power generation becomes substantial in the power system, all pertinent factors that may influence the quality and the security of the power system operation must be considered. Therefore, the traditional concept is no longer relevant. Thus, wind power generation is required to provide a certain reliability of supply and a certain level of stability.

Motivated by the issues above, many grid operators have started to introduce more demanding grid codes for wind power generation. In response to these grid codes, wind turbine manufacturers provide their products with features that cope with the new grid requirements, including fault ride-through (FRT) capabilities and other relevant features.

Meanwhile, as wind power generation is relatively new in power system studies, no standardized model is currently available. Many studies of various wind turbine technologies have been presented in literature, however most of the studies focus mainly on detailed machine studies. Only a few studies discuss the effects and applicability of the models in the power system. It has been found that the models provided in many studies are oversimplified or the other way around, some models are far too detailed for power system stability studies.

Hence, the main idea of this thesis is to provide wind turbine models that are

appropriate for power system stability studies. Consequently, some factors that are essential for stability studies are elaborated in detail. Such factors are mainly related to simulation efficiency and result accuracy. The first factor requires a model construction for a specific standardized simulation tool, while the latter factor requires validation of the models.

The development of aggregated models of wind farms is also an important issue as the size of wind farms and number of turbines in wind farms increases. Consequently, representing a wind farm using individual turbines increases complexity and leads to time-consuming simulation, which is not desired in stability studies involving large power systems. The aggregated models of wind farms are therefore addressed specifically in the thesis.

1.2 Wind Turbine Concepts

Wind turbine technologies can be classified into four main concepts. A detailed comparison of the different concepts has been addressed in [4].

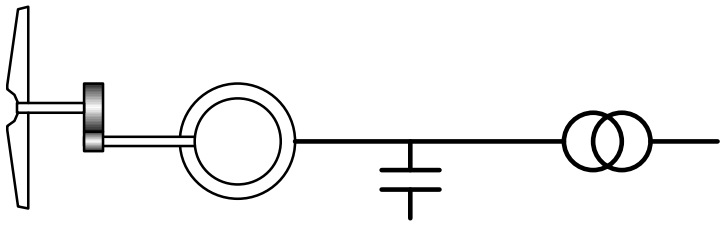

(a) Fixed-speed wind turbine

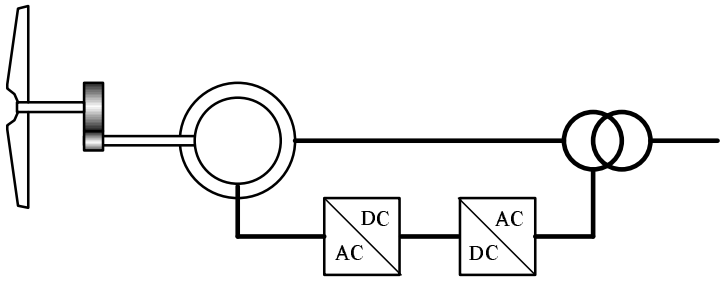

(b) Wind turbine with DFIG

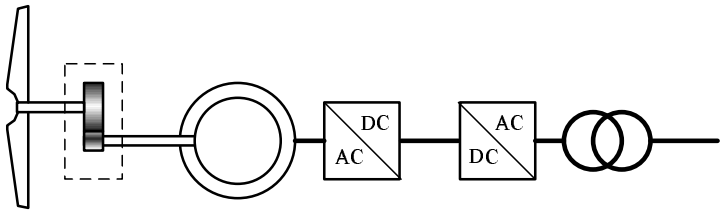

(c) Wind turbine with power converter

Figure 1.1. Various wind turbine concepts.

The first concept is a fixed-speed wind turbine equipped with a squirrel cage induction generator. The older generation of this concept uses a passive stall mechanism to

limit aerodynamic torque, while the newer generation employs an active stall mechanism.

The second concept is a variable speed wind turbine with variable rotor resistance, which is used by Vestas in their Vestas OptiSlip wind turbine class [5]. This wind turbine concept uses a wound rotor induction generator equipped with variable rotor resistances. The rotor resistances are regulated by means of a power converter. This concept is known as the limited variable speed concept.

The third concept is a variable speed wind turbine with a partial power converter or a wind turbine with a doubly fed induction generator (DFIG). The rating of this power converter is normally less than 30 percent of the generator rating.

The fourth concept is a variable speed full converter wind turbine (FCWT). This concept can employ different generator types, such as an induction generator or a synchronous generator, either with permanent magnets or external electrical excitation.

In the past, the majority of installed wind turbines were fixed-speed wind turbines with a squirrel cage induction generator, known as the 'Danish concept.' However, the dominant technology in the market at the moment is DFIG wind turbines [6]. This concept accounts for more than 65% of the newly installed wind turbines (in MW unit), followed by the fixed-speed wind turbine concept, which accounts for 18% of the market share. The market share of FCWTs is slightly below that of fixed-speed wind turbines. Wind turbines of the variable rotor resistance concept account for less than 2% of the market and are predicted to be phased out of the market. Consequently, this wind turbine concept is not discussed in this thesis. Schematic diagrams of the three wind turbine concepts are shown in Fig. 1.1.

1.3 Brief Review of Previous Works

A detailed FSWT model for stability studies with stator transient included has been addressed in the PhD thesis by Akhmatov [7]. The inclusion of the stator current transient allows an accurate speed deviation prediction. A DFIG wind turbine model for power system stability studies was also proposed in the same thesis with the stator flux transient included. By doing so, the FRT scheme can be modeled in detail. However, this representation poses difficulties in the model implementation into positive sequence fundamental frequency simulation tools due to a very small time step requirement and incompatibility with standardized power system components.

A reduced order model of a DFIG wind turbine model has been introduced in [8] where the stator transient is neglected during a normal operation. However, the involvement of current a controller still requires high simulation resolution. A simplified model of a DFIG wind turbine that is compatible with the fundamental frequency representation was proposed in [9]. The DFIG was modeled by neglecting both stator and rotor flux dynamics. This model is equivalent to a steady state representation, while the rotor current controller is assumed to be instantaneous. Consequently, iteration procedure - which is not preferable in the model implementation - is needed to solve algebraic loops between the generator model and the grid model. By introducing time lags, which represent delays in the current control, the algebraic loops are avoided [10]. However, the maximum power tracking (MPT) in this model is assumed to be a direct function of incoming wind speed, whereas in common practice, the MPT is either driven

by the generator speed or the generator power output. Another simplified DFIG model was presented in [11, 12]. According to this model, the generator is simply modeled as a controlled current source, thus the rotor quantities are omitted. The things that are missing from the proposed simplified models mentioned earlier are that the rotor current limiters are excluded and the FRT schemes are not clearly modeled.

Representations of detailed FCWT models for power system studies are presented in [13, 7]. In these papers the generators are modeled in detail. Consequently, these models require very small time step and thereby complicate the implementation in a standardized fundamental frequency simulation tool. A simplified of an FCWT model was proposed in [12].

Several remarks can be drawn from the review of previous works:

- Each model presented in the papers is associated with a particular type of controller and uses a particular FRT scheme if it exists. The sensitivity and influences of different control and FRT schemes on wind turbine responses have not been treated in the papers.
- The FRT schemes are often excluded from the simplified models, whereas the FRT schemes substantially characterize the response of wind turbines during grid faults.
- Most of the simplified models are not validated against more detailed models or measurement data. This leads to uncertainty in the accuracy of the model responses.

1.4 Purpose of the thesis

The main purpose of this thesis is to provide wind turbine models and aggregated wind farm models for power system stability studies. The models comprise three wind power generation concepts; a fixed-speed wind turbine with a squirrel cage induction generator, a variable speed DFIG wind turbine and a variable speed full converter wind turbine. The models must satisfy three main criteria: First, the models must be compatible with the standardized positive sequence fundamental frequency representation. Second, the models must have necessary accuracy. Third, the models must be computationally efficient.

1.5 Contributions

The results of this work are expected to provide valuable contributions in the following aspects:

- Generic models for three different concepts of wind turbines are proposed for stability studies. In developing these models, a comprehensive approach considering simulation efficiency, accuracy and consistency with standardized power system stability models, is applied. Furthermore, the proposed generic models are expected to be a significant step towards realizing standardized models of wind turbines for power system stability studies.

- Comparisons between and evaluations of various fault ride-through strategies for different wind turbine concepts are made. The uniqueness, advantages and drawbacks of each of the control alternatives are addressed. The results of this investigation are expected to provide valuable knowledge for selecting the best fault ride-through strategy for different wind turbine concepts.

- A fixed-speed wind turbine model and an aggregated model of a wind farm consisting of fixed-speed wind turbines are validated against field measurement data. The validations show good agreement between the models and measurement data. The results also emphasize the significance of having good knowledge of wind turbine parameters.

In addition to the main contributions mentioned above, several minor contributions can also be mentioned as follows:

- Influences of frequency deviation on the response accuracy of wind turbine models are demonstrated.

- A modified fifth-order model of an induction generator for a fundamental frequency simulation of an FSWT model is proposed.

- An effect of a mismatch between load-flow data and generator model initialization of an FSWT is addressed. Subsequently, a recommendation to overcome this problem is proposed.

- A new direct solution method for initialization of a DFIG wind turbine model is proposed. This method makes the model implementation in power system simulation tools simpler.

- Two main types of active power control schemes of a DFIG wind turbine are identified.

- Two critical events of DFIG wind turbines during fault are identified: (1) rotor-side converter deactivation at sub-synchronous operation leads to reverse power flow which potentially confuses a wind farm protection, (2) delayed rotor-side converter reactivation during a grid fault leads to large reactive power absorption.

- Effectiveness of different wind farm aggregation methods is evaluated. Effects of non-linearities in wind turbine electrical controllers are taken into account. Based on this evaluation, appropriate aggregation methods for different types of power system studies are suggested.

- A wind transport delay influence in a large wind farm is investigated. As a result, it is found that a wind speed dynamics in the wind farm cannot be considered as a short-term phenomenon.

- A new torsional active damping control scheme for a DFIG wind turbine is presented.

- A model of a dc-link braking resistor with limited energy capacity in an FCWT model is proposed. As a result, a unified model of an FCWT for a power system stability analysis can be derived.
- Effects of device location, grid strength and wind turbine FRT capability on the dynamic reactive power compensation requirements for an offshore wind farm consisting of fixed-speed wind turbines are presented.

1.6 Publications

Parts of the results presented in this thesis are also found in the following papers.

1. O. Carlson, A. Perdana, N.R. Ullah, M. Martins and E. Agneholm, "Power system voltage stability related to wind power generation," in *Proc. of European Wind Energy Conference and Exhibition (EWEC)*, Athens, Greece, Feb. 27 - Mar 2, 2006.
2. T. Lund, J. Eek, S. Uski and A. Perdana, "Fault simulation of wind turbines using commercial simulation tools," in *Proc. of Fifth International Workshop on Large-Scale Integration of Wind Power and Transmission Networks for Offshore Wind Farms*, Glasgow, UK, 2005.
3. M. Martins, A. Perdana, P. Ledesma, E. Agneholm, O. Carlson, "Validation of fixed-speed wind turbine dynamics with measured data," *Renewable Energy*, vol. 32, no. 8, 2007, pp. 1301-1316.
4. A. Perdana, S. Uski, O. Carlson and B. Lemström, "Validation of aggregate model of wind farm with fixed-speed wind turbines against measurement," in *Proc. Nordic Wind Power Conference 2006*, Espoo, Finland, 2006.
5. A. Perdana, S. Uski-Joutsenvuo, O. Carlson, B.Lemström", "Comparison of an aggregated model of a wind farm consisting of fixed-speed wind turbines with field measurement," *Wind Energy*, vol. 11, no. 1, 2008, pp. 13-27.
6. A. Perdana, O. Carlson, "Comparison of control schemes of wind turbines with doubly-fed induction generator," in *Proc. Nordic Wind Power Conference 2007*, Roskilde, Denmark, 2007.
7. A. Perdana, O. Carlson, J. Persson, "Dynamic response of a wind turbine with DFIG during disturbances," in *Proc. of IEEE Nordic Workshop on Power and Industrial Electronics (NORpie) 2004*, Trondheim, Norway, June 14-16, 2004.
8. A. Perdana, O. Carlson, "Dynamic modeling of a DFIG wind turbine for power system stability studies," submitted to *IEEE Transaction on Energy Conversion.*
9. A. Perdana, O. Carlson, " Factors influencing design of dynamic reactive power compensation for an offshore wind farm," submitted to *Wind Engineering.*

Chapter 2

General Aspects in Modeling Wind Power Generation

This chapter introduces a definition and classification of power system stability studies and its relevance for wind power generation. Various important issues in modeling wind power generation for power system stability studies are also presented in this chapter.

2.1 Power System Stability Studies

2.1.1 Definition and classification of power system stability

Power system stability, as used in this thesis refers to the definitions and classifications given in [14]. The definition of power stability is given as the ability of an electric power system, for a given initial operating condition, to regain a state of operating equilibrium after being subjected to a physical disturbance, with most system variables bounded so that practically the entire system remains intact.

Power system stability can be divided into several categories as follows:

Rotor angle stability This stability refers to the ability of synchronous machines of an interconnected power system to remain in synchronism after being subjected to a disturbance. The time frame of interest is between 3 to 5 seconds and can be extended to 10 to 20 seconds for a very large power system with dominant inter-area swings.

Short- and long-term frequency stability This term refers to the ability of a power system to maintain steady frequency following a severe system upset resulting in a significant imbalance between generation and load. The time frame of interest for a frequency stability study varies from tens of seconds to several minutes.

Short- and long-term large disturbance voltage stability This term refers to the ability of a power system to maintain steady voltages following large disturbances such as system faults, loss of generation, or circuit contingencies. The period of interest for this kind of study varies from a few seconds to tens of minutes.

Short- and long-term small disturbance voltage stability This stability refers to a system's ability to maintain steady voltages when subjected to small perturbations such as incremental changes in system load. For a large power system, the time frame of the study may extend from a few seconds to several or many minutes.

Current power system stability definitions, however, do not explicitly comprise speed instability of induction generators due to voltage dips in a power system. In fact, this phenomenon is very relevant for wind turbines equipped with grid-connected induction generators such as fixed-speed wind turbines and variable-speed DFIG wind turbines. For this reason, Samuelsson [15] has proposed a rotor speed stability definition, which is defined as the ability of an induction machine to remain connected to the electric power system and run at mechanical speed close to the speed corresponding to the actual system frequency after being subjected to a disturbance.

2.2 Modeling Power System Components

According to [16], a dynamic model of a power system component is essential in stability simulations if it satisfies three criteria. First, the model must have a significant impact on the phenomena being studied. Second, the model must respond rapidly enough for the impact to be observed before the simulation ends. Third, the model response must not settle out too fast to be modeled as a dynamic model.

The last two criteria are related to simulation time frames. In a typical power system stability study, the smallest constant is approximately 0.1 seconds [17]. However, the entire time frame involved in stability studies may extend up to several hours. Fig. 2.1 shows several power system component time constants, where typical phenomena involved in a wind turbine model are also depicted in the figure.

Such a large discrepancy in the time constants in a power system stability study is a challenge. On one hand, the inclusion of small time constant phenomena in a long time frame simulation leads to a time consuming simulation. On the other hand, however, excluding small time frame phenomena reduces simulation accuracy.

A number of solutions to alleviate the difficulty associated with time response discrepancy among power system element models have been proposed. One of the solutions is to use a multi-rate simulation technique [20, 21, 22, 23]. According to this technique, the system differential equations are partitioned into fast and slow subsystems. Models containing fast dynamics are solved in a smaller time step, while the ones containing slow dynamics are solved in a larger time step. Another solution is to utilize an implicit integration method for power system stability studies [24, 25]. An underlying concept of implicit integration method is described in section 2.5.

2.3 Issues in Modeling Wind Turbines

As wind power is a relatively new technology in power generation, modeling wind power generation entails several consequences. A number of substantial issues in modeling wind turbines for power system stability studies are addressed below.

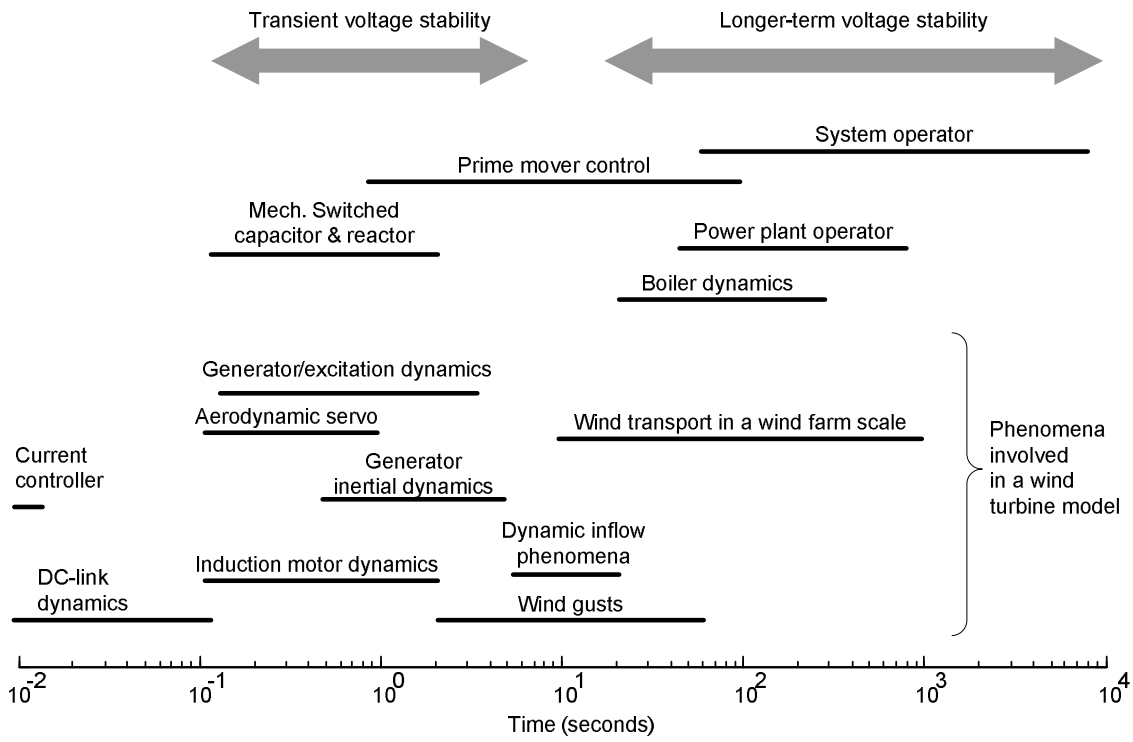

Figure 2.1. Power system and wind turbine component time constant. Data are compiled from [17, 18, 19].

2.3.1 Absence of standardized model

Built-in wind turbine models are lacking in power system stability simulation tools. This causes problems for utility companies that want to investigate the influence of wind power generation on the power system. Developing user-defined models for wind power generation obviously requires substantial efforts.

Many built-in models provided in power system simulation tools do not sufficiently represent the current wind turbine technologies in the market. This is because different wind technologies continuously emerge into the market while earlier technologies are being rapidly improved to adapt to new requirements. The situation faced by utility companies is more difficult as models provided by manufacturers are usually received by the companies as "black-box" components without sufficient information on how the models work. This problem is a consequence of the fact that wind turbine product models are commonly treated as confidential matters by manufacturers.

This situation explains why, thus far, there has been no agreement on standardized models of wind power generation. Despite a consensus on different basic concepts of wind turbine technologies as described in Section 1.2, there is currently no common consensus among experts on representing the level of detail of wind power generation models for power system stability studies.

There is an ongoing effort led by the Western Electricity Coordinating Council (WECC) to establish an industry standard for wind turbine models [26]. Nevertheless, experts disagree on the level of detail of the models specifically related to drive train and aerodynamic models.

In addition, there has also been a joint effort by a number of utility companies to

establish a common test network, to be used to compare and verify the response of various wind turbine models [27]. This effort can be seen as another alternative towards establishing generic models of wind power generation. However, without understanding the actual control and pertinent physical mechanisms of wind turbine models, this effort may not be sufficient to establish standardized models.

2.3.2 Validation

In order to provide a confidence model for power system stability studies, a power generation dynamic model must be validated. The importance of such a validation from a power industry perspective as well as current practice in the validation procedure has been addressed by Feltes et.al in [28]. However, wind power generation models are in many aspects different from conventional power generation units. Uncontrolled input power and the complexity of system components, which involves a large frequency range, are among the challenges faced in validating a wind power generation model. Hence it is not surprising that, until now, very few wind turbine models have been validated against actual measurement data.

In [29], three different types of testing are proposed for validating a wind power generation model, namely; staged generator testing, staged full-scale turbine testing and opportunistic testing.

Staged generator testing includes only the generator, power converter and controls. This type of test can be conducted by making use of a test bench facility. The test can be carried out under well-defined conditions and can be repeated several times. The performance of the power converter and its controller, especially during severe transient disturbances, can be sufficiently demonstrated using this type of test. However, the lack of a complete representation of drive-train and blade components means that this type of validation is unable to capture the dynamic response of these components in a stability study. An example of this type of testing can be found in [30].

In staged full-scale turbine testing, the test is performed with a full-scale turbine at a dedicated test facility. The test must be designed in such way that the unit does not interfere with the power system. Alternatively, the test unit can be designed as a mobile unit, as reported in [31]. Such a mobile test unit is capable of triggering a voltage dip at any wind turbine terminals, while maintaining the adjacent power system undisturbed. The results of a wind turbine validation using this mobile test unit are presented in [31].

Opportunistic testing is carried out by installing measurement devices on an existing wind farm site. This measurement device records naturally occurring power system disturbances. Such testing and validation have been reported in [32, 33, 34, 35].

2.3.3 Technical issues in model implementation

This section elaborates several technical issues related to the implementation of wind power generation models in power system simulation tools.

Integration time step issues

Very small integration time steps required by wind turbine models is one of the most common issues in modeling wind power generation for power system stability studies. The maximum integration time step of a power system simulation is typically set based on the complexity and the size of the system being investigated, in order to avoid excessive simulation time.

With the typical time frame used in large power system stability studies, it is impractical to model a wind turbine or a wind farm that requires a very small time step. Normally, a smaller integration time step is needed as the complexity of a wind turbine model increases. Inline with this issue, a performance-oriented model for a wind turbine has been proposed as an alternative to a component-oriented model [36]. Accordingly, the complexity of a wind turbine model must be reduced as much as possible without jeopardizing the performance of the model performance for any particular study.

This is particularly relevant considering that, in most cases, wind power generation currently accounts only for a small part of the power system. Reducing a simulation time step to accommodate wind power generation models in a large power system model is obviously not beneficial.

This issue is highly relevant when a utility company needs to perform several simulation scenarios. Current development of computer technology enables faster power system simulations than those in the past. Nevertheless, today's power system sizes are becoming larger and more complex.

The Irish transmission system operator (ESB National Grid), for instance, clearly states in its grid code that wind turbine models must be able to run with an integration time step no less than 5 ms [37, 29]. Although it is not mentioned in the grid code, the Swedish transmission company Svenska Kraftnät specifies 10 ms as the minimum integration time step.

Compatibility with fundamental frequency simulation tools

In order to accurately simulate converter protection, including stator current dc components in a wind turbine stability model is suggested in some papers [38, 8]. On the other hand, including dc-components introduces oscillating output at system frequency into the network model, which is typically represented as a fundamental frequency model. Including dc-components poses the problem of compatibility between the wind turbine and the network models. Accordingly, any dynamic response of a wind turbine model associated with the presence of dc-components is not taken into account. Including dc-components in stability studies also contradicts the common notion of the classic stability-approach as described in [39].

Initialization

The initialization process is a crucial step in a dynamic simulation. A typical power system dynamic simulation procedure is presented in Fig. 2.2. A dynamic simulation is started by incorporating the dynamic model data into the simulator. Thereafter, state variables and other variables of the dynamic simulation models must be initialized based on initial load flow data. If the initialization is not carried out correctly, the system will start at an unsteady condition. In some cases, the system may move toward an

equilibrium condition after some time, and the desired state, as obtained from the initial load flow, may not be achieved. In a worst case scenario, instead of moving toward a convergence, the system may become unstable and finally the simulation may come to a halt.

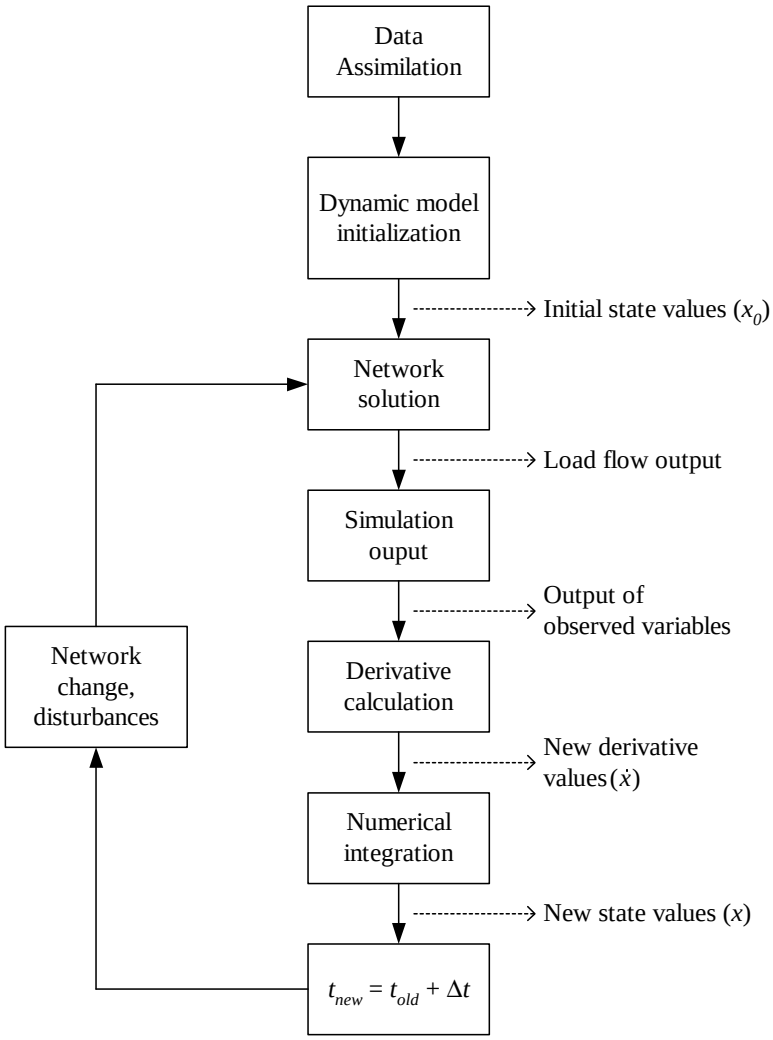

Figure 2.2. Dynamic simulation flow.

As a part of dynamic models, the wind turbine model must be properly initialized. However, as reported in [29], many wind turbine models exhibit unexpected responses due to inappropriate initialization. These unexpected responses include uncharacteristic and unsteady initial responses in the beginning of the simulations. A false initialization may also lead to undesired results without causing simulation instability or a strange dynamic response. One of such a case is given in section 3.12.

2.4 Interconnection Requirements for Wind Power Generation

Recent growth in wind power generation has reached a level where the influence of wind turbine dynamics can no longer be neglected. Anticipating this challenge, power system operators have imposed requirements for grid-connected wind turbines to assure the stability of the system. Consequently, a wind turbine model must be capable of simulating pertinent phenomena corresponding to these requirements.

Grid requirements can generally be summarized into several categories as presented in [40]. Some categories related to power system stability are described below.

2.4.1 Operating voltage and frequency range

Many grid codes specify the operating voltage and frequency ranges in which wind farms must be able to stay connected for a certain period of time with a certain level of power production. This specification is commonly given in the form of a voltage and frequency chart. Fig. 2.3 shows a voltage and frequency chart in the Svenska Kraftnät grid code [41]. This specification entails wind turbine models to be able to simulate correct responses for different areas defined in the chart.

2.4.2 Active power control

A number of grid codes require wind power production to fulfill certain conditions. These requirements may include:

Maximum power limit Normally, a wind generation-related grid code sets a certain maximum limit on wind farm production. According to Svenska Krafnät's grid code [41], a wind farm is not allowed to produce active power beyond its power rating.

Power maneuver The rate of change in active power production for a wind farm is specified in several grid codes. Maximum power ramp during normal operation such as during start up and normal shut down of wind farms must not exceed a certain value. This power ramp limit can also be imposed for abnormal situations such as during recovery following a grid fault or when wind speed reaches the cut-off limit.

Svenska Kraftnät grid code stipulates that the maximum ramp up of power during the start up of a wind farm shall not be higher than 30 MW per minute. In contrast, during shut down of a wind farm due to cut-off, wind speed shall not result in power ramp down more than 30 MW per minute. On the other hand, a wind farm is required to be able to reduce power production below 20 percent of maximal power production within 5 seconds when necessary [41].

Frequency control A number of grid codes, such as in Denmark [42], Ireland and Germany, clearly specify that wind farms are required to participate in frequency control.

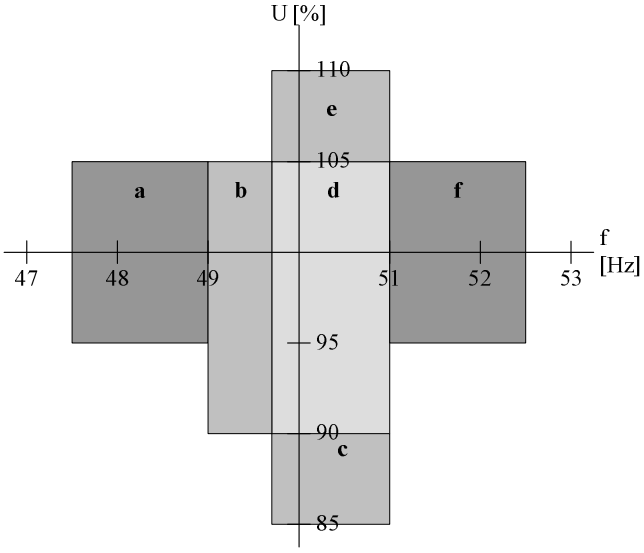

Area	Frequency/ voltage	Power output	Operation time	Misc.
a	47.5 – 49.0 95-105%	5% reduction	>30 min	
b	49.0 – 49.7 90-105%	Uninterrupted	Continuously	
c	49.7 – 51.0 85 – 90%	< 10% reduction	> 1 hour	Not applied for wind farms
d	49.7 – 51.0 90 – 105%	Uninterrupted	Continuously	
e	49.7 – 51.0 105 – 110%	< 10% reduction	> 1 hour	
f	51.0 – 52.5 95 – 105%	Reduced	> 30 min	Back to normal production within 1 min when f < 50.1 Hz. For wind farms the frequency interval is 51.0 – 52.0 Hz.

Figure 2.3. Voltage and frequency limits chart for large generating unit, including wind farms with capacity larger than 100 MW, according to Svenska Krafnät's grid code.

A uniqueness of wind power generation compared to conventional power generation is that input power is unregulated. On the other hand, the relation between wind speed and the mechanical input of a wind turbine are highly non-linear. This fact underlines the importance of involving wind speed and aerodynamic models in a wind turbine model.

2.4.3 Voltage and reactive power control

Reactive power requirements are specified differently among grid codes. In Denmark, the reactive power demand must be maintained within the control band. The range limits of the control band are a function of wind farm active power production [42].

In Ireland, the national grid operator EirGrid assigns wind farm reactive power requirements in the form of power factor [43]. EonNetz and VDN, two grid operators in Germany, require that the reactive power demand of a wind farm is regulated based on the voltage level at the connection point.

According to Svenska Krafnät grid code, a wind farm must be provided with an automatic voltage regulator which is capable of regulating voltage within ±5% of nominal voltage. In addition, the wind farm must be designed to be able to maintain zero reactive power transfer between the farm and the grid.

2.4.4 Fault ride-through capability

Another noteworthy grid connection requirement for wind farm operators is intended to provide wind turbines with fault ride-through capabilities. This means that a wind farm may not be disconnected during a grid fault. Typically, a grid code specifies a voltage profile curve in which a wind farm is not allowed to be disconnected if the voltage during and following a fault is settled above a specified curve. This curve is defined based on the historical voltage dip statistics of the network system such as explained in [44].

Svenska Kraftnät, for instance, has stated that wind farms with installed capacity of more than 100 MW are not allowed to be disconnected in the event of a grid fault if the voltage on the point of common coupling (PCC) is above the curve depicted in Fig. 2.4 [41]. In other words the wind farm must stay connected to the grid as long as the voltage of the main grid where the farm is connected is above the criteria limit.

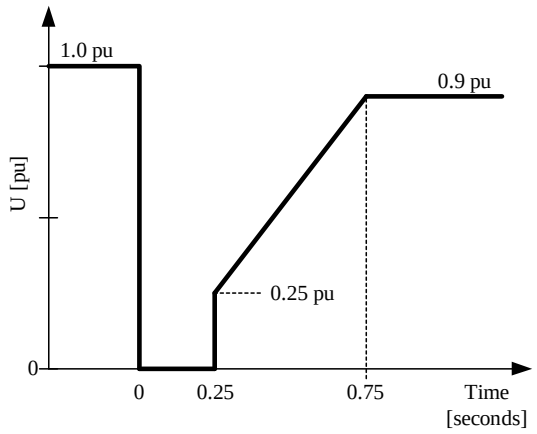

Figure 2.4. Voltage limit criteria during fault for large generation unit, including wind farm larger than 100 MW, according to Svenska Krafnät's grid code.

For a medium-sized wind farm (25 - 100 MW), the grid code specifies that the farm must be able to stay connected during a fault that causes the voltage at the main grid where the farm is connected to step down to 0.25 pu for 250 ms followed by a voltage step up to 0.9 pu and staying constant at this level.

Each type of wind turbine has specific vulnerabilities when subjected to a voltage dip due to a grid fault. Consequently, a wind turbine model must be able to simulate fault ride-through capability correctly. The main challenge is that the fault ride-through procedure often requires discontinuities in the simulation routine. Such

discontinuities, for example, can be caused by changes in wind turbine circuit topology. If not treated correctly, these discontinuities may eventually cause model instability.

2.5 Numerical Integration Methods

In a broad sense, the efficiency of a simulation is mainly governed by the time required to simulate a system for a given time-frame of study.

Two factors that affect simulation efficiency are the numerical integration method used in a simulation tool and the model algorithm. The first factor is explored in this section, while the latter is discussed in other chapters of this thesis. The two different integration methods used in the simulation tool PSS/E are described in this section.

The examination of numerical integration methods presented in this section is intended to identify the maximum time step permitted for a particular model in order to maintain simulation numerical stability. Ignoring a numerical stability limit may lead to a model malfunction owing to a very large integration time step. To avoid such a problem, either the simulation time step must be reduced or the model's mathematical equations must be modified. A typical time step used in two commercial simulation tools is shown in Table 2.1.

Table 2.1: Typical simulation time step in commercial simulation tools[45, 46].

PSS/E	**PowerFactory**
Standard simulation: half a cycle (0.01 s for 50 Hz and 0.00833 s for 60 Hz system)	Electromagnetic Transients Simulation: 0.0001 s
Extended-term simulation: 0.05 to 0.2 s	Electromechanical Transients Simulation: 0.01 s
	Medium-term Transients: 0.1 s

2.5.1 Numerical stability and accuracy

Two essential properties of numerical integration methods are numerical stability and accuracy.

The concept of stability of a numerical integration method is defined as follows [47]: If there exists an $h_0 > 0$ for each differential equation, such that a change in starting values by a fixed amount produces a bounded change in the numerical solution for all h in $[0, h_0]$, then the method is said to be stable. Where h is an arbitrary value representing the integration time step.

Typically, a simple linear differential equation is used to analyze the stability of a numerical integration method. This equation is given in the form

$$\dot{y} = -\varphi y, \quad y(0) = y_0 \tag{2.1}$$

where y is a variable and φ is a constant. This equation is used to examine the stability of the numerical integration method discussed sections below. The accuracy of a numerical method is related to the concept of convergence. Convergence implies that any desired degree of accuracy can be achieved for any well-posed differential equation by choosing a sufficiently small integration step size [47].

Power system equations as a stiff system

The concept of stiffness is a part of numerical integration stability. A system of differential equations is said to be stiff if it contains both large and small eigenvalues. The degree of stiffness is determined by the ratio between the largest and the smallest eigenvalues of a linearized system. In practice, these eigenvalues are inversely proportional to the time constants of the system elements.

Stiff equations pose a challenge in solving differential equations numerically, since there is an evident conflict between stability and accuracy on one hand and simulation efficiency on the other hand.

By nature, a power system is considered to be a stiff equation system since a wide range of time constants is involved. This is certainly a typical problem when simulating short- and long-term stability phenomena. In a broad sense, time constants involved in power systems can be classified into three categories: small, medium and large time constants.

Among system quantities and components associated with small time constants, that reflect the fast dynamics of the power system, are stator flux dynamics, most FACTS devices and other power electronic-based controllers. Rotor flux dynamics, speed deviation, generator exciters and rotor angle dynamics in electrical machines belong to quantities and components with medium time constants. Large time constants in power system quantities can be found, for instance, in turbine governors and the dynamics of boilers.

Appropriate representations in stability studies for most conventional power system components with such varied time constants are discussed thoroughly in the book [39]. This book also introduces a number of model simplifications and their justification for stability studies. Most simplifications can be realized by neglecting the dynamics of quantities with small time constants. Since wind turbines, as a power plant, are comparatively new in power system stability studies, they are not mentioned in the book.

Like other power system components, a wind turbine consists of a wide range of time constants as shown in Fig. 2.1. Small time constants in a wind turbine model are encountered, for instance, in the stator flux dynamics of generators and power electronics. While mechanical parts, aerodynamic components and rotor flux dynamics normally consist of medium time constants. Even larger time constants are involved in wind transport phenomena. Hence, it is clear that wind turbine models have the potential to be a source of stiffness for a power system model if they are not treated carefully.

2.5.2 Explicit vs implicit numerical integration methods

Numerical integration methods can be divided into two categories: the explicit method and the implicit method. In order to illustrate the difference between the two methods, let us take an ordinary differential equation

$$\dot{y}(t) = f(t, y(t)) \tag{2.2}$$

Numerically, the equation can be approximated using a general expression as follows

$$\dot{y}(t_n) \approx \frac{y(t_{n+1}) - y(t_n)}{h} = \phi \left(\begin{array}{l} t_{n-k}, \ldots, t_n, t_{n+1}, \\ y(t_{n-k}), \ldots, y(t_n), y(t_{n+1}) \end{array} \right) \tag{2.3}$$

where h denotes the integration time step size and ϕ is any function corresponding to the numerical integration method used. Since $y(t_{n+1})$ is not known, the right-hand side cannot be evaluated directly. Instead, both sides of the equation must be solved simultaneously. Since the equation may be highly nonlinear, it can be approximated numerically. This method is called the implicit method.

Alternatively, $y(t_{n+1})$ on the right-hand side can be replaced by an approximation value $\hat{y}(t_{n+1})$. One of the methods discussed in this thesis is the modified Euler method (sometimes referred to as the Heun method).

As stated previously, the simulation tool PSS/E uses the modified Euler method for the standard simulation mode and the implicit trapezoidal method for the extended term simulation mode. These two integration methods are described below.

Modified Euler method

The modified Euler integration method is given as

$$w_{i+1} = w_i + \frac{h}{2} \left[f(t_i, w_i) + f(t_{i+1}, w'_{i+1}) \right] \tag{2.4}$$

where w'_{i+1} is calculated using the ordinary Euler method

$$w'_{i+1} = w_i + h \left[f(t_i, w_i) \right] \tag{2.5}$$

For a given differential equation $\dot{y} = -\varphi y$, the stability region of the modified Euler method is given as

$$\left| 1 + h\varphi + \frac{(h\varphi)^2}{2} \right| < 1 \tag{2.6}$$

This means that in order to maintain simulation stability, $h\varphi$ must be located inside the closed shaded area as shown in Fig. 2.5. If φ is a real number or if real parts of φ are considerably larger than its imaginary parts, h can be estimated as

$$h < -\frac{2}{\varphi} \tag{2.7}$$

However, if a complex number of φ is dominated to a great extent by its imaginary part, the h must fulfill the following relation

$$h < -\frac{1}{2\varphi} \tag{2.8}$$

Thereby, a φ dominated by imaginary parts must constitute a smaller simulation time step in order to maintain simulation stability.

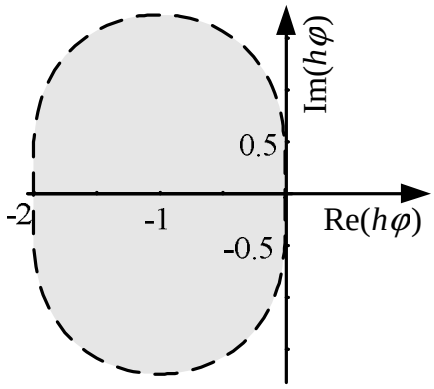

Figure 2.5. Stable region of modified Euler integration method.

Implicit trapezoidal method

The implicit trapezoidal method belongs to A-stable methods. A method is said to be A-stable if all numerical approximations tend to zero as a number of iteration steps move towards infinity ($n \to \infty$) when it is applied to the differential equation $\dot{y} = \varphi y$, with a fixed positive time step size h and a (complex) constant φ with a negative real part [47].

Consequently, as long as the eigenvalue of the differential system lies in the left-hand side of the complex plane, the system is stable regardless of time step size h, as shown in Fig. 2.6. This method allows for variable integration step size.

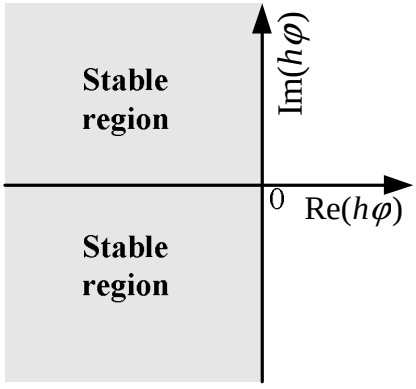

Figure 2.6. Stable region of modified implicit trapezoidal integration method.

Chapter 3

Fixed-speed Wind Turbines

Models of various FSWT components, controls and FRT schemes are described in this chapter. The importance of these components and controls in characterizing FSWT model responses is examined. A validation of an FSWT model against field measurements is also presented in this chapter.

3.1 Introduction

A fixed-speed wind turbine with a squirrel cage induction generator is the simplest electrical topology in a wind turbine concept. The schematic structure of the turbine is illustrated in Fig. 3.1.

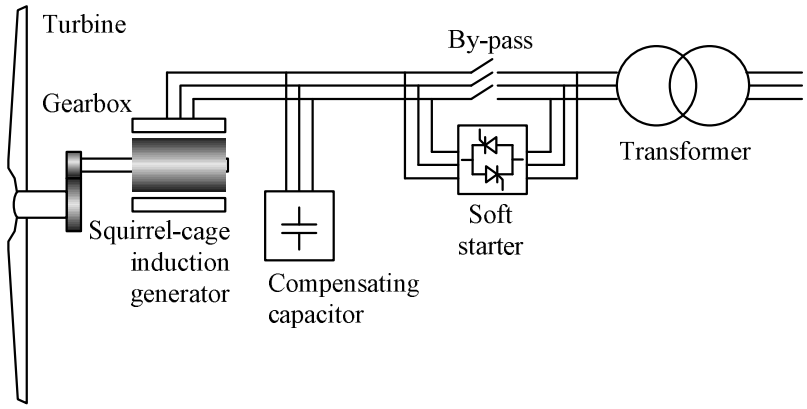

Figure 3.1. System structure of fixed-speed wind turbine with direct connected squirrel cage induction generator.

The turbine blades convert the kinetic energy of wind into rotational mechanical energy. The squirrel cage induction generator transforms the mechanical energy into electrical energy and delivers the energy directly to the grid. Note that the rotational speed of the generator is relatively high − in the order of 1000-1500 rpm for a 50 Hz system frequency. Such rotational speed is too high for the turbine rotor speed with respect to turbine efficiency and mechanical stress. Thus, the generator speed must be stepped down using a multiple-stage gearbox with an appropriate gear ratio.

An induction generator consumes a significant amount of reactive power even during zero power production. The reactive power consumption increases along with active power output. Accordingly, a capacitor bank must be provided close to the generator terminal in order to compensate for this reactive power consumption so that the generator does not burden the grid.

Since mechanical power is converted directly to a three-phase electrical system by means of an induction generator, no complex controller is involved in the electrical part of a fixed-speed wind turbine. For an active stall fixed-speed wind turbine, however, a pitch controller is needed to regulate the pitch angle of the turbine.

The advantages of a fixed-speed wind turbine are that it has a simple design with high reliability and has low investment and maintenance costs. However, low aerodynamic efficiency, high mechanical stress during gusty wind speeds, and difficulties in adapting to new grid compliances, such as fault ride-through and reactive power support, are among the shortcomings of this concept.

The share of fixed-speed wind turbines in the wind power market is steadily decreasing. Some product examples of this type of wind turbine are the Siemens SWT-2.3-82 [48], and the Vestas V82-1.65 MW [49].

3.2 Induction Generator Model

Depending on the level of detail of the model, an induction generator can be represented in different ways. The detail of the model is mainly characterized by the number of phenomena included in the model. There are several major phenomena in an induction generator such as:

The stator and rotor flux dynamics Stator and rotor flux dynamics are related to the behavior of the fluxes in the associated windings. Since the current in an inductive circuit is considered to be a state variable, it cannot change instantaneously. The same behavior applies to stator and rotor fluxes because they are proportional to currents.

Magnetic saturation Magnetic saturation is encountered due the nonlinearity of the inductance. Main and leakage flux saturations are associated with nonlinearity in magnetic and leakage inductances, respectively.

Skin effect As frequency gets higher, the rotor current tends to move towards the periphery of the rotor conductor. This causes an increase in the effective rotor-resistance.

Core losses Eddy current losses and hysteresis are among other phenomena that occur in an induction generator and are known as core losses.

It is possible to include all the dynamics of an induction generator in a highly detailed model. Nevertheless, such a model may not be beneficial for stability studies because it increases complexity and can be computationally prohibitive. More importantly, not all of these dynamics have a significant influence on a stability analysis.

A comprehensive discussion of a comparison of different induction generator models can be found in [50]. The inclusion of iron losses in a model needs a complicated task.

On the other hand, the influence of these losses on stability studies is insignificant. Main flux saturation is only of importance when the flux level is higher than the nominal level. Hence, this effect can be ignored for most operating conditions. The skin effect should only be taken into account for a large slip operating condition, which is not the case for a fixed-speed wind turbine generator.

Another constraint of inclusion dynamics in the model is the availability of data. Typically, saturation and skin effect data are not provided by manufacturers. Therefore, it is generally impractical to include the phenomena in a wind turbine model.

These argumentations lead to the conclusion that only stator and rotor dynamics are the major factors to be considered in an induction generator model. Accordingly, in this thesis, a model that includes both stator and rotor flux dynamics is used as the reference model.

In modeling an induction generator, a number of conventions are used in this report as follows:

- The model is written based on a dq reference frame fixed to a synchronous reference frame.
- The q-axis is assumed to be 90° ahead to the d-axis in respect to the frame rotation direction.
- The d-axis and q-axis are chosen as the real and imaginary parts of the complex quantities, respectively.
- The stator current is assumed to be positive when it flows into the generator. This convention is normally adopted in a motor model rather than in a generator model. This convention is preferred because, in most literature, an induction machine exists as a motor rather than as a generator. Hence, representation of the model using a motor convention is used because of familiarity.
- All parameters are given in per unit quantities.

The following assumptions are also applicable: First, no zero-sequence current is present. Second, the generator parameters in each phase are symmetrical and the windings are assumed to be equivalent sinusoidally distributed windings. Air-gap harmonics are therefore neglected.

3.2.1 Fifth-order model

As stated earlier, the detailed model of an induction generator involves both stator and rotor dynamics. This model is also referred to as the fifth-order induction generator model, since it consists of five derivatives, i.e. four electrical derivatives and one mechanical derivative. In some papers, this model is also known as the electromagnetic transient (EMT) model. The equivalent circuit of the dynamic model is represented in Fig. 3.2.

Stator and rotor voltage equations can be written according to the well-known representation as follows

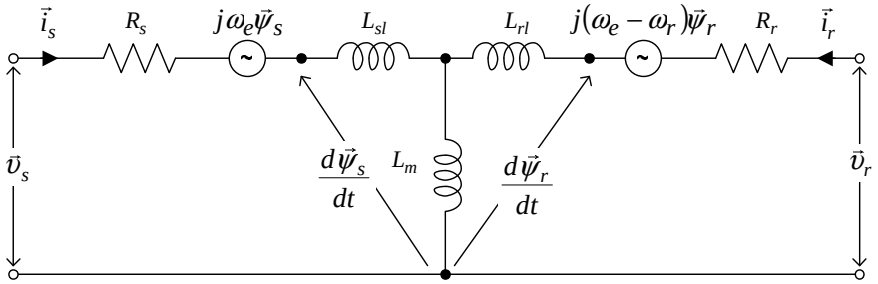

Figure 3.2. Equivalent circuit of an induction generator dynamic model.

$$\vec{v_s} = \vec{i_s}R_s + j\omega_e\vec{\psi_s} + \frac{d\vec{\psi_s}}{dt} \tag{3.1}$$

$$\vec{v_r} = 0 = \vec{i_r}R_r + j(\omega_e - \omega_r)\vec{\psi_r} + \frac{d\vec{\psi_r}}{dt} \tag{3.2}$$

where $\vec{v}$, $\vec{i}$ and $\vec{\psi}$ denote the voltage, current and flux quantity, respectively, and ω is the rotational speed. The subscripts $\vec{s}$ and $\vec{r}$ refer to quantities of the stator and rotor, respectively.

The relation between flux and currents is given by

$$\vec{\psi_s} = \vec{i_s}L_s + \vec{i_r}L_m \tag{3.3}$$

$$\vec{\psi_r} = \vec{i_r}L_r + \vec{i_s}L_m \tag{3.4}$$

where L_m is the magnetizing reactance, L_s and L_r stand for the stator and rotor inductances, respectively. The two latter parameters are given by

$$L_s = L_{sl} + L_m \tag{3.5}$$

$$L_r = L_{rl} + L_m \tag{3.6}$$

where L_{sl} and L_{lr} are the stator and rotor leakage inductances, respectively.

The electromagnetic torque produced by the generator can be calculated as a cross-product of flux and current vectors

$$T_e = \vec{\psi_s} \times \vec{i_s} \tag{3.7}$$

This is equivalent to

$$T_e = \Im\left[\vec{\psi_s}^* \vec{i_s}\right] \tag{3.8}$$

The complex power of the stator is given by

$$\vec{S} = \vec{v_s}^* \vec{i_s} \tag{3.9}$$

In a double squirrel-cage induction generator, where the rotor consists of two layers of bar, both are short-circuited by end rings. This arrangement is employed to reduce the starting current and to increase the starting torque by exploiting the skin effect.

However, such an arrangement is not used in wind power applications, therefore it is not included in this thesis.

The mechanical equation is given by

$$J_g \frac{d\omega_r}{dt} = T_e - T_m \tag{3.10}$$

where J_g is the generator inertia and T_m is the mechanical torque.

3.2.2 Third-order model

Less detailed representation of an induction generator can be achieved by neglecting stator flux dynamics. This is equivalent to removing two stator flux derivatives from (3.1). Subsequently, the stator and rotor voltage equations become

$$\vec{v_s} = \vec{i_s} R_s + j\omega_e \vec{\psi_s} \tag{3.11}$$

$$0 = \vec{i_r} R_r + j(\omega_e - \omega_r)\vec{\psi_r} + \frac{d\vec{\psi_r}}{dt} \tag{3.12}$$

The electromagnetic torque and the power equations remain the same as in a fifth-order induction generator model.

The exclusion of the stator flux transient in a third-order induction generator model is equivalent to ignoring the dc component in the stator transient current. As a consequence, only fundamental frequency goes into effect. This representation preserves the model compatibility with commonly used fundamental frequency simulation tools. In some literature, this model is referred to as the electromechanical transient model [51].

3.2.3 First-order model

The simplest dynamic model of an induction generator is known as the first-order model. Sometimes this model is referred to as the steady state model, since only dynamics of the mechanical system are taken into account, i.e. no electrical dynamic is involved. The typical steady state equivalent circuit of the first-order model of an induction generator is shown in Fig. 3.3.

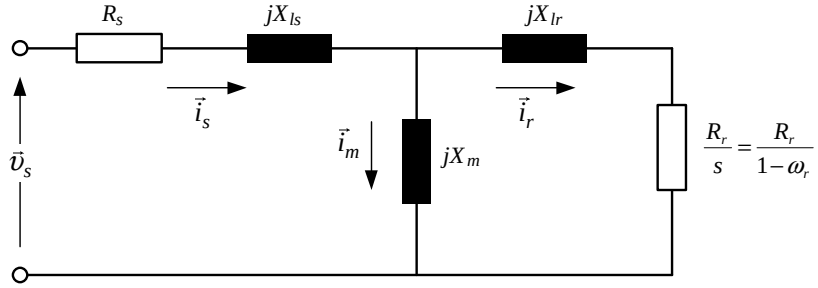

Figure 3.3. Steady state equivalent circuit of induction generator.

3.3 Model of Induction Generator as a Voltage Source

The different induction generator models discussed earlier are basically represented as a current source. In power system stability studies, however, a generator is normally represented as a voltage source behind a transient impedance. In order to adapt to this representation, the models must be modified into voltage source components [39].

3.3.1 Fifth-order model

Representation of a fifth-order induction generator model as a voltage source behind a transient impedance is given as

$$\vec{v_s} = \vec{i_s}R_s + j\vec{i_s}X' + \vec{v_e'} + \frac{d\vec{\psi_s}}{dt} \tag{3.13}$$

$$\frac{d\vec{v_e'}}{dt} = \frac{1}{T_o}[\vec{v_e'} - j(X_s - X')\vec{i_s}] + js\vec{v_e'} + j\frac{X_m}{X_r}\vec{v_r} \tag{3.14}$$

where X_s, X_r, X_m and X_s' refer to the stator, rotor, magnetizing and transient reactances, respectively. T_o is the transient open-circuit time constant of the induction generator. These variables are given by

$$X_s = \omega_e L_s \tag{3.15}$$
$$X_r = \omega_e L_r \tag{3.16}$$
$$X_m = \omega_e L_m \tag{3.17}$$
$$X' = \omega_e(L_s - \frac{{L_m}^2}{L_r}) \tag{3.18}$$
$$T_o = \frac{L_r}{R_r} \tag{3.19}$$

The electromagnetic torque can be expressed as

$$T_e = \frac{\vec{v_e'}\vec{i_s}^*}{\omega_e} \tag{3.20}$$

3.3.2 Third-order model

Similarly, representation of the third-order model as a voltage source behind a transient impedance can be obtained by removing the stator flux derivative in (3.14), while keeping the remaining equations the same.

$$\vec{v_s} = \vec{i_s}R_s + j\vec{i_s}X' + \vec{v_e'} \tag{3.21}$$

Equation (3.21) can further be represented as a voltage source behind a transient impedance as shown in Fig. 3.4, which is a standardized representation in power system stability studies.

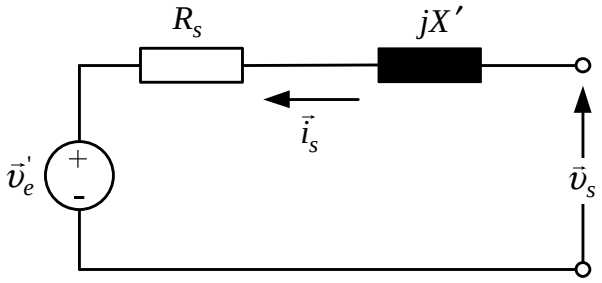

Figure 3.4. Transient representation of the third-order induction generator model.

3.3.3 First-order model

For the first-order induction generator model, all equations for the third-order model remain valid except for the transient voltage source which is calculated as

$$\frac{d\vec{v_e'}}{dt} = \frac{jX_m{}^2 R_r \vec{v_s}^2}{X_r\left(X_m{}^2 + R_r R_s - sX_s X_r\right)} \tag{3.22}$$

In practice, this model does not contribute short-circuit current to the grid, therefore it is recommended that the first-order model of an induction generator is represented as a negative load rather than as a generator.

3.4 Modified Fifth-Order Induction Generator Model

A fifth-order induction generator model cannot be implemented directly into a fundamental frequency network model owing to the involvement of stator flux dynamics, which are equivalent to the presence of a dc-offset in the stator current, as explained in subsection 3.2.1. In fact, the fundamental frequency network model is the most commonly used in stability simulation tools rather than the instantaneous network model. This is because a much more efficient simulation time can be performed by utilizing the fundamental frequency network model.

Accordingly, in order to interface a fifth-order induction generator model with the fundamental frequency network model, the dc-offset component in the stator current of a fifth-order induction generator model must be removed. This can be done by using the procedure proposed below.

Dc-offset removal contained in the stator current

Based on (3.13), the Thevenin equivalent of a fifth-order induction generator model can be derived as shown in Fig. 3.5.

Considering Fig. 3.5, according to the superposition theorem for electric circuits, the stator current is composed of two components which correspond to two voltage sources, namely: the rotor flux linkage $\vec{v}_e'$ and the rate of change of the stator flux $d\vec{\psi}_s/dt$.

The stator current delivered into the network $\vec{i}_{sf}$ includes only the first component, while the second component is removed. By doing so, the grid recognizes only

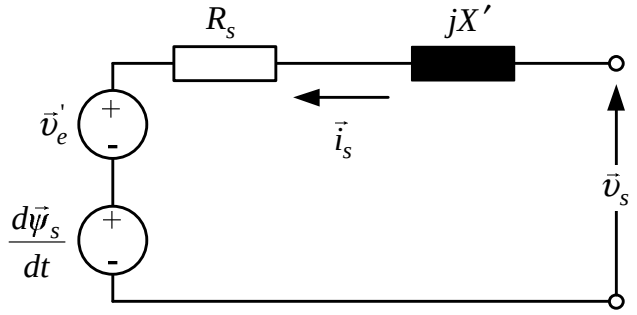

Figure 3.5. Transient representation of the fifth-order induction generator. Observe that the current direction is expressed according to motor convention.

the fundamental frequency component of the stator current. The grid injected stator component is calculated using the following equation

$$\vec{i}_{sf} = \frac{\vec{v}_s - \vec{v}_e'}{R_s + jX'} \tag{3.23}$$

Fig. 3.6 illustrates the stator current and the stator current component that is injected into the grid.

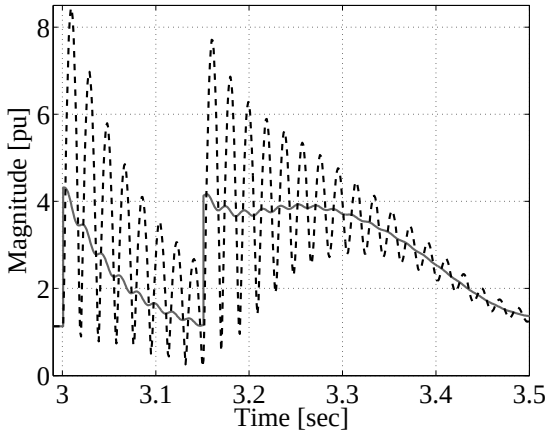

Figure 3.6. Actual stator current magnitude (dash) and stator current component injected into the grid (solid).

The electromagnetic torque of the generator remains to be calculated using the actual stator current. This leads to a more accurate prediction of rotor speed.

Model adaptation with a larger simulation time step

A fifth-order induction generator model requires a considerably small integration time step (approximately 1 ms) in order to maintain numerical stability, while the standard integration time step for stability studies is much larger (10 ms). It is a challenge to keep the model running at such a constraint. In this thesis, utilization of an internal integration loop is proposed as an alternative. In this way, the model will execute an internal loop procedure iteratively at a smaller time step size for each standard integration time step. The Heun integration method has been chosen in this study because this method is relatively simple yet delivers sufficient accuracy.

At each internal loop execution, the model calculates derivatives, performs integrations and advances the internal time sample. This sequence is carried out continuously until it reaches the next standard integration time sample. The stator voltage, as an input to the model, is updated by the network calculation every standard time step. The internal integration loop can be performed by assuming a constant stator voltage at each standard time step. However, this assumption is no longer valid when the stator voltage changes rapidly and continuously, such as in the case of a large frequency deviation. Hence, the value of the stator voltage at each internal integration time step must be estimated. The estimation is derived from the rate of change (slope) of the voltage from the last two standard simulation time samples (t_{n-2} and t_{n-1}).. Subsequently, the rate of change of the voltage at current time sample (t_n) can be estimated. By doing so, the estimated value of the stator voltage of the following integration interval (from t_n to t_{n+1}) can be obtained. A conceptual diagram of the modified model is shown in Fig. 3.7.

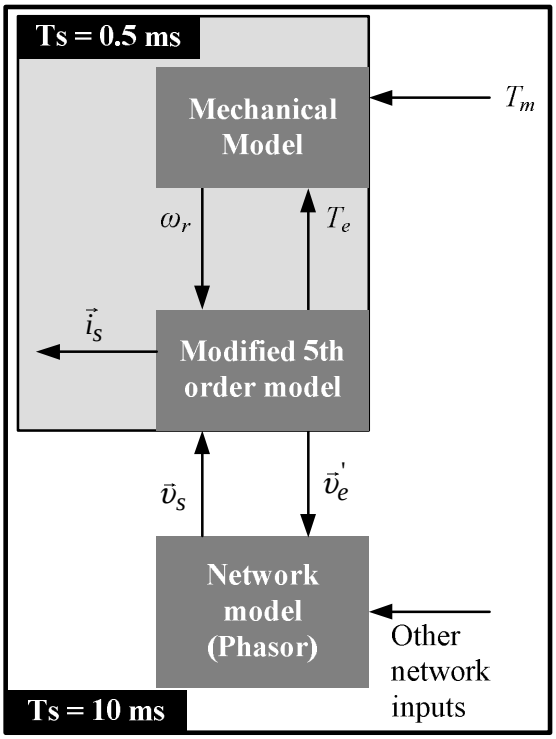

Figure 3.7. Implementation of modified fifth-order induction generator model in PSS/E.

3.5 Drive Train

Different mechanical dynamics take place in a wind turbine. Among the dynamics that may influence electrical response are a 3p effect, tower vibration effects, and torsional dynamics. The 3p effect is caused by a non-homogenous wind speed across the turbine rotor plane and the presence of a tower. For power system stability studies, the 3p and tower vibration effects are of secondary importance because the oscillation magnitude generated by these dynamics is negligible. Hence, only torsional dynamics are taken into account in stability studies.

Compared to other conventional turbine generators, the stiffness of a wind turbine drive-train is significantly lower. The exceptionally low stiffness of a drive train shaft was first addressed by Wasynczuk [52] based on a study performed on a two-blade MOD-2 wind turbine. The study concluded that a lightly damped and low frequency torsional and electric power oscillation can be excited by wind variations due to the flexible drive-train. Later, Hinrichsen [53] pointed out the importance of flexible drive train influence on power system stability when subjected to a grid disturbance, such as fault and load rejection. However, authors disagree on how to define the inertia and the stiffness of a wind turbine drive-train.

According to Wasynczuk [52], a wind turbine drive train can be seen as a multi-mass system consisting of three inertias, which include the generator rotor, the turbine hub and the blades. As a multi-mass system, the system exhibits multi-torsional modes. In the first torsional mode, the blades and hub swing against the generator. The second torsional mode is associated with an oscillation caused by edgewise bending between the blades and the hub. Higher torsional modes are also present due to self oscillation of the hub and the generator.

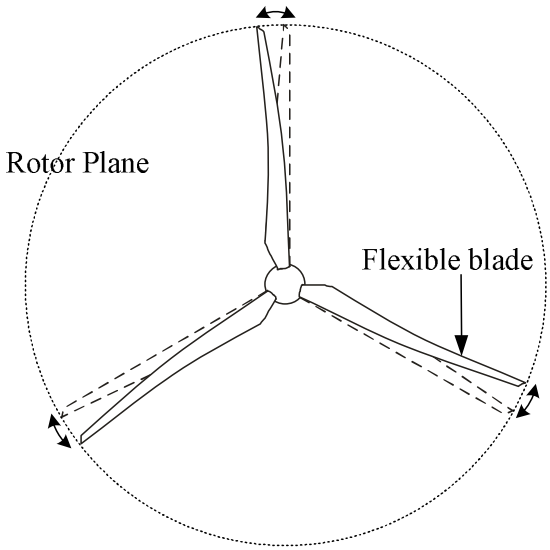

Figure 3.8. In-plane rotor symmetric bending mode.

Similar to [52], in [54, 55], the drive train is modeled as a three-mass model. However, the definition of the inertias is slightly different. These authors consider the blades as flexible. This flexibility is associated with the bending effect of the blades that acts symmetrically in the rotor plane and collinear with the shaft torque as shown in Fig. 3.8. Accordingly, the first inertia consists of the outer sections of the blades, which are flexibly bent. The second inertia consists of the turbine hub, parts of blades that are rigidly connected to the hub, the low speed-shaft, and rotating parts of the gearbox that are stiffly connected to the low speed shaft. It should be noted, however, that defining the first and the second inertia is not straightforward due to the non-uniform distribution of mass and stiffness along the blades. The third inertia includes the generator rotor, the high-speed shaft including a disk brake and rotating parts of the gearbox that are stiffly connected to the high-speed shaft. The second and the third inertias are connected through a shaft and gearbox that are considered to be

flexible. According to the authors, the blade flexibility plays a more important role in the torsional response of a wind turbine. The conceptual model of a three-mass drive-train model is shown in Fig. 3.9.

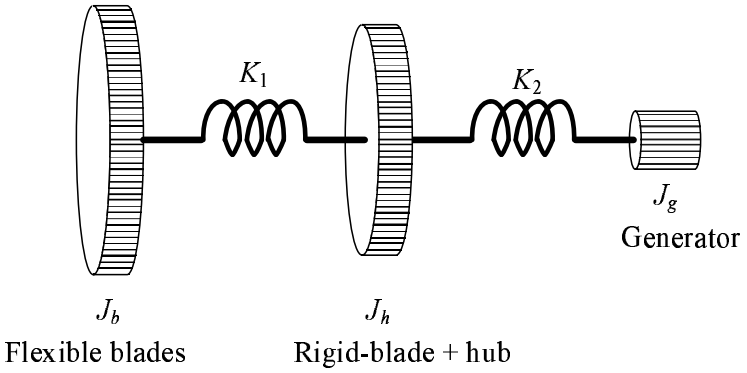

Figure 3.9. Three-mass model of drive train.

A two-mass model of a wind turbine drive train first appeared in [53]. The mathematical model of the two-mass model was elaborated in more detailed in [56]. In a two-mass model, the drive-train of a wind turbine is modeled as two inertias that are connected to each other through a spring. The spring represents the low stiffness of the drive-train shaft. The presence of a gearbox is also believed to be one of main sources of shaft flexibility. In addition to shaft stiffness, different dampings that exist in the two-mass model have been presented in [57].

Trudnowski [58] proposed another two-mass model by considering the turbine blades as the most flexible components of the drive train rather than the gearbox and the shaft. Hence, this model supports the presence of the bending effect of the blades as described earlier. According to this two-mass model, the flexible point is located between the blade tip and the blade root or the so-called blade break point. The first mass consists of the blade tip and the second mass consists of the blade root, the hub, the low and high speed shaft of the turbine. The challenge of adopting this model is that the blade break point is rarely provided by manufacturers.

Representation of a wind turbine drive-train as a three-mass model increases the complexity of the model, which is not desired in power system stability studies. In addition, only the lower frequency is of interest in such a study. Therefore, the representation needs to be reduced into a two-mass model. The derivation of a two-mass model from a three-mass model is presented in [55].

Regardless of disagreements in determining the inertia and stiffness constants of a drive train model, there is major consensus that a two-mass model is sufficient for representing the important dynamics of a turbine drive-train for a power system stability analysis. [59], [60] and [61], reported the importance of a two-mass drive train model for short-term voltage stability studies.

A first validation of a two-mass model against an actual wind turbine is reported in [62]. The adequacy of the two-mass model in the validation of fixed-speed wind turbine model responses to a fault is reported in [33], [34] and [35].

As shown in Fig. 3.10, the structure of a mechanical drive train consists of two inertias. Three different damping components are present in the model, namely the turbine self damping (D_t), the generator self damping (D_g) and the mutual damping

(D_m). The turbine self damping represents the aerodynamic resistance that takes place in the turbine blade. The generator self damping represents mechanical friction and windage. The mutual damping represents balancing dynamics that occur because of different speeds between the generator rotor and the turbine shaft. The mathematical equations of a two-mass drive train model obtained by neglecting the turbine and the generator self dampings are given as

$$2H_t\frac{d\omega_t}{dt} = T_t - K_s(\theta_r - \theta_t) - D_m(\omega_r - \omega_t) \quad (3.24)$$

$$2H_g\frac{d\omega_r}{dt} = -T_e + K_s(\theta_r - \theta_t) + D_m(\omega_r - \omega_t) \quad (3.25)$$

$$\frac{d\theta_t}{dt} = \omega_t \quad (3.26)$$

$$\frac{d\theta_r}{dt} = \omega_r \quad (3.27)$$

where H_t and H_g are the turbine and the generator inertia constant, respectively. K_s is the shaft stiffness, ω_t and ω_r denote the turbine and the generator rotor speed, respectively. θ_t and θ_r denote the turbine and the generator rotor angle, respectively.

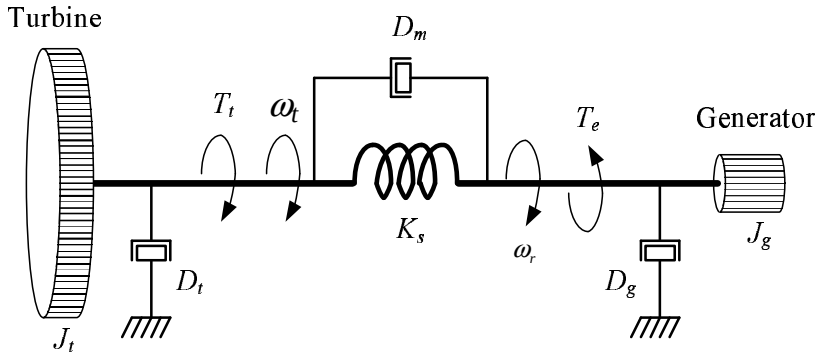

Figure 3.10. Drive train structure of a wind turbine.

One-mass model

A simplified model of the drive train can be obtained by removing shaft stiffness and mutual damping from the drive-train model. Hence, there is only a single inertia which is equivalent to the sum of the generator rotor and the turbine inertias. The mathematical equation of a one-mass model is given by

$$2(H_t + H_g)\frac{d\omega_r}{dt} = T_t - T_e \quad (3.28)$$

3.6 Turbine Rotor Aerodynamic Models

Power extraction from a wind stream in a wind turbine model can be performed using different approaches. The relation between mechanical power input and wind speed passing a turbine rotor plane can be written as follows

$$P_{mec} = 0.5\rho\pi R^2 \upsilon_w^3 C_p(\lambda, \beta) \tag{3.29}$$

where P_{mec} is the mechanical power input, ρ is the air density, R is the rotor blade radius, υ_w is the wind speed and C_p is the coefficient of performance of the turbine rotor, which is a function of pitch angle β and tip speed ratio λ. The tip-speed ratio is obtained from $\lambda = (\omega_t R)/\upsilon_w$.

There are different possible alternatives for modeling the aerodynamic system of a wind turbine such as using the blade element method, $C_p(\lambda, \beta)$ lookup table, analytical calculation and the wind speed-mechanical power lookup table.

3.6.1 The blade element method

According to the blade element method [56, 63], a turbine blade is divided into several cross-sections along the radius. The total forces applied to the blade are the sum of force on each section. Two major force components act on each blade segment, namely a lift force and a drag force. The lift force occurs because of the pressure difference between the two sides of the blade. The force direction is orthogonal to the equivalent wind speed. The drag force acts on the same direction of the equivalent wind speed.

3.6.2 $C_p(\lambda, \beta)$ lookup table

The blade element method agrees rather well with measurement data [56]. The disadvantage of the method is that the model requires time-consuming computational efforts. As an alternative, a $C_p(\lambda, \beta)$ lookup table can be used. Further, mechanical power from the aerodynamic model must be divided by the corresponding rotational speed to obtain mechanical torque. However, the mechanical torque cannot be calculated from the given mechanical power at zero rotational speed. To avoid this difficulty, a torque coefficient lookup table, or a $C_q(\lambda, \beta)$ lookup table, can be used instead. The $C_q(\lambda, \beta)$ lookup table can be found by dividing each element in the $C_p(\lambda, \beta)$ lookup table with the tip speed ratio λ.

3.6.3 Analytical approximation

$C_p(\lambda, \beta)$ characteristic of a turbine aerodynamic model can also be approximated by non-linear functions. One such function is given by [56] in the following form

$$C_p(\lambda, \beta) = c_1 \left(c_2 - c_3\beta - c_4\beta^x - c_5\right) e^{-c_6} \tag{3.30}$$

Coefficients c_1 to c_6 are dependent on the characteristic of the wind turbine in question. The following are exemplary values for c_1 to c_6 as given in [56]

$$\begin{array}{lll} c_1 = 0.5 & c_2 = 116/\lambda_i & c_3 = 0.4 \\ c_4 = 0 & c_5 = 5 & c_6 = 21/\lambda_i \\ x = 1.5 & & \end{array}$$

where

$$\lambda_i = \left(\frac{1}{\lambda + 0.08\beta} - \frac{0.035}{\beta^3 + 1}\right)^{-1}$$

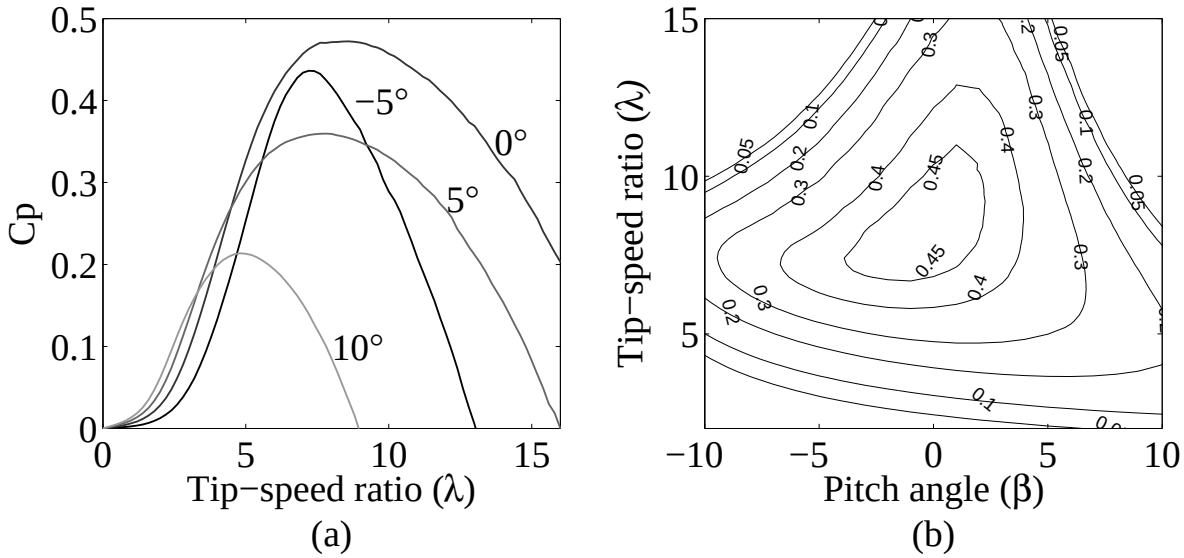

Figure 3.11. Cp-curve for different pitch angles (a) and contoured view (b).

Another approximation method of $C_p(\lambda, \beta)$ characteristic is presented in [64]. The expression of the approximation function is given as

$$C_p(\lambda, \beta) = \sum_{i=0}^{4} \sum_{j=0}^{4} \alpha_{i,j} \beta^i \lambda^j \tag{3.31}$$

The coefficients $\alpha_{i,j}$ are given in the following table where the approximation is only accurate for $2 < \lambda < 13$.

Table 3.1. Coefficient $\alpha_{i,j}$.

i\ j	0	1	2	3	4
0	$-4.19 \cdot 10^{-1}$	$2.18 \cdot 10^{-1}$	$-1.24 \cdot 10^{-2}$	$-1.34 \cdot 10^{-4}$	$1.15 \cdot 10^{-5}$
1	$-6.76 \cdot 10^{-2}$	$6.04 \cdot 10^{-2}$	$-1.39 \cdot 10^{-2}$	$1.07 \cdot 10^{-3}$	$-2.39 \cdot 10^{-5}$
2	$1.57 \cdot 10^{-2}$	$-1.10 \cdot 10^{-2}$	$2.15 \cdot 10^{-3}$	$-1.49 \cdot 10^{-4}$	$2.79 \cdot 10^{-6}$
3	$-8.6 \cdot 10^{-4}$	$5.7 \cdot 10^{-4}$	$-1.05 \cdot 10^{-4}$	$5.99 \cdot 10^{-6}$	$-8.92 \cdot 10^{-8}$
4	$-1.48 \cdot 10^{-5}$	$-9.48 \cdot 10^{-6}$	$1.62 \cdot 10^{-6}$	$-7.15 \cdot 10^{-8}$	$4.97 \cdot 10^{-10}$

3.6.4 Wind speed - mechanical power lookup table

If wind speed and rotor speed dynamics are considered to be slow throughout a study, the relation between wind speed and mechanical power can be presented as a two-dimensional lookup table (see Fig. 3.12). This model is suitable for long-term power system stability studies where the dynamics of the aerodynamic system can be ignored without neglecting the influence of wind speed fluctuation on mechanical and electrical output power.

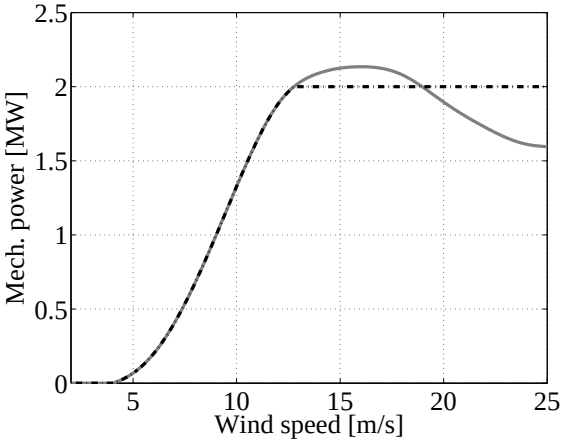

Figure 3.12. Mechanical power input as a function of wind speed for typical 2-MW fixed-speed wind turbine: passive stall (grey solid) and active stall (black dash-dotted).

3.7 Active Stall Control

Limiting mechanical input power so that rated power is not exceeded is an essential aspect for a wind turbine. This can be done using different alternatives, for instance, a pitch control, a passive stall control, and an active stall control. The last two alternatives are commonly used in a fixed-speed wind turbine, while the first alternative are used in a variable speed wind turbine (see section 5.2.5).

The passive stall control utilizes rotor blade geometry that limits the lift force when the wind speed becomes too high by creating a turbulence behind a rotor blade. A pitch-controlled wind turbine limits the output power by turning or pitching the rotor blades slightly out of the wind.

The active stall control is similar to the pitch control in the way that it uses pitch mechanism to limit the output power. When the input power reaches the rated power of the generator, the stall controller moves the blade in such a direction that increases the angle of attack, which is in the opposite direction from what the pitch controller does.

For wind speeds higher than the rated value, the active stall mechanism allows a wind turbine to operate at almost constant power output. Another advantage of the active stall mechanism is that this mechanism can avoid an active power overshoot beyond the rated power.

The active stall controller block is depicted in Fig. 3.13. First, the actual power of the turbine is measured and compared with the active power reference value, which is equal to the turbine rated power. The error between the reference and the actual values of active power is passed through a PI-controller to provide a pitch angle reference value. In order to limit the pitch rate, the pitch reference value is passed through a pitch rate limiter. Further, the limited-rate reference value is fed into a pitch actuator. The pitch actuator is modeled as a first-order time-lag system in order to model the hydraulic system of the actuator.

In order to avoid unnecessary continuous changes in pitch angle, which may wear the pitch mechanic, the pitch is moved by utilizing a “sample and hold” controller in

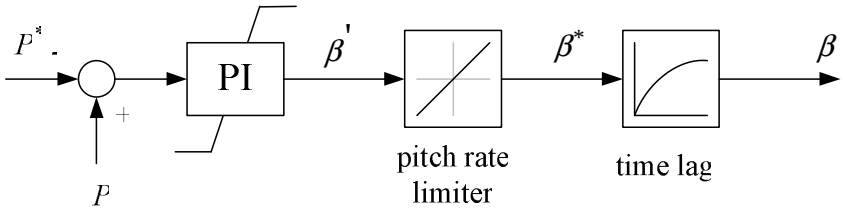

Figure 3.13. Pitch control for active stall wind turbine.

combination with a threshold controller block [65]. This mechanism allows the pitch to move only for every specified period of sample time and if the difference between the new and the old set point exceeds a certain minimum value. For power system stability studies, however, this mechanism can be excluded from the model.

3.8 Influence of Generator and Drive Train Model on Fault Response

In order to investigate the influence of generator model in the wind turbine response subject to a grid fault, a number of simulations were performed. In the simulations, a 2 MW wind turbine was used. As shown in Fig. 3.14, a fault was applied to one of the transmission lines close to the wind turbine bus leading to a voltage drop to 0.2 pu. The fault was then cleared after 100 ms by tripping the faulty line. Simulation results are shown in Fig. 3.15 and Fig. 3.16.

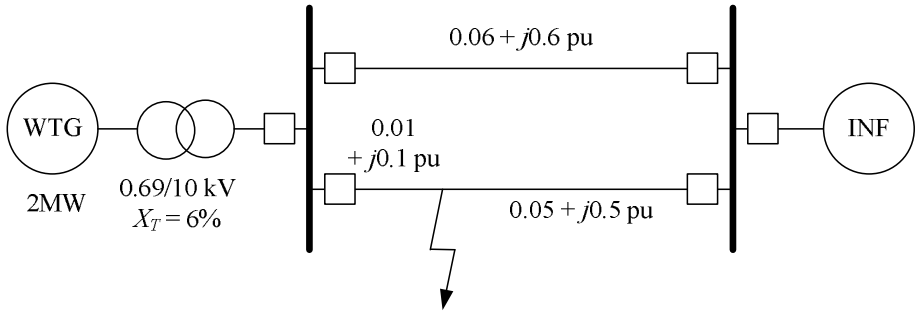

Figure 3.14. Test-grid model. The values of the impedances are on a 10 MW basis.

As clearly shown in Fig. 3.15, the fifth-order model exhibits 50 Hz oscillations reflected in the current and power responses due to the present of dc-components. During the fault, the active power of the first-order model dropped drastically, this corresponds to the magnitude of the terminal voltage. For the third- and the fifth-order induction generator models, the active power stayed at a higher value due to rotor dynamics. Furthermore, a reactive power injection during the fault in the third-order and the fifth-order induction generator models was encountered due to demagnetization of the magnetizing inductance.

The first-order induction generator model predicts a significantly higher speed deviation. This is because of the drastic electromagnetic torque reduction once the fault is initiated. In the third- and the fifth-order induction generator models, the main flux

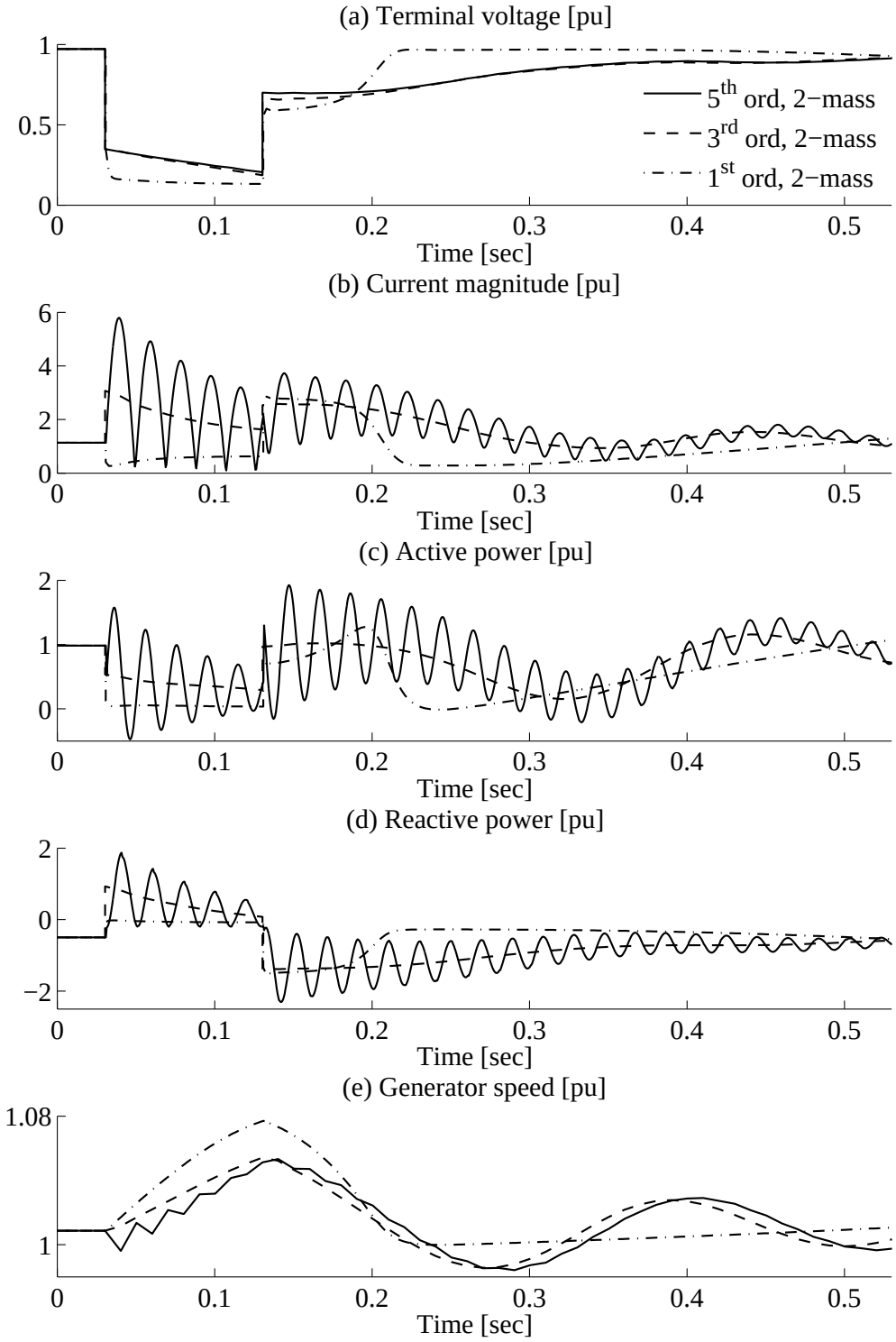

Figure 3.15. Response of fixed-speed wind turbine to grid fault for different generator models.

does not drop instantaneously and hence the electromagnetic torque decays slower, which results in a smaller speed deviation.

The third- and the fifth-order induction generator models also exhibit similar oscillations following the fault at a frequency of around 5 Hz, which are governed by the

dynamics of the drive-train in combination with the generator.

The simulation results show that, despite the inability to trace the 50 Hz transient current, the third-order model can generally offer a sufficiently accurate estimation of wind turbine behaviors during the fault.

The influence of drive train models is simulated. The simulation results presented in Fig. 3.16 show that the use of a one-mass drive train model is not able to accurately predict the wind turbine response during a grid fault. This is because the high lumped inertia of the generator and turbine masses provides less speed deviation, which results in highly optimistic results.

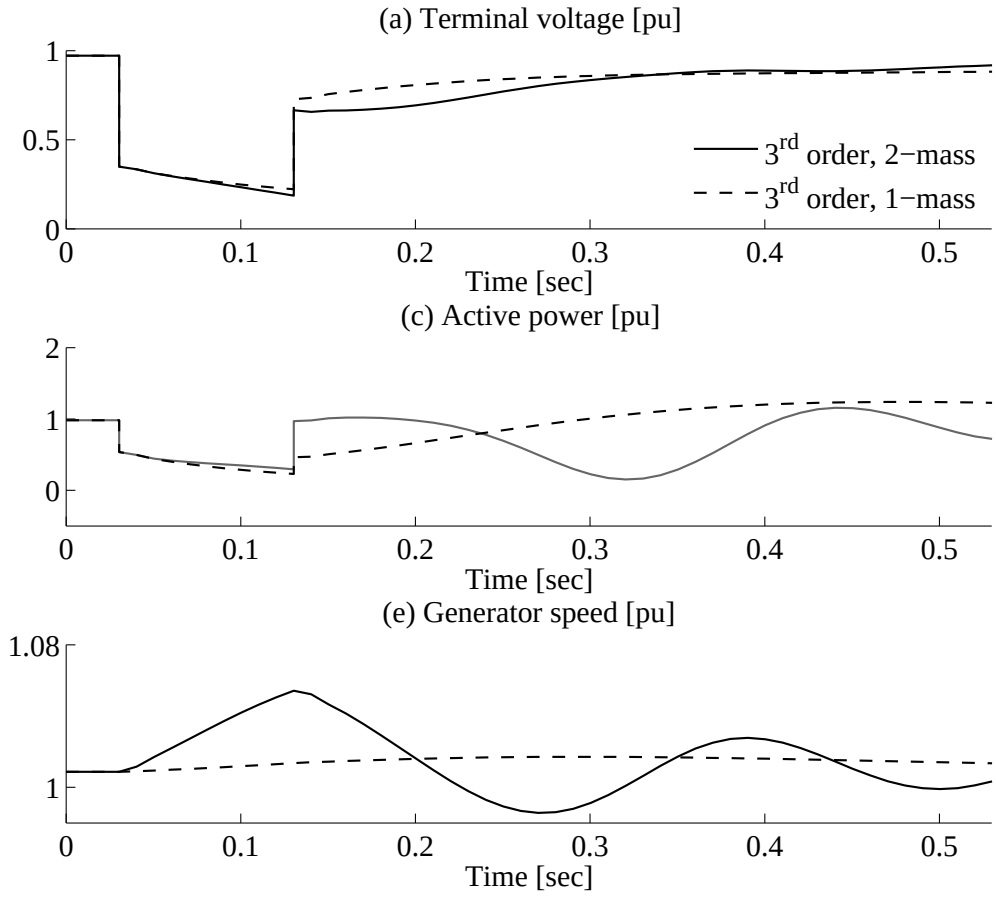

Figure 3.16. Response of fixed-speed wind turbine to grid fault for different drive train models.

3.9 Influence of Generator Models on Frequency Deviation

In this section, the validity of the wind turbine models subjected to a frequency deviation is investigated. Fig. 3.17 shows the test-grid used to simulate the effect of frequency deviation on the behavior of the wind turbine models. The test system consists of 4 busses, namely: an infinite bus (bus 1), a substation bus (bus 2), a load bus (bus 3) and a wind turbine bus (bus 4).

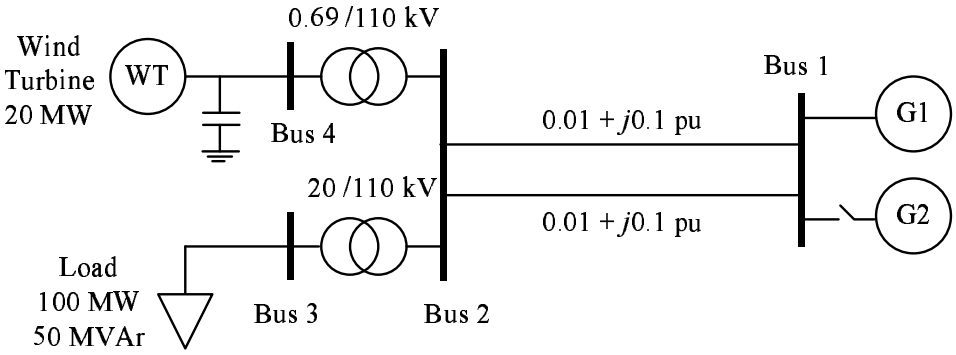

Figure 3.17. Test-grid model for frequency deviation. The values of the impedances are on a 100 MW basis.

The two generators at the infinite bus resemble conventional power plants, which are hydro power plants in this case. The load was a composite load dominated by large and small size motors, lightings and constant MVA loads. The total active and reactive power consumption of the load were 100 MW and 50 MVAr, respectively.

A 20 MW wind farm consisting of fixed-speed wind turbines was connected at bus 4. Bus 4 was connected to bus 2 through a step up transformer 0.69/110 kV. Simulation results are shown in Fig. 3.18. In the beginning of the simulation, two synchronous generators G1 and G2 supplied the load with an output power of 90 MW and 10 MW, respectively.

At $t = 20$ s, the G2 unit was tripped. This resulted in an unbalance between load and generation which lead to a frequency drop of 5% (equivalent to a 2.5 Hz frequency drop). After some time, the action of the hydro governor at G1 was able to recover frequency closer to the nominal value.

At $t = 20$ - 26 s, the system frequency continuously decreased. During this period, a fraction of the mechanical energy contained in the turbine rotor was released into the grid as the rotor was decelerating. Because the mechanical input was constant throughout the simulation, the deceleration power results in a higher electrical power output compared the pre-fault level. In contrary, at $t = 26$ - 43 s, when the frequency increased, the mechanical rotor required more power to accelerate the generator speed. This resulted in a lower electric power output (see Fig. 3.18.c). Once the frequency became stable, the active power returned to its nominal value.

The active power of the two models was different during the frequency deviation. This difference was caused by the disregard of the stator flux component $d\vec{\psi}/dt$ in the third-order model as it was explained earlier. In addition, ignoring the stator flux dynamics also causes a higher reactive power consumption in a third-order induction generator model than in a fifth-order induction generator model. As a consequence, the voltage response of the generator was also different in the two models. Nevertheless, 1 - 4% of a maximum difference in voltage and reactive power transient responses may be still acceptable.

The difference of active power response marginally influences frequency deviation of the system. The system with third-order induction generator model wind turbines provides a more optimistic estimation of the frequency response. The figure shows that the system with a third-order induction generator model predicts a maximum frequency deviation 0.4% smaller than the one with a fifth-order induction generator

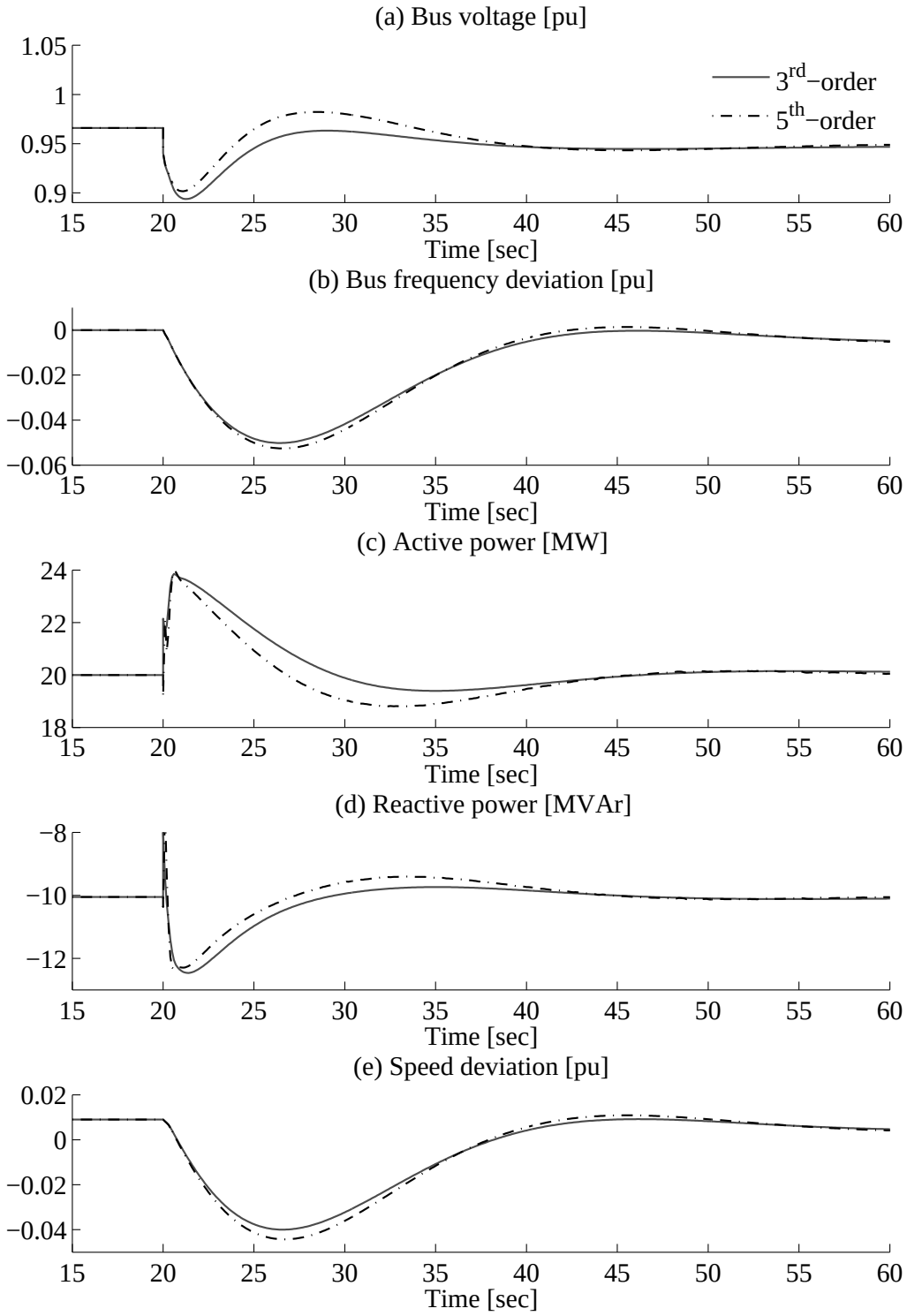

Figure 3.18. Response of induction generator models to frequency deviation with high wind power penetration (±20%).

model.

It can be concluded that the use of a wind turbine model with a third-order induction generator and one-mass drive train models is adequate for a frequency stability study. For a large frequency deviation (more than 10%) with high wind power pene-

tration (more than 20%), however, the use of a fifth-order induction generator model may be beneficial.

Based on a simulation, which is not shown here, the effect of a drive train model was also investigated. Simulation results show that the drive-train model is insignificant for this type of study due to slow dynamics.

3.10 Model Validation

In this section, models of a fixed-speed wind turbine with a squirrel cage induction generator were validated against field measurement data. The aim of these validations is to assure the validity of the models for power system stability studies. Two cases were used for validations, which were based on measurement data from the Alsvik and the Olos wind farms. The measurement data consist of the voltage and current of the wind turbines, which extend from a few cycles preceding faults until a few seconds following fault clearing. The main parts of this chapter can also be found in [34, 35].

3.10.1 Alsvik case

The measurement data were taken from the Alsvik wind turbine. The measurement set-up is depicted in Fig. 3.19. The relevant data of the measured wind turbine are given in Appendix A. All per unit parameters in the data were calculated on a 210 kVA, 400 V base system.

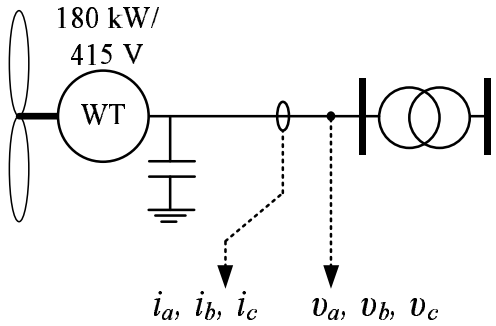

Figure 3.19. Alsvik measurement set up.

The recorded data consist of phase voltages (v_a, v_b and v_c) and phase currents (i_a, i_b and i_c), which were measured on the low-voltage side of the step up transformer of the wind turbine unit. The measurement data were recorded at a sampling frequency of 256 Hz. As this sampling frequency is relatively low, any dynamics that involve unsymmetrical grid quantities cannot be observed accurately. For this reason, a symmetrical grid condition was assumed in the validation procedure. This means only the positive sequence components of the grid were simulated.

The magnitude of the voltage (v_{p-p}), as shown in Fig. 3.20, was obtained from the available measurement data according to the following relation:

$$v_{p-p} = \sqrt{v_a^2 + v_b^2 + v_c^2} \tag{3.32}$$

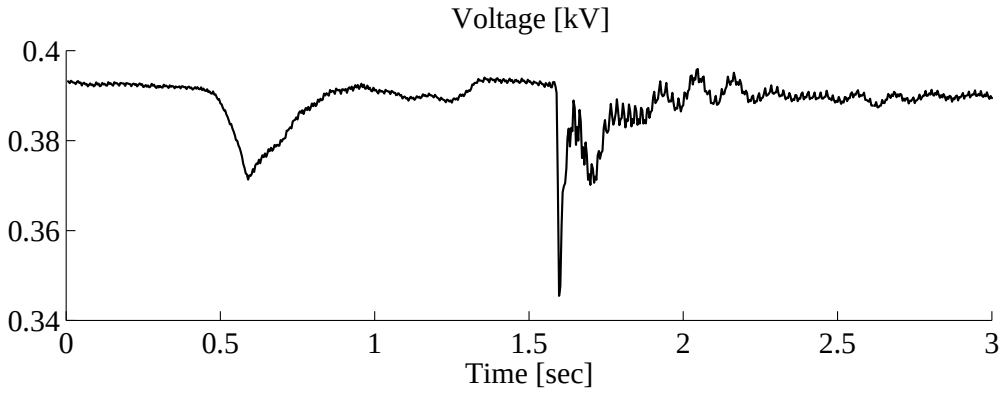

Figure 3.20. Voltage magnitude data calculated from measured phase voltage.

By referring the system to a particular frequency, which is 50 Hz in this case, the phasor angle of the voltage can be derived and is shown in Fig. 3.21. It is shown in the figure that, following the fault event, the phasor angle changes continuously. This indicates that the system frequency slightly changed at the time.

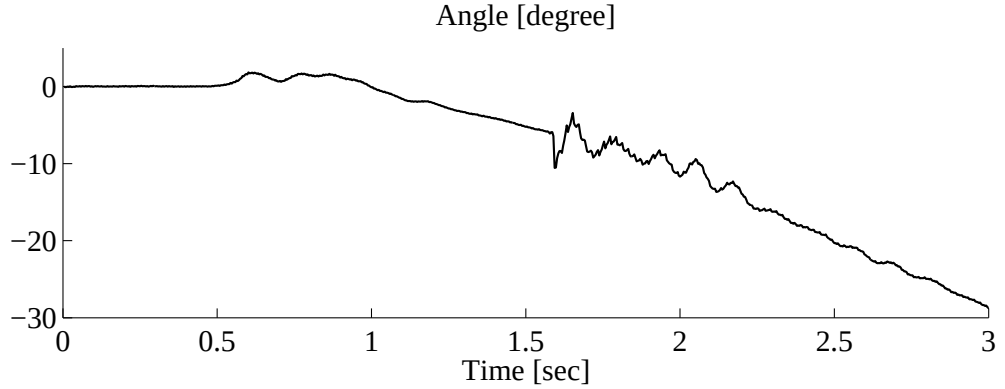

Figure 3.21. Voltage angle deviation.

The active and reactive power of the turbine were calculated from the measured voltage and current using the following expressions:

$$P = v_a i_a + v_b i_b + v_c i_c \tag{3.33}$$

$$Q = \frac{1}{\sqrt{3}}\{(v_a - v_b)i_c + (v_b - v_c)i_a + (v_c - v_a)i_b\} \tag{3.34}$$

The calculated active and reactive power are depicted in Fig. 3.22.

According to Figures 3.20, 3.21 and 3.22, initially, the wind turbine was running at very low power output, which was around 0.05 pu. The induction generator absorbed reactive power of 0.33 pu. However, there was no information regarding the reactive power compensation at the time. Two different transients can be observed:

1. At time 0.5 s the terminal voltage dropped by approximately 5%, followed by a slow recovery and slight frequency oscillations due to angle oscillations. The

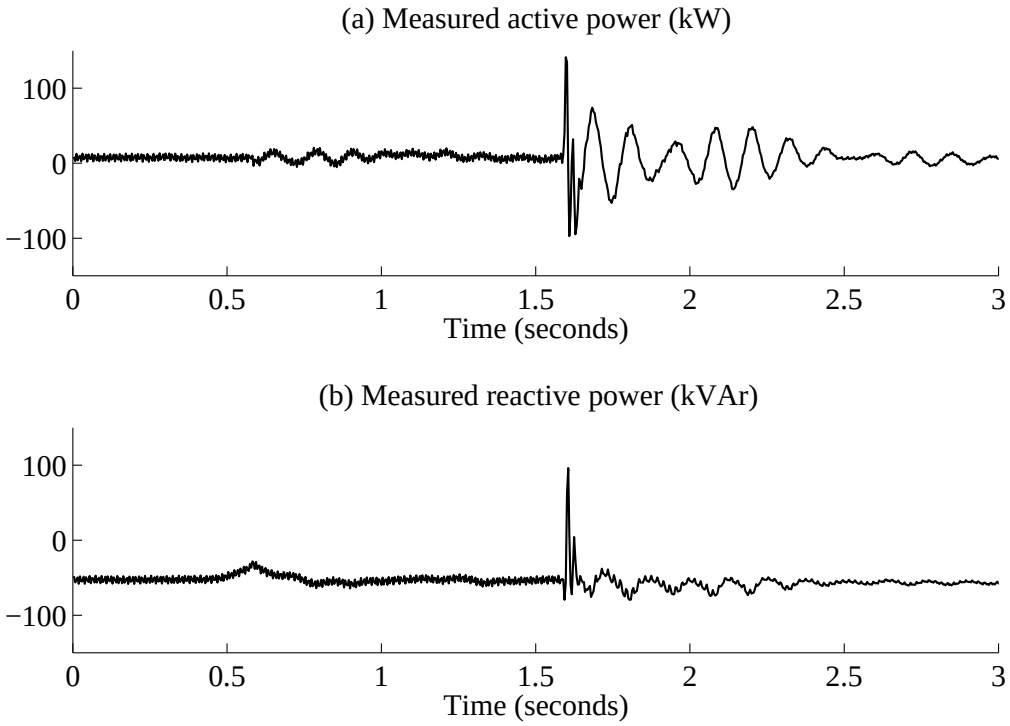

Figure 3.22. Calculated active and reactive power.

active power suffered oscillations of around 10 kW in amplitude and around 8 Hz in frequency. The reactive power absorption decreased as a result of the voltage decay, and slightly increased after the transient in order to recover the rotor flux.

2. At time 1.6 s there was a sharp voltage drop of about 10% below the nominal value, followed by voltage and angle oscillations. There were also high active power oscillations of more than 50 kW in amplitude with a frequency of approximately 8 Hz. The behavior of the reactive power after the disturbance was mainly governed by voltage oscillations. A more careful observation in Fig. 3.22 shows that there was a slight increase in reactive power consumption after the fault.

Since the second transient had a more rapid and larger voltage drop than the first transient, hence it is more representative to explain responses of the wind turbine. Therefore, only the second transient is discussed in the following sections.

Simulation

The simulations were performed using the simulation tool Matlab/Simulink. The terminal voltage was used as an input of the wind turbine model. Since the voltage data resolution is poor, it cannot be used directly as an input for the simulation. Instead, a new set of input data must be generated by interpolating the voltage and the angle data sample given in Figures 3.20 and 3.21 assuming that the three-phase voltages are fully symmetrical. By doing so, a new voltage data set can be obtained as presented in Fig. 3.23.

Fig. 3.24 shows detail of the active and reactive power oscillations obtained from the measurement data and the simulation using a fifth-order induction generator model

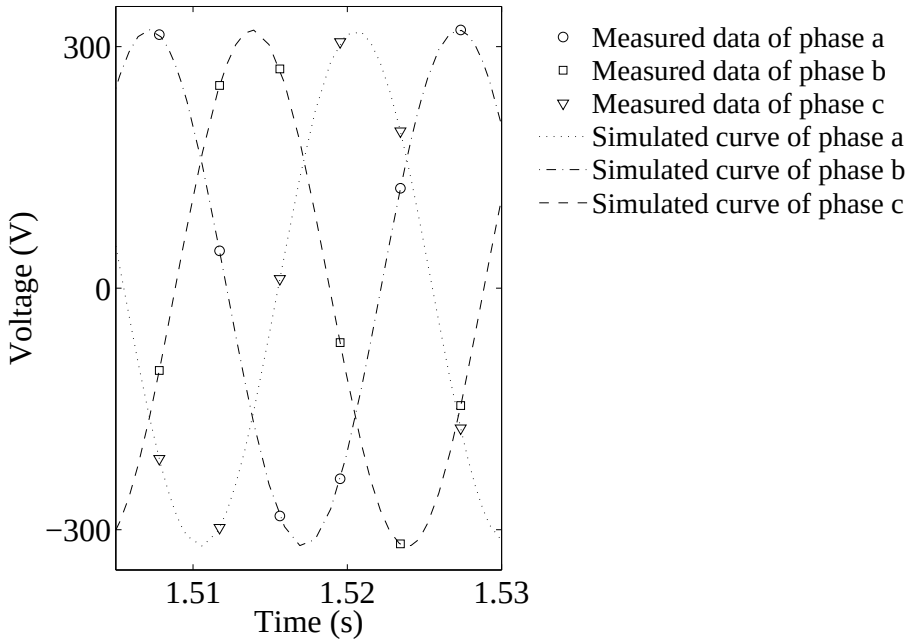

Figure 3.23. Discrete actual data obtained from measurement compared with continuous voltage data used for simulation.

and a two-mass drive train model without a mechanical damping. It can be seen that, in spite of the presence of 50 Hz oscillations, the results provided by the model show fairly good agreement with the measurement data.

The following are a number of considerations obtained from Fig. 3.24a:

- The power oscillations in the measurement data and the simulation results have a similar frequency.
- The fast transients in the first few cycles in the simulation and the measurement data have a similar magnitude.
- The amplitude of the simulated and the measured power oscillations are similar during the first oscillations following the fault event. Later, the simulated oscillations are higher than the measured ones.

From Fig. 3.24b, it can be seen that:

- There is a good accordance between the measured and the simulated reactive power, despite a small shift in the reactive power after the disturbance. This shift could be due to the disconnection of some compensating capacitors as a result of the disturbance. However, this event was not recorded, so it is not possible to confirm this supposition.

50 Hz oscillations are apparent in the active and reactive power output due to the presence of a dc-offset in the voltage measurement data.

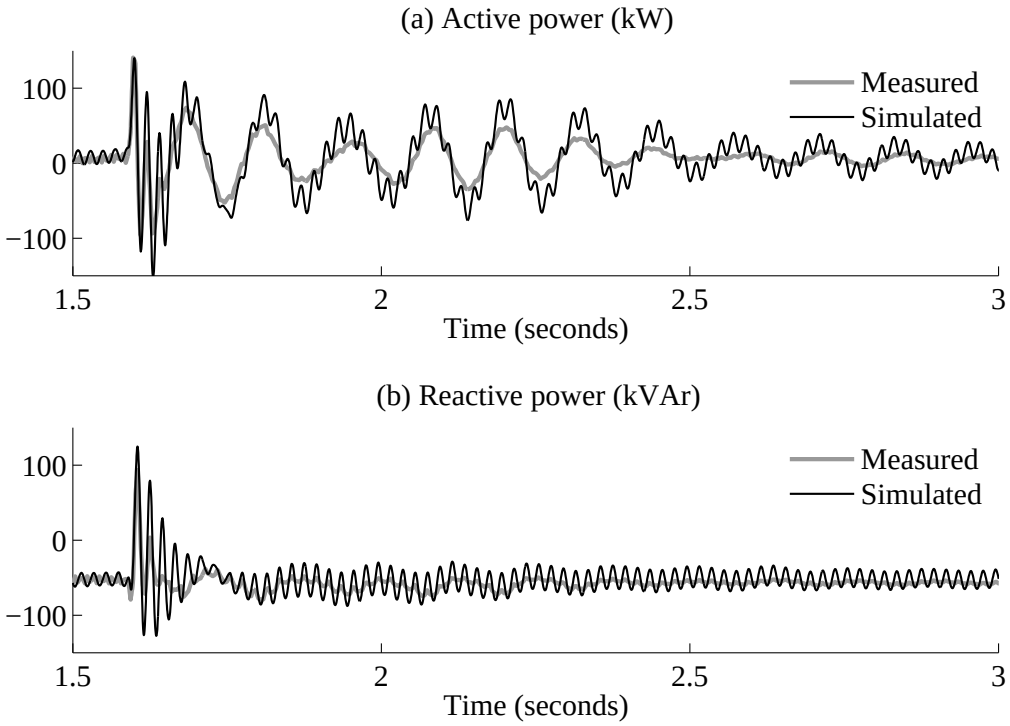

Figure 3.24. Active and reactive power responses of fifth-order induction generator model and two-mass drive train model without mechanical damping (black) compared with measurement data (grey).

Removing dc-offset from the measurement data

In order to remove 50 Hz oscillations in the active and reactive power, the dc offset contained in the measurement data was filtered out. Simulation results of the model after removing the dc-offset from the voltage measurement data are presented in Fig. 3.25. As seen in the figure, the result is now relatively free from 50 Hz oscillations in the active and reactive power. The 50 Hz oscillations that remain at the beginning of the fault, are caused by unsymmetrical voltage during that period.

Influence of generator models

In the following, a third-order induction generator model is used. The result is then compared with a fifth-order induction generator model in order to examine the influence of different generator models on simulation results.

As can be seen in Fig. 3.26, the third-order model fails to predict the peak electromagnetic transient current that occurred immediately after the fault event. This is because the stator flux derivative component is not involved in the third-order model. However, in general, a third-order induction generator model is able to capture the electro-mechanical transients of the wind turbine.

Influence of drive train models

As seen in Fig. 3.27, if the drive train of the wind turbine is represented as the one-mass model, the simulated active power oscillation frequency differs from the measurement

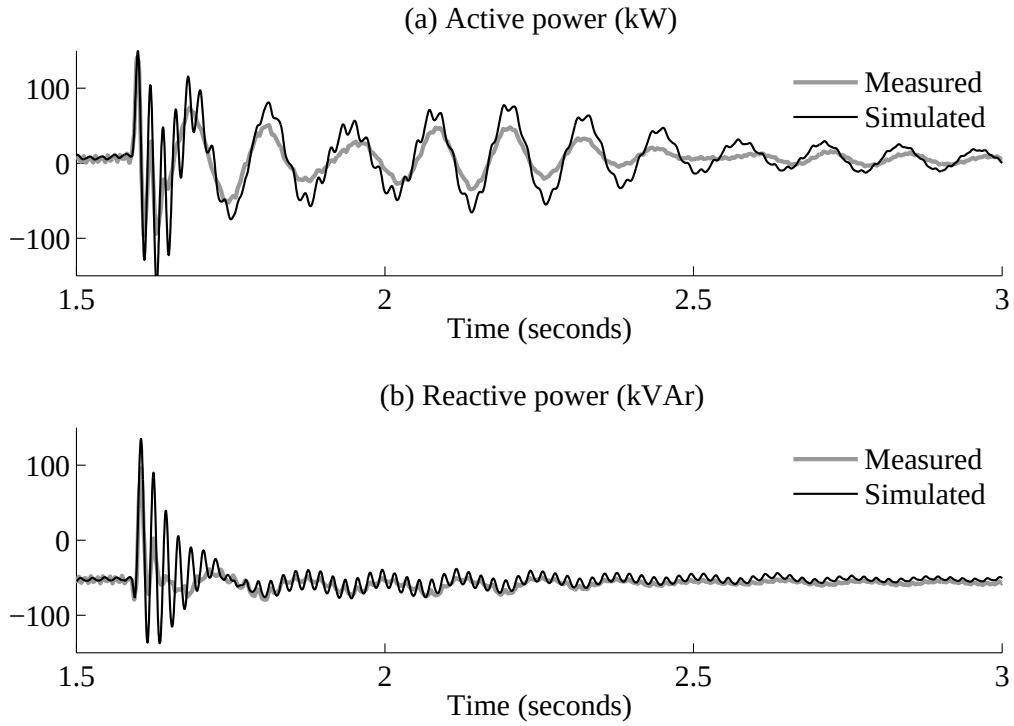

Figure 3.25. Active and reactive power responses of fifth-order induction generator model and two-mass drive train model with dc-filtered input voltage and without mechanical damping (black) compared with measurement data (grey).

data. This is because by using the single-mass model of a drive train, soft shaft oscillations are omitted. The remaining oscillations apparent in the active power were governed by a rapid fluctuation of the angle deviation as shown in Fig. 3.21. The result shows that the one-mass model predicts more optimistic results than the two-mass model.

Introducing a mechanical damping

Poorly damped active power oscillations in Fig. 3.26 suggest the convenience of introducing a mechanical damping constant into the drive train model. Fig. 3.28 shows simulation results of the model including a mechanical damping constant of 3 pu.

It is shown in Fig. 3.28 that after introducing the mechanical damping constant, the model is able to predict the magnitude of active power oscillations more accurately. While reactive power oscillations are virtually unaffected by the mechanical damping since reactive power is more dependent on voltage oscillations as discussed previously.

However, the mechanical damping constant is often not provided in wind turbine data. Nevertheless, since the model without the mechanical damping constant provides more conservative results, the exclusion of the mechanical damping constant from the model is not critical in power system studies.

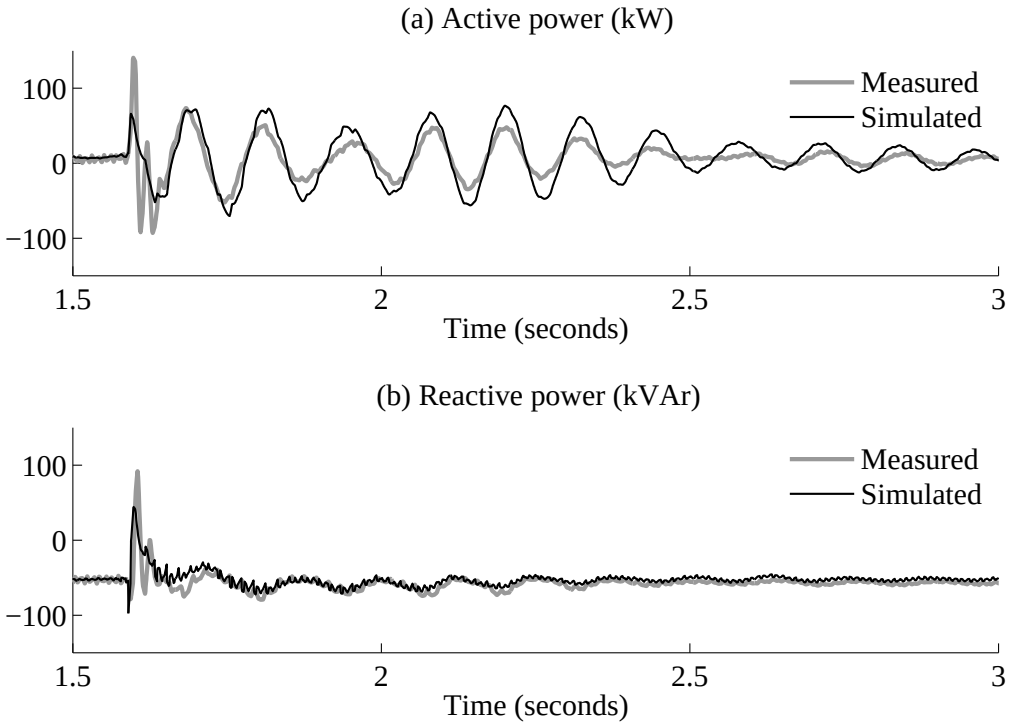

Figure 3.26. Active and reactive power responses of third-order model of induction generator and a two-mass drive train model with dc-filtered input voltage and without a mechanical damping (black) compared with the measurement data (grey).

3.10.2 Olos case

The second measurement data were taken from the Olos wind farm situated in the northern part of Finland. The farm consists of 5x600 kW wind turbines with an operating voltage of 690 V. Each turbine is connected to a 21 kV grid by means of a step-up transformer with a rating capacity of 800 kVA. The generator is equipped with two separate sets of windings, which correspond to 600 kW/4-poles for a high-speed operation mode, and 120 kW/6-poles for a low-speed operation mode. During the measurement, the generator was operating in the high-speed operation mode. Each wind turbine is equipped with a 3-step capacitor bank with a reactive power compensation of 50 and 162 kVAr for the low- and high-speed operation modes, respectively. In this study, only turbine number 2 is investigated. The measurement data contain phase voltages and phase currents recorded using two different sampling frequencies, namely 500 Hz and 3.7 kHz.

500 Hz measurement data

The measurement data with a 500 Hz sampling frequency are explained in the following. The phase voltages and currents of the turbine are shown in Fig. 3.30. The active and reactive power of wind turbine 2 presented in Fig. 3.31 were calculated from the measured currents and voltages according to (3.33) and (3.34), respectively. Note that the latter equation is only valid for calculating reactive power in balanced 3-phase quantities. Therefore, it must be kept in mind that the instantaneous reactive power

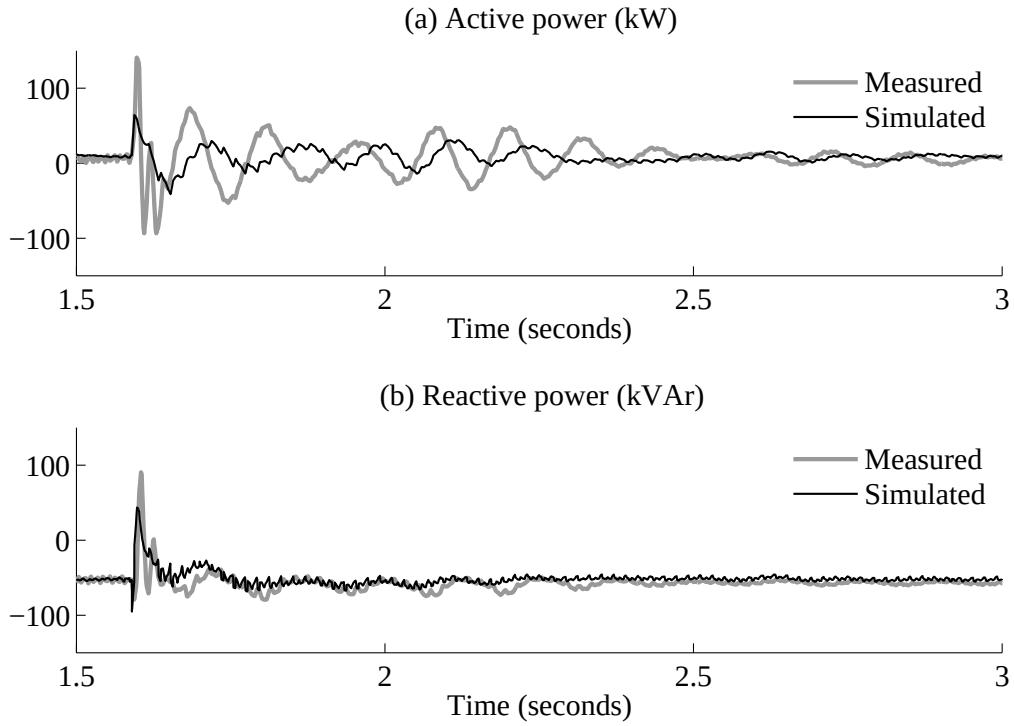

Figure 3.27. Third-order model of induction generator and single-mass model of drive train (black) compared with measurement data (grey).

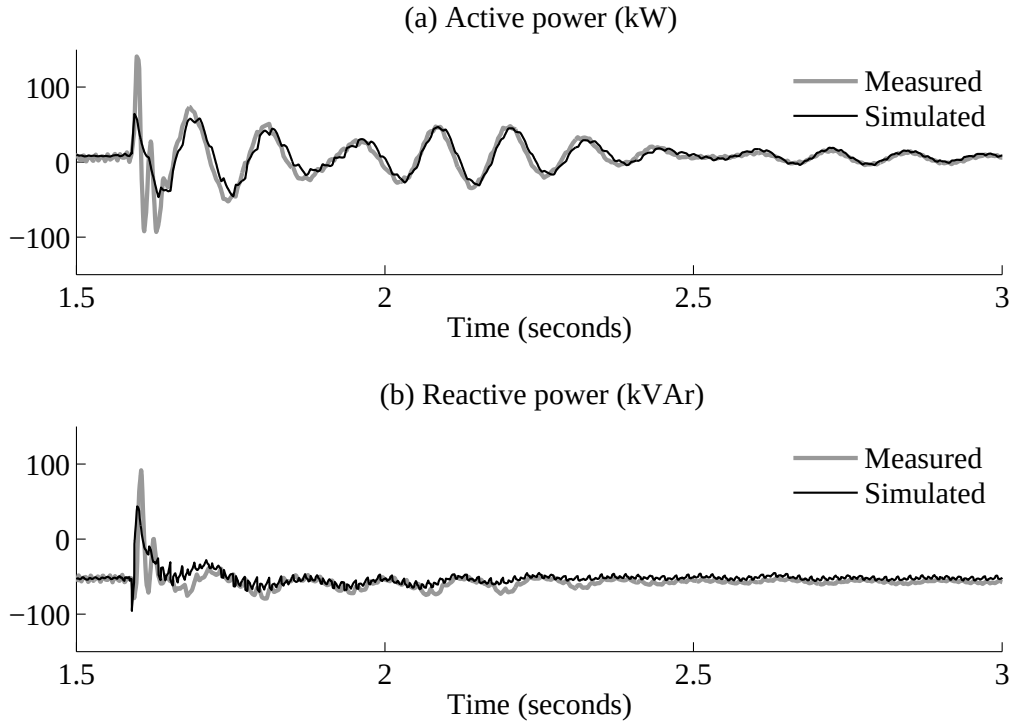

Figure 3.28. Active and reactive power responses of third-order model of induction generator and two-mass drive train model with dc-filtered input voltage and mechanical damping constant (black) compared with measurement data (grey).

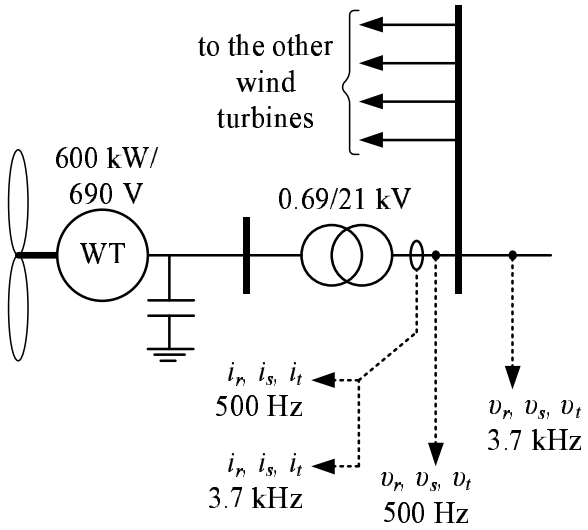

Figure 3.29. Olos single turbine measurement set up.

calculated for unbalanced conditions, as presented in several figures in the remaining parts of this chapter, is intended merely for comparisons between simulation results and measurement data rather than for providing accurate values.

Initially, wind turbine 2 was producing active power at approximately 130 kW and the reactive power consumption was about 76 kVAr. Such a high reactive power consumption was due to a lack of one of the 50 kVAr capacitor bank steps at the time.

A fault occurred in the grid at $t = 0.92$ s and was cleared at $t = 1.18$ s while the voltage continued to oscillate due to the breaker switching (opening), before the voltage oscillations finally died out at $t = 1.8$ s. The voltage oscillations were characterized by the presence of dc-components due to discharging earth capacitance, which was charged during earth-fault, and formed an oscillation circuit with the line inductance.

Meanwhile, the current oscillations were sustained for a longer period. Unlike the voltage oscillations, the current oscillations are likely to be attributed to the natural frequency of the drive train and the generator. Using spectrum analysis, the oscillation frequency was found to be 5.8 Hz.

As shown in Fig. 3.31, the current oscillations affected the active power whereas the reactive power was hardly affected. This indicates that the grid was strong enough for the terminal voltage to be relatively insensitive to active power oscillations. The reactive power was influenced to a great extent by the voltage and was loosely correlated with the behavior of active power. Furthermore, this indicates that the active power oscillations were related to drive-train dynamics.

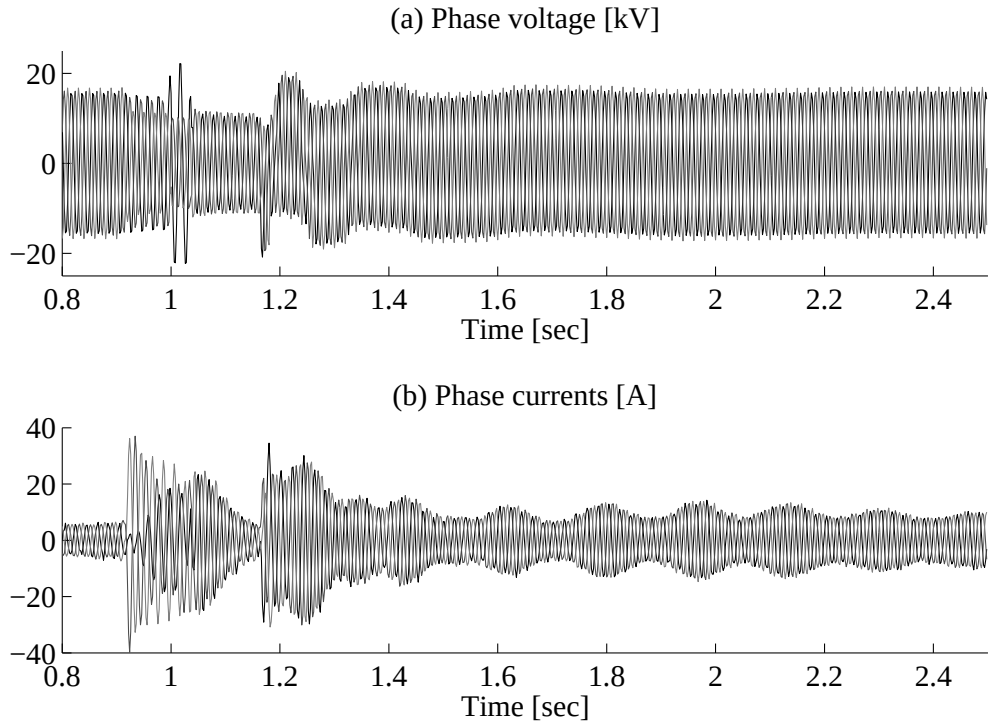

Figure 3.30. Measured voltage and current of a single turbine at Olos wind farm with 500 Hz sampling frequency.

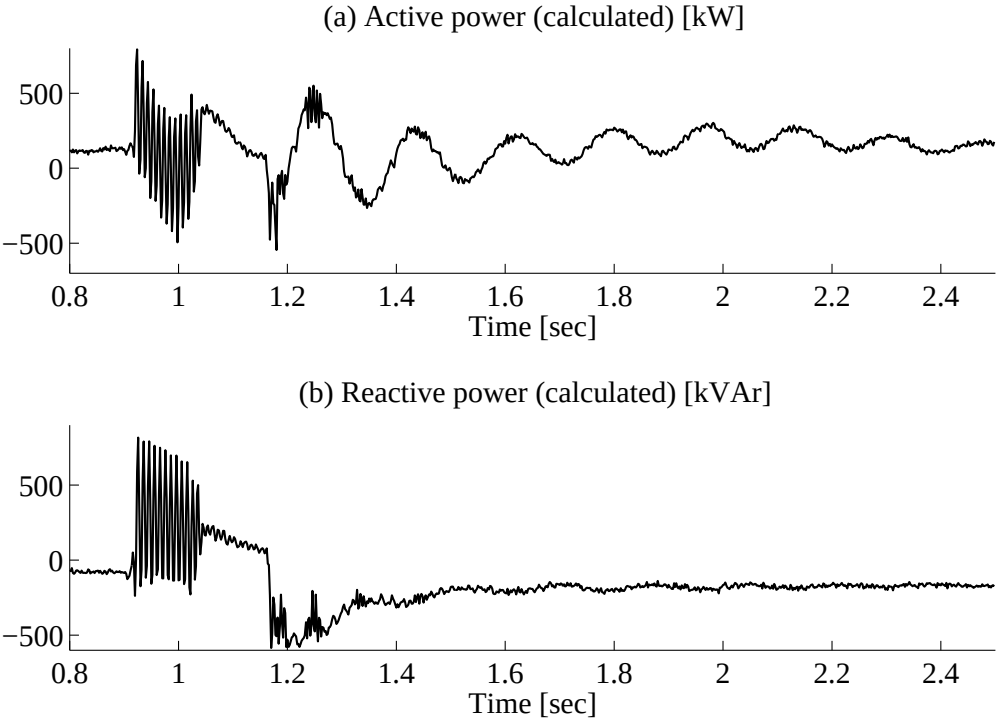

Figure 3.31. Calculated active and reactive power of single turbine at Olos wind farm with 500 Hz sampling frequency.

As a typical response of an induction generator, a large amount of reactive power was absorbed by the generator during voltage recovery, as shown in Fig. 3.31b. Additionally, the figure shows that the reactive power consumption increased by nearly 100 kVAr after the fault, which was likely prompted by a disconnection of the capacitor bank. The 100 kVAr drop in reactive power production at 0.98 pu voltage well corresponds to the disconnection of capacitors of 112.5 kVAr at the nominal voltage.

Another finding was a relatively high transient current during the fault clearing, which was initiated by the opening of a breaker at a faulty line. Although the opening of the breaker occurred at the zero crossing point, a sudden voltage magnitude change and voltage angle jump were still present on the generator terminal. Consequently, a high transient current response of the generator could not be avoided. Hence, the fault-clearing transient cannot be neglected.

3.7 kHz measurement data

The same event as discussed earlier was also measured at a sampling frequency of 3.7 kHz. Such high resolution data permit a detailed observation of events during the fault. The measured phase voltages and currents of wind turbine 2 are shown in Fig. 3.32. The voltage measurement data were recorded at the end of the collector line of the wind farm (see Fig. 3.29). The calculated active and reactive power of WT-2 are as shown in Fig. 3.33.

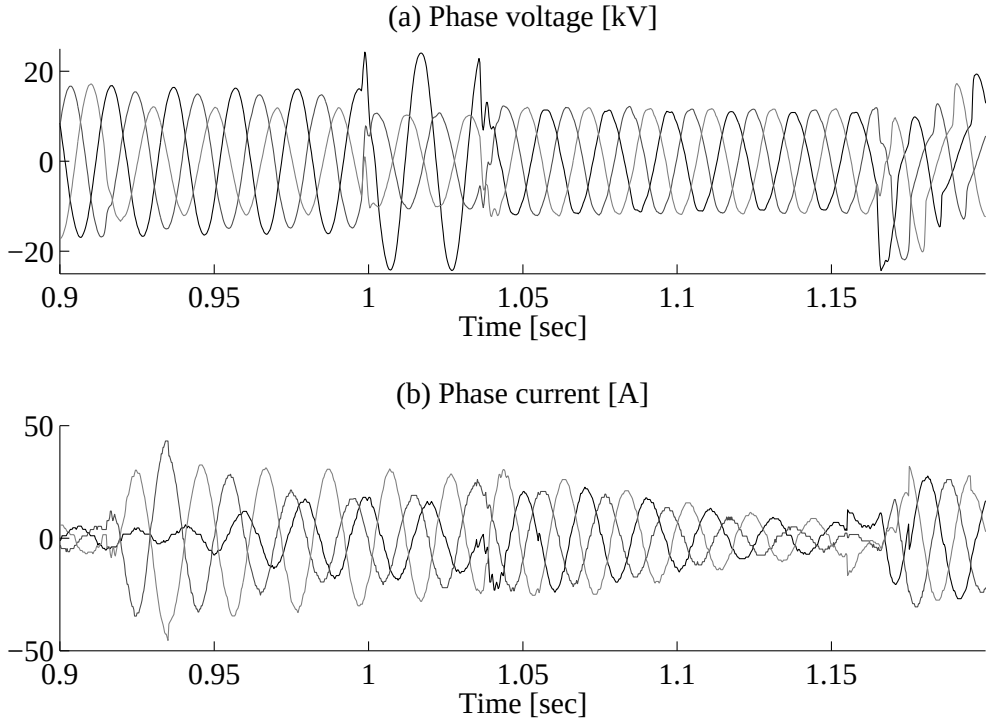

Figure 3.32. Measured voltage and current of single turbine at Olos wind farm with 3.7 kHz sampling frequency.

The 3.7 kHz measurement data provide detailed information on events during the fault. A two-phase fault occurred in the grid at $t = 0.92$ s lasting for 0.083 s. The fault

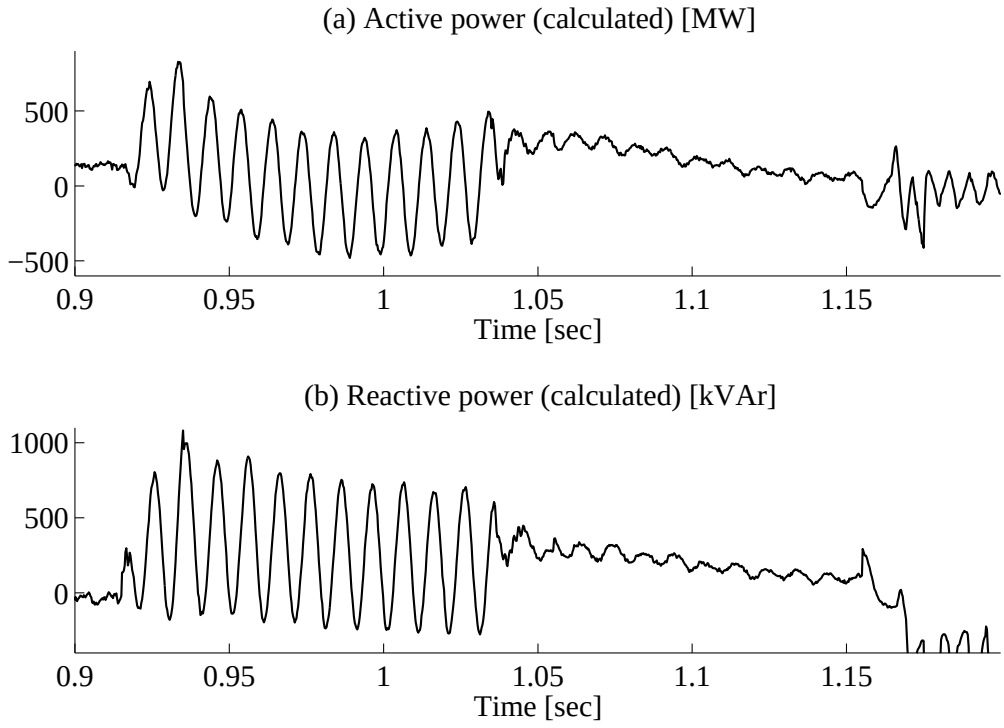

Figure 3.33. Calculated active and reactive power from measured voltage and current of a single turbine at Olos wind farm with 3.7 kHz sampling frequency.

then turned into a two-phase to ground and lasted for 0.038 s before it finally became a three-phase fault at $t = 1.04$ sec, which caused the voltage to drop to 0.7 pu. The fault was cleared at $t = 1.18$ s.

Note that transient current was encountered at $t = 1.154$ s, in which there was a sudden change in current magnitude and phase angle. This event was originated from the disconnection of the compensating capacitors as indicated earlier.

The presence of negative sequence components in the voltages and currents during the asymmetrical fault resulted in 100 Hz oscillations of active power during $t = 0.92$-1.04 s. Again, it is necessary to mention that the reactive power calculated during this unbalanced condition should be interpreted with caution as explained earlier.

Simulation

The simulation was performed using the simulation tool Matlab/SimPowerSystem. In the simulation, the generator was represented by a fifth-order induction generator model. Unsymmetrical conditions during fault prevent a third-order model of an induction generator to simulate the case correctly. The terminal voltage was used as an input of the wind turbine model. The drive-train was represented by a two-mass model.

The mechanical input power of the turbine model was set so that the generator produced the same level of active power as before the fault, which was equivalent to 130 kW, and stayed constant throughout the simulation period.

As shown in Fig. 3.34a, the simulated currents agree well with the measured ones

(see Fig. 3.32 for comparison). The model predicts a higher transient current for the first cycle, but the prediction is better for the rest of the cycles. The same conformity applies to active and reactive power, as shown in Fig. 3.34b and 3.34c, respectively.

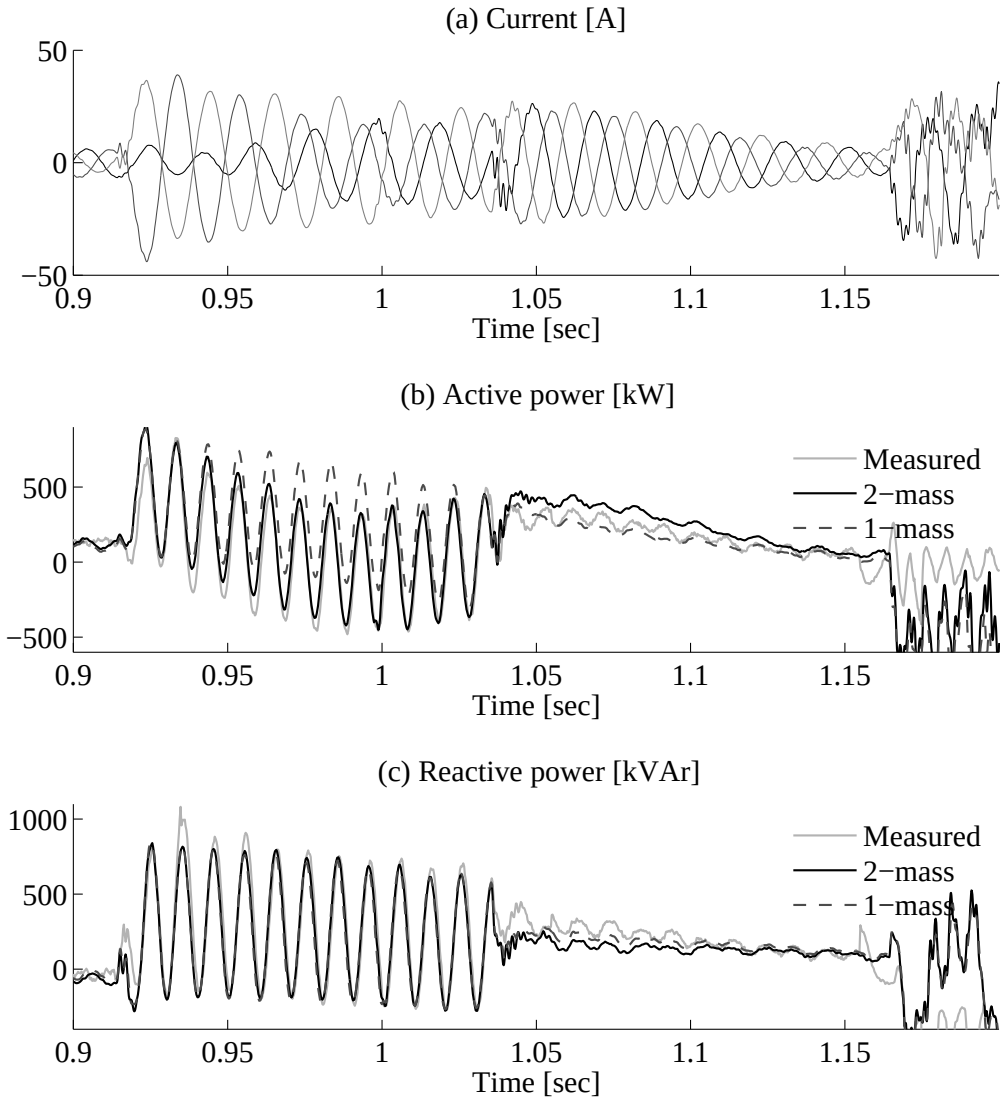

Figure 3.34. Simulated current, active and reactive power of single turbine at Olos wind farm with voltage from 3.7 kHz sampling frequency data as input.

As shown in Fig. 3.34b, during the first cycle after the fault, two- and one-mass drive train models do not differ in predicting the peak transient power. This shows that the accuracy of the mechanical drive train parameters is not essential for this short period of study. During the first few cycles of a transient event, wind turbine responses are characterized by the dynamics of the generator and other electrical components of the wind turbine. This is because the mechanical system time constants are usually much larger than the electrical system time constants.

Differences between the measured and simulated results at the end of the active and reactive power curves in Fig. 3.34b and 3.34c are caused by an inaccuracy of the model to simulate switching events. Therefore, the simulation results of this event are

disregarded.

The simulation results for a longer time frame are shown in Fig. 3.35. The figure shows an agreement between the measured and the simulated reactive power despite a 50 Hz ripple due to poorly filtered dc-offset components in the input voltage. The drive train dynamics can be clearly observed in the active power oscillations.

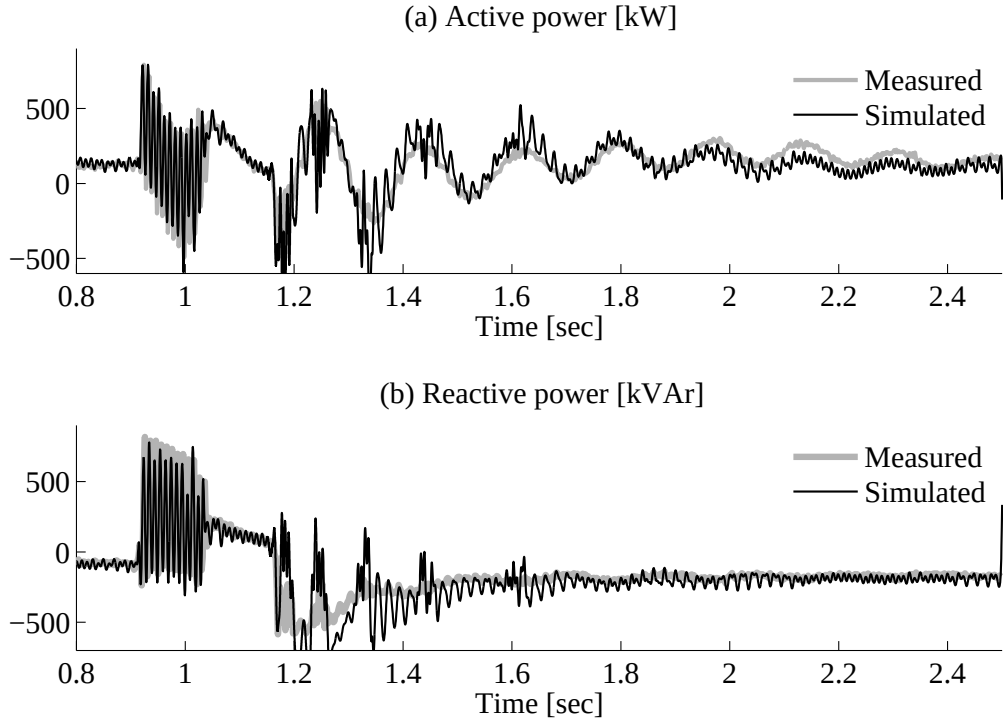

Figure 3.35. Simulated active and reactive power of a single turbine at Olos wind farm with voltage from 500 Hz sampling frequency data as an input (black) compared with measurement data (grey).

3.11 Ride-Through Capability

In this section, the phenomena that occur in an induction generator with and without fault ride-through capability during a grid fault are described. A model of a wind farm consisting of 50 units of 2 MW fixed-speed wind turbines is used in the following simulations. The wind farm is modeled as a single equivalent wind turbine with a total nominal rating of 100 MW. The test system is given in Fig. 3.36. The turbine and grid parameters are given in Table 3.2.

The generator is modeled as a third-order model and the drive train is modeled as a two-mass model. The wind farm transformer is a lumped representation of the medium and high voltage transformers of the wind farm. The internal wind farm cable impedances are neglected. The simulations are performed using the simulation tool PSS/E with the standard simulation time step of 10 ms.

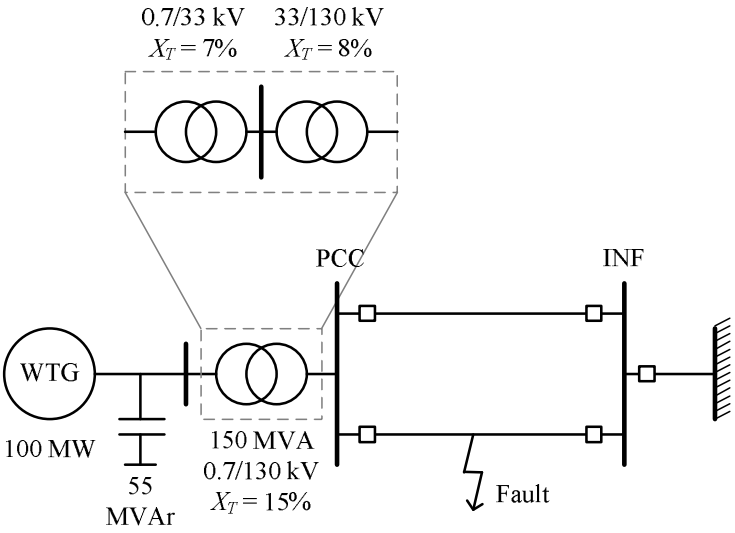

Figure 3.36. Test grid.

Table 3.2: Wind turbine and grid parameters.

Parameters	Values	Units
Number of wind turbines	50	units
Wind turbine rating	2	MW
R_s	0.00539	pu
$L_{\sigma s}$	0.09062	pu
L_m	3.31065	pu
R_r	0.100718	pu
$L_{\sigma r}$	0.007616	pu
Short circuit capacity at PCC	100	MVA

3.11.1 Speed instability of a wind turbine without fault ride-through capability

In this subsection, a grid fault is applied to a fixed-speed wind turbine without any fault ride-through capability. As depicted in Fig. 3.37, at $t = 1$ s a fault occurs in the grid resulting in a terminal voltage drop. Due to the reduced terminal voltage, the generator loses electromagnetic torque leading to rotor acceleration. When the fault is cleared and the voltage starts to recover, the generator speed may already exceed the pullout slip. If the electromagnetic torque at this point is higher than the mechanical torque, the generator speed will eventually return to the normal operating point. However, the electromagnetic torque normally remains low since the voltage has not fully recovered due to generator magnetization, which absorbs a large amount of reactive power from the grid. As a result, generator speed continuously increases leading to speed instability.

In the case of a two-mass drive train model, the situation is more severe. Even if the generator speed is able to recover back to the normal operating point at the instance of voltage recovery, turbine speed does not decrease instantaneously due to the twisted shaft. This allows turbine speed to continuously increase for a short time.

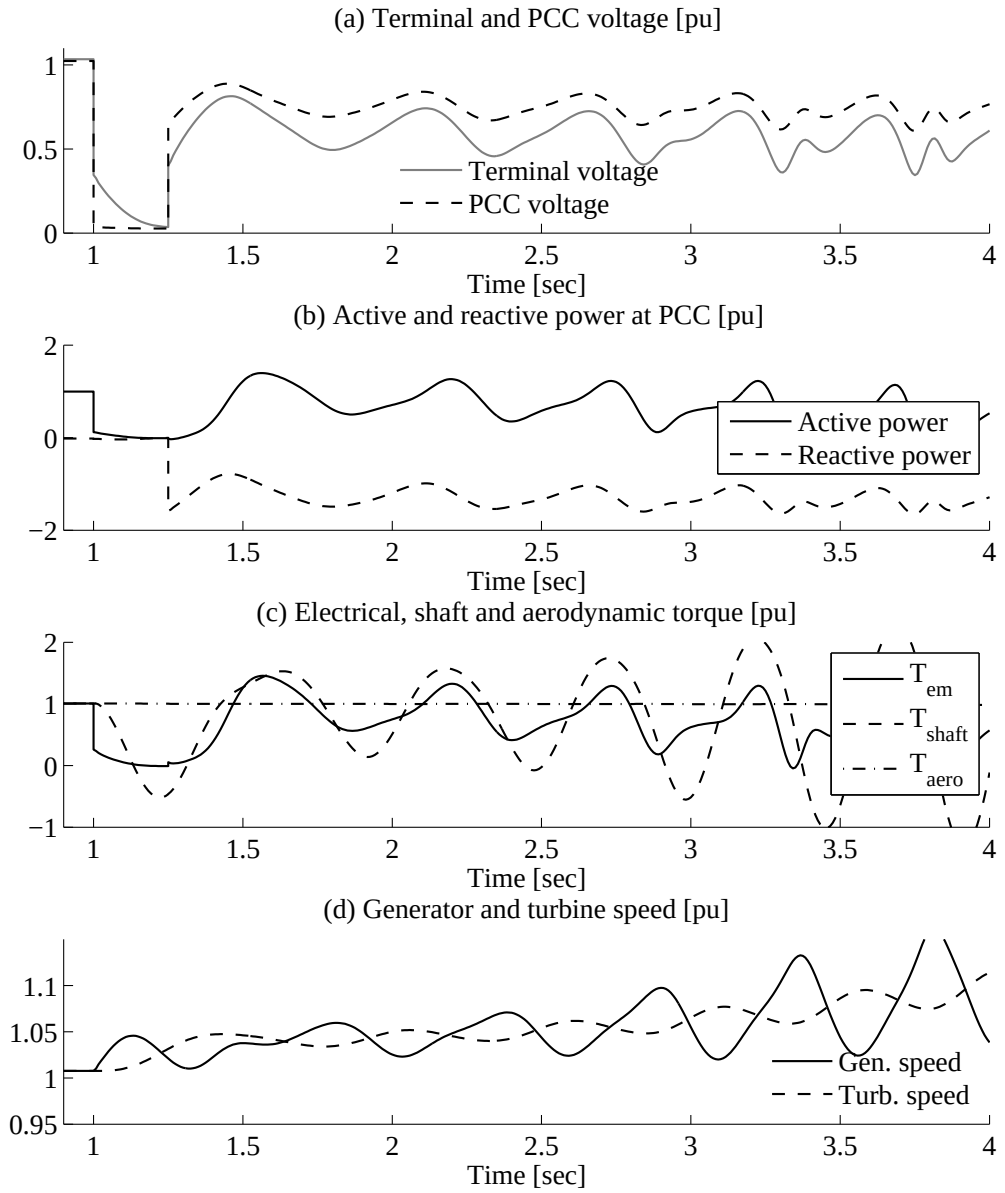

Figure 3.37. Speed instability of passive stall fixed-speed wind turbine without fault ride-through capability following grid fault.

During the next time period, the twisted shaft releases energy and creates the opposite effect. This charge and discharge of twisted shaft energy creates oscillations in the generator and turbine speed. In reality, electromagnetic torque also suffers oscillations due to terminal voltage variation caused by active and reactive power fluctuations. All these factors interact with each other creating composite oscillations as shown in Fig. 3.37. This event clearly indicates that the grid fault not only provokes speed instability in the turbine but also generates a considerably high mechanical stress on the drive train.

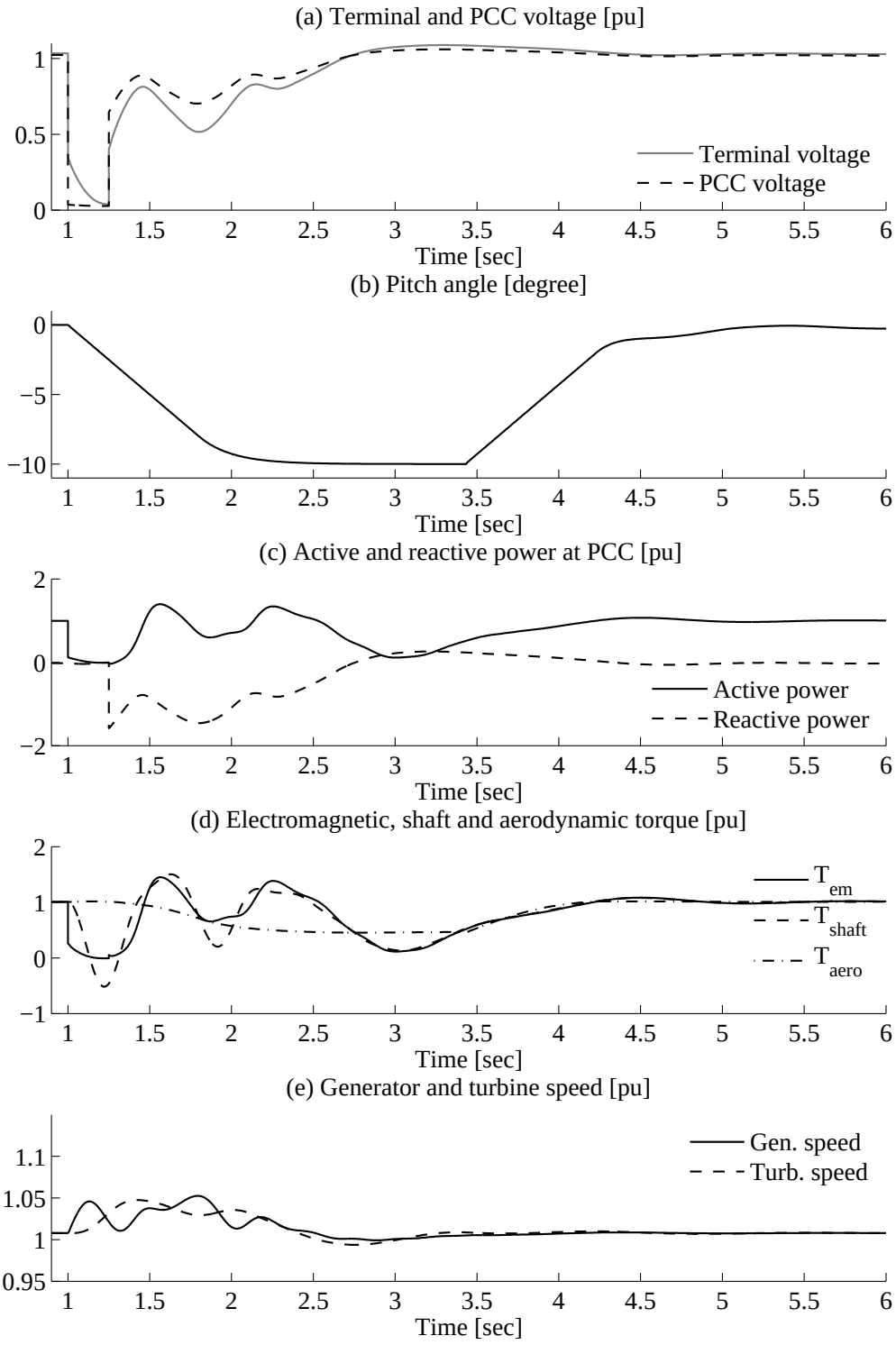

Figure 3.38. Fault ride-through response of active stall fixed-speed wind turbine.

3.11.2 Active stall strategy

One alternative to avoid speed instability in a fixed-speed wind turbine subjected to a grid fault is employing an active stall strategy. The response of a fixed-wind turbine equipped with active stall capability is shown in Fig. 3.38.

Once the fault is detected, the pitch is regulated toward a stall position in order to reduce aerodynamic torque. As illustrated in Fig. 3.13, the active-stall control is able to reduce C_p faster than the pitch control. Due to mechanical restrictions of the actuator, the pitch rate is limited to 10°/s.

At the event of fault clearing, the voltage starts to recover. At the same time, electromagnetic torque develops. As the generator is magnetized, a large amount of reactive power is absorbed from the grid prompting a prolonged voltage recovery. As electromagnetic torque is recovered, generator speed decreases. Within one second, the pitch reaches a value that is able to reduce the C_p so that the mechanical input is reduced by 40% of the pre-fault level, meaning less stress on the shaft.

When the voltage is recovered, the pitch angle does not return directly to the pre-fault level. Instead, the pitch angle is held constant until the grid status returns to its normal state. In this case, the grid status is said to be normal if the grid voltage is not less than 0.8 pu. Once the grid status is normal, a 2-second time delay is introduced to assure that the grid is fully stable. Two seconds later, the pitch angle gradually returns to the pre-fault value. As a result, the turbine successfully rides out the severe fault with less mechanical stress on the drive train.

3.11.3 Series dynamic breaking resistors

The fault ride-through capability of a fixed-speed wind turbine can also be realized by means of a series dynamic breaking resistor (SDBR) [66] − also known as the transient booster [67]. The concept employs resistors inserted between the turbine terminal and the grid. In a normal operation, the resistors are bypassed using fast mechanical switches. During a fault condition leading to a grid voltage drop, the switches are opened creating voltage drop across the resistances. As a consequence, less severe voltage dips are sensed on the stator voltage.

The test grid arrangement for dynamic braking resistor simulation is given in Fig. 3.39. The effectiveness of this strategy is illustrated in Fig. 3.40.

50 ms after the fault occurs, the braking resistors are activated. This effectively boosts the electromagnetic torque, which results in less generator speed deviation. After the grid voltage is recovered, the braking resistors are bypassed at t=1.8 s.

In general, this fault ride-through scheme is able to recover the power and voltage level faster than in the previous scheme. However, the simulation results show that a large amount of reactive power absorption remains unavoidable. Further, a high overshoot of electromagnetic torque during fault clearing is also noticeable meaning more mechanical stress on the drive-train.

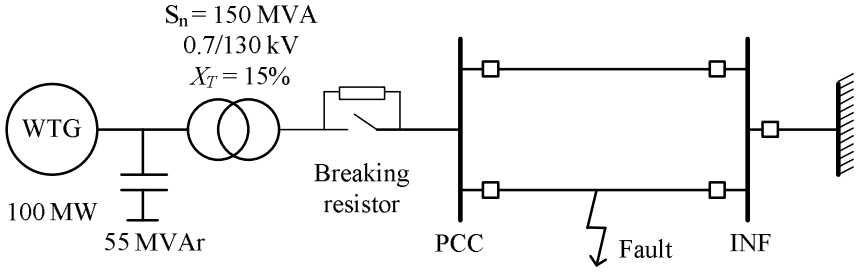

Figure 3.39. Test grid with wind farm equipped with series dynamic braking resistors.

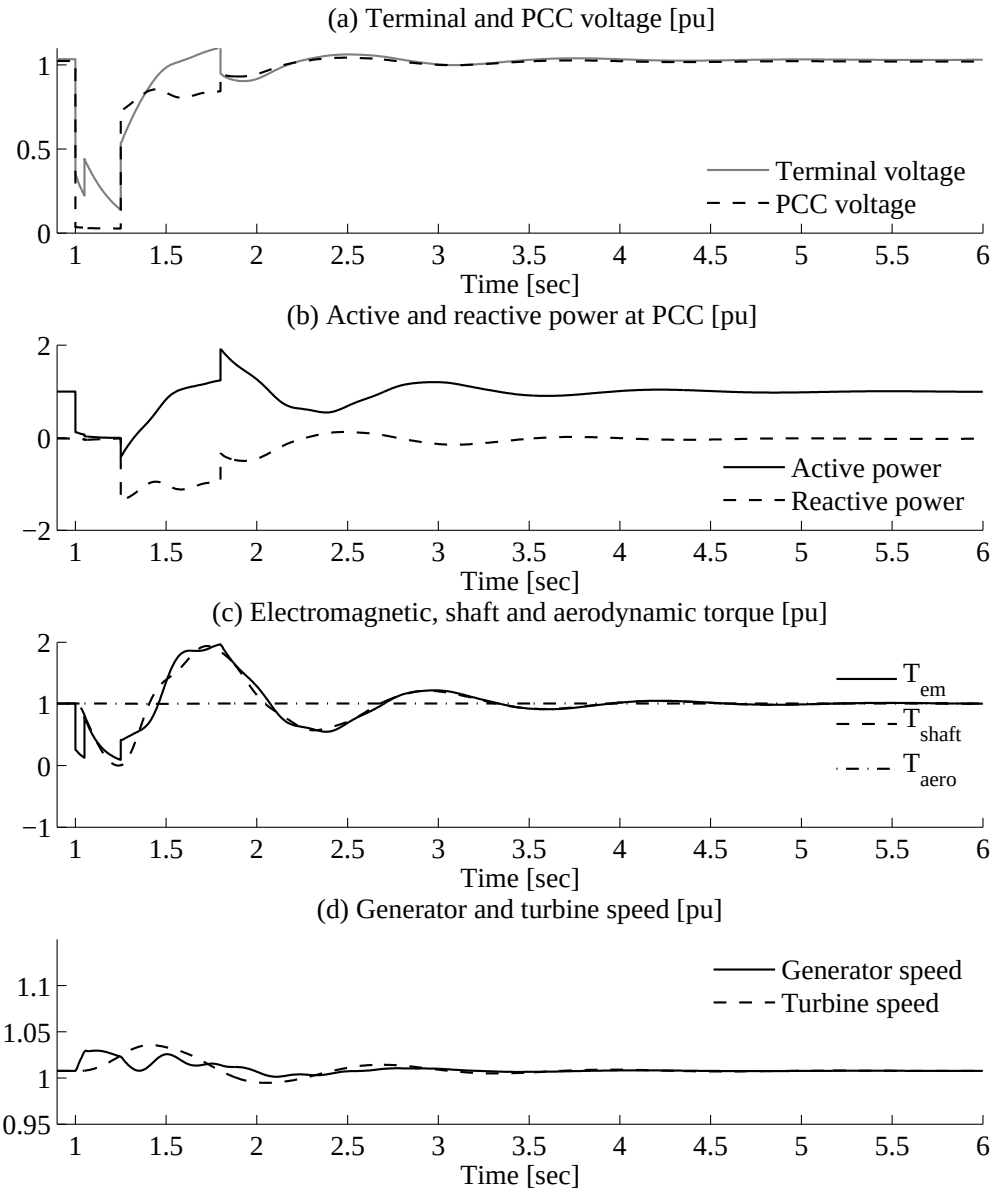

Figure 3.40. Fault ride-through response of fixed-speed wind turbine with SDBR.

3.12 Initialization

The dynamic simulation flow in the power system simulation tool PSS/E is presented in Fig. 2.2. As depicted in the figure, the dynamic simulation is started by incorporating the dynamic model data into the simulator. Thereafter, state variables of the dynamic simulation models must be initialized based on the initial load flow data. If the initialization is not carried out correctly, the system will start at an unsteady condition. In some cases, it may move toward the equilibrium condition after some time. However, the desired states as obtained from the initial load flow may not be achieved. In the worst situation, the system may become unstable and finally the simulation may halt.

As a part of dynamic models, a wind turbine model must be initialized. The initialization procedure is described in the following.

3.12.1 Initialization procedure

For a large induction generator representing a large wind farm, for instance, initialization of the generator is highly important. In such a case, an inaccurate initialization may lead to numerical instability. The induction generator initialization can be done by finding the unknown variables $\vec{i_s}$, $\vec{i_r}$, $\vec{\psi_s}$, $\vec{\psi_r}$ and s using (3.1), (3.2), (3.3), (3.4) and (3.9). Note that all of the derivatives in these equations are set to zero.

Since (3.9) is a quadratic expression, the solutions are not in the form of simple expressions. Using mathematical tools, such as Maple or Mathematica, the solution for slip can be obtained analytically. Alternatively, the solution can be obtained numerically by using the Newton-Raphson method. The initialization procedure should be implemented internally into the dynamic model for the sake of practicality.

Once the initial values of these variables are known, the mechanical power input can be calculated using (3.8) and (3.10). Depending on the aerodynamic model used, the corresponding wind speed input can be derived using one of the methods given in Section 3.6.

The initial value of the shaft twist-angle in the drive train model can be initialized using the following equation:

$$\Delta\theta = \frac{T_t}{K_s} = \frac{T_e}{K_s} \tag{3.35}$$

3.12.2 Mismatch between generator initialization and load flow result

In the load flow, active and reactive powers injected into the generator bus are known variables. Subsequently, the bus voltage can be defined. In the generator model in contrast, the active and reactive power are calculated by first knowing the stator voltage, which is equivalent to the bus voltage. For this reason, there is a mismatch between the actual reactive power calculated in the generator model and the reactive power provided by the load flow calculation. Several methods have been proposed to overcome this problem:

Method 1: An iteration procedure is performed between the power flow and the dynamic model until a steady state condition is reached. This method is prone to a numerical instability when it is used for a power system with a large number of induction generators.

Method 2:

An artificial admittance is inserted into the generator terminal. The value of the admittance is determined by the difference between the reactive power on the bus obtained from the load flow calculation, and the actual reactive power absorbed by the generator. This method is applied by several power system simulation tools including PSS/E [68]. However, a large mismatch between the initial value in the power flow and the actual value may lead to an incorrect result in a stability study. Special attention is needed particularly when initialization is performed for a generator with active power production far from unity. In such a case, reactive power is very sensitive to the voltage level on the generator terminal as illustrated in Fig. 3.41. The situation will be more critical for a weak grid because of a strong coupling between generator reactive power and generator terminal voltage.

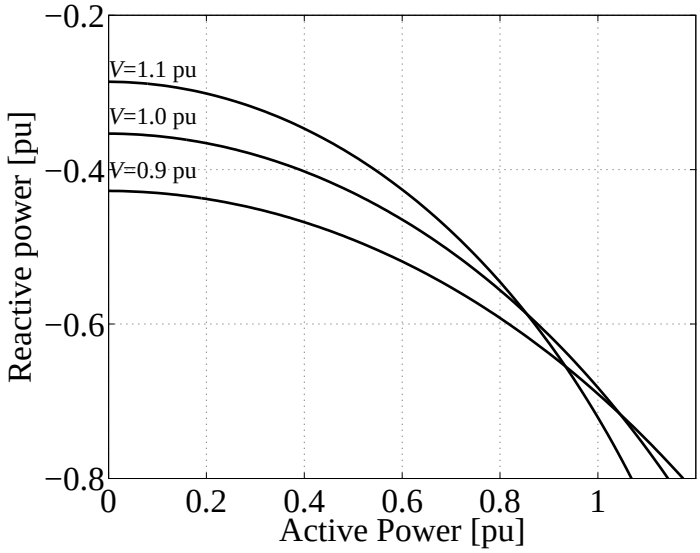

Figure 3.41. Voltage sensitivity of PQ curve for typical induction generator.

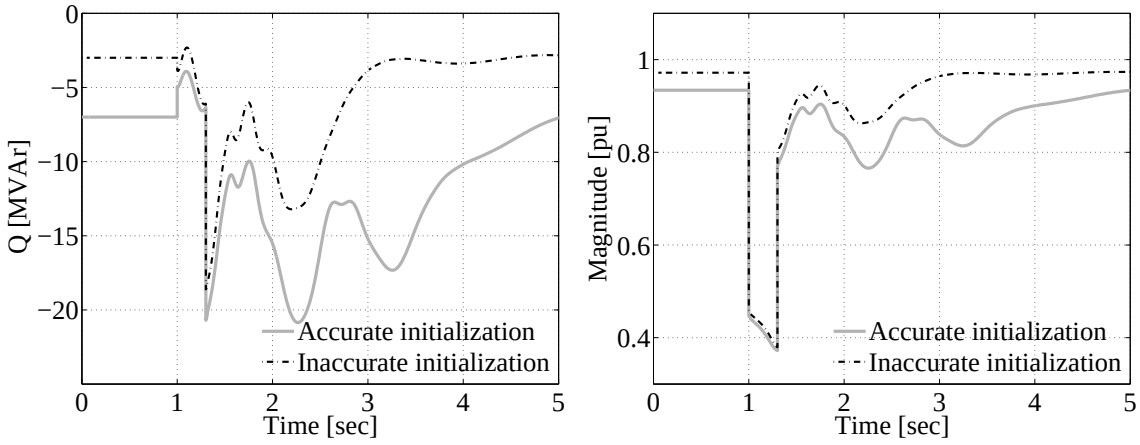

(a) Reactive power

(b) Terminal Voltage

Figure 3.42. Fault simulation with correctly initialized induction generator and inaccurate estimation of initial reactive power with admittance insertion.

Method 3: The steady state induction generator model is included in the initial step of the power flow calculation [69]. This method gives a more accurate result, i.e. the reactive power in the load-flow is close to the actual reactive power calculated using the dynamic model. However, since this method must implement additional equations into the network/load flow calculation, it is impractical for most simulation tools.

It is recommended, however, to utilize the PQ-characteristic curve of the generator to approximate a set point of the reactive power in the load flow. This will minimize the artificial admittance used in Method 2.

Inaccurate estimation of the initial generator reactive power may lead to unexpected simulation results as illustrated in Fig. 3.42. The actual reactive power of the simulated generator at unity power output is 0.7 pu, whereas the reactive power given by load flow data is 0.3 pu. The difference between the two reactive powers is compensated by

inserting 0.4 pu of susceptance. In this case, the presence of the susceptance results in overly optimistic generator responses during fault.

3.13 Conclusions

The validation results suggest that a fifth-order induction generator model is sufficient for accurately representing the detailed response of an induction generator in its interaction with a power system. As a consequence, saturation effects, core losses and skin effects in an induction generator can be ignored in such a study. For symmetrical grid faults, a third-order induction generator model has proven to be sufficient for predicting the electromechanical response of the generator.

Based on comparisons between induction generator models, it was found in most cases that the third order model of induction generator is sufficient for use in stability studies. The use of a third-order induction generator model is beneficial due to its compatibility with fundamental frequency simulation tools.

On one hand, when the aggregated size of induction generators in a system is very substantial with a large system frequency deviation, the use of a fifth-order induction generator model may be beneficial. On the other hand, the use of this model poses some difficulties. Incompatibility with the fundamental frequency network model and requirements for a small simulation time step are the main obstacles in implementing a fifth-order induction generator model into typical power system stability studies. Therefore, a modified model was proposed in this chapter as an alternate solution to the aforementioned problems.

The following are recommendations for a fixed-speed wind turbine model for different stability studies

- **Short-term voltage stability study:** A short-term voltage stability study generally requires detailed representation of the wind turbine. The mechanical model must be represented at least by a two-mass model. For a passive stall wind turbine, the aerodynamic model is sufficient for representing the constant mechanical power or the constant mechanical torque. However, for an active stall wind turbine, the use of $C_p(\lambda, \beta)$ curve together with a pitch controller is required. This is because the action of the pitch controller must be taken into account.

  Although a third-order induction generator model is less accurate in predicting speed and peak current, the use of the model is still considered as an optimum option. This is due to the fact that the overall inertia of the wind turbine is considerably large. As a consequence, the speed deviation during fault events between a fifth-order induction generator model and a third-order induction generator model is insignificant. While the lack of ability of the third-order model to estimate the peak transient current can be overcome by using an analytical estimation method [70].

- **Long-term voltage stability study:**A first-order induction generator model in combination with a one-mass drive train model is the bottom limit for a fixed-speed wind turbine model to be used for a stability study. However, the use of a

third-order induction generator model with the two-mass model is recommended since the two-mass model of a drive train does not significantly influence simulation efficiency. The use of a fifth-order induction generator model does not increase the accuracy of results.

- **Frequency stability study:**

  For a temporary and small frequency deviation (±5%) with medium wind power penetration (less than 20%), the induction generator model can be adequately represented by a third-order model. However, when the penetration is higher and the frequency deviation is significantly large for a long period of time, the use of a fifth-order induction generator model may provide a more accurate prediction of active and reactive power responses and energy production. The influence of the mechanical and aerodynamic models can be disregarded.

A recommendation for fixed-speed wind turbine models for different stability studies is summarized in Table 3.3.

Table 3.3. Minimum requirements for a fixed-speed wind turbine model for stability studies.

	Type of stability studies		
Turbine component	Short-term voltage stability	Long-term voltage stability	Frequency stability
Aerodynamic model	constant torque[1]	wind speed vs. power	wind speed vs. power
Drive-train model	two-mass model	one-mass model	one-mass model
Generator model	third-order model	first-order model	third-order model[2]

Two alternatives for fault ride-through strategies for a fixed-speed wind turbine were proven to be effective in riding out a severe grid fault. The fault ride-through scheme that employs series dynamic braking resistors demonstrates better dynamic performance in term of voltage, generator speed, active and reactive power compared to the one that relies on active stall control. However, the fault ride-through alternatives are not able to avoid high reactive power absorption by the generator following a fault.

[1] For active stall wind turbine $cp(\lambda, \beta)$ curve or it's linearized model must be used.

[2] A fifth-order induction generator model is beneficial if the level of penetration of fixed-speed wind turbines is considerably high (more than 20 percent)

Chapter 4

Aggregated Model of a Wind Farm consisting of Fixed-speed Wind Turbines

This chapter discusses different aspects of aggregating fixed-speed wind turbines in a wind farm. A validation of an aggregated model of a wind farm against field measurements is also presented in this chapter.

4.1 Introduction

Typical utility-scale wind farms may consist of tens to hundreds of identical wind turbines. As a consequence, representing a wind farm with individual wind turbines for power system stability studies increases the complexity of the model, and thus requires time-consuming simulation. Hence, a simplification of wind farms consisting of a large number of wind turbines is essential. However, this simplification must not result in incorrect predictions of wind farm behaviors, especially under grid faults.

In normal operation, it is essential for the equivalent model of the wind farm to reflect the smoothing effect of wind power fluctuations [71]. This implies that a model of wind plays a more significant role than the electrical and the mechanical parts of wind turbines.

In contrast, an appropriate model of the mechanical and the electrical systems of wind turbines are highly important for dynamic stability studies of power systems. Different methods for aggregating a wind farm have been proposed in [72, 73, 22]. Nevertheless, until now, validations of wind turbine aggregated models during a fault event against field measurement data have been rarely treated in the literature.

The main objective of this chapter is to present an aggregated model of a wind farm with fixed-speed wind turbines validated against field measurement data. The study emphasizes transient events of a wind farm due to a grid fault.

4.2 Aggregation method

For identical machines, a single-machine aggregated model of a wind farm can simply be made by summing all machine ratings. Consequently, the equivalent generator rating is given by

$$S_{eq} = \sum_{i=1}^{n} S_i \tag{4.1}$$

where S_i is the $i-$th generator rating and n is the number of turbine units. Since all parameters are given in per unit, this implies that all parameter values remain the same.

Among the other electrical parts of a wind farm, the transformers and the compensating capacitors are of importance in modeling because of relatively high impedances and admittances, respectively. Wind farm cable impedances, on the other hand, can be ignored. Similar to the generator, the equivalent representation of the transformers is derived by summing up the rating of the transformer by means of (4.1).

It is worth noting that an aggregation of a wind farm is somewhat different from the aggregation of a typical induction machine, for several reasons:

- A wind turbine drive train cannot be considered as a stiff shaft due to the presence of the gearbox and a relatively soft shaft. This factor causes an oscillation in the output power of the turbine when subjected to a grid disturbance. Drive train dynamics dominate the response of the wind turbine rather than the electrical properties of the generator. This is even more critical since the inertia of the turbine is much larger than the inertia of a typical induction machine. Each turbine is also likely to deliver varying mechanical power to the generator.

- During a grid fault, induction motor speed normally slows down. However, the opposite occurs in a wind turbine, where the decrease in voltage due to the grid fault accelerates the generator rotor speed.

4.3 Simulation of an aggregated model

In order to comprehend the problem of wind turbine aggregation, this section presents a comparison between a wind farm modeled as individual wind turbines (a detailed model) and a wind farm modeled as a single equivalent wind turbine (an aggregated model).

This simulation uses a wind farm consisting of 24 x 2 MW wind turbines. The layout of the turbines is shown in Fig. 4.1. The wind turbine data are given in Table 4.1 and 4.2. The wind turbines are modeled using a third-order induction generator model and a two-mass drive train model. The simulation is performed using the simulation tool PSS/E.

The wind speed was assumed to be distributed unevenly during the simulation, which results in a difference in the output power of the turbines. Power outputs of the turbines in the first to the fourth rows were 100%, 80%, 60% and 40%, respectively. The total output power of wind farm was equivalent to 33.6 MW. This power distribution

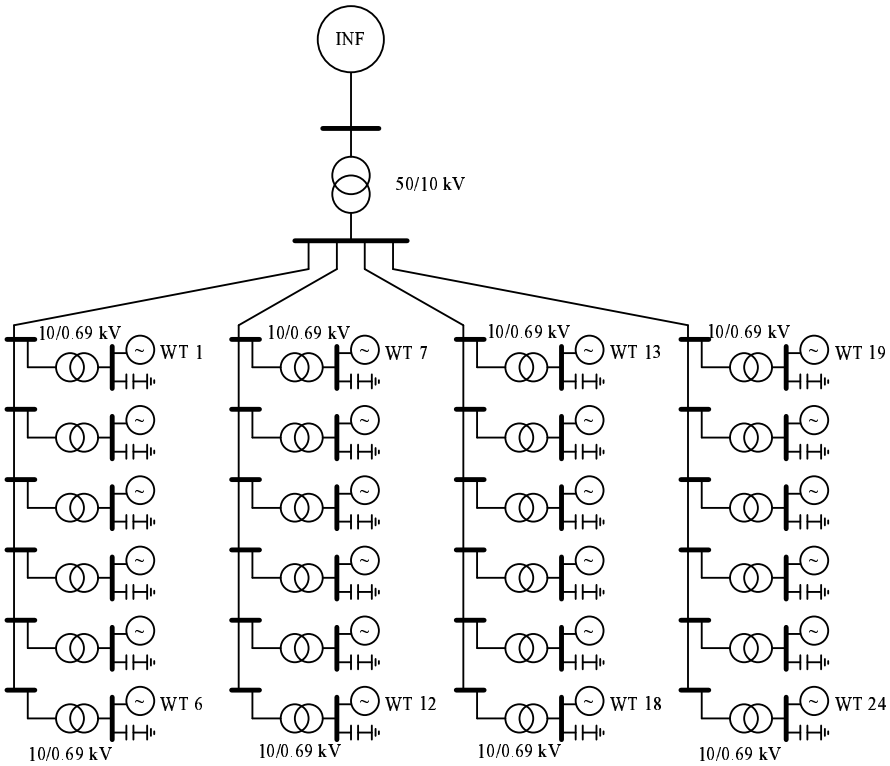

Figure 4.1. Layout of wind farm.

Table 4.1: Generator parameters.

Parameters	Values	Units
Power base (P_{base})	2	MW
Voltage base (V_{base})	690	V
Stator resistance (R_s)	0.00539	pu
Stator leakage reactance (X_{sl})	0.09062	pu
Magnetizing reactance (X_m)	3.31065	pu
Rotor resistance (R_r)	0.007616	pu
Rotor leakage reactance (X_{rl})	0.100718	pu
Generator rotor inertia constant (H_g)	0.53273	s

is given as an exemplary case. In a more realistic case, however, the difference in the output power of the turbines would be smaller.

For the aggregated model, a single generator was used to represent all the turbines in the farm. The output power of the generator was equal to the total output power of the farm, which was 33.6 MW. The transformers and the compensating capacitors were lumped together into a single transformer and a single compensating capacitor.

The voltage, active and reactive power responses of the detailed and the aggregated model are shown in Fig. 4.2. There was no significant difference between the two models

Table 4.2: Drive train parameters.

Parameters	Values	Units
Power base (S_{base})	781	kVA
Turbine rotor and low speed shaft inertia constants (H_t)	5.8	s
Shaft stiffness (K_s)	0.5603	

of the wind farm.

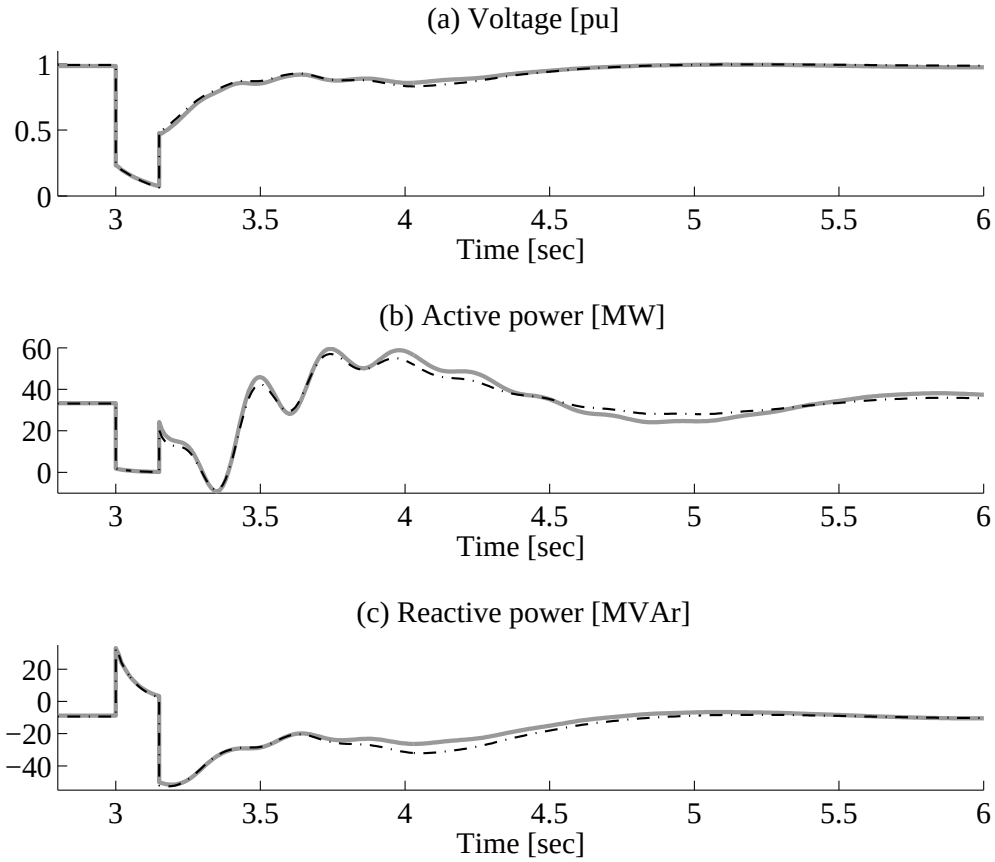

Figure 4.2. Voltage, active and reactive power at collector bus: detailed model (dash-dot) and single machine aggregated model (solid-grey).

Examination of the individual turbines, however, shows that the behavior of each wind turbine was not the same. For example, wind WT-24 suffered the least severe voltage dip, while generating the least power output during the fault. The worst case was encountered by WT-1, which endured the most severe voltage dip at rated power output. This resulted in a difference in speed deviation, as shown in Fig. 4.3. During the transient event, the maximum speed deviation of WT-1 was 40% higher than the maximum speed deviation of the single equivalent turbine. In contrast, the speed deviation of WT-24 was 40% lower than the equivalent wind turbine. Under more

severe conditions, this may lead to a trip of wind turbines in the first row, while the rest of the turbines would remain intact.

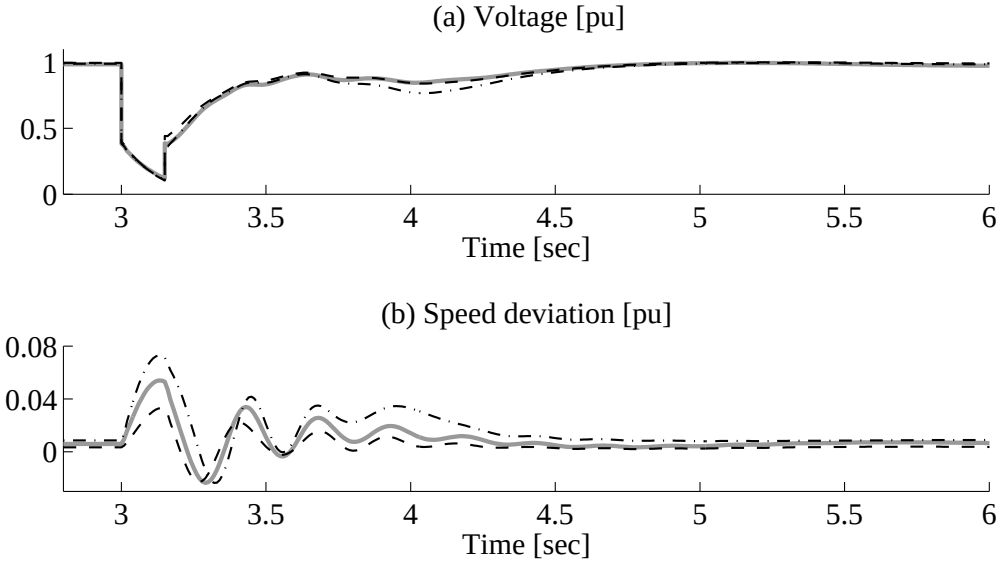

Figure 4.3. Voltage and speed of wind turbines: single turbine model (solid-grey), turbine 1 (dash-dot) and turbine 24 (dash).

A more accurate representation of a wind farm can be achieved by representing the wind farm as several clusters of wind turbines according to wind speed distribution. However, the cluster representation a wind farm conflicts with the idea of aggregation. Moreover, a trip of some of the wind turbines in a wind farm due to uneven wind distribution will not end up as the worst case scenario anyway. In fact, a worst case scenario would be obtained if all wind turbines were operating at rated value. In such a case, the speed estimation of each wind turbine would be practically the same as the estimation provided by a single equivalent wind turbine model. Hence, the representation of a wind farm as a single machine is sufficient for predicting the best and the worst scenarios. Nevertheless, the cluster representation of a wind farm is beneficial when investigating the impact of the wake effect and wind transport phenomena in a large wind farm as suggested in Chapter 7.

4.4 Validation

In the following, the model is validated against the field measurement data acquired from the Olos wind farm.

4.4.1 Measurement location and data

A detailed description of the wind turbines in the Olos wind farm is presented in Subsection 3.10.2. The farm was connected to a substation bus through a single three-phase overhead line. Observe that there is a load connected to the same feeder where the farm is connected.

The farm measurements were taken at the wind farm collector bus. Another measurement system was located at the substation feeder where the farm is connected. The location, sampling frequency and the measured parameters of each measurement system are given in Fig. 4.4. More detailed information on the wind turbines and farm network parameters is provided in 3.10.2.

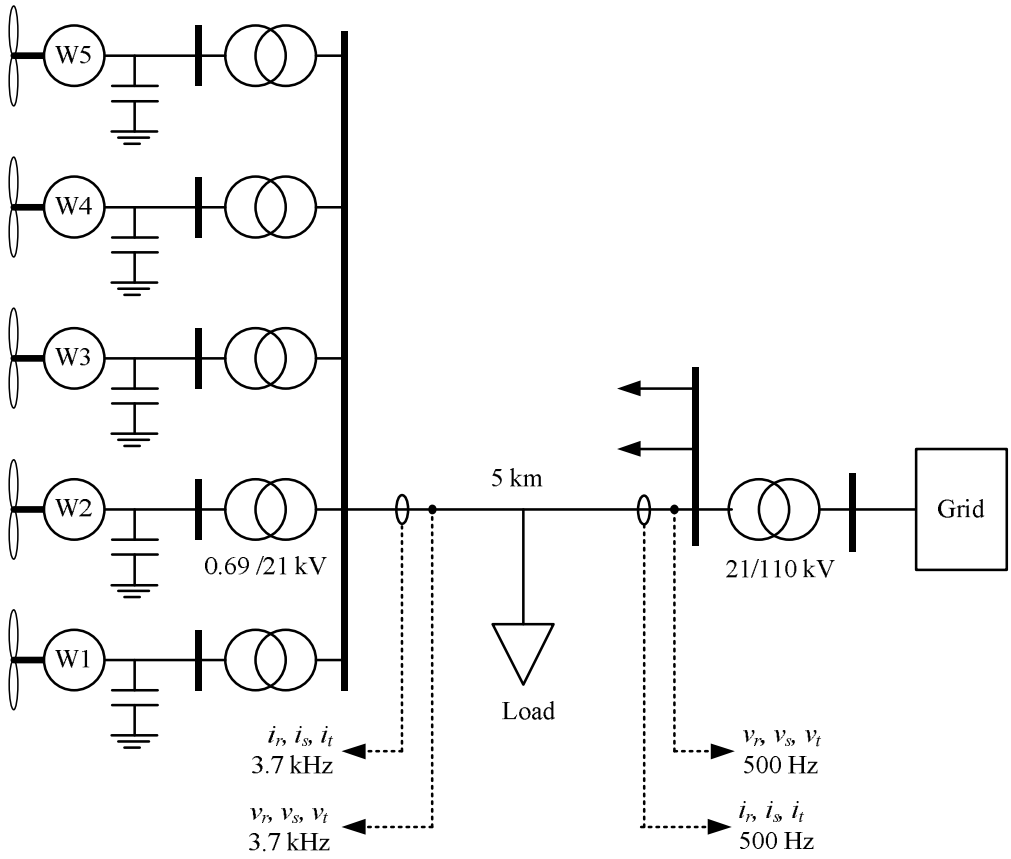

Figure 4.4. Olos wind farm measurement set up.

3.7 kHz measurement data

The voltage and current from a 3.7 kHz measurement at the collector bus are presented in Fig. 4.5. By using these quantities, the active and reactive power output of the farm can be obtained as shown in Fig. 4.6.

500 Hz measurement data at substation

The voltages and currents along with the calculated active and reactive power from 500 Hz measurement data of the wind farm feeder at the substation are shown in Fig. 4.7. As mentioned earlier, the presence of the load in the same feeder where the farm is connected makes the current at the wind farm collector and the wind farm feeder at the substation significantly different.

As shown in Fig. 4.8, the total production of the farm measured at the wind farm collector before the fault was approximately 932 kW and the reactive power consumption was 430 kVAr.

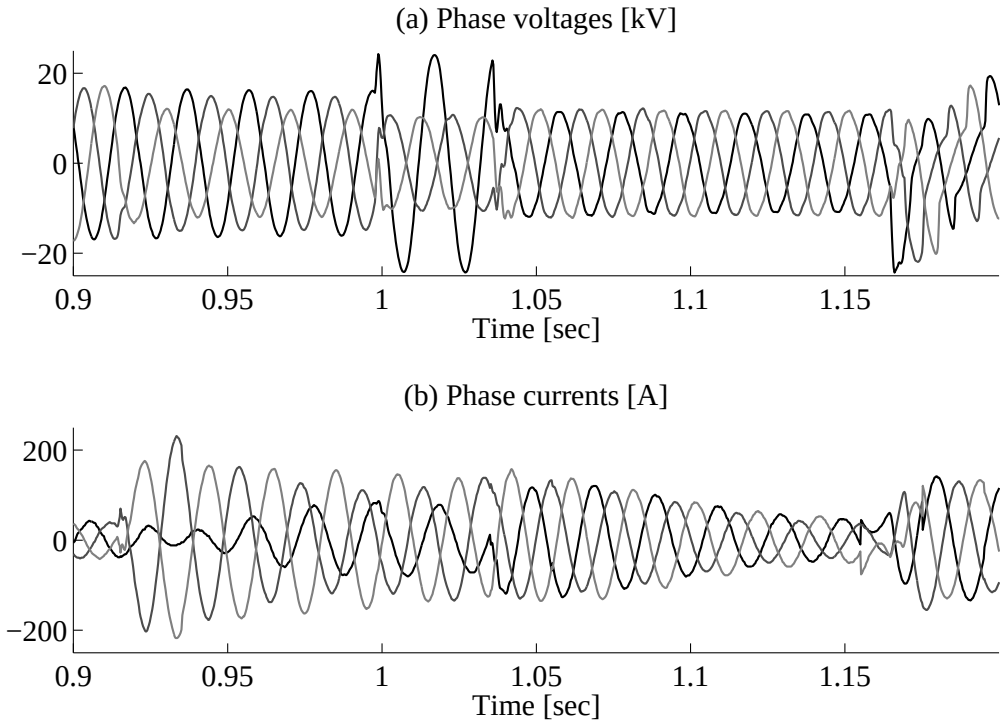

Figure 4.5. Measured voltage and current of at wind farm collector with 3.7 kHz sampling frequency.

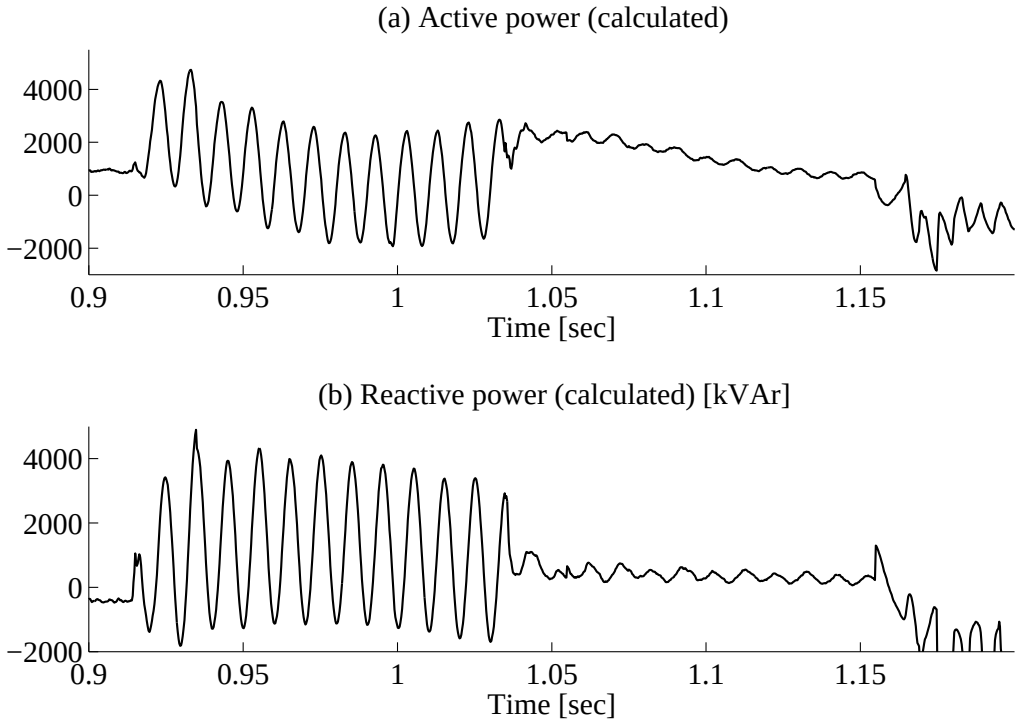

Figure 4.6. Calculated active and reactive power from measured voltage and current of wind farm with 3.7 kHz sampling frequency.

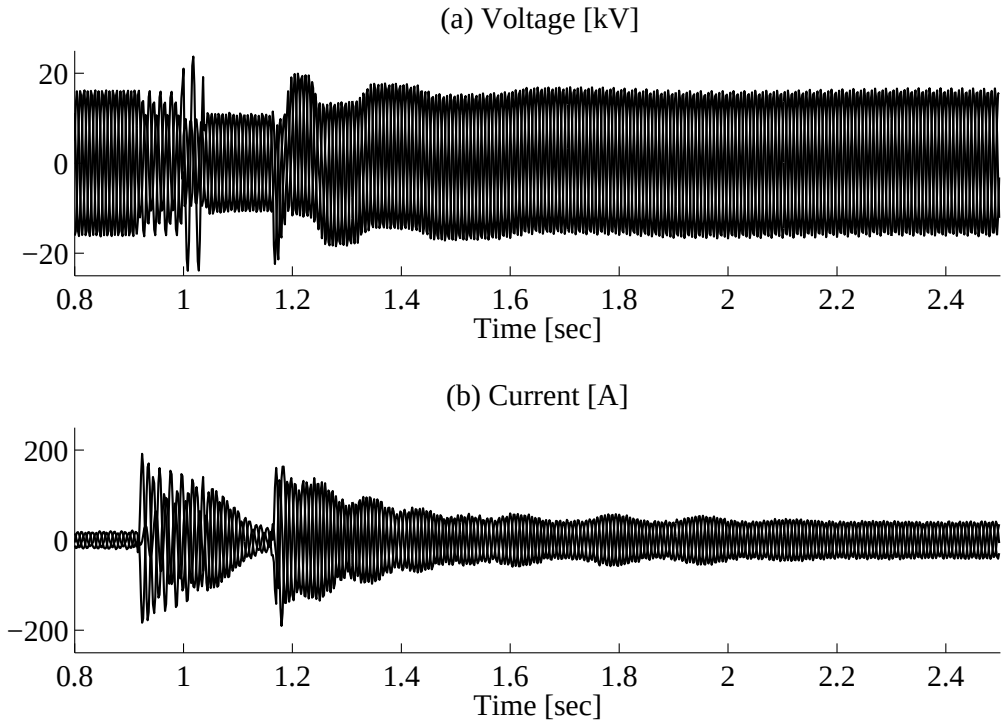

Figure 4.7. Measured voltage and current of wind farm feeder at the substation with 500 Hz sampling frequency.

As shown in Fig. 4.8, the total production of the farm measured at the wind farm collector before the fault was approximately 932 kW and the reactive power consumption was 430 kVAr.

It should be noted that one of the compensating capacitors at wind turbine 2 was out of operation, and thus the turbine took the corresponding lacking reactive power from the grid. The change in reactive power in pre- and post-fault situations, mainly due to a disconnection of capacitor banks in the wind farm, can be calculated from the substation 500 Hz data. The calculated change in reactive power is about 500 kVAr.

Active power production and reactive power consumption of the other turbines, as known from continuous 1 Hz measurement data not shown in this thesis, are presented in Table 4.3.

Table 4.3: Initial wind turbines active power output and reactive power consumption recorded before fault.

Turbine	P (kW)	Q (kVAr)
1	200	50
3	250	60
4	200	50
5	200	90

Reactive power consumption values suggest that all three steps of the capacitor

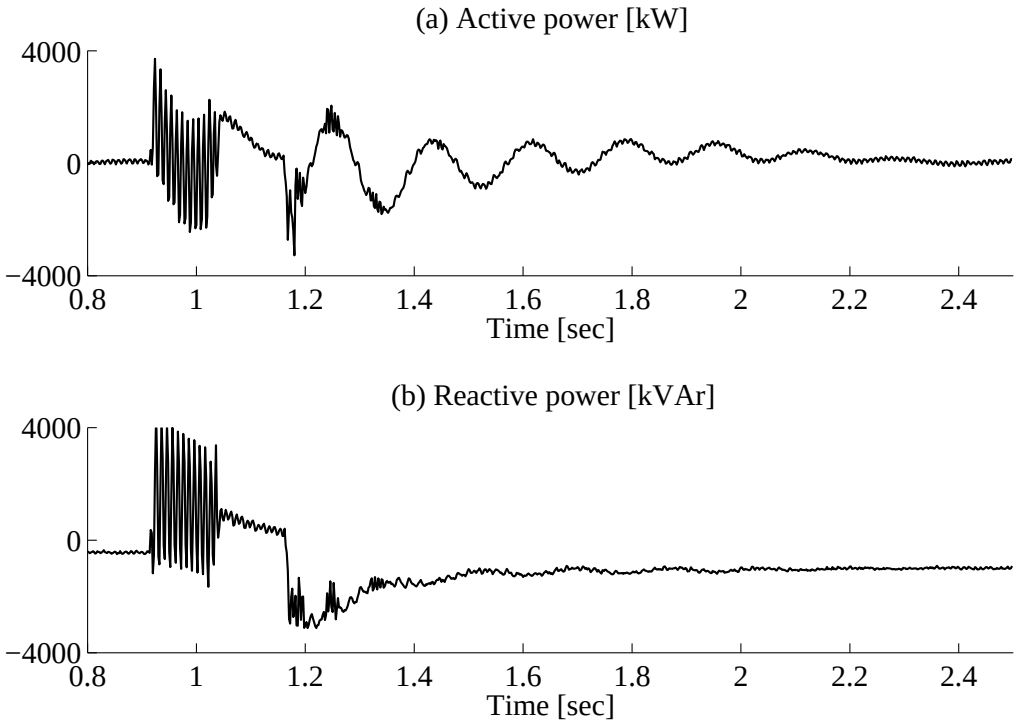

Figure 4.8. Calculated active and reactive power from measured voltage and current of wind farm feeder at the substation with 500 Hz sampling frequency.

banks in turbines 1, 3 and 4 were in operation. In turbine 5, only 2 steps of the capacitor banks were in operation. The change in reactive power between pre-fault and post-fault stages, based on 1 Hz continuous data, suggests that all the operating capacitors were disconnected during the grid fault.

The active and reactive power flow at the substation feeder measurement point towards the substation was about 50 kW and -450 kVAr, respectively. As shown in the measurement data, despite differences in magnitude, profiles of the measurement data at the collector bus and at the substation feeder are similar to the single turbine measurement data presented in Section 3.10.2. This similarity indicates that all wind turbines in the farm respond synchronously.

Although the measurement point at the substation feeder does not exactly represent farm quantities, wind farm dynamics can be clearly seen in the substation feeder measurement due to the following conditions:

- No influential dynamics of the load occurred during the fault, i.e. the load can be treated as a constant impedance.

- The line impedance connecting the wind farm to the substation is relatively small. Therefore the influence of the load current response on the voltage at the point of measurement is marginal.

4.4.2 Simulation

Simulation of 3.7 kHz measurement data at wind farm collector

The farm was modeled as a single equivalent turbine with a rated power of 3 MW (5×600 kW). The mechanical power input was set at a constant value that produced electric power output of 930 kW, as given by the measurement data. A fifth-order induction generator model and a two-mass drive train model were used in the simulation. The terminal voltage was used as an input of the generator model.

Simulation results from the aggregated model of the wind farm, and the comparison with corresponding measurement data are presented in Fig. 4.9. The simulated current in Fig. 4.9a shows fairly good agreement with the measured current shown in Fig. 4.5b. The active and reactive power responses between the model and the measurement data, as shown in Fig. 4.9a and 4.9b., agree similarly.

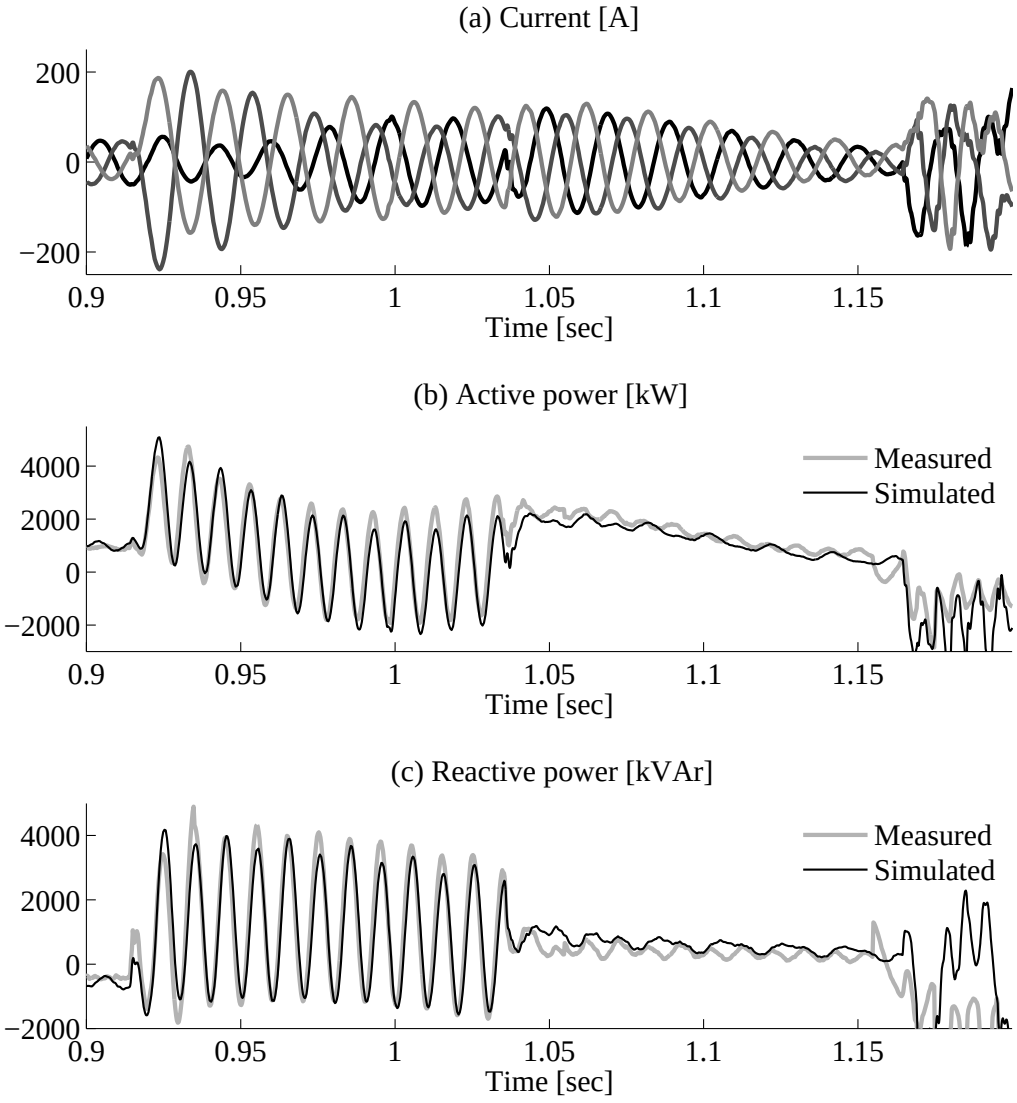

Figure 4.9. Simulated current, active and reactive power of wind farm with 3.7 kHz sampling frequency voltage data as an input.

Simulation of the 500 Hz measurement data of the wind farm feeder at the substation

Wind farm simulation results based on the 500 Hz measurement data are shown in Fig. 4.10. There is a slight difference in the magnitude of active power between the simulation and the measurement data at the substation feeder measurement point after $t = 1.4$ s This is because a constant mechanical input power was assumed in the model, while in reality there may be power fluctuations due to variations in wind speed. The slight difference in oscillation frequency was likely due to inaccurate mechanical parameters used in the simulation. The dynamics of the load may also contribute to this discrepancy, although not significantly.

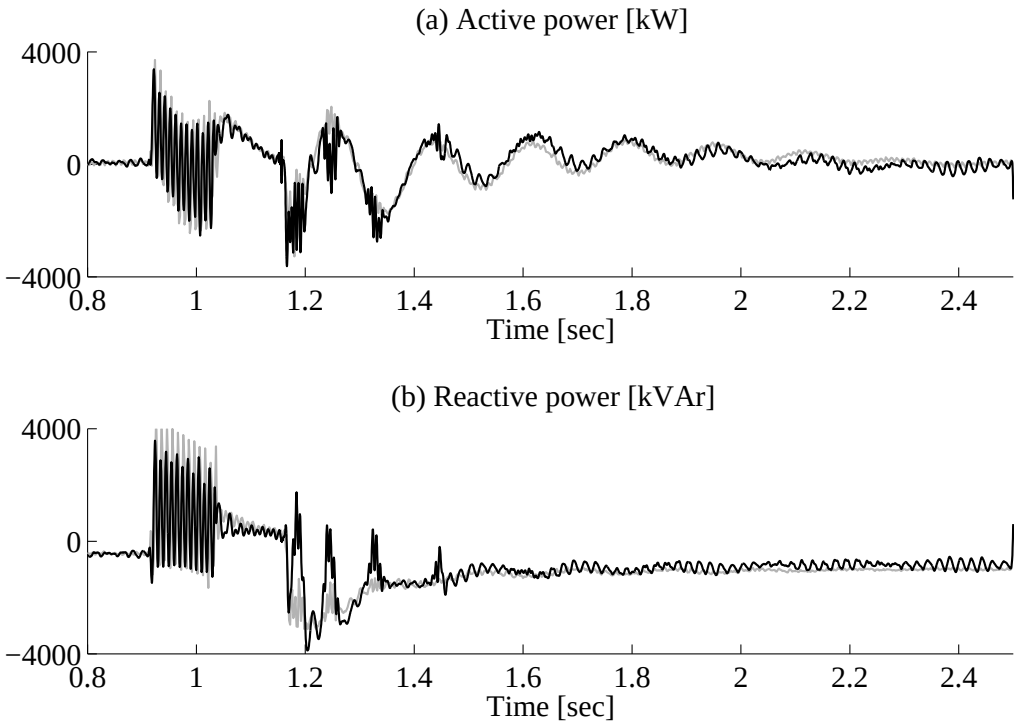

Figure 4.10. Active and reactive power of wind farm feeder at substation: simulated (black), the 500 Hz measurement data (grey).

From simulation results including low and high sampling frequencies, it can be concluded that the behaviors of the wind farm subjected to a grid fault can be accurately modeled as a single equivalent wind turbine.

4.5 Conclusion

The generators, the compensating capacitors and the transformers are some of the electrical components that are essential to be considered in an aggregated model of a wind farm. Effects of wind farm cables can be neglected in an aggregated model. In a grid fault simulation, a small wind farm can be adequately represented by a single equivalent wind turbine. Simulation results show that all turbines in the wind farm respond in phase to a fault. For a large wind farm, the speed response of individual

wind turbines may not be the same due to the uneven distribution of wind speed. This may lead to tripping of some wind turbines in the farm. This situation cannot be simulated by a single machine representation of the wind farm. Nevertheless, a single machine representation of a wind farm is capable of representing a worst case scenario corresponding to total wind turbine disconnection.

Chapter 5

Doubly Fed Induction Generator Wind Turbines

Models of various DFIG wind turbine components, controls and FRT schemes are described in this chapter. The importance of these components and controls in characterizing DFIG wind turbine model responses is examined.

5.1 Introduction

This chapter provides a detailed discussion of a DFIG wind turbine system. The overall arrangement of the system is first discussed. Then the working principles and significance of each part of the system are explained. In the remaining sections of this chapter, the operation modes and the operating strategy of the system are presented.

Among wind turbine concepts, a DFIG wind turbine is the most dominant concept in the market. Table 5.1 shows examples of DFIG wind turbine products from a number of manufacturers.

Table 5.1: Wind turbine products with DFIG concept.

Manufaturer/ type	Power (MW)	Rotor Ø (m)	Nom. wind (m/s)	Turb. speed (rpm)	Gear ratio
Nordex N100/2500 kW	2.5	99.8	12.5	9.6 - 14.9	1:77.4
Nordex N80/2500 kW	2.5	80	15	10.9 - 19.1	1:68
Vestas V80-2.0, 50 Hz	2.0	80	15	9.0 - 20.7	1:92.6
GE 1.5sle, 60 Hz	1.5	77	14	12.1 - 22.2	1:72

5.2 Wind Turbine Components

Components of a DFIG wind turbine are shown in Fig. 5.1. The stator of the DFIG is connected directly to the network meaning that it operates synchronously at grid

frequency. The rotor current is controlled by a power converter to vary the electromagnetic torque and machine excitation. The power converter size is a fraction of the generator rating, normally in the range between 15 to 30 percent. Since the power converter operates in bi-directional power mode, the DFIG can be operated either in sub-synchronous or in super-synchronous operational modes.

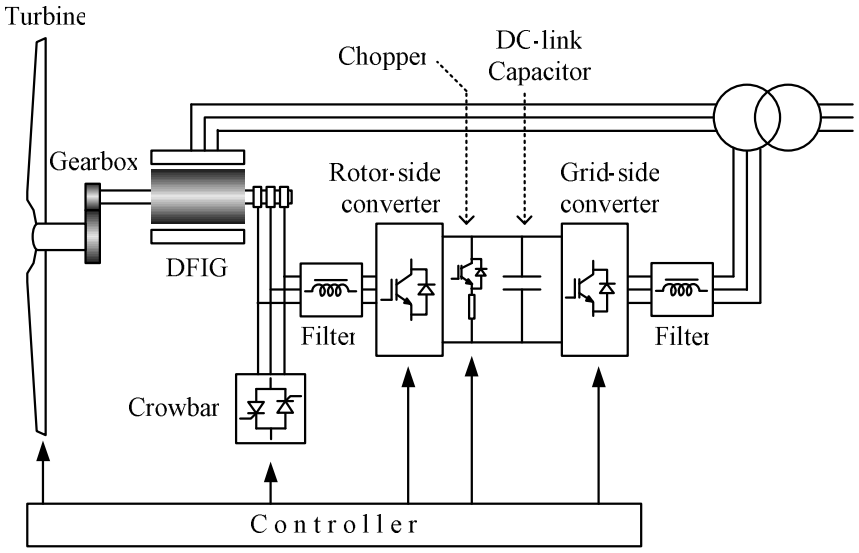

Figure 5.1. Components of DFIG wind turbine.

The general control structure of the wind turbine model is shown in Fig. 5.2. A model of a DFIG wind turbine basically consists of (1) a generator and drive train, (2) a turbine rotor model, (3) a grid-side converter and dc-link capacitor, (4) a pitch controller, and (5) a rotor-side controller that controls the active and reactive power of the generator.

5.2.1 DFIG model

The main construction of a DFIG consists of two essential components, namely the stator winding and the rotor winding equipped with slip rings. The stator is provided with three-phase insulated windings making up a two- or four-pole design. This part is connected to the grid through a three-phase transformer. Similar to the stator, the rotor is also constructed of three-phase insulated windings. The rotor windings are connected to an external stationary circuit via a set of slip rings and brushes. By means of these components, the controlled rotor current can be either injected to or absorbed from the rotor windings.

The stator and rotor are usually coated in a closed assembly to protect the machine from dust, damp and other unwanted intrusions. In wind turbine applications, this generator is mounted in the nacelle of the wind turbine system. The typical stator voltages for the megawatt-class of wind turbines are 690 and 960 V [74].

The stator and rotor voltage equation can be written as

$$\vec{v_s} = \vec{i_s} R_s + j\omega_e \vec{\psi_s} + \frac{d\vec{\psi_s}}{dt} \tag{5.1}$$

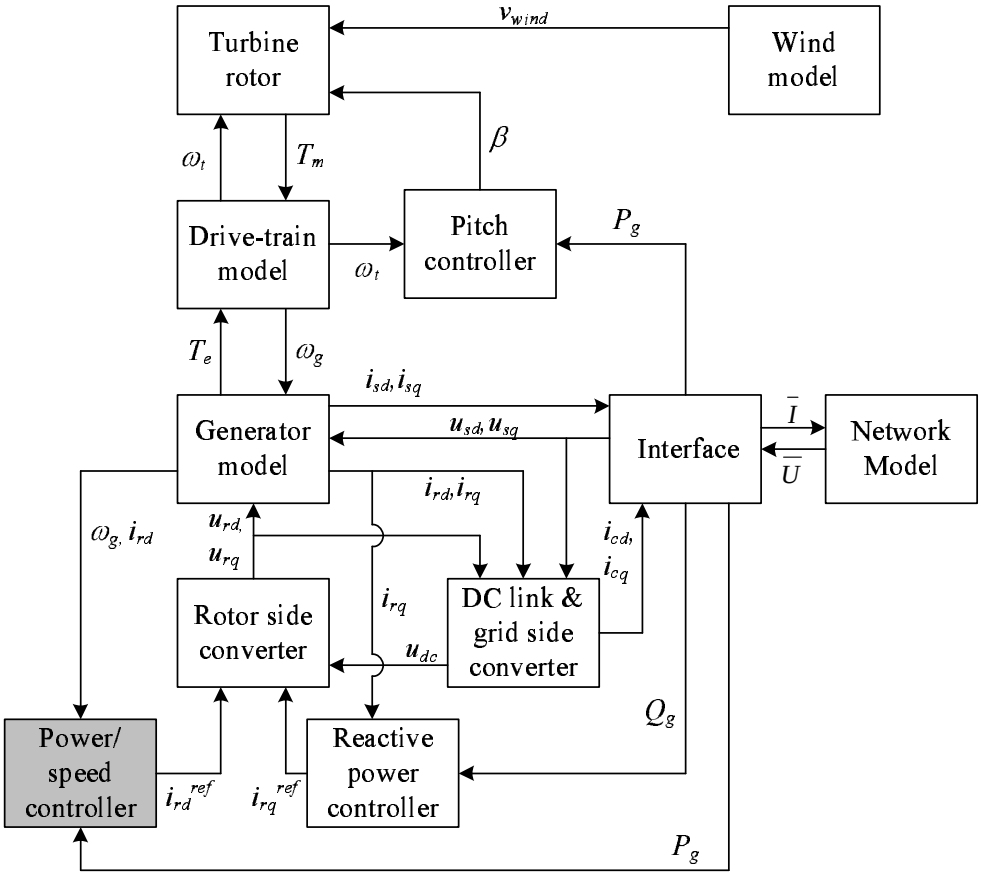

Figure 5.2. Control block diagram of DFIG wind turbine.

$$\vec{v_r} = \vec{i_r} R_r + j(\omega_e - \omega_r)\vec{\psi_r} + \frac{d\vec{\psi_r}}{dt} \tag{5.2}$$

The complex power is given as

$$\vec{S} = \vec{v_s}^* \vec{i_s} + \vec{v_r}^* \vec{i_r} \tag{5.3}$$

Similar to a fixed-speed wind turbine, the generator model of a DFIG wind turbine can be represented in detail using a fifth-order model or represented in a simplified version using a first-order model.

5.2.2 Drive-train

Similar to a fixed-speed wind turbine, a generator in a DFIG wind turbine is driven by the wind turbine through a gearbox system to attain a suitable speed range for the rotor. By means of the gearbox, the low rotational speed of the wind turbine (9-21 rpm) is transformed into high rotational speed on the generator side (900-2000 rpm for 50 Hz system frequency). For 2 - 3 MW wind turbines, a gearbox ratio of around 80-100 is common.

The actual gearbox ratio is chosen considering the optimum operation speed of the generator. The optimum speed of the generator is selected based on two factors, namely the annual wind speed distribution and the size of the power converter. The

annual efficiency of the generator is somehow influenced by the operating speed of the generator, whether it operates at sub-synchronous or super-synchronous speed. Another aspect to be considered when selecting a gearbox ratio is the weight of the gearbox, which increases along with gearbox ratio. Further discussion of the influence of gearbox ratio on the wind turbine system can be found in [75, 76].

The drive train system of a DFIG wind turbine can be modeled using a two-mass model as discussed in section 3.5. Despite the minor influence of shaft natural damping, it is important to note that a wind turbine with a power converter, such as the one with a DFIG, is often supplied with shaft torsional active damping [26].

5.2.3 Power converter

As shown in Fig. 5.1, the power converter is made up of a back-to-back converter connecting the rotor circuit and the grid, which is known as a Scherbius scheme. The converters are typically made of voltage-fed current regulated inverters, which enable a two-directional power flow. The inverter valves make use of IGBTs provided with freewheeling diodes (see Fig. 5.3). An LC-filter is provided on each converter output to minimize switching harmonics and to protect component insulation.

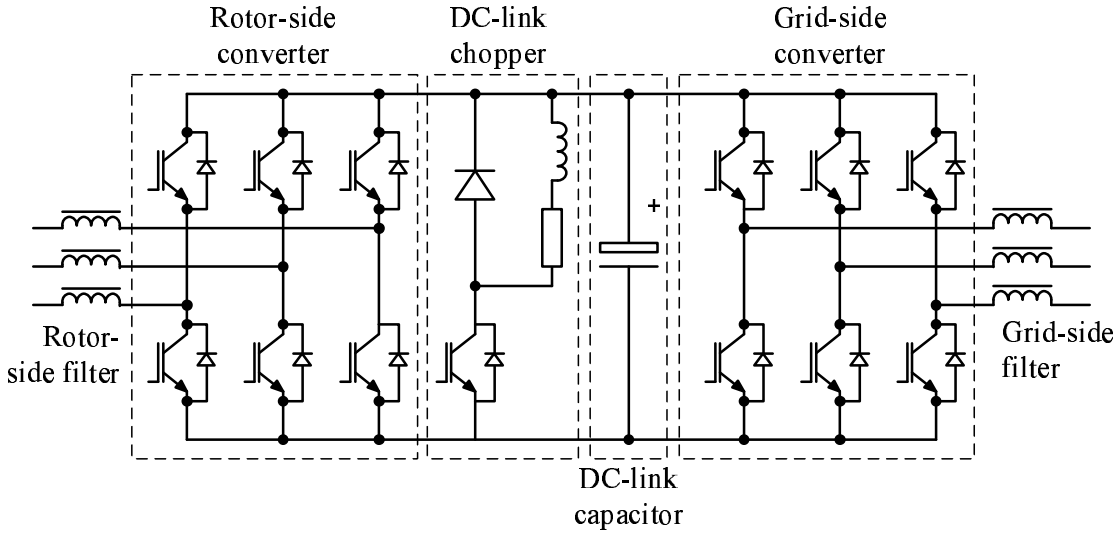

Figure 5.3. Power converter in DFIG wind turbine.

Rotor-side converter

The power rating of the rotor-side converter is dictated by two factors, namely maximum slip power and reactive power control capability. The rotor-side converter can be seen as a current controlled voltage source converter. The rotor current can be controlled in several ways. The most common method is by utilizing a PWM modulation as presented in [77, 78]. Another option is to employ a hysteresis modulation method to the rotor-side converter [79]. The principle is also referred to as current-regulated modulation with a tolerance band control [80] or an adaptive current control PWM [81]. In this method, the current control tracks the phase rotor current to be within the hysteresis band by turning on the upper or lower valves of the converter

based on a hysteresis control. When the rotor phase current exceeds the upper band, the lower valve of the corresponding phase is turned on and the upper valve is turned off. Similarly, when the actual current is below the lower band, the upper valve of the corresponding phase is turned on and the lower valve is turned off. This mechanism, in turn, forces the actual current to follow the current reference within a tolerance band. The hysteresis band width is defined by considering the switching frequency limitations and the switching losses of the IGBTs [82].

DC-link and grid-side converter

The power rating of the grid-side converter is mainly dictated by maximum slip power since it usually operates at a unity power factor. A typical output voltage of the gride-side converter is 480 V [83].

The grid-side converter is normally dedicated to controlling the dc-link voltage only. The converter can also be utilized to support grid reactive power during a fault [84]. The grid-side converter can also be used to enhance grid power quality [85]. However, these abilities are seldom utilized since they require a larger converter rating.

In stability studies, it is well accepted to disregard the switching dynamics of the converter. In addition, converters are assumed to be able to follow the demanded values of the converter current [86].

A detailed model of a grid-side converter control is presented in [77] where the converter is modeled as a current-controlled voltage source. This constitutes a representation of the dc-link capacitor and the grid-side filter in the model.

The amount of energy stored in the dc-link capacitor can be written as

$$E_c = \int P dt = \frac{1}{2} C v_{dc}^2 \tag{5.4}$$

where P is the net power flow into the capacitor, C is the dc-link capacitor value and v_{dc} is the capacitor voltage. P is equivalent to $P_r - P_c$, where P_r is the rotor power inflow and P_c is the grid power outflow. Derivative of (5.4) can be written as

$$\frac{dv_{dc}}{dt} = \frac{P}{v_{dc}C} = \frac{P_r - P_c}{v_{dc}C} \tag{5.5}$$

Fig. 5.4.a shows a single-line diagram of the dc-link and grid-side converter circuit. The grid-side converter equations expressed in the dq-components aligned to the grid voltage vector can be written as

$$v_{gd} = R_g i_{gd} + L_g \frac{di_{gd}}{dt} - \omega_e L_g i_{gq} + v_{cd} \tag{5.6}$$

$$v_{gq} = R i_{gq} + L_g \frac{di_{gq}}{dt} + \omega_e L_g i_{gd} + v_{cq} \tag{5.7}$$

where R_g and L_g are the grid filter resistance and reactance, respectively, i_{gd} and i_{gq} denote the grid current vector components, v_{gd} and v_{gq} denote the grid voltage vector components, v_{cd} and v_{cq} denote the converter voltage vector components and ω_e is the grid frequency. The control scheme of the dc-link voltage by means of the grid-side converter is shown in Fig. 5.4.b.

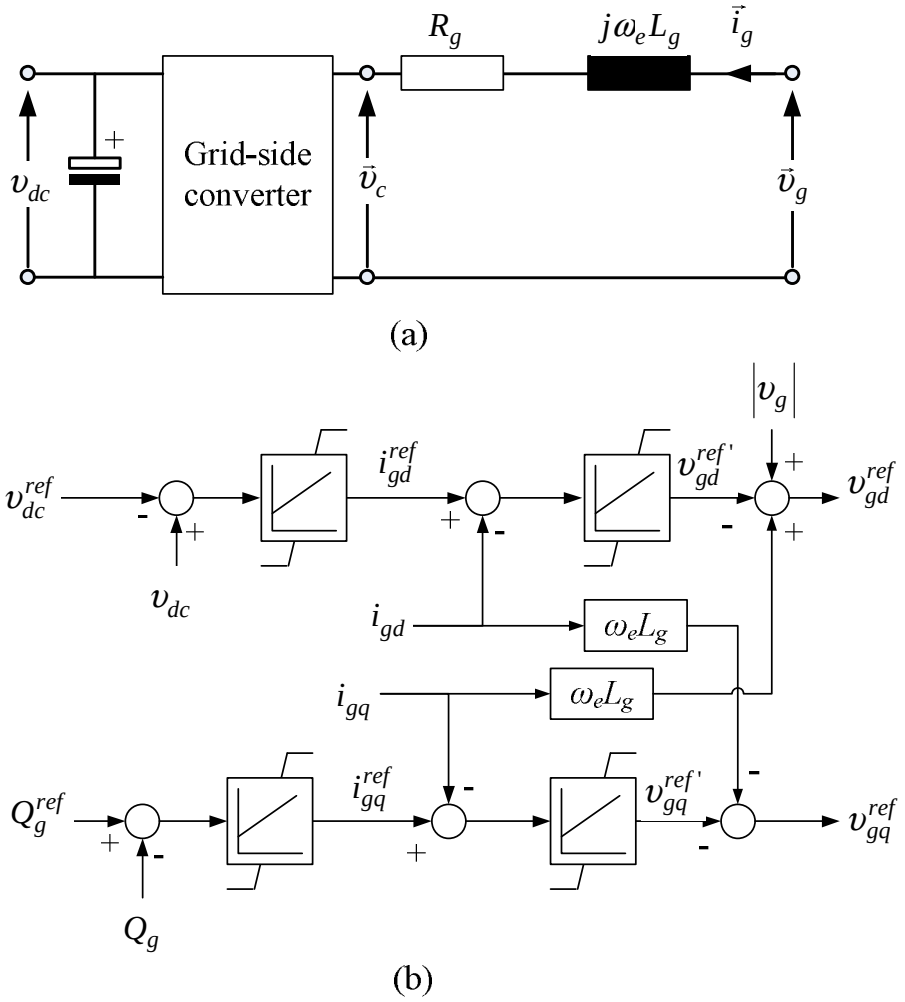

Figure 5.4. Grid-side converter and dc-link voltage: (a) schematic diagram, (b) controller block.

A simpler model of a grid-side converter can be found in [87], where the converter is modeled as a current source. Consequently, the grid filter representation can be omitted from the model. In some cases, such as in [88, 89], the grid-side converter is omitted from the model by assuming a constant dc-link voltage and a unity power exchange between the grid-side converter and the grid. In this case. As a consequence, the converter can be modeled as an active current injector or absorber. The amount of active power injection or absorption is determined directly from the rotor active power. If necessary, reactive power injection or absorption can be modeled independent of rotor reactive power, which is subject to the limitations of the grid-side converter size.

Dc-link braking resistor

A dc-link braking resistor, which is also known as a dc-link chopper, is provided in the dc-link bus to dissipate excess energy in the dc-link capacitor during a grid fault. The arrangement consists of a resistor and an electronic switch, usually an IGBT. Several units of dc-link braking resistors can be arranged in parallel to increase energy dissipation capacity. A further description of the dc-link braking resistor can be found

in section 8.5.3 where its application in a full power converter wind turbine is discussed.

5.2.4 Crowbar

A rotor crowbar is designed to bypass the rotor-side converter, i.e. to short-circuit the rotor, in order to avoid overcurrent on the rotor-side converter as well as overvoltage on the dc-link capacitor. The crowbar consists of thyristor(s) with an external resistance insertion. As shown in Fig. 5.5, the crowbar can be constructed by placing two pairs of anti-parallel thyristors between the phases or by using a combination of a diode bridge and a single thyristor [90].

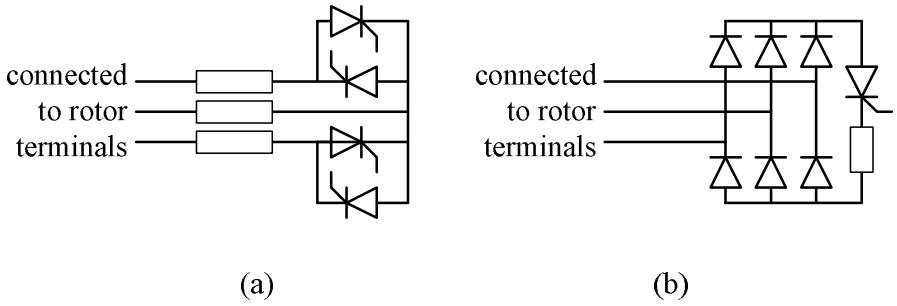

Figure 5.5. Crowbar arrangement.

Typically, the crowbar resistance value is between 1 to 10 times the rotor resistance [38], however the dimension is actually dependent on machine parameters. A higher crowbar resistance value is favorable to quickly dampen rotor transient current. On the other hand, a resistance value that is too high may lead to the risk of overvoltage on the converter. Therefore, the value of the resistance must be designed as a compromise between these two factors. The maximum value for the crowbar resistance is estimated by [91]

$$R_{cb,max} = \frac{v_{r,max} {X_s}'}{\sqrt{1.7|\vec{v}_s|^2 - {v_{r,max}}^2}} \tag{5.8}$$

where $v_{r,max}$ is the maximum allowable rotor voltage, ${X_s}'$ is the stator transient reactance, and v_s is the stator voltage vector.

The crowbar action can be triggered either by dc-link overvoltage or by rotor-side converter overcurrent. The dc-link overvoltage protection is typically designed to activate when the dc-link voltage reaches approximately 12% above the nominal value [83, 92, 30]. Normally IGBTs in the converter can handle peak current twice as much as the nominal current for 1 ms. For this reason the converter overcurrent protection is typically set at 1.8 pu [93].

Once the crowbar is activated, it takes tens of ms for the crowbar to disconnect the rotor current. This is because the thyristor can only disconnect the current at a zero crossing, whereas during the fault there may be dc-components in the current. The problem is more severe for the crowbar arrangement shown in Fig. 5.5.b since the rotor current flowing through the thyristor is continuous. An inability to quickly cease the rotor transient current restrains the rotor converter restarting process, which is obviously undesirable for a fault ride-through strategy.

To resolve the limitations of a thyristor-equipped crowbar, an active crowbar is proposed in [90]. Accordingly, the thyristor is substituted by a GTO-thyristor or an IGBT as shown in Fig. 5.6. In an active crowbar, the rotor current can be ceased with the forced commutation of the GTO-thyristor or the IGBT.

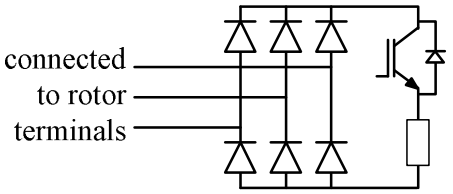

Figure 5.6. Active crowbar.

5.2.5 Aerodynamic model and pitch controller

The aerodynamic system in a wind turbine system converts kinetic energy from a wind flow into rotational mechanical energy in the form of mechanical torque and speed. The mechanical torque of a wind turbine is expressed as

$$T_t = \frac{1}{2\omega_t S_b} \rho \pi R^2 v_w^3 Cp(\lambda, \beta) \tag{5.9}$$

where ρ is the air density in kg/m^3, v_w is the wind speed in m/s, R is the blade length in m, Cp is the power coefficient, S_b is the generator power base value, β is the pitch angle, and λ is the tip-speed ratio obtained from

$$\lambda = \frac{\omega_t R}{v_w} \tag{5.10}$$

When wind speed increases beyond the rated value, the electromagnetic torque is not longer sufficient to control rotor speed since this leads to an overload on the generator and the converter. To prevent rotor speed from becoming too high, the extracted power from incoming wind must be limited. This can be done by reducing the coefficient of performance of the turbine or the C_p value. As explained earlier, the C_p value can be manipulated by changing the pitch angle β (see section 3.6).

Altering the pitch angle β means slightly rotating the turbine blades along the axis. The blades are considerably heavy in a large turbine. Therefore, the rotation must be facilitated by either hydraulic or electric drives.

The pitch controller model is given in Fig. 5.7. The lower part of the pitch controller shown in the figure is the rotor speed regulator, while the upper part is an aerodynamic power limiter. The entire control can be realized by means of PI controllers.

5.3 Operation Modes

The operation modes of the DFIG can be differentiated into two categories, namely super-synchronous and sub-synchronous operations. The distinctions between these operations can be determined from the relative speed of the rotor over the synchronous speed and the power-flow direction passing the power converter.

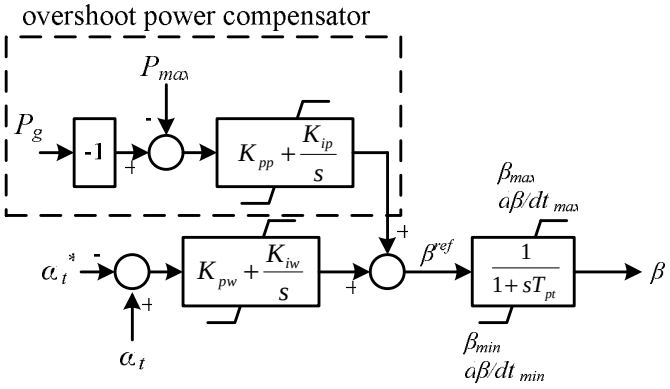

Figure 5.7. Pitch controller model.

Fig. 5.8.a shows the power flow of a DFIG operating in sub-synchronous operation mode. In this operation, the rotor speed is slower than the synchronous speed, which means the slip is positive. In order to enable generation mode, positive slip power must be obtained by injecting power from the grid into the rotor by means of a power converter. Therefore, closed loop power flow occurs through the rotor and the stator.

As shown in Fig. 5.8.b, in super-synchronous operation mode, mechanical power from the shaft is split into two parts, the largest part of the power goes to the stator and a fraction of the power passes through the rotor causing a negative slip.

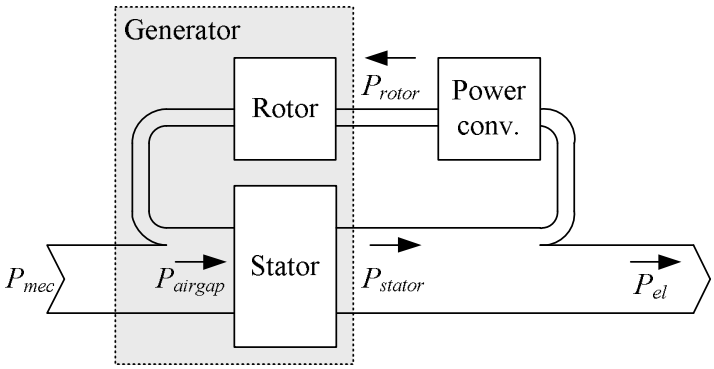

(a) Sub-synchronous operation

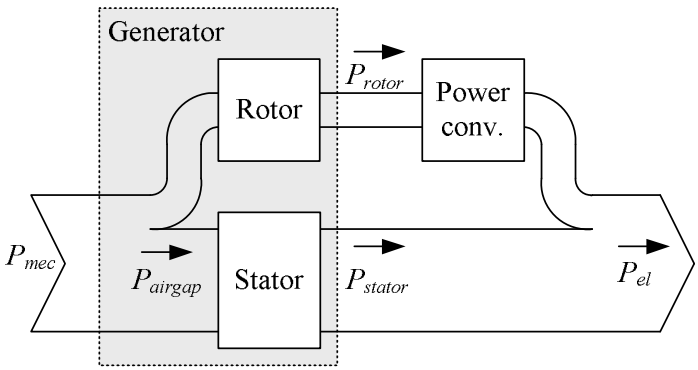

(a) Super-synchronous operation

Figure 5.8. Sub and super-synchronous operation mode of DFIG.

5.4 Operating Regions

Several operating regions of a DFIG wind turbine can be defined based on incoming wind speed, generator speed and generator power. These operating regions are illustrated in Fig. 5.9.

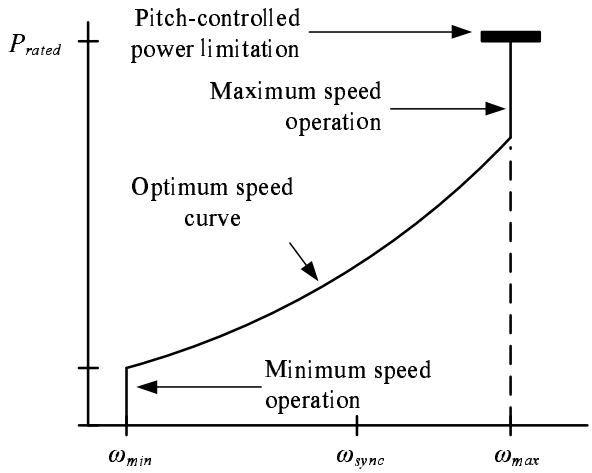

Figure 5.9. Power speed curve.

Minimum speed operating region The minimum speed operating region is chosen when the turbine operates at low wind speed. At this operating point, the generator speed is kept constant at its minimum speed, which is usually around 30% below synchronous speed.

Optimum speed operating region In the optimum speed operating region, the speed of the turbine is adjusted to yield a maximum power capture at a given wind speed. This strategy is also called the 'wind-driven mode.' However, this operation may cause generator power output fluctuations due to variations in wind speed. This principle is appropriate in circumstances where the rated power of the wind turbine is not reached. Generator speed is electromagnetically controlled by the rotor-side converter.

Maximum speed operating region At high wind speed, generator speed is not able to continuously follow optimum operation since generator speed is not allowed to exceed a certain limit. At this point, the controller attempts to maintain generator speed at maximum speed, typically around 15-20 percent above synchronous speed. As a consequence, wind power conversion is no longer optimized. Still, this maximum speed regulation is mainly achieved by means of the rotor-side converter.

Power limitation operating region If wind speed exceeds rated value, the rotor-side converter is no longer able keep generator speed below maximum value. Alternately, generator speed must be limited by reducing aerodynamic torque. This can be done through the action of a pitch controller. By pitching the blade angle, aerodynamic conversion efficiency is reduced, and thus less mechanical torque acts on the generator and speed can be maintained at a constant level.

5.5 Rotor-control Schemes

The rotor control in a DFIG wind turbine allows decoupled control of active and reactive power. This facilitates high maneuverability that enables the turbine to capture maximum energy from wind and to provide reactive power support to the grid.

The controller is based on the dq rotating frame. In the following rotor-control derivation, the direct-axis of the rotating reference frame is aligned to the stator flux. The control principle for a variable speed wind turbine is described in [77]. The stator flux vector can be expressed as

$$\begin{aligned} \psi^s_{sd} &= |\vec{\psi}_s| && (5.11)\\ \psi^s_{sq} &= 0 && (5.12) \end{aligned}$$

Superscript s indicates that the corresponding variable is seen from the stator flux reference frame. Further, the magnetizing current vector $|\vec{i}_{ms}|$ is introduced. This quantity is conceptually defined as the stator current component which is collinear with the stator flux vector. The relation between the stator flux and the stator magnetizing current is given by

$$\vec{\psi}_s = L_m \vec{i}_{ms} \tag{5.13}$$

Since

$$\vec{\psi}_s = L_s \vec{i}_s + L_m \vec{i}_r \tag{5.14}$$

then, combining 5.13 and 5.14 yields

$$\vec{i}_{ms} = \frac{L_s}{L_m} \vec{i}_s + \vec{i}_r \tag{5.15}$$

By decomposing the vectors into their respective dq-components, current component relationships can be expressed as

$$i^s_{msd} = \frac{L_s}{L_m} i^s_{sd} + i^s_{rd} \tag{5.16}$$

$$i^s_{msq} = 0 = \frac{L_s}{L_m} i^s_{sq} + i^s_{rq} \tag{5.17}$$

In other expressions, the above equations can be written as

$$\begin{aligned} \psi^s_{sd} &= L_m i^s_{msd} && (5.18)\\ i^s_{sd} &= \frac{L_m}{L_s} \left(i^s_{msd} - i^s_{rd} \right) && (5.19)\\ i^s_{sq} &= -\frac{L_m}{L_s} i^s_{rq} && (5.20) \end{aligned}$$

By substituting (5.13) into the stator voltage equation, we have

$$\vec{v}_s = \vec{i}_s R_s + j\omega_e L_m i^s_{msd} + L_m \frac{d i^s_{msd}}{dt} \tag{5.21}$$

It can be assumed that the influence of the stator resistance R_s is very small, and the stator flux is relatively constant, i.e. the stator flux rate of change is close to zero. Subsequently, (5.21) can be written as

$$\vec{v}_s = j\omega_e L_m i^s_{msd} \tag{5.22}$$

Equation (5.22) indicates that the stator vector is perpendicular to the stator flux vector. Considering that $\omega_e = 1$ pu and $v^s_{sd} = 0$, equation (5.22) can be written as

$$v_{sq} = L_m i^s_{msd} \tag{5.23}$$

The stator active and reactive power can be written as

$$P_s = v^s_{sq} i^s_{sq} \tag{5.24}$$
$$Q_s = v^s_{sq} i^s_{sd} \tag{5.25}$$

Substitution of 5.19 and 5.20 into the above equations produces the following expressions

$$P_s = -\frac{v^s_{sq} L_m}{L_s} i^s_{rq} \tag{5.26}$$
$$Q_s = \frac{v^s_{sq} L_m}{L_s}\left(i^s_{msd} - i^s_{rd}\right) = \frac{v^{s2}_{sq}}{L_s} - \frac{v^s_{sq} L_m}{L_s} i^s_{rd} \tag{5.27}$$

As can be seen from the above equations, P_s and Q_s are proportional to i_{rq} and i_{rd}, respectively.

The rotor current can be regulated by means of rotor voltages. The relation between rotor current and rotor voltages is obtained by substituting (3.4) into (5.2) and decomposing the equation into dq components as follows

$$v^s_{rd} = i^s_{rd} R_r - (\omega_e - \omega_r)(L_r i^s_{rq} + L_m i^s_{sq}) + \frac{d(L_r i^s_{rd} + L_m i^s_{sd})}{dt} \tag{5.28}$$
$$v^s_{rq} = i^s_{rq} R_r + (\omega_e - \omega_r)(L_r i^s_{rd} + L_m i^s_{sd}) + \frac{d(L_r i^s_{rq} + L_m i^s_{sq})}{dt} \tag{5.29}$$

By substituting (5.19) and (5.20) into (5.28) and (5.29), respectively, the following expressions are obtained

$$v^s_{rd} = i^s_{rd} R_r - (\omega_e - \omega_r)(L_r i^s_{rq} - \frac{L^2_m}{L_s} i^s_{rq}) + \frac{d(L_r i^s_{rd} + \frac{L^2_m}{L_s}\left(i^s_{msd} - i^s_{rd}\right))}{dt} \tag{5.30}$$
$$v^s_{rq} = i^s_{rq} R_r + (\omega_e - \omega_r)(L_r i^s_{rd} + \frac{L^2_m}{L_s}\left(i^s_{msd} - i^s_{rd}\right)) + \frac{d(L_r i^s_{rq} - \frac{L^2_m}{L_s} i^s_{rq})}{dt} \tag{5.31}$$

By assuming that i^s_{msd} is constant and by introducing a leakage factor σ, which is defined as

$$\sigma = 1 - \frac{L^2_m}{L_s L_r} \tag{5.32}$$

the rotor voltage equation can be written as

$$v_{rd}^s = i_{rd}^s R_r + \sigma L_r \frac{i_{rd}^s}{dt} - (\omega_e - \omega_r)\sigma L_r i_{rq}^s \tag{5.33}$$

$$v_{rq}^s = i_{rq}^s R_r + \sigma L_r \frac{i_{rq}^s}{dt} + (\omega_e - \omega_r)\left(\frac{L_m^2}{L_s} i_{ms}^s + \sigma L_r i_{rd}^s\right) \tag{5.34}$$

The last terms in the two equations above are termed cross-coupling elements of the *dq*-controller. The implementation of the current controller is shown in Fig. 5.10.

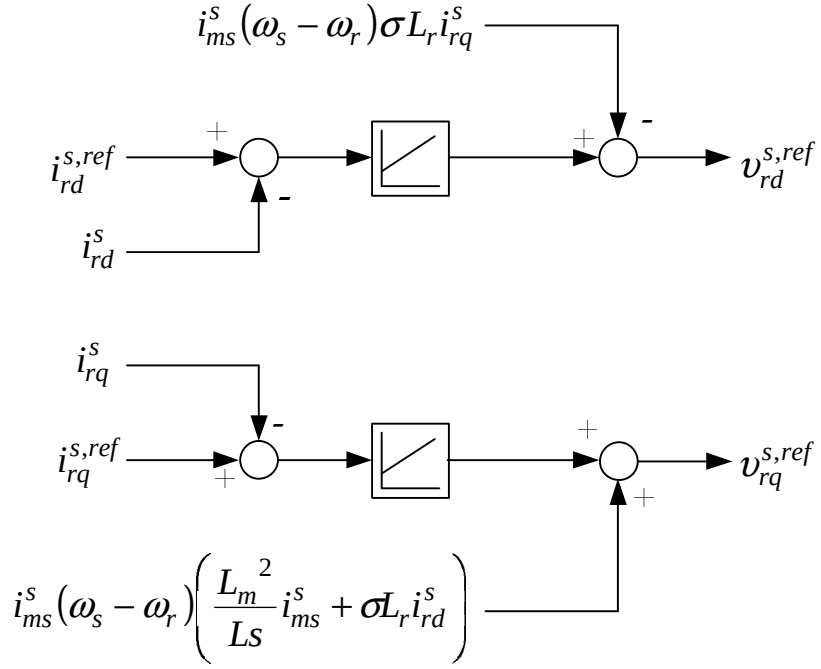

Figure 5.10. Current controller.

In practice, however, the influence of cross-coupling components on controller performance is minor. Therefore, these components can be omitted from the controller without compromising accuracy [94].

FMAC Method

As an alternative to the decoupling *dq*-controller, a DFIG control strategy based on rotor flux magnitude and angle is proposed in [95, 96]. By solving $\vec{i_r}$ using (3.3) and substituting the resulting equation into (3.4), the expression can be used to solve $\vec{i_s}$. By substituting the last expression into (3.8), the electromagnetic torque can be expressed by

$$T_e = \frac{x_m}{x_s x_r - x_m^2} |\vec{\psi_s}||\vec{\psi_r}| \sin\delta \tag{5.35}$$

where δ is the angle between the stator and the rotor flux. Subsequently, the torque can be controlled by varying the rotor voltage angle and the reactive power is regulated by adjusting the rotor voltage magnitude.

5.5.1 Reference frame selection

The rotor control formulas explained earlier were derived based on the stator flux reference frame. It should be noted that if the stator resistance is considered as small, the stator voltage reference frame is principally identical to the stator flux reference frame without any significant error [97, 98]. As an alternative to using the stator flux and voltage reference frames, Yamamoto and Motoyoshi [99], and Xu and Cheng [100] propose the air-gap flux as the rotating reference frame for DFIG control. Fig. 5.11.shows graphical definitions of different reference frames.

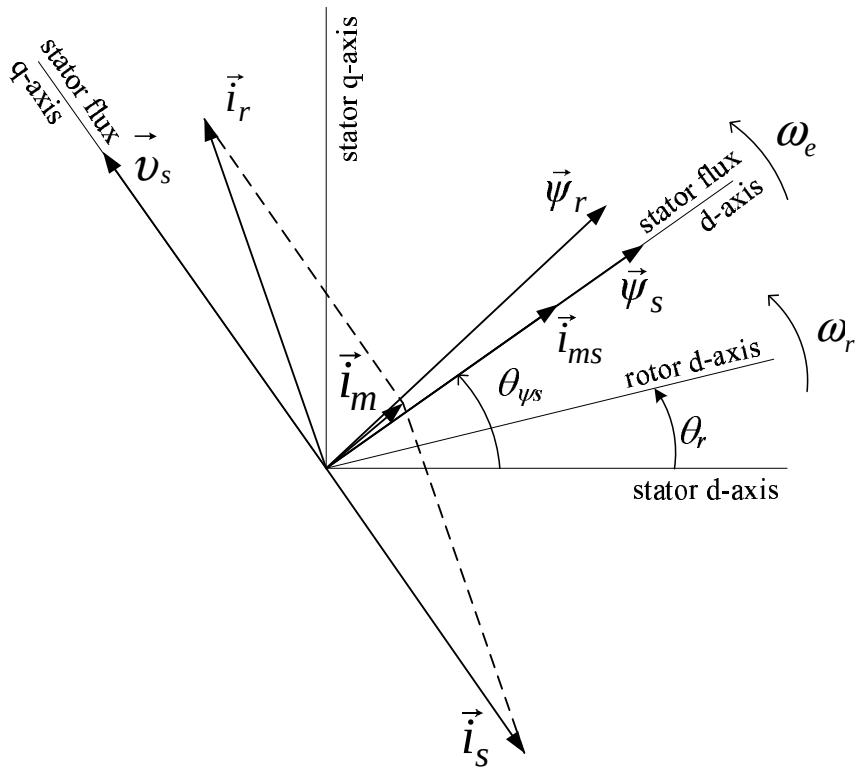

Figure 5.11. Definitions of reference frame.

A detailed study presented in [101] shows that a stator voltage reference frame provides better damping on the system than the stator flux reference frame. Based on an investigation not shown in this thesis, it was found that the selection of the reference frame does not influence the simulation accuracy. For power system stability study, therefore, it is more convenient to use the stator voltage reference frame since the quantity can be directly defined. In this thesis, therefore, the DFIG control model is aligned to the stator voltage reference frame, thus $x_d \approx x_q^s$ and $x_q \approx -x_d^s$.

5.5.2 Speed/active power control

The speed and active power control of a DFIG wind turbine can be realized in several ways. Fig. 5.12 illustrates different possible speed/active power control combinations in a DFIG.

Block A, B and C in Fig. 5.12 represent different forms of control characteristic curves. Block A shows a lookup table that converts measured generator speed into the

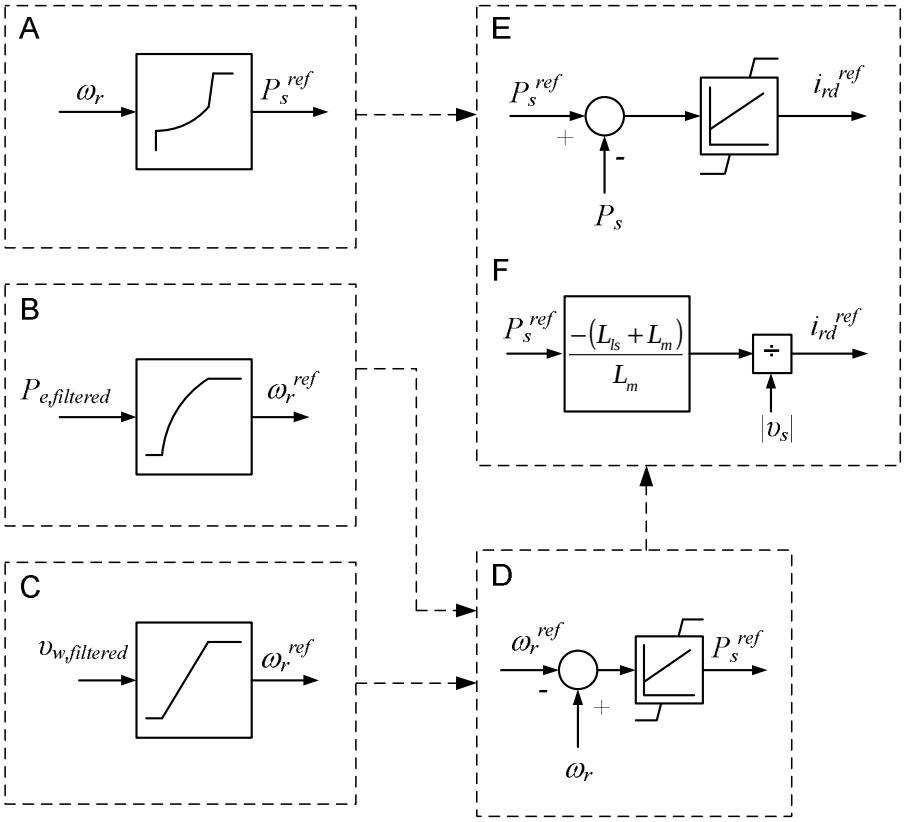

Figure 5.12. Different possible rotor control scheme combinations in DFIG.

stator power reference. Block B converts the filtered generator power output into the rotor speed reference value. In block C, the filtered wind speed is transformed into the corresponding generator speed reference value.

Block D represents the generator speed controller where the speed is controlled by varying the stator power. In this discussion, the stator resistance is ignored, therefore the stator power and the electromagnetic torque can be assumed to be equal. In block E, the stator power is controlled by means of a PI-controller. While in block F, the stator power is realized using an analytical expression to provide the corresponding d-component of the rotor current, which is given by

$$i_{rd}^{ref} = \frac{-P_s^{ref}(L_{ls} + L_m)}{v_{sd} L_m} \tag{5.36}$$

Given the fast PI-controller response in block E, block E and F can be considered to be equal. Thus, in the following, block E will be excluded and block F will be used instead. Accordingly, there will be three possible combinations, which can be referred as types 1, 2 and 3 as follows:

- Type-1 consists of block A and block F.
- Type-2 consists of block B + block D + block F.
- Type-3 consists of block C + block D + block F.

Type 1 speed/active power control can be found in [102, 103, 104, 105, 78, 106]. Type 2 speed/active power control is presented in [8, 11, 64, 30]. Type 3 speed/active control is used in [86, 83]. Normally time constant of $P_{e,filtered}$ in type 2 speed/active power control is large. Consequently, for a short-term voltage stability analysis, responses of type 2 and type 3 speed/active power control schemes can be considered as similar provided that the wind speed is constant during period of investigation.

5.5.3 Reactive power control

The reactive power in a DFIG is controlled by regulating the direct axis component of the rotor current i^s_{rd} in the stator flux reference frame as given in (5.27). By employing a cascade PI-controller the stator voltage can also be regulated. The block diagram of reactive power and voltage control for a DFIG in the stator voltage reference frame is given in Fig. 5.13, note that $i^s_{rd} \approx -i_{rq}$.

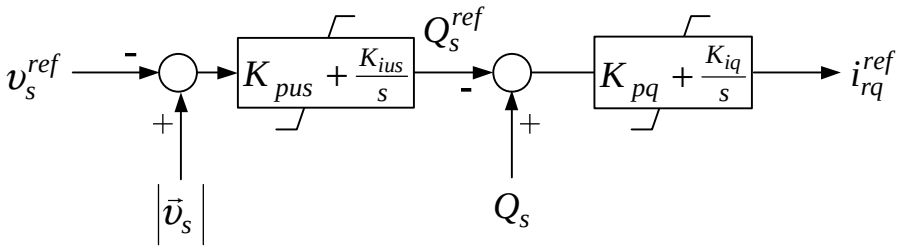

Figure 5.13. Reactive control block in DFIG.

5.6 Fault Ride-Through Procedure

A fault that occurs on the grid may cause a voltage dip on the wind turbine terminal. This leads to a high transient rotor current, which may harm the rotor converter and also may cause overvoltage on the dc-link capacitor. A detailed sequence of a grid fault that leads to converter overcurrent or dc-link overvoltage is explained in [107]. In the past, wind turbines were allowed to be disconnected from the grid during such a situation. This is no longer the case, since many transmission operators require wind turbines to stay connected during such a situation.

Different alternatives for fault ride-through schemes are proposed in [108] and further discussed as well in [109, 101]. In the following, different fault ride-through alternatives are described and evaluated.

5.6.1 Fault ride-through scheme based on crowbar activation

A fault ride-through using a rotor crowbar basically consists of several sequences, e.g. fault occurrence, triggering overvoltage or overcurrent protection, converter blocking and crowbar activation, converter de-blocking and crowbar deactivation, synchronization, and finally a return to normal operation. The sequences are explained in detail in the following.

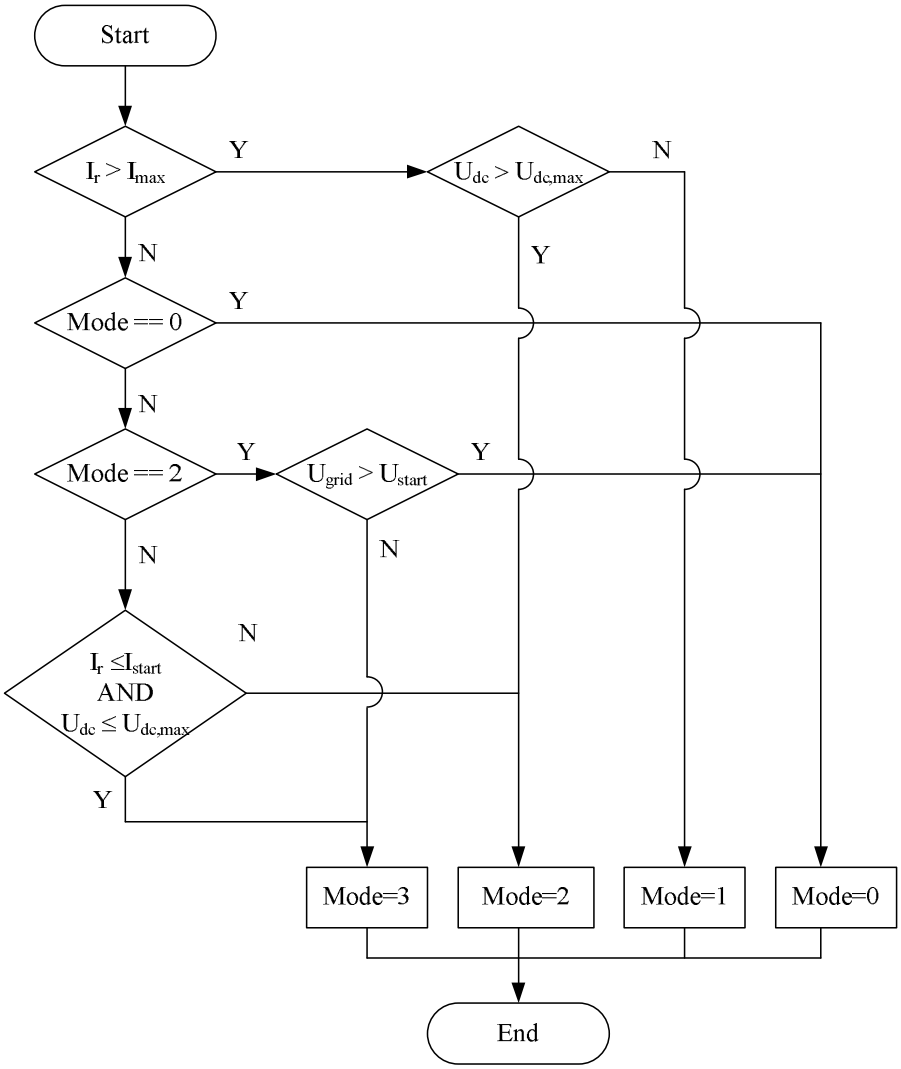

Figure 5.14. Fault ride-through mode.

Wind turbine operation mode during fault ride-through can be differentiated into four categories: normal operation (Mode 0), converter deactivation (Mode 1), crowbar activation (Mode 2), and rotor-side converter reactivation (Mode 3). The operation modes are chosen in accordance to the logic given in Fig. 5.14.

In the following simulations, wind turbine parameters are given in Appendix A.3, the protection setting parameters are given in Table 5.3, and the applied voltage dip profile is given in Fig. 5.15.

When a fault occurs in the network, the terminal voltage drops instantaneously. In this case, the retained voltage of the voltage dip is 0.3 pu. The duration of the voltage dip is 250 ms and voltage recovery is assumed to take one cycle, i.e. 20 ms. The fault ride-through response of the wind turbine is shown in Fig. 5.16. Details of the fault ride-through sequence are described in the following.

Table 5.2: Fault ride-through operation mode selection logic.

Mode	Rotor-side converter	Free-wheeling diodes	AC crowbar	Notes
0	ON	OFF	OFF	Normal operation mode
1	OFF	ON	OFF	Rotor converter deactivation
2	OFF	OFF	ON	Crowbar activation
3	ON	OFF	OFF	Rotor converter is operating at zero active power and maximum reactive current

Table 5.3: Parameters used in fault ride-through scheme.

Parameters	Values	Units
Maximum dc-voltage	1.12	pu
Maximum rotor converter current	1.8	pu
Crowbar deactivation current level	1.0	pu

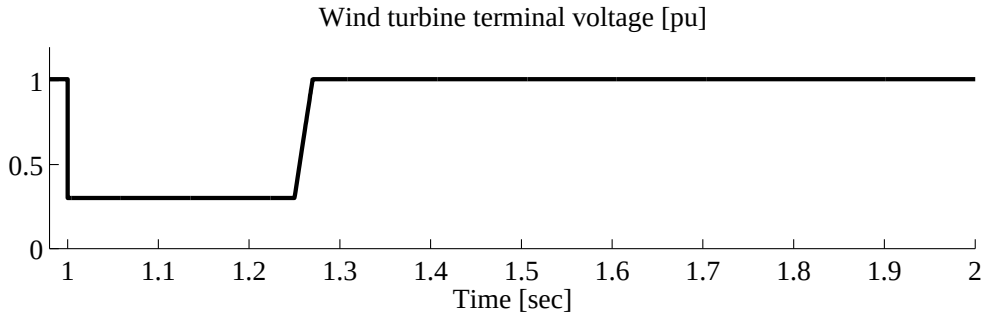

Figure 5.15. Applied voltage on wind turbine terminal to simulate fault ride-through capability.

Converter deactivation

At t=1 s, terminal voltage drops to 0.3 pu leading to a high transient rotor current up to 5.5 pu (see Fig. 5.16.a). When the rotor current surpasses the maximum instantaneous value, i.e. 2 pu, the rotor-side converter is blocked, leading to Mode 1 operation at which the rotor current continues to flow through the freewheeling diodes as illustrated in Fig. 5.17.

During the operation of the freewheeling diodes, the rotor-side converter can be seen as a diode bridge rectifier. Since this is a discrete phenomenon, in a simulation, the diode bridge rectifier must be modeled using *abc* (per-phase) representation rather than using a *dq* representation [110].

The diode gate states are modeled using a lookup table as given in Fig. 5.18. Note that the current in the diode model (i_k) has an opposite sign than the one in the generator model.

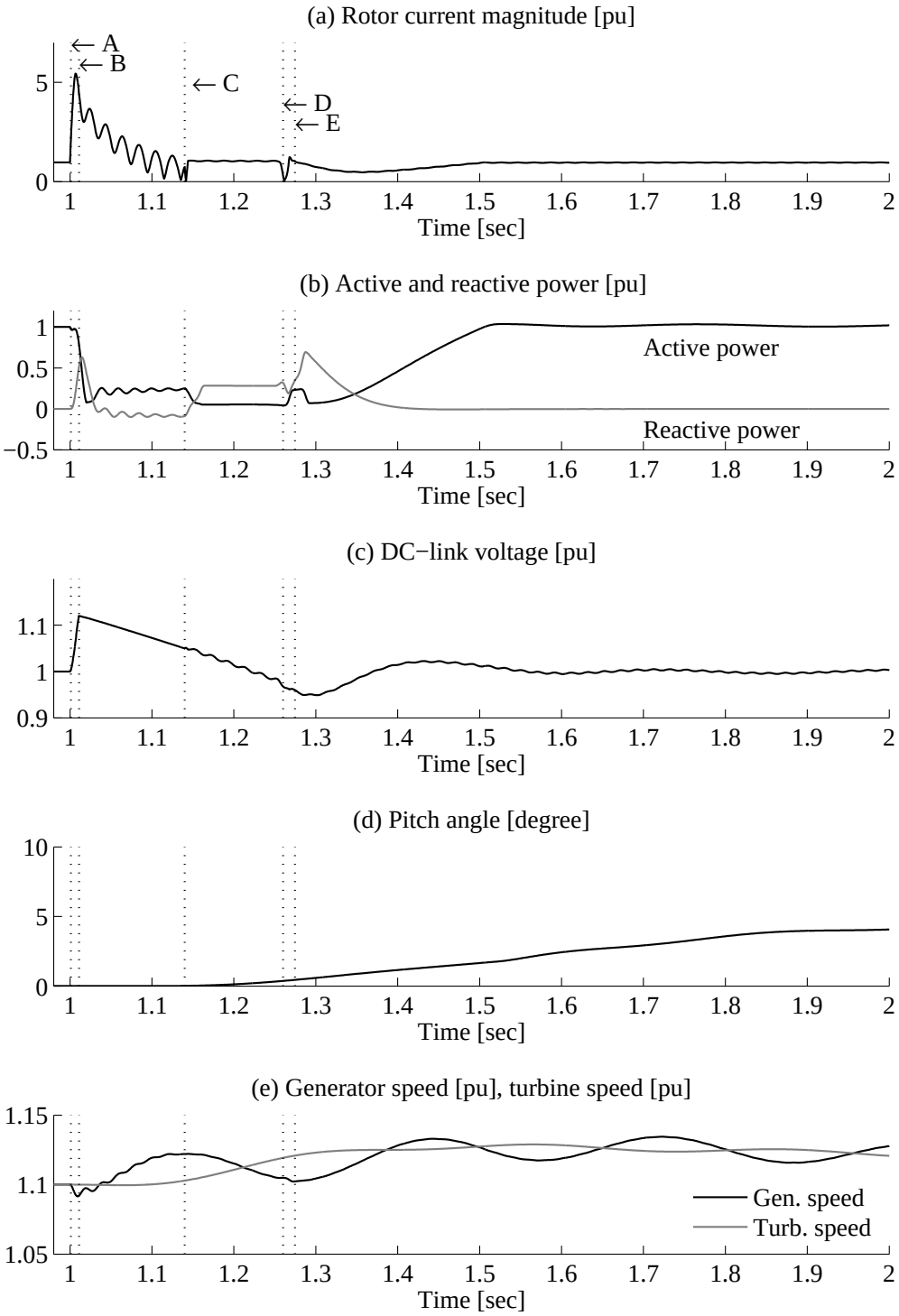

Figure 5.16. Fault ride-through response of a DFIG wind turbine using crowbar. A: converter deactivation, B: crowbar activation, C: crowbar disconnection and converter reactivation with zero power mode, D: fault clearing and E: returning to normal operation mode.

Phase voltage can be calculated using the following expressions

$$e_{12} = (g_1 - g_2)v_{dc} \tag{5.37}$$

$$e_{23} = (g_2 - g_3)v_{dc} \tag{5.38}$$

$$e_{31} = (g_3 - g_1)v_{dc} \tag{5.39}$$

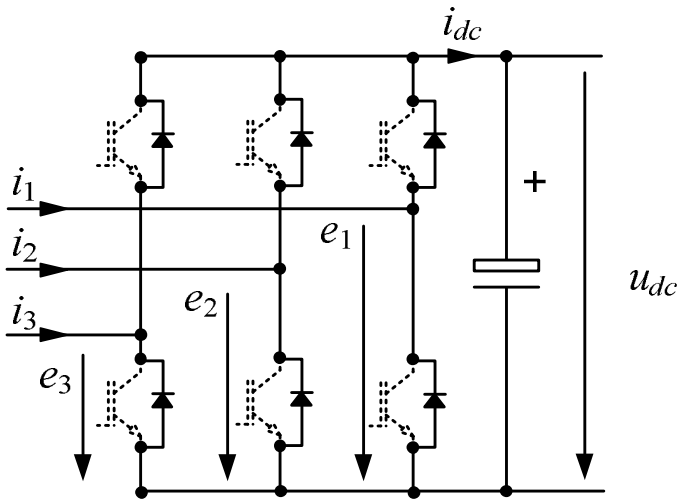

Figure 5.17. Rotor-side converter with blocked IGBT.

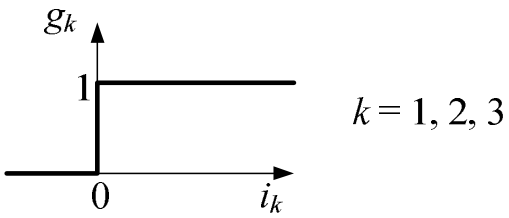

Figure 5.18. g_k function.

The line to neutral voltages, v_a,v_b, and v_c are given by

$$v_a = \frac{(2g_1 - g_2 - g_3)}{3} v_{dc} \tag{5.40}$$

$$v_b = \frac{(2g_2 - g_3 - g_1)}{3} v_{dc} \tag{5.41}$$

$$v_c = \frac{(2g_3 - g_1 - g_2)}{3} v_{dc} \tag{5.42}$$

After the phase voltage is calculated, the quantities are transformed into a dq reference frame to be used in the generator model.

Crowbar activation

The continuous rotor current leads to a rapid increase on the dc-link voltage. As seen in Fig. 5.16.c, at t=1.02, the dc-link voltage reaches the maximum limit, which was set at 1.12 pu. As a result, the crowbar protection is activated. At this stage, the fault ride-through is in Mode 2.

At this moment the stator and rotor flux is very low. Consequently, the electromagnetic torque is not able to maintain generator and turbine rotor speed at a nominal value. This gives rise to an increase in rotor speed. In order to avoid overspeed, the pitch controller must be activated to reduce aerodynamic torque.

Crowbar deactivation and restarting converter

For around 140 ms, the crowbar remains active while the rotor current continuously decreases. It should be noted that the rate of current decay is significantly influenced by stator resistance. As shown in Fig. 5.19, the larger the stator resistance the faster the current decays.

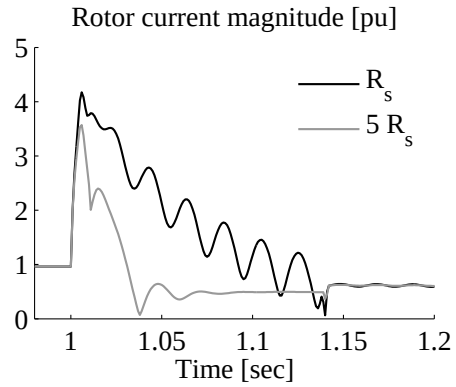

Figure 5.19. Effect of stator resistance R_s on transient current decay rate.

At the same time, the grid-side converter continuously discharges the excess of energy in the dc-link capacitor leading to dc-link capacitor voltage decay. The rate of capacitor discharge is limited by the rated current of the converter.

When the rotor current falls below the nominal value, the crowbar is deactivated, subsequently the rotor-side converter is reactivated and takes over the rotor control. During the transition between crowbar deactivation and rotor-side converter reactivation, the current flows through the freewheeling diodes. However, since the transition takes a very short time, it is fair to assume an instantaneous transition.

Once the converter is reactivated, the fault ride-through scheme goes into Mode 3. In this mode, the electromagnetic torque reference is set to zero, while the reactive current is set at a maximum value. As a result, the DFIG generates roughly 0.2 pu of reactive power into the grid (see Fig. 5.16.b).

Electromagnetic torque ramp limiter

At t=1.25 the fault is cleared. When the grid voltage exceeds the minimum limit for normal operation, i.e. 0.8 pu, the rotor-side converter goes into normal operation mode (Mode 0). When entering normal operation mode, the electromagnetic torque or electrical power reference value increases at a limited rate. If the rate is too high or even not limited at all, it is likely that it may excite shaft oscillations following the fault clearing.

Fig. 5.20 illustrates the different responses of wind turbine controllers, with and without an electromagnetic torque rate limiter. On the first turbine, the electromagnetic torque rate is limited at 10 pu/s, whereas the electromagnetic torque for the second turbine is not limited. As a result, the first turbine has smooth power recovery following a fault. In contrast, the second turbine suffers from a higher speed oscillation which is triggered by an abrupt voltage recovery.

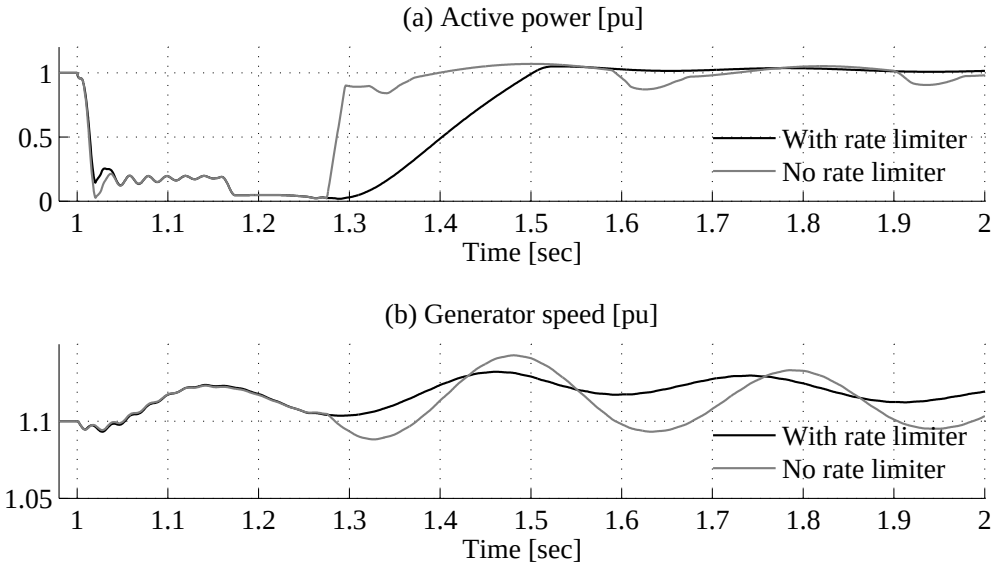

Figure 5.20. Wind turbine fault response with and without electromagnetic torque ramp rate limiter.

In [30, 31], the application of a torque rate limiter for a full-scale wind turbine test is demonstrated.

Risk of delayed converter reactivation

There is a possibility that a grid fault may be cleared before the rotor-side converter is reactivated. This may happen if the fault is quickly cleared or if the rotor current transient takes a long time to decline.

To exercise this possibility, a simulation was performed. The simulation results are presented in Fig. 5.21. The fault duration was simulated to be 100 ms, which is shorter than the time needed for the converter to restart.

As we can see from the voltage profile, the grid fault is cleared at t=1.1 ms, when the rotor current transient is still above its nominal value. The abrupt change in grid voltage due to fault clearing triggers a high rotor transient current. The magnitude of the transient current is mostly influenced by the rate of the terminal voltage change and the angle between the stator flux and the grid voltage vectors. The most severe situation occurs when the grid terminal changes abruptly and arrives at 90° behind the stator flux vector. This is equivalent to saying that the voltage phase-angle jump is close to 180 . In such a case, the grid voltage forces the stator flux into the opposite direction, although normally, the grid voltage phase-angle jump occurs between 0-80° [111].

The high transient current postpones the restart of the rotor-side converter. Subsequently, the converter loses control over the generator. In this situation, the generator behaves similar to a squirrel cage induction generator with a higher rotor resistance.

Looking at the power response, a high overshoot of active power is clearly observed. This can be explained as follows: When the grid voltage quickly returns to its nominal value, the electromagnetic torque builds up excessively. At the same time, the generator speed is still very high in relation to the new torque-speed characteristic of the generator. While the generator operating point moves toward a new value, i.e. a

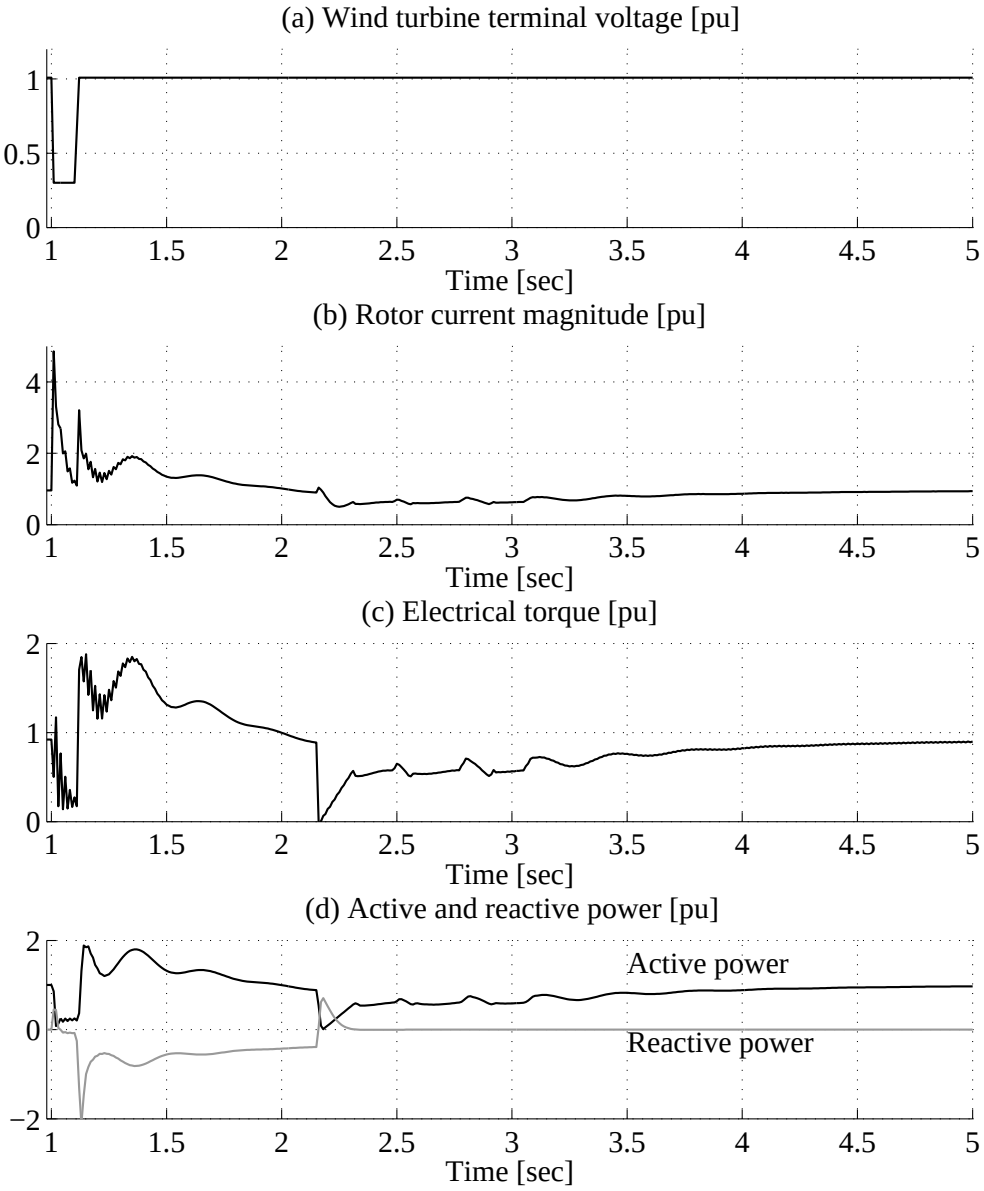

Figure 5.21. Network fault response of DFIG wind turbine with delayed rotor-side converter activation.

smaller slip, it generates excessive electrical power into the grid. Converter disconnection at nominal grid voltage also leads to large reactive power absorption. This situation may occur for few hundred milliseconds before the rotor current falls below nominal value, which enables the converter to restart.

This situation highlights the importance of the rotor-side converter regaining control as quickly as possible following a fault. This also suggests that a shorter fault-duration is not always favorable when it deals with the fault response of a DFIG wind turbine.

5.6.2 Fault ride-through scheme using dc-link chopper

Another alternative to grid fault ride-through is utilizing a dc-link chopper. The sequence and operation modes of the fault ride-through in this scheme are basically

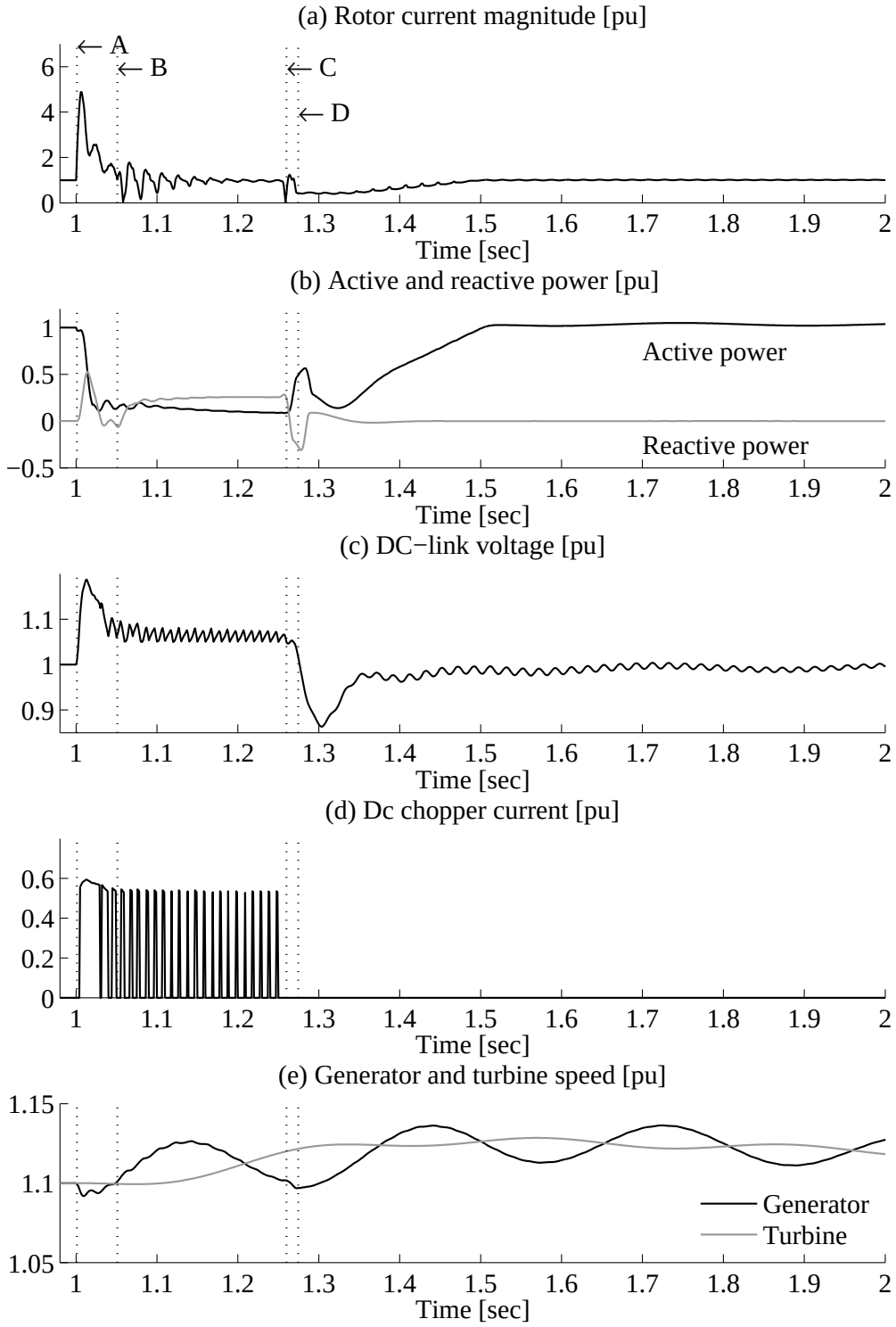

Figure 5.22. Fault ride-through of a DFIG wind turbine using over-dimensioned freewheeling diodes and dc-link chopper. A: converter deactivation, B: converter reactivation with zero power mode, C: fault clearing and D: returning to normal operation mode.

similar to the one with an active crowbar, except the role of the crowbar is replaced by the dc-link chopper.

Simulation results of a wind turbine provided with a dc-link copper fault ride-through scheme subjected to a grid fault are presented in Fig. 5.22.

When a fault results in excessive rotor transient current, the converter is disabled (marked by A in Fig. 5.22). Subsequently, rotor transient current flows through the freewheeling diodes of the rotor-side converter. As long as the current flows through the freewheeling diodes, the dc-link voltage introduces high rotor voltage. This helps suppress the transient current. As a result, the rotor-side converter can be restarted quicker than the one with an ac crowbar (indicated with B in Fig. 5.22). On the other hand, such high-rotor voltage may create a high transient current during the start of the rotor-side converter. This may trigger the converter overcurrent protection. However, in this case, the transient current normally decays quite fast. This situation enables a quick restart of the rotor-side converter. Normally, the transient current during the second restart attempt is not high enough for the overcurrent protection to act.

The dc-link voltage is regulated by means of the dc-link chopper which dissipates excess energy through a resistor. The discharge current through the dc-link chopper is shown in Fig. 5.22.d. Subsequently, the dc-link voltage is maintained within a tolerable range during the fault.

This scheme requires overrated freewheeling diodes, since they must be dimensioned to carry the rotor transient current. On the other hand, this option makes the role of an ac-crowbar less important.

5.6.3 Active crowbar equipped with capacitor

Another fault ride-through scheme can also be implemented using an active crowbar equipped with a capacitor, as proposed in [108]. The capacitor is connected in parallel to the IGBT switch and the crowbar resistor. The arrangement of the crowbar is shown in Fig. 5.23.

During normal operation, the IGBT is switched off. When a grid fault occurs, the rotor converter is deactivated. Consequently, the transient rotor current flows through the crowbar diode and charges the crowbar capacitor. When the voltage across the crowbar capacitor reaches the maximum limit, the IGBT turns on, making the current flow through the resistor. As a consequence, the capacitor voltage falls below the voltage limit value. Subsequently, the IGBT turns off again. The on-off switching of the IGBT occurs continuously, with switching frequency depending upon the rotor transient current level, until the rotor current falls below a certain limit. This regulation results in a relatively constant back e.m.f. of rotor voltage [108], which gives raise to faster rotor transient current decay. From a simulation perspective, this scheme provides effects identical to the previous fault ride-through scheme that utilizes a dc-link chopper.

5.6.4 Switched stator resistance

A high transient current can also occur during fault clearing. The fault breaker activation for isolating the faulty line may cause a grid voltage phase-angle jump. Despite the breaker disconnection at zero current, a voltage phase-angle jump is sensed at the turbine terminal. This is because a zero current disconnection is seen as an unbalanced phenomenon, which is then transported trough transformers from the fault location to

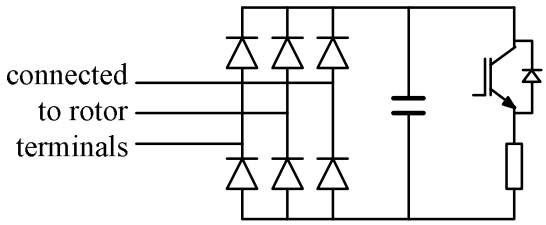

Figure 5.23. Active crowbar equipped with a capacitor.

the wind turbine terminal. This voltage phase-angle jump results in a high transient current similar to the one at the beginning of the fault.

Feddersen [108] proposes a method to limit such high transient current by inserting resistances at the generator terminal. The arrangement of the stator resistances is shown in Fig. 5.24.

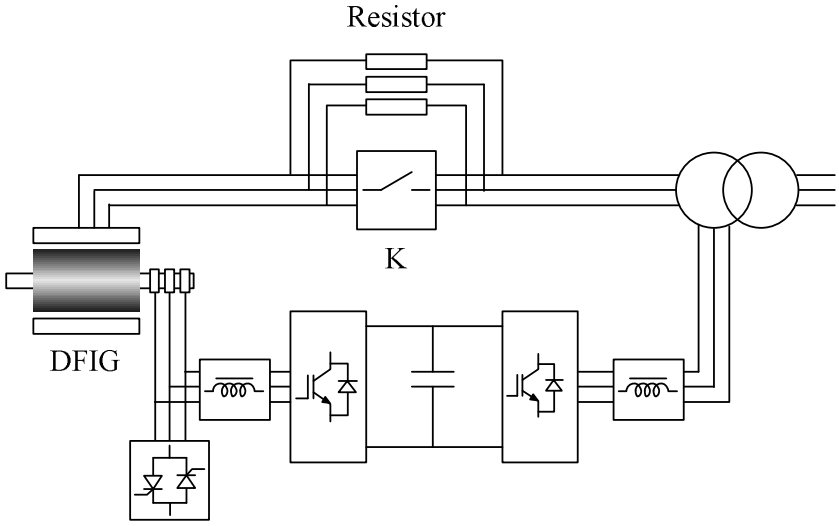

Figure 5.24. DFIG fault ride-through scheme using stator switched resistor.

Contactor K opens when the grid fault occurs making the stator current flow through the resistances. These resistances cause the stator and rotor transient currents decay more rapidly. To effectively dampen the transient current following a fault and to avoid transient current at fault clearance, the contactor $K1$ must act quickly. For a fast response, anti-parallel thyristors can be used. However, this option has the disadvantage of higher losses during normal operation due to the presence of the thyristors.

As shown in Fig. 5.25, a voltage dip was applied that resulted in 0.25 remaining terminal voltage for 250 ms. At the instant of fault clearing, the grid voltage jumped to 1 pu with a phase-angle jump of -14°.

Without switched stator resistance, it took more than 100 ms for the rotor transient current to fall below the nominal value. When the fault was cleared, the rapid voltage recovery and voltage phase-angle lead to a power overshoot up to 1.5 pu and gave raise to a rotor current transient up to 4 pu. This lead to the second deactivation of the converter and activation of the crowbar, which lengthened the time taken by the converter to regain the control over the generator. During the loss of the converter,

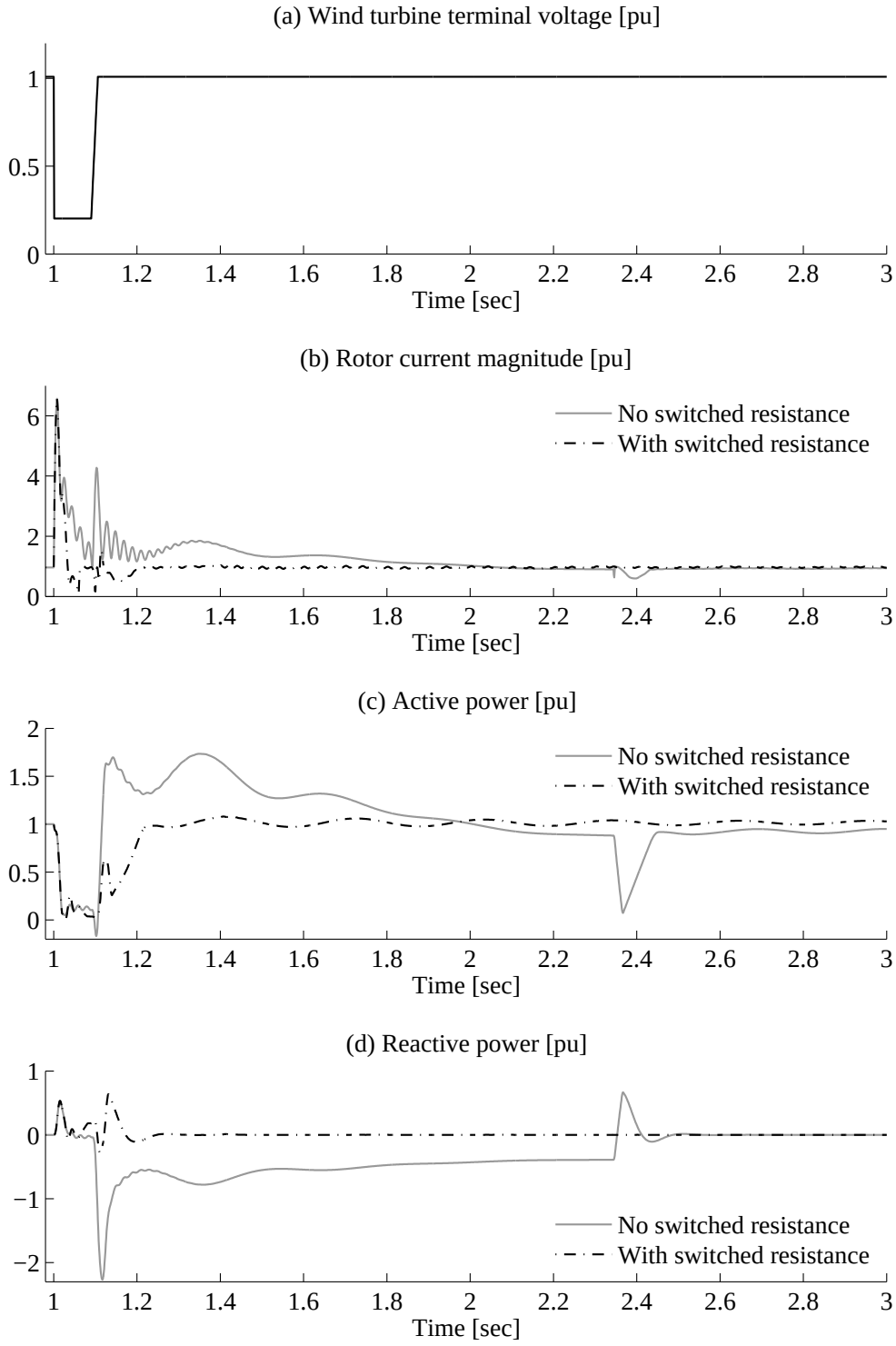

Figure 5.25. Influences of stator switched resistor on fault response of DFIG.

the reactive power absorbed by the wind turbine was as high as 0.5 pu on average, with a peak value at 2.2 pu. This is obviously unfavorable from a system stability point of view. It took more than 1 second before the rotor converter was reactivated at t=2.35 s.

In the second case, a switched stator resistance was employed. The switched resis-

tance value was equivalent to 5 times the stator resistance. In this scheme, the rotor current decayed faster and within 32 ms the current fell below the nominal value. This permitted a faster restart of the converter. Furthermore, the voltage jump at the moment of fault clearing did not lead to a rapid current transient, and the second crowbar activation could be avoided. This also caused a less oscillating power response. Since the converter fully took control over the generator, the reactive power response was within allowable limits. Once the grid voltage and turbine response were settled, at t=1.4 s, the switched resistor was bypassed without causing a significant transient.

5.7 Influence of Different Control Parameters and Schemes on Fault Response

In this section, the effects of the different control parameters and schemes on fault responses are evaluated in order to determine the significance of each parameter and scheme in stability studies. In this way, a more generalized approach in modeling a DFIG wind turbine can be derived.

5.7.1 Generator operating speed

In earlier simulations, the faults were applied when the generator operated at super-synchronous speed. At such a condition, the response of the wind turbine is characterized by a positive active power output. However, when the fault occurs during a sub-synchronous operating point, as shown in Fig. 5.26, the wind turbine response during converter loss is characterized by a reverse power flow. In other words, the generator absorbs power from the grid.

When the rotor-converter is disconnected due to a fault, the generator behaves like a conventional squirrel-cage induction generator operating in motoring mode. As the generator operating point moves toward super-synchronous speed (negative slip), the generator draws active power from the grid. Even though the magnitude of active power absorption is not significant, i.e. is less than 0.2 pu on the average, the power flow reverse, particularly in a large wind farm, may be problematic when dealing with a power system protection design. Thus, this investigation points out that one should not only focus on a rated power operating condition when investigating the interaction between a wind farm and the network. This is very relevant considering that a typical wind turbine operates at partial power most of the time.

5.7.2 Pitch controller

The simulations presented earlier involved the actions of the pitch controller in a fault ride-through scheme. The pitch controller contributes to maintaining generator speed close to nominal speed.

As shown in Fig. 5.27, with the absence of the pitch controller, the generator speed can no longer be maintained at its nominal value. However, the electrical power output of the wind turbine is less affected by such speed deviation. This is because the active power output is mostly determined by the electromagnetic torque acting on the machine, which is limited to nominal value in this case. It is worth noting that

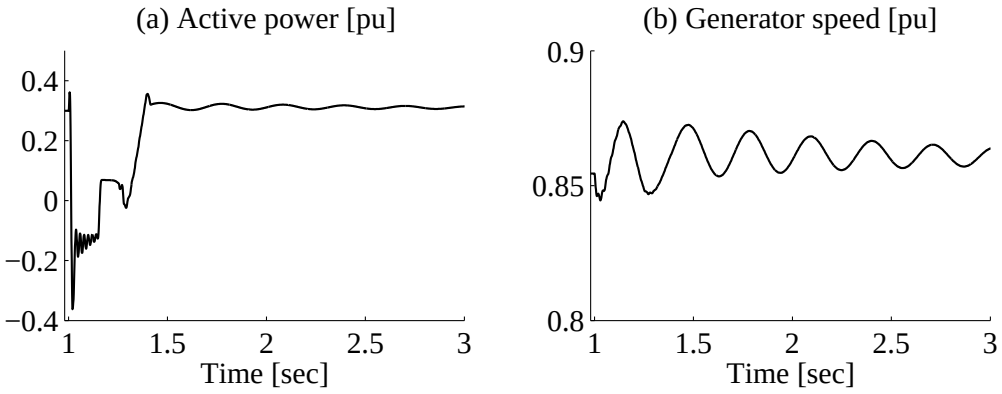

Figure 5.26. Response of DFIG wind turbine during fault at sub-synchronous speed operation.

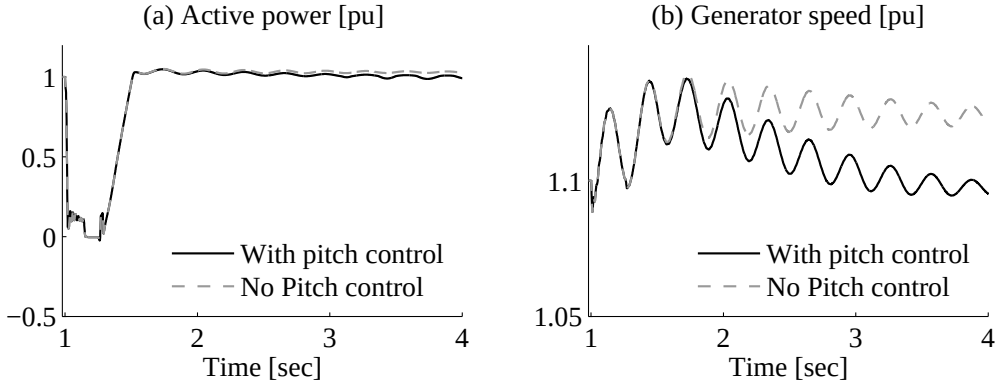

Figure 5.27. Effects of pitch controller on fault ride-through response of DFIG wind turbine.

if the upper limit of the electromagnetic torque or the rotor current increases, the difference in power response between the models becomes more noticeable. This finding suggests that failing to include a pitch controller in the model may lead to an inaccurate identification of the generator stability margin.

5.7.3 Active control schemes

In this section, the responses of type 1 and type 2 speed/active control schemes are compared. The comparisons are made at three different power operating conditions.

In the first case, a comparison is made at full power operating condition. The results of the simulation are presented in Fig. 5.28. At this operating point, the responses of the speed/active power controllers are characterized by torque limit. As the controllers operate in the saturation region, the active power responses of the two controllers are almost flat, while the generator speeds are poorly damped. In general, the responses of the two controllers are similar. The response similarity of controller types subjected to wind speed transient during rated power operation is also reported in [112].

In the second case, a comparison is made at 0.7 pu power operating condition At this point, the controllers are in maximum speed operation. As shown in Fig. 5.29, following the fault clearing, an overshoot can be seen on the power output of the two

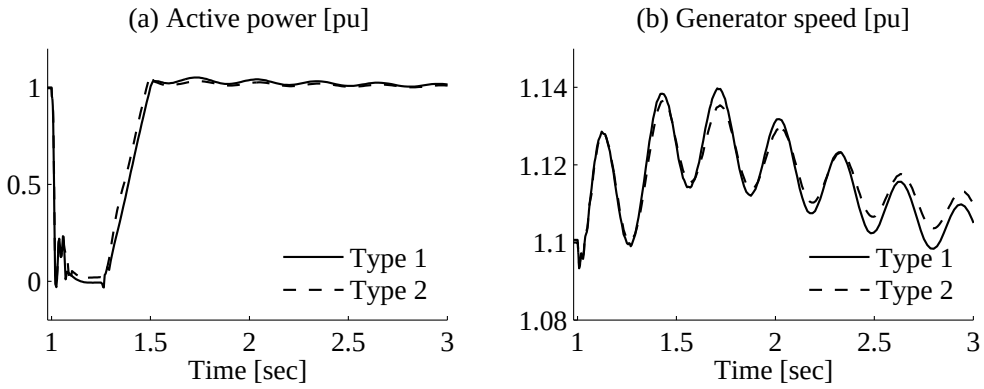

Figure 5.28. Response of two different speed/active power controls in DFIG at rated power output.

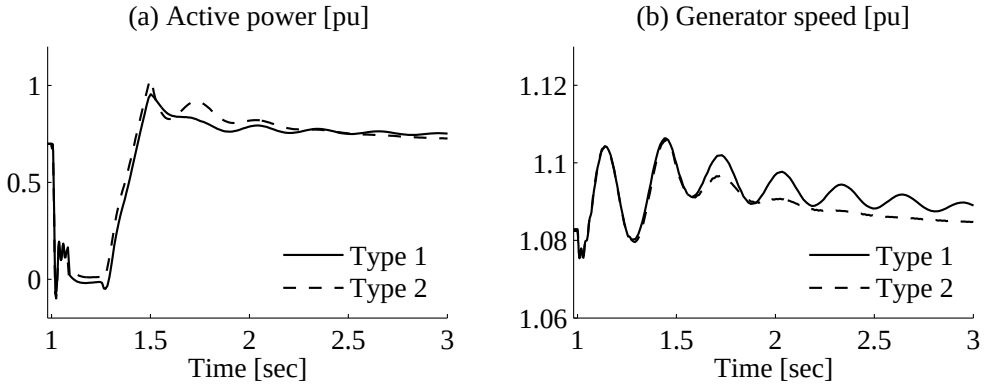

Figure 5.29. Response of two different speed/active power controls in DFIG at 0.7 pu power output.

models. At this point, the type 1 controller can be seen as a speed controller with a high proportional gain. Whereas, the type 2 controller response is governed by the speed controller given in block D in Fig. 5.12 with a relatively constant speed reference.

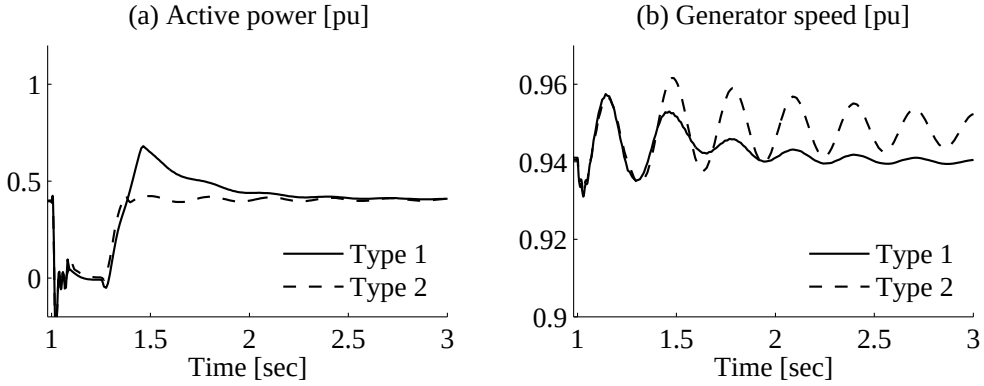

Figure 5.30. Response of two different speed/active power control in DFIG at 0.4 pu power output.

In the third case, the controllers were operating in the optimum speed operating

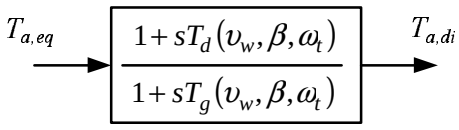

Figure 5.31. Dynamic inflow phenomenon modeled as a first order lead-lag filter.

region. For the type 1 controller, this operating region is characterized by a flat stator power reference. This means any disturbance in speed will not be followed by a significant change in stator power. This is why speed response is under-damped. In contrast, speed controller performance is preserved in the case with a type-2 controller.

From the investigations above, it can be concluded that at rated power the responses of the two controllers are similar. However, the response differences between the two controllers are evident when the turbine operates in the optimum speed operating region.

5.8 Dynamic Inflow Phenomena

The dynamic inflow phenomena are related to the influence of the time varying trailing wake vorticity on the inflow velocity in the rotor plane [18]. The characteristic time scale of these phenomena is proportional to the ratio between turbine rotor diameter and wind speed. The measurement taken from the Tjaereborg 2 MW three-bladed wind turbine with 60 m of rotor diameter shows that pitch change from 1 degree to 3 degrees at a pitch speed of 1 deg/s at wind speed 7.4 m/s produces a shaft torque overshoot by a factor of 2 to 3 of torque change. The time constant of the transient response was around 10 seconds.

The dynamic inflow phenomena are more pronounced for larger turbine rotor diameters and lower wind speed. According to [18], dynamic inflow phenomena are not only important for blade pitching action but also for simulating coherent wind gust. This issue was brought up in relation to the wind turbine control strategy for electric generation by Leithead [113]. Later Akhmatov [7] elaborated the phenomena in relation to power system stability analysis. Representing the phenomena in pitch control loops by using a lead-lag filter is proposed in [114, 115]. The block diagram of the filter is given in Fig. 5.31.

However, the main challenge of implementing the dynamic inflow phenomena in power system stability studies is that the lead and lag time constants of the phenomena are difficult to determine. This is because the time constants vary with wind speed. An algorithm to compensate for dynamic inflow effects in a pitch control loop is suggested in [115] and [116].

In addition, Leith and Leithead [117] report that, based on experimental control studies, there is no evidence of the presence of dynamic inflow. This raises a question concerning the influence of the phenomena on system dynamics. In the case with wind gust, as it is stated in [18], that the effect of dynamic inflow is predicted to be limited due to relatively small changes in induced wind velocity between the equilibrium states.

Fig. 5.32 shows the effect of dynamic inflow phenomena on wind turbine response during grid fault. The result shows that in terms of the active power response of the wind turbine generator, the influence of dynamic inflow phenomena is not critical.

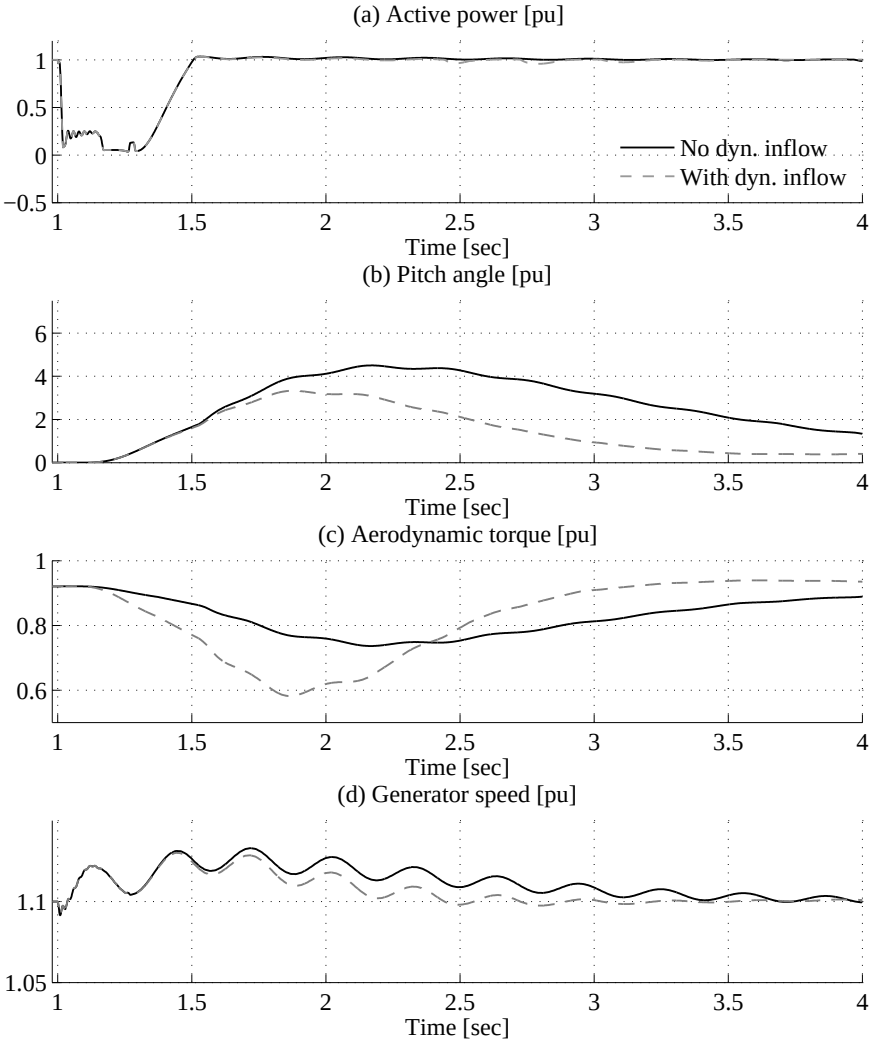

Figure 5.32. Effect of dynamic inflow phenomena in ride-through response of wind turbine.

The model without dynamic inflow phenomena exhibits a slightly conservative result particularly for speed response. Therefore, excluding the phenomena from the model for stability analysis may not lead to any serious error in wind turbine response.

5.9 Torsional Damping Control

Torsional oscillations triggered by a grid fault may cause short- and long-term damage to a wind turbine. To avoid risking this, electromagnetic torque damping can be introduced.

For a type 2 controller, torsional damping can be realized by increasing the gain of the speed controller. This method is reasonable, given that the change in rotor speed reference is slow for a short period following a fault. Thus, torsional damping is inherently provided in the type 2 controller. However, an inherent damping is absent in the type 1 controller. In this case, electrical damping torque must be introduced into the controller. Electrical damping torque can be realized in different ways as described

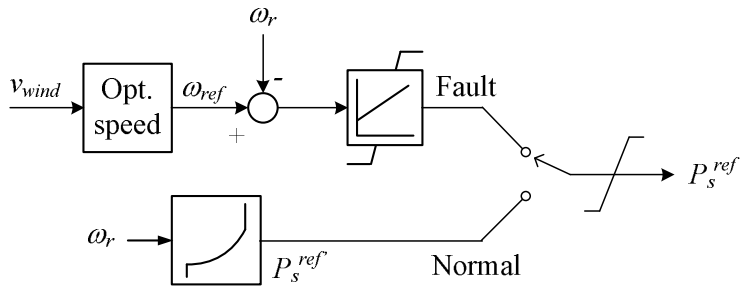

(a) Damping metod 1

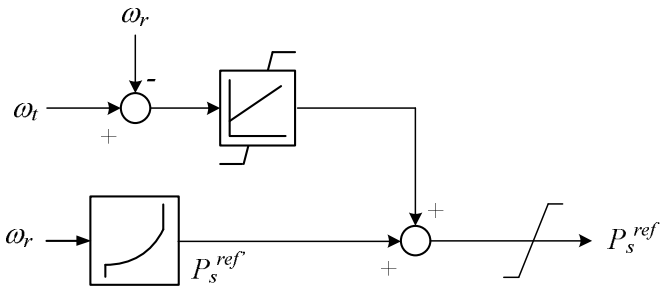

(b) Damping metod 2

Figure 5.33. Different torsional damping methods for wind turbine.

below.

One method is proposed in [118, 119]. According to this method, the active power control scheme given in Fig. 5.33.a is used during a grid fault. In this way, generator speed can be controlled better, which results in better damping as shown in Fig. 5.34.b.

In this thesis, another damping method that utilizes the turbine rotor speed as a speed reference is presented. This method is based on the assumption that turbine speed fluctuates much less than generator speed due to greater inertia. The proposed controller is shown in Fig. 5.33.b. The power and speed responses of the generator are shown in Fig. 5.34.c.

Simulation results show the effectiveness of these damping methods. However, it can be observed that the active power response of the generator is somewhat distorted since a fraction of generator active power is 'borrowed' to dampen torsional oscillations.

Instead of using active damping, passive damping by introducing higher mutual damping on the drive train model can be used as an alternative to emulating active damping. According to [26], passive damping for a two-mass drive train model has been verified to reasonably approximate the response of the drive train model that employs the active damping control. The response of a wind turbine that uses passive damping is presented in Fig. 5.34.d.

5.10 Frequency Deviation Response

The importance of wind power generation in network frequency support is addressed in [120]. The paper also discusses various options which can be used to realize frequency

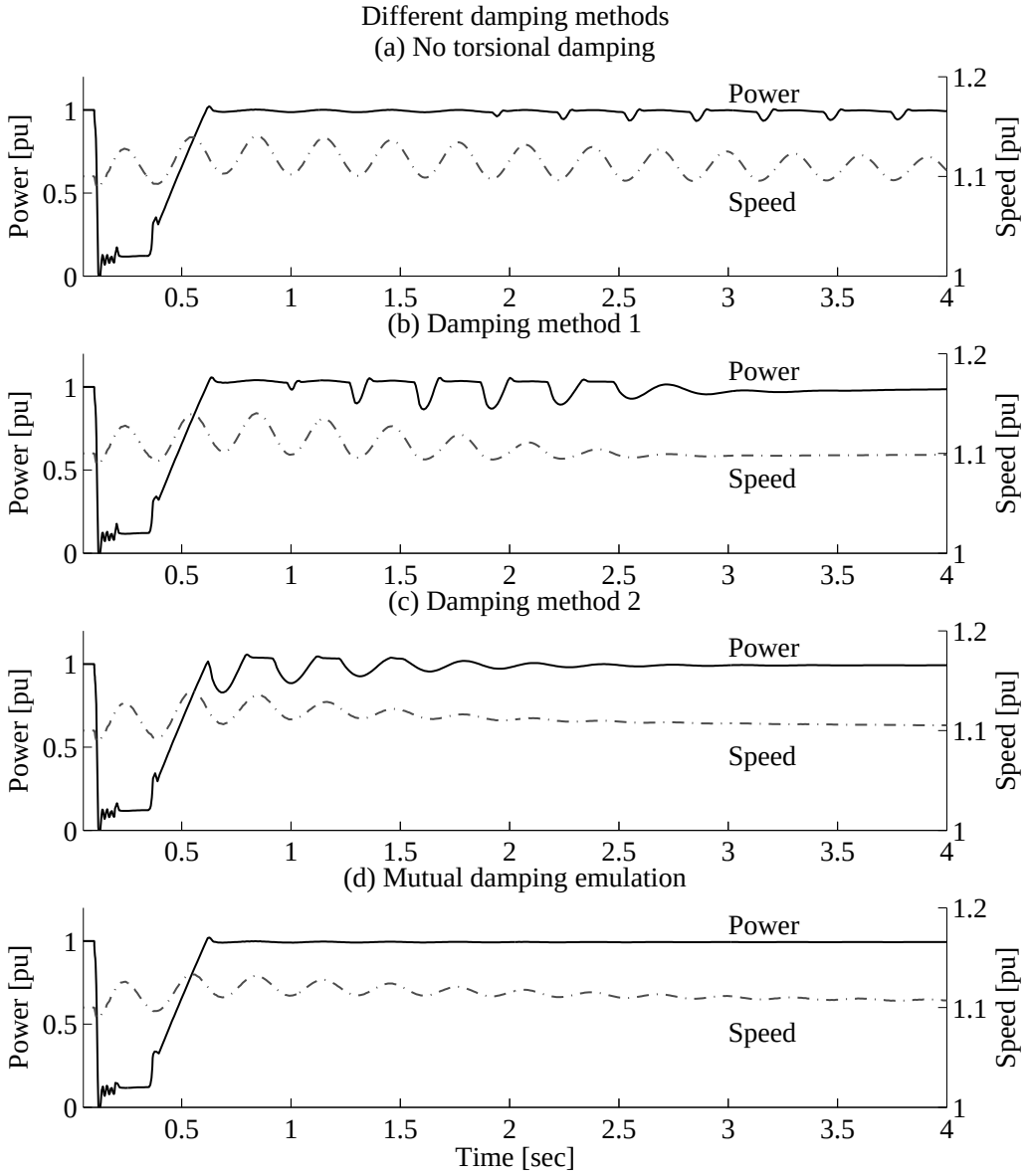

Figure 5.34. Wind turbine response with different torsional damping methods.

control support.

The response of the wind turbine model during frequency excursion is examined in this section. For simplicity, frequency is gradually decreased from 50 Hz to 45 Hz, with a frequency ramp-down rate of 0.25 Hz per second. As shown in Fig. 5.35, rotor current decreases by approximately 10%. In this case, the active and reactive power responses are almost constant during the frequency excursion. Therefore, it can be said that frequency deviation does not significantly affect the model response because the active and reactive power responses are the most important aspect to be investigated in a frequency stability study.

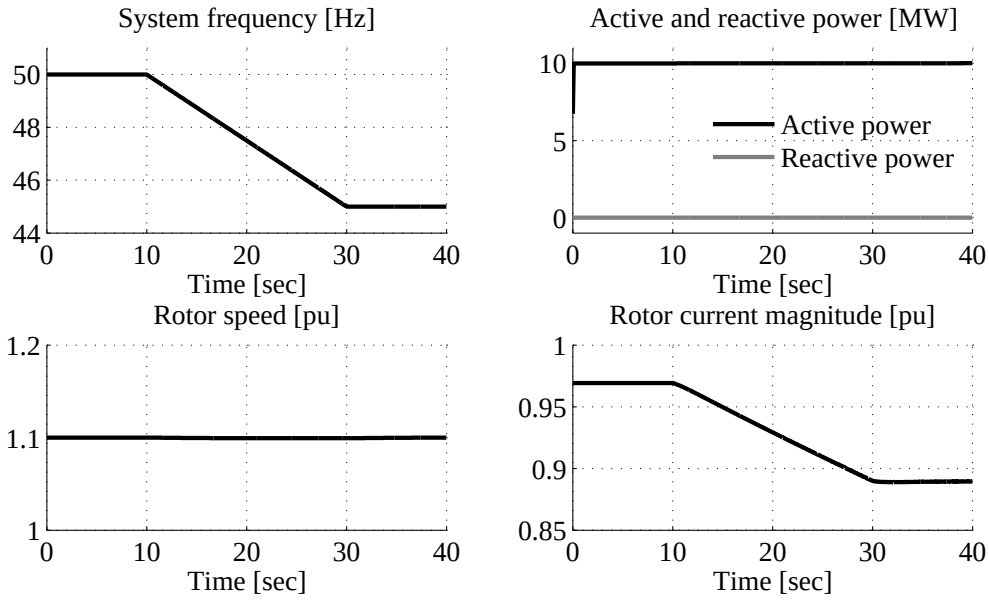

Figure 5.35. Response of DFIG wind turbine during frequency excursion/deviation.

5.11 Conclusion

In this chapter, different parts and control methods of a DFIG wind turbine were described. Various FRT schemes were demonstrated and evaluated. Based on simulation results, it can be concluded that the fault response of a DFIG wind turbine is mainly governed by converter system limits. The most influential limiting factors are the maximum allowed rotor current, rotor voltage, and dc-link voltage. Therefore, having detailed knowledge of the wind turbine envelope is highly important in modeling a DFIG wind turbine. A number of DFIG speed/active power control schemes were presented.

Chapter 6

Power System Stability Model of DFIG Wind Turbine

Based on the examination of DFIG wind turbine component models provided in the previous chapter, a proposed model of a DFIG wind turbine for power system stability studies is derived in this chapter.

6.1 Introduction

In a detailed model of a DFIG wind turbine, the generator is modeled as a fifth-order induction generator and the rotor current is regulated using PI controllers. However, despite its ability to demonstrate wind turbine responses at a high level of precision, the detailed model has practical problems when implemented in large-scale and long-term transient studies.

The first problem appears due to the inclusion of stator transient components, which prevents the model from being implemented in fundamental frequency simulation tools. Another problem is related to the small simulation time step required to run the model. Generally, the detailed model requires a time step size less than 1 ms. This figure is too small in relation to the typical time step for a transient study performed in a standardized simulation tool, such as PSS/E. Depending on the system frequency, the time step for such a simulation tool is normally in the range of $8 - 10$ ms. This clearly makes the detailed model impractical for transient studies.

Models of DFIG wind turbines in fundamental frequency representation have been proposed in several papers and reports such as in [9, 10, 11].

In [9], the DFIG is modeled as a set of algebraic equations. The generator speed is regulated using a PI controller, which provides a rotor current reference value. In this way, the generator loss quantities are preserved in the model. On the other hand, a complex iterative procedure is then necessary to solve a large number of equations involved in the generator and controller models.

Another model is proposed in [10], in which the DFIG is modeled as algebraic equations while the rotor controller is modeled as a combination of algebraic equations and time-lags. In order to avoid non-linearity of the generator model, the electromagnetic torque is assumed to be equal to the stator power, meaning that the generator losses

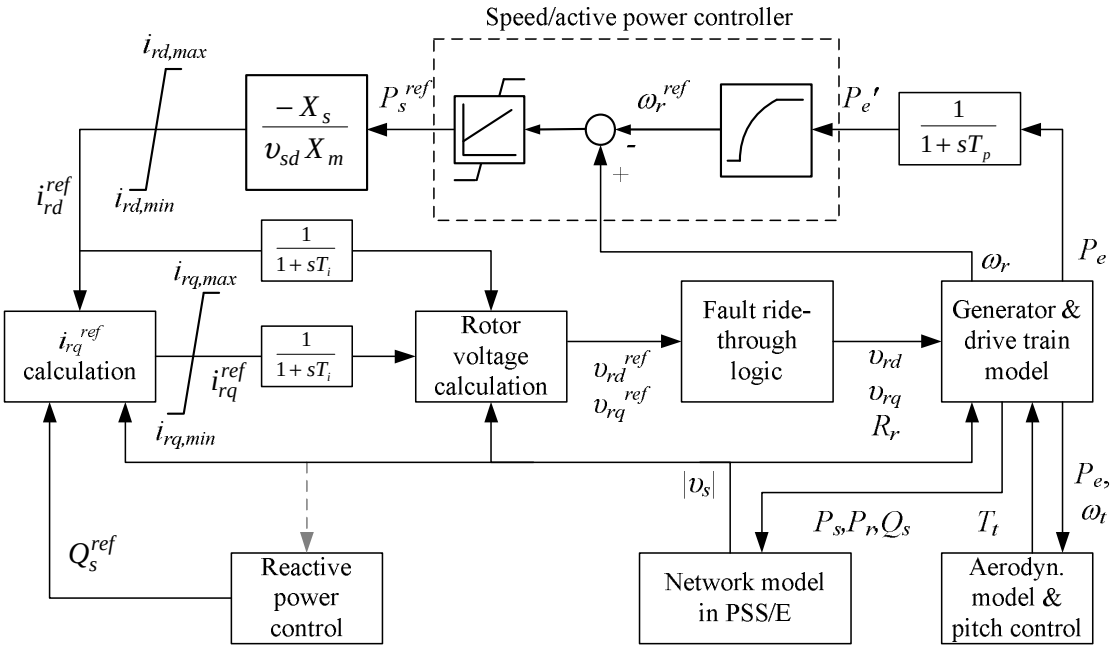

Figure 6.1. Block diagram of proposed model of DFIG wind turbine.

are omitted. The reference value of the turbine output power is obtained directly from the turbine maximum power tracking curve as a function of incoming wind speed.

In [11] and later was refined in [12], the DFIG is modeled as an ideal controlled-current source driven by active and reactive current commands of the wind turbine system. This model allows the controller to cover a wide-range of speed because it is not limited by the nonlinearity of the machine. However, the model is incapable of differentiating stator and rotor quantities.

Rotor current limiters were not involved in the models mentioned earlier. Therefore it is not possible to simulate the effects of current limitations during contingencies, such as during a long-term voltage sag. Apart from this, a head-to-head comparison between a positive-sequence phasor model and a detailed model is rarely found in literature.

In response to these problems, a model of a DFIG wind turbine for power system stability analyses is proposed in this thesis. In the proposed model, the electrical part of the generator is constructed from a set of algebraic equations, while the controller is modeled as a combination of PI controllers and time lags. Simple expressions are derived to solve the generator equations. Rotor current limiters are involved in the proposed model. Rotor converter disconnection as a part of a fault-ride through procedure is included in the proposed model.

The proposed model is implemented in the simulation tool PSS/E with a simulation time step of 10 ms. In order to achieve a high level of confidence, the transient responses of the proposed model are validated against the equivalent detailed model implemented in Matlab/Simulink. The overall structure of the proposed model is depicted in Fig. 6.1. The detailed explanation of each part of the model is given below.

6.2 Generator Model

The generator is represented as a first-order model, considering that the rotor controller is fast enough to control the fast transient event due to rotor dynamics. The stator and rotor voltage equations aligned to the stator voltage reference frame are given by

$$
\begin{aligned}
v_{sd} &= R_s i_{sd} - \omega_e \psi_{sq} && (6.1)\\
v_{sq} = 0 &= R_s i_{sq} + \omega_e \psi_{sd} && (6.2)\\
v_{rd} &= R_r i_{rd} - s\omega_e \psi_{rq} && (6.3)\\
v_{rq} &= R_r i_{rq} + s\omega_e \psi_{rd} && (6.4)
\end{aligned}
$$

where v, i, ψ and R are the voltage, the current, the flux linkage and the generator resistance, respectively; ω_e and s is the synchronous speed and the generator slip, respectively. Subscripts s and r refer to the stator and rotor quantities, respectively. The subscripts d and q denote the direct and quadrature axis components of the reference frame, respectively.

Flux linkage equations are obtained from

$$
\begin{aligned}
\psi_{sd} &= X_s i_{sd} + X_m i_{rd} && (6.5)\\
\psi_{sq} &= X_s i_{sq} + X_m i_{rq} && (6.6)\\
\psi_{rd} &= X_r i_{rd} + X_m i_{sd} && (6.7)\\
\psi_{rq} &= X_r i_{rq} + X_m i_{sq} && (6.8)
\end{aligned}
$$

where X_s, X_r and X_m represent the stator reactance, the rotor reactance and the mutual reactance, respectively.

Electromagnetic torque is calculated as

$$T_e = \psi_{rq} i_{rd} - \psi_{rd} i_{rq} \tag{6.9}$$

Active power of the DFIG can be written as

$$
\begin{aligned}
P_s &= v_{sd} i_{sd} && (6.10)\\
P_r &= v_{rd} i_{rd} + v_{rq} i_{rq} && (6.11)\\
P_c &= v_{cd} i_{cd} + v_{cq} i_{cq} && (6.12)\\
P_e &= P_s + P_c && (6.13)
\end{aligned}
$$

where P_s, P_r, P_c and P_e represent the stator power, the rotor power, the grid-side converter power and the net machine-generated power, respectively.

Power converter losses can generally be ignored, and consequently the converter power is assumed to be equal to the rotor power, $P_c \approx P_r$. Thus (6.13) can be written as

$$P_e = v_{sd} i_{sd} + v_{sq} i_{sq} + v_{rd} i_{rd} + v_{rq} i_{rq} \tag{6.14}$$

The reactive power of the DFIG can be calculated as

$$Q_s = v_{sq} i_{sd} - v_{sd} i_{sq} \tag{6.15}$$
$$Q_c = v_{cq} i_{cd} - v_{cd} i_{cq} \tag{6.16}$$
$$Q_{gen} = Q_s + Q_c \tag{6.17}$$

where Q_s, Q_c, and Q_{gen} represent the stator, grid-side converter and net machine-generated reactive power, respectively. Typically, Q_c is set to zero.

6.3 The Rotor Controller Model

The active power part of the rotor control regulates the speed of the generator using the type 2 control scheme given in section 5.5.2. By using a power-speed characteristic curve, as shown in Fig. 5.9, the reference value for generator speed can be determined. By means of the relatively slow action of the PI-controller, generator speed is transformed into the stator power reference P_s^{ref}, which is assumed to be proportional to the electromagnetic torque.

Since R_s in (6.1) and (6.2) is negligible, therefore $v_{sd} \approx \psi_{sq}$ and $\psi_{sd} \approx 0$. Subsequently, by solving i_{sd} using (6.5), and substituting the resulting equation into (6.10), the d-axis component of the rotor current reference can be written as

$$i_{rd}^{ref} = -\frac{P_s^{ref} X_s}{v_{sd} X_m}$$

The reactive power is modeled as a feed-forward control. If necessary, reactive power reference can be driven by a voltage controller.

i_{sq} is obtained from (6.15) and (6.17) by assuming $Q_c = 0$

$$i_{sq} = -\frac{Q_s}{v_{sd}} \tag{6.18}$$

i_{sd} is then calculated by (6.2) and (6.5)

$$i_{sd} = \frac{-r_s i_{sq} - X_m i_{rd}^{ref}}{X_s}$$

Finally, the q-axis component of the rotor current reference i_{rq}^{ref} can be calculated using (6.1) and (6.6)

$$i_{rq}^{ref} = \frac{1}{X_m}(R_s i_{sd} - X_s i_{sq} - v_{sd})$$

As seen in Fig. 6.1, the rotor current components are subjected to limitation. Time lag blocks with a time constant T_i are introduced in the model to resemble delays associated with measurement and current controller dynamics.

To enable representation of a deactivated-converter during a fault ride-through procedure, a rotor voltage-controlled generator representation is needed. Therefore, the ordered rotor current must be transformed into the corresponding rotor voltage. This can be done by solving i_{sd} and i_{sq} using (6.1) and (6.2), and substituting the results into (6.3) and (6.4).

$$
\begin{aligned}
v_{rd}^{ref} &= i_{rd}^{ref} R_r - i_{rq}^{ref} s X_r \\
&\quad + \frac{i_{rd}^{ref} R_s s X_m^2 + s v_{sd} X_m X_s + i_{rq}^{ref} s X_m^2 X_s}{R_s^2 + X_s^2} \qquad (6.19) \\
v_{rq}^{ref} &= i_{rq}^{ref} R_r + i_{rd}^{ref} s X_r \\
&\quad + \frac{R_s s v_{sd} X_m + i_{rq}^{ref} R_s s X_m^2 - i_{rd}^{ref} s X_m^2 X_s}{R_s^2 + X_s^2} \qquad (6.20)
\end{aligned}
$$

6.4 Other Parts of The Model

In a power system stability study, the dc-link voltage can be assumed to be stiffly constant. Consequently, grid-side converter power output is equal to rotor power output. Meanwhile, the pitch controller, drive-train and aerodynamic models in the detailed model can be implemented directly in the proposed model without causing difficulties owing to low time-constants.

6.5 Fault Ride-Through Procedure

The thresholds of the converter protection setting are mainly determined by the allowed maximum transient current of the rotor-side converter and the maximum dc-link voltage.

The rotor-side converter transient current magnitude and the dc-link voltage are influenced by several factors including fault severity, generator parameters, dc-link capacitor size, the maximum allowable rotor voltage and wind turbine power level. Fig. 6.2 shows a typical capability limit of the converter subjected to a voltage dip at different power levels for particular maximum rotor current and dc-voltage limits. According to the figure, the converter is disconnected if the power versus voltage dip operating point is situated above the curve, otherwise the converter remains intact.

In stability studies, however, it is fair to assume that the thresholds of converter protection setting are determined only by the rate of change and magnitude of the stator voltage. A low-voltage threshold of 0.7 pu (i.e. 0.3 pu voltage dip) is prevalent. Once the rotor-side converter protection is activated, the rotor voltage is dictated by the fault ride-through routine, which comprises two phases.

The first phase is crowbar activation. In this phase, a resistance is inserted in the rotor circuit. In the model, this is simply realized by increasing the rotor resistance. At this stage, the rotor voltage is set to zero. Typically, this phase lasts for about 50-100 ms.

In the second phase, the converter is reactivated, while the rotor resistance is reset to the original value. At this stage, the electromagnetic torque is set to zero while the reactive current is set to the maximum value. When the fault is cleared, and grid voltage rises above the minimum threshold, the converter mode is switched back to normal operation.

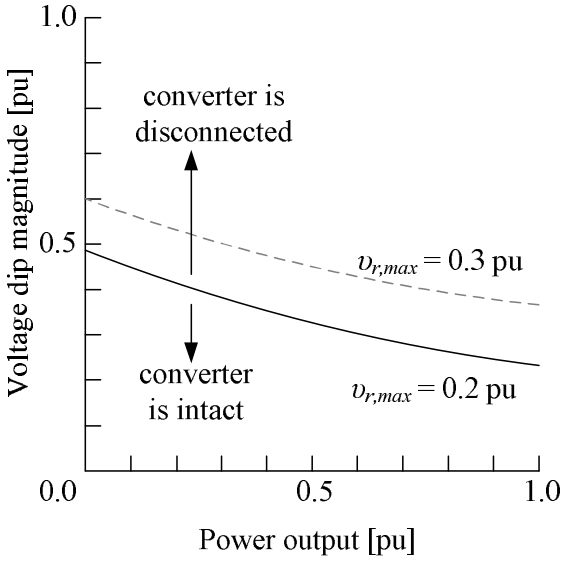

Figure 6.2. Rotor-side converter capability limits during voltage dip.

6.6 Model Initialization

Various methods of initializing a DFIG model for power system stability studies have been suggested in several papers [121, 86, 104]. In [121], the initialization is performed by assuming a lossless DFIG. Consequently, this assumption may result in less accurate initial values, which are undesired for simulating a large power system where the size of the model is substantial for the system. In [86], the initialization is performed using a steady state representation of a DFIG by employing an iteration procedure. However, the iteration procedure creates a difficulty in the model implementation. In [104], the initialization is carried out using a direct solution method based on torque balance equations. In this way, more accurate initialization results can be obtained without using an iteration procedure. However, this method is only applicable for the type 1 speed/active power control where the relation between electrical torque and generator speed is known.

In this thesis, the method of initialization of a DFIG is performed using a steady state model of a DFIG and a power-speed curve. As a result, this method is able to provide accurate results for a DFIG model with the type 2 speed/active power control. Furthermore, the initialization can be done without employing an iteration procedure. In order to realize this method, the steady state model of a DFIG is represented in a dq-reference frame aligned with stator voltage, i.e. $v_{sd} = |\vec{v}_s|$ and $v_{sq} = 0$.

The initial total active power P_e and reactive power Q_{gen} are given from the load flow. The grid-side converter reactive power Q_c is defined according to the control design, although normally this value is set to zero. The stator reactive power is calculated by $Q_s = Q_{gen} - Q_c$. The corresponding generator speed is defined according to the power-speed curve presented in Fig. 5.9.

The initial q-component of the stator current i_{sq} can be calculated by (6.18). By substituting (6.1)-(6.8) into (6.14), i_{sd} can be calculated using the following quadratic expression

$$0 = a\, i_{sd}^2 + b\, i_{sd} + c \tag{6.21}$$

where

$$\begin{aligned} a &= sR_s + \frac{R_r\left(R_s^2 + X_s^2\right)}{X_m^2} \\ b &= v_{sd}\left(1 - s - \frac{2R_rR_s}{X_m^2}\right) \\ c &= \frac{R_r v_{sd}^2 - P_e X_m^2 + 2i_{sq}R_r v_{sd}X_s + i_{sq}^2\left(sR_sX_m^2 + R_r\left(R_s^2 + X_s^2\right)\right)}{X_m^2} \end{aligned}$$

Since (6.21) gives two solutions, the one with the smallest absolute value is chosen. Once i_{sd} and i_{sq} are found, the rotor current reference values (i_{rd}^{ref} and i_{rq}^{ref}) can be found using (6.1),(6.2),(6.5) and (6.6)

$$i_{rd}^{ref} = -\frac{1}{X_m}(R_s i_{sq} + X_s i_{sd}) \tag{6.22}$$

$$i_{rq}^{ref} = \frac{1}{X_m}(R_s i_{sd} - X_s i_{sq} - v_{sd}) \tag{6.23}$$

At steady state, the generator and the turbine speed are equal, $\omega_r = \omega_t$. Correspondingly, the shaft twist angle ($\Delta\theta = \theta_r - \theta_t$) can be calculated using

$$\Delta\theta = \frac{T_e}{K_s} \tag{6.24}$$

The corresponding wind speed is calculated by means of (5.10) by assuming the pitch angle is at its minimum value. Alternatively, if wind speed is known and is above the rated value, then the corresponding pitch angle can be found numerically from the $C_p(\lambda, \beta)$-curve lookup table.

6.7 Model Simulations

The proposed wind turbine model was simulated to investigate the responses of the model subjected to various disturbances. The simulations of the proposed model were performed in PSS/E using a standard time step which is 10 ms for a 50 Hz system frequency. A test network as shown in Fig. 6.3 was used throughout the simulations. Wind turbine parameters are given in Table A.11 and Table A.12 in the Appendix. The terminal voltage data from the simulations are then used as inputs for the detailed model, which was implemented in Matlab/Simulink. Subsequently, the simulation results of the proposed model are compared with those of the detailed model.

6.7.1 Wind speed transient

The aim of simulating wind speed transient is to assess the responses of the proposed model when subjected to an extreme increase in wind speed. In the simulation results, responses of the detailed model and the proposed model are compared.

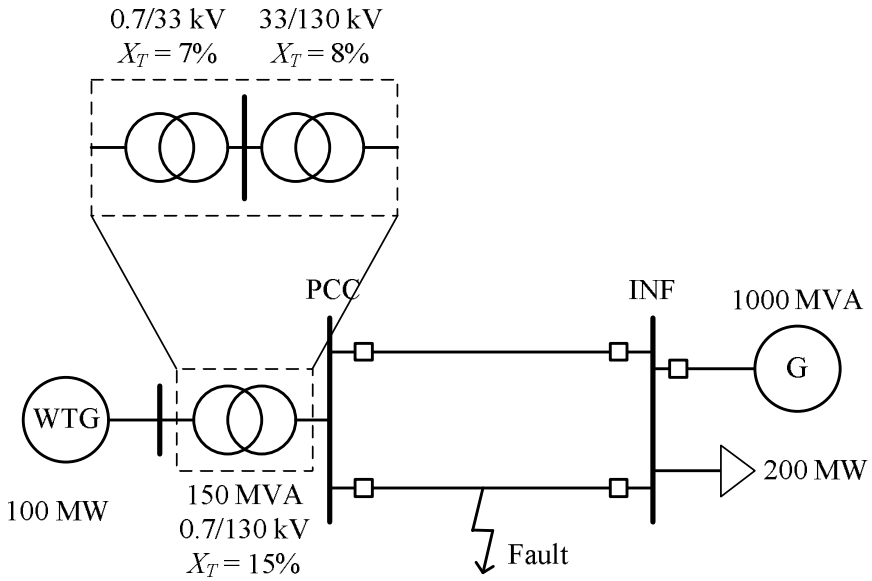

Figure 6.3. Test grid.

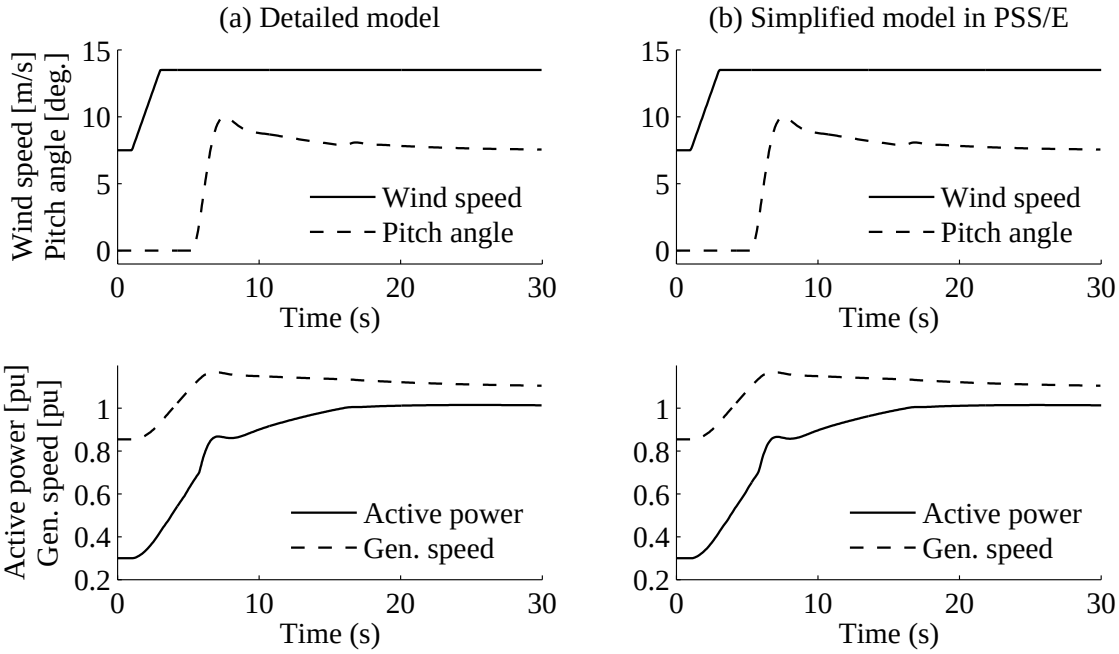

Figure 6.4. Comparison between detailed and simplified models of DFIG wind turbine when subjected to wind gust.

As shown in Fig. 6.4, the wind speed is initially 7.5 m/s, which gives 0.3 pu of wind turbine power. The generator speed is 0.85 pu (15% slip), meaning that the generator operates at subsynchronous speed. Since wind speed and rotor speed are below the rated value, the pitch angle is set at 0°. At this moment, the turbine runs within an optimum speed operating region.

At t=1 s, the wind speed increases rapidly to 13.5 m/s within 2 seconds. Once the rotor speed exceeds the maximum speed (1.1 pu), the pitch controller reacts by increasing the pitch angle. At this stage, the turbine operation mode switches from

the optimum speed operating region to the maximum speed operating region and subsequently to the power limitation operating region. The rapid change in wind speed, however, cannot be compensated by the relatively slow reaction of the pitch controller. As a consequence, there is a small overshoot in aerodynamic power. By letting the rotor speed increase to around the nominal value, part of the mechanical energy is diverted into rotating inertia, which results in a higher rotor rotation speed. This allows a smoother electric power output.

The responses of the wind turbine models when subjected to wind transient are mainly governed by the pitch controller and aerodynamic models, which are identical for both the detailed and the proposed models. Therefore, the responses of these models are unsurprisingly very similar.

6.7.2 Fault response without crowbar activation

In the second simulation, the responses of the proposed model subjected to a small grid fault was investigated. The controller is designed to limit the maximum rotor current reference at 1.0 pu. Note that the rotor rating is normalized to the actual rating of the rotor converter, which is equivalent to 20% of the generator rating.

During the simulation, wind speed is assumed to be constant at the nominal value. The wind turbine operates at a unity power factor. At $t = 0.1$s, a three-phase to ground fault occurs at one of the transmission lines causing a wind turbine terminal voltage dip by 0.25 pu for 250 ms (see Fig. 6.5). As seen in the figure, the terminal voltage suffers from a sustained undervoltage of 20% below the nominal value.

Since the voltage dip is not severe, converter disconnection does not occur. As a consequence, the wind turbine controller responds quite well to the disturbance. The reactive power can be maintained constant, while the active power drops by 0.2 pu during the fault. Generator and turbine speeds are slightly affected, as they undergo oscillations at less than 5% of the nominal values due to the drive train dynamics. As seen in the figure, the terminal voltage suffers from a sustained undervoltage of 10% below the nominal value after the fault. Since the rotor current is limited at 1 pu, this undervoltage results in slightly higher generator speed and lower active power output than the nominal values.

A slight discrepancy between the detailed and the proposed models can be observed in the reactive power responses where the detailed model is able to capture a transient at the moment of fault and fault clearing, while no transient is seen in the proposed model. Nevertheless, the results of the comparison between the two models demonstrate that the proposed model is capable of simulating the response of the wind turbine accurately.

6.7.3 Fault response with crowbar activation

In the following, the same turbine and network models are used except the applied fault is more severe than in the previous simulation. As shown in Fig. 6.6, a grid fault leads to a voltage drop on the wind turbine terminal to 0.25 pu. As a consequence, the rotor-side converter is disconnected. The time delay for the converter reconnection in the proposed model is set to 50 ms. Once the converter is reconnected, a reactive power injection of 0.15 pu by the wind turbine can be observed. During the fault clearing event, the converter increases the power gradually, and consequently a power overshoot

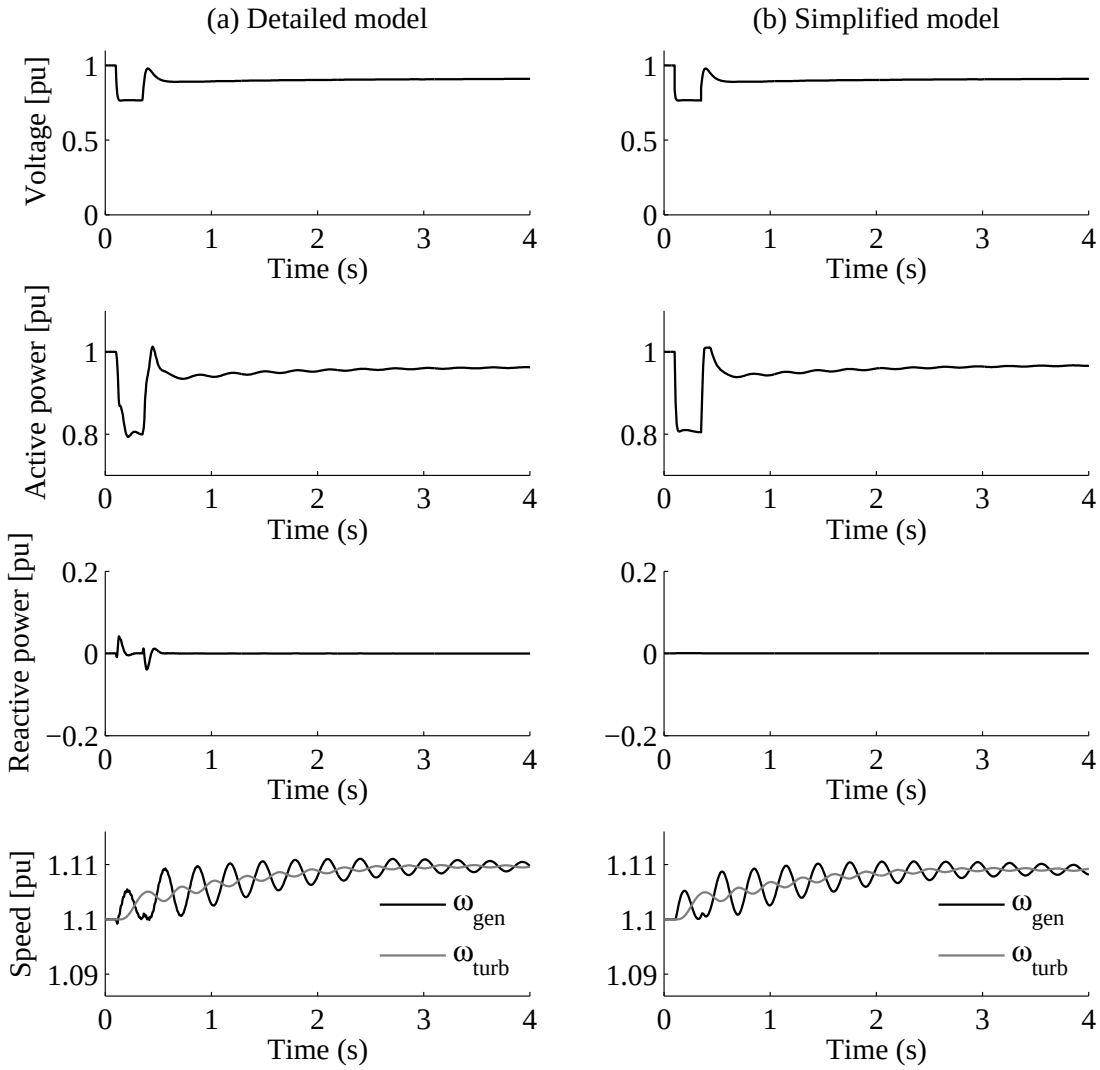

Figure 6.5. Comparison between detailed and simplified models of DFIG wind turbine in case of a grid fault without rotor converter disconnection.

can be avoided. The flat course of the active power following the fault indicates that the converter reached the maximum continuous current limit, which was set at 1.0 pu. Meanwhile oscillation is noticeable in generator and turbine speeds.

The active and reactive power response would be higher if the rotor current limiter had been removed from the proposed model. Without the current limiter, the proposed model also fails to predict generator speed accurately. This emphasizes the importance of including the current limiter in a model of a DFIG wind turbine.

Again, a head-to-head comparison between the proposed model and the detailed model shows the ability of the proposed model to capture important responses of a DFIG wind turbine.

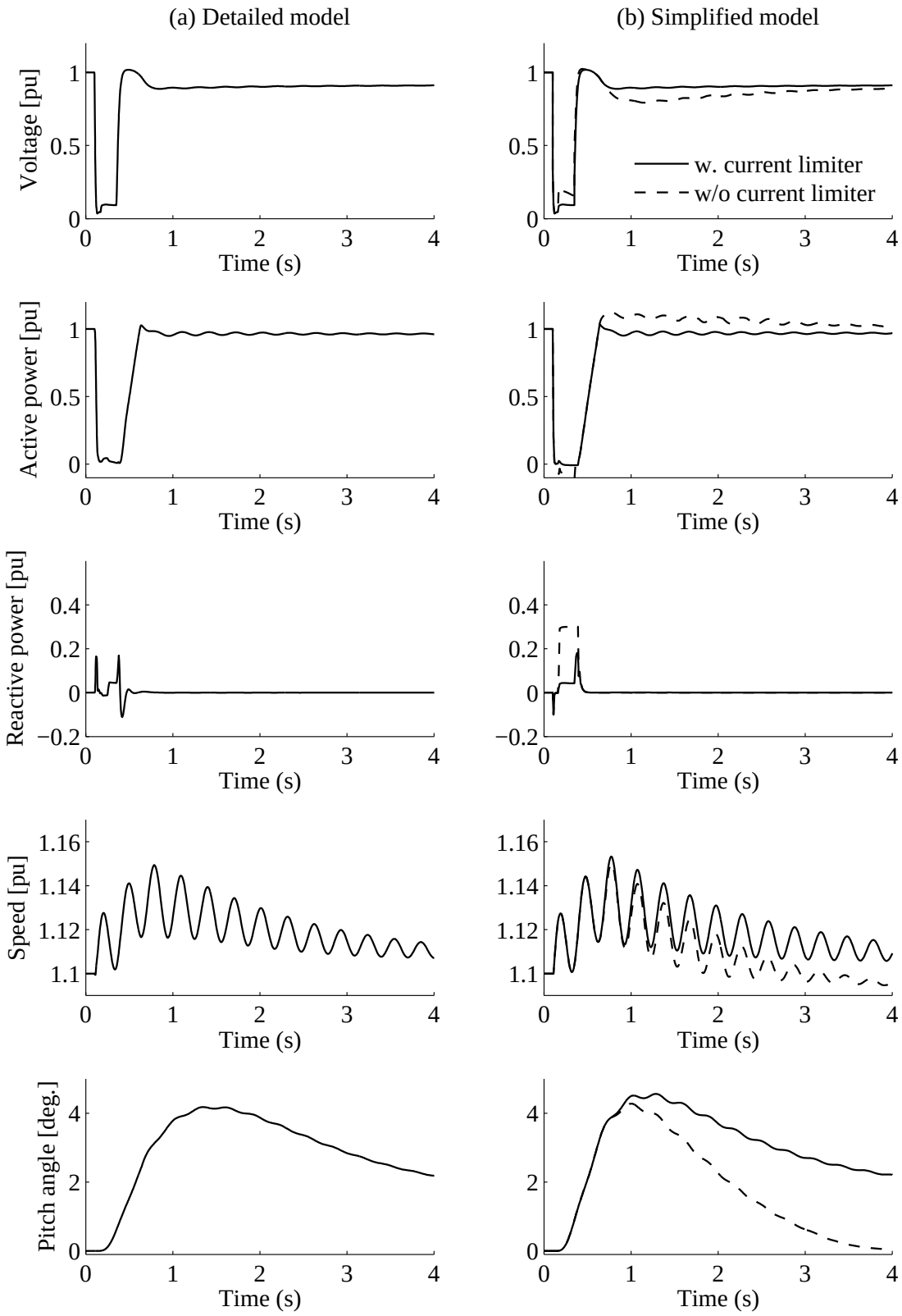

Figure 6.6. Comparison between detailed and simplified models of DFIG wind turbine in case of a grid fault with rotor converter disconnection.

6.7.4 Applicability for different speed/active power control schemes

A type 2 control scheme was employed in the model discussed earlier. Nevertheless, other speed/active power control schemes including type 1 and type 3 can also be implemented in the model without any complications. This can be done by simply replacing the speed/active power controller block in Fig. 6.1 with the desired one.

Simulation results of the proposed model with type 1 speed/active power control scheme are shown in Fig. 6.7. As seen in the figure, the power response following a fault is relatively flat due to the influence of the current limiter. Generator speed oscillations due to shaft torsional dynamics are slightly higher in the proposed model than in the detailed model. Nevertheless, the damping responses of the two models are similar.

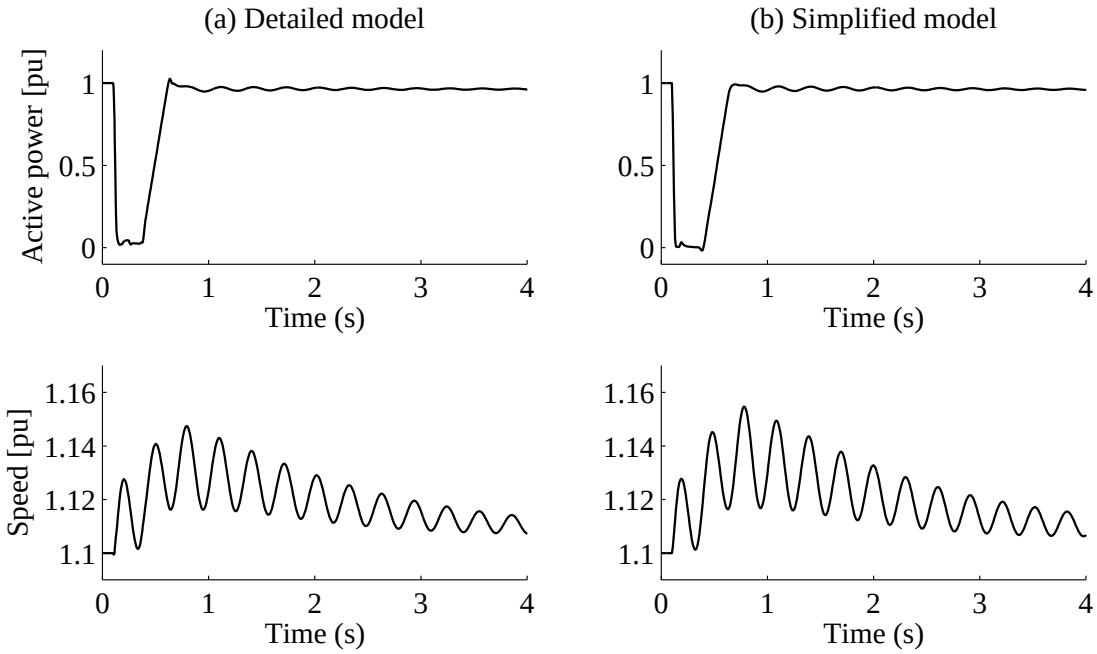

Figure 6.7. Comparison between detailed and simplified models of DFIG wind turbine in case of a grid fault for active power controller type 1.

6.8 Conclusion

In this chapter, a model of DFIG for power system stability studies was proposed. In the proposed model, the electrical part of the generator was constructed from a set of algebraic equations, while the controller was modeled as a combination of PI controllers and time lags. Simple expressions were derived to solve the generator equations. Rotor current limiters and rotor converter disconnection as a part of a fault-ride through procedure were involved in the proposed model. A model initialization using a direct solution method was introduced in this chapter.

The proposed model was implemented in the simulation tool PSS/E using the standard simulation step of 10 ms. In order to achieve a high level of confidence,

the transient responses of the proposed model were validated against the equivalent detailed model implemented in Matlab/Simulink.

The simulation results showed that the responses of the proposed model matched very well with the ones of the detailed model at various operating conditions, including wind speed transients and grid fault with and without rotor converter disconnection. The proposed model involved rotor current limiters, which were proven to be essential in producing accurate responses of a DFIG wind turbine during a transient event. Different active power control schemes can also be implemented in the proposed model with only minor modifications.

Chapter 7

Aggregated Models of DFIG Wind Turbines

This chapter presents different aspects and methods of aggregating a wind farm consisting of DFIG wind turbines. The chapter also provides a recommendation for choosing appropriate aggregated models for different types of studies.

7.1 Introduction

In the following sections, a variety of aggregated models for a wind farm consisting of DFIG wind turbines are discussed. Important aspects in aggregated modeling of a wind farm consisting of DFIG wind turbines for short-term voltage stability studies are described. The influences of the wake effect and wind speed time delay on wind farm response are investigated. Finally, the chapter is concluded by providing a recommendation for choosing appropriate aggregated models for different types of studies.

7.2 Aggregation methods

Aggregating a wind farm consisting of DFIG wind turbines can be realized in different ways, such as using a single unit representation, a cluster representation [122] or a compound representation [123, 124].

In a single unit representation, the entire wind turbines in a wind farm are represented by a single equivalent unit of wind turbine (see Fig. 7.1a). The electrical power output and rating of the equivalent unit is a sum of the individual wind turbines.

In a cluster representation, wind turbines in the wind farm that have equal wind speed input are grouped into one cluster and then are replaced by a single equivalent unit, where the power rating and output of the equivalent unit are the sum of the individual wind turbines being represented (see Fig. 7.1.b). The number of clusters in the aggregated model depends on the largest wind speed difference between the wind turbines and the accuracy required. Normally, wind turbines with incoming wind speed above rated value can be grouped into a single equivalent unit. As the pattern of wind speed in a wind farm is influenced by wind direction and the structure of the wind

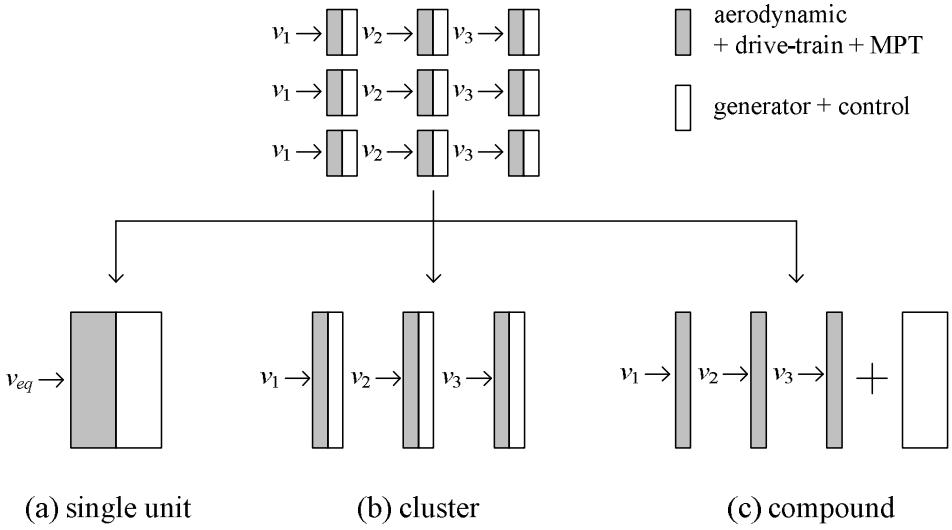

Figure 7.1. Aggregation methods.

farm, a coherency matrix proposed in [122] can be used to define the number and size of wind turbine clusters. It is assumed that the clusters remain unchanged during the time frame of the study.

Compound representation is a compromise between a single unit representation and a cluster representation. As given in Fig. 7.1.c, the method can be realized by representing aerodynamic, drive train, pitch-controller and MPT models into several groups based on similarities of operating conditions, as in the cluster representation. The electrical model, in contrast, is represented by a single equivalent unit.

7.3 Aggregation method for short-term voltage stability studies

For application in short-term voltage stability studies, the following assumptions are used in the investigation: First, wind speed is assumed to be constant during the simulation time frame. Further, rotor speed variation is assumed to be small enough to such an extent that it does not significantly alter aerodynamic efficiency, hence aerodynamic power variations are marginal. Second, the speed control response is relatively slow, and thereby the electromagnetic torque and current reference do not enter the saturation region during transients following a grid fault.

In such a case the wind farm can be sufficiently represented by a single equivalent unit. For the purpose of verifying this proposition, a short-term voltage stability study of a wind farm using two different representations is performed.

The wind farm capacity is 8 MW, consisting of 4x2 MW wind turbines. In this case, it is assumed that 2 turbines operate at a full power level while the other 2 turbines operate at half of capacity. This power composition is intended to illustrate an extreme situation where wind turbines in the wind farm are segregated into two groups with considerably different operating points.

In the aggregated model, the wind turbines are represented as a single equivalent unit. Wind turbine transformers are also lumped into a single transformer. The sizes

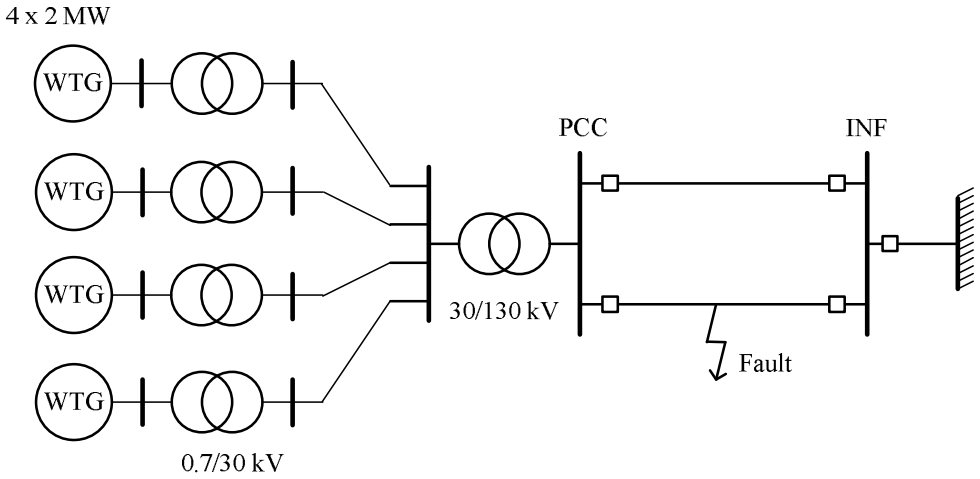

Figure 7.2. Wind farm layout.

of the equivalent units are the sum of the individual units.

To study short-term voltage stability responses of the aggregated model, a fault is applied on one of the transmission lines for 250 ms. As a consequence, the turbine terminal suffers a voltage dip of 0.8 pu. The fault is finally cleared by disconnecting the faulted line.

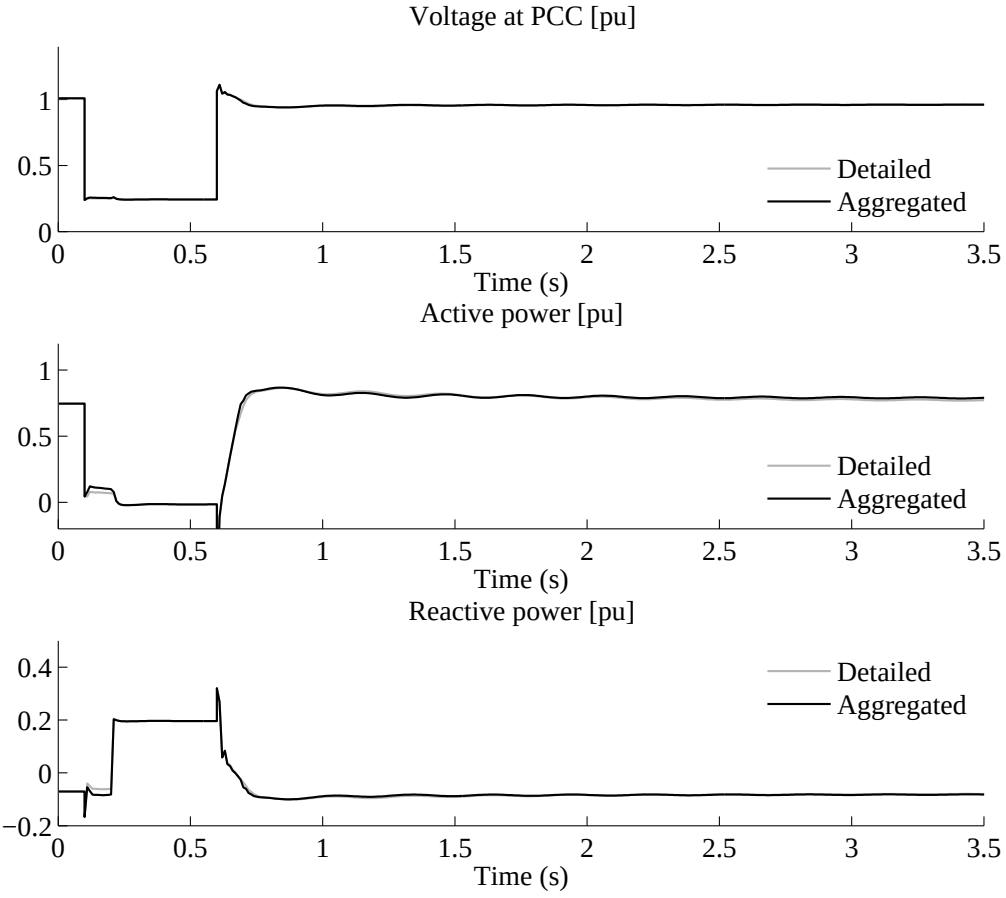

Figure 7.3. Comparison between aggregated and individual model of DFIG wind turbines.

As shown in Fig. 7.3, the active and reactive power responses of the aggregated model match very well with the response of the detailed model. This suggests that a single unit aggregated model is sufficiently accurate to resemble wind farm behavior consisting of DFIG wind turbines, despite considerably different power levels and the operating points of the turbines.

As stated earlier, slow response from the speed controller was assumed in the previous simulation. If the speed controller response is fast, the torque reference may reach the saturation region due to the maximum torque limitation. In such a case, the wind turbines that operate at full power may reach the saturation region, while the ones that operate at partial power may be within the linear region. Consequently, the single equivalent unit representation of a wind farm may not be sufficient. As seen in Fig. 7.4, the single equivalent unit is not able to predict farm behavior accurately.

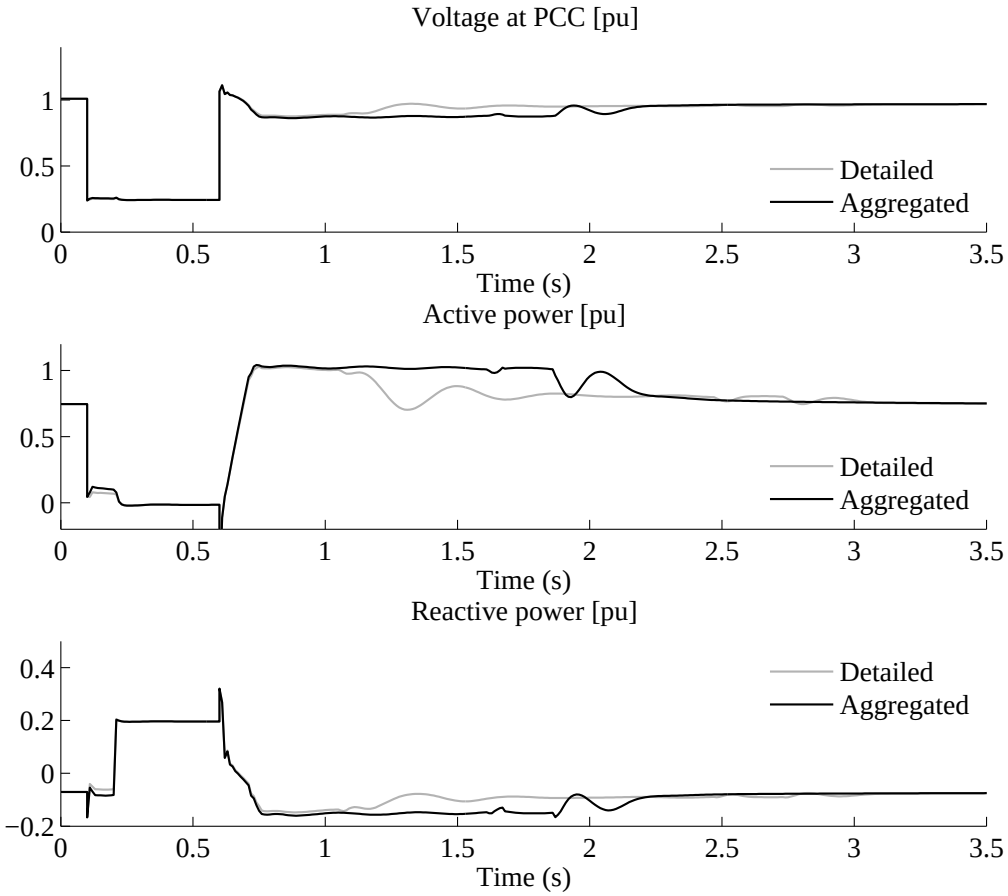

Figure 7.4. Comparison between aggregated and individual model of DFIG wind turbines considering torque limit.

A closer look at the individual turbines presented in Fig. 7.5 shows that the power response of wind turbines at full power output is dominated by a flat response. This is because the controller goes into the saturation region. While the response of the wind turbines with partial power is characterized by well damped power oscillations with an overshoot in the beginning of the transient. The response of the wind turbine for the two operating conditions is clearly not linearly correlated. It is also important to note that wind turbines that are not in operation, i.e. at the zero power operating point,

must be excluded when defining the rating of the aggregated model. Otherwise, this will cause errors in predicting an operating point in the aggregated model.

The reactive power at the PCC is influenced to a great extent by the voltage profile at the location. However, the reactive power responses at the generator terminals of the two turbines are actually similar, as shown in Fig. 7.5. It should be noted that reactive power similarity is only valid for a constant reactive power mode. If a turbine operates in a constant power factor mode, the reactive power of the two clusters will not be identical, since the reactive power response is coupled with active power response.

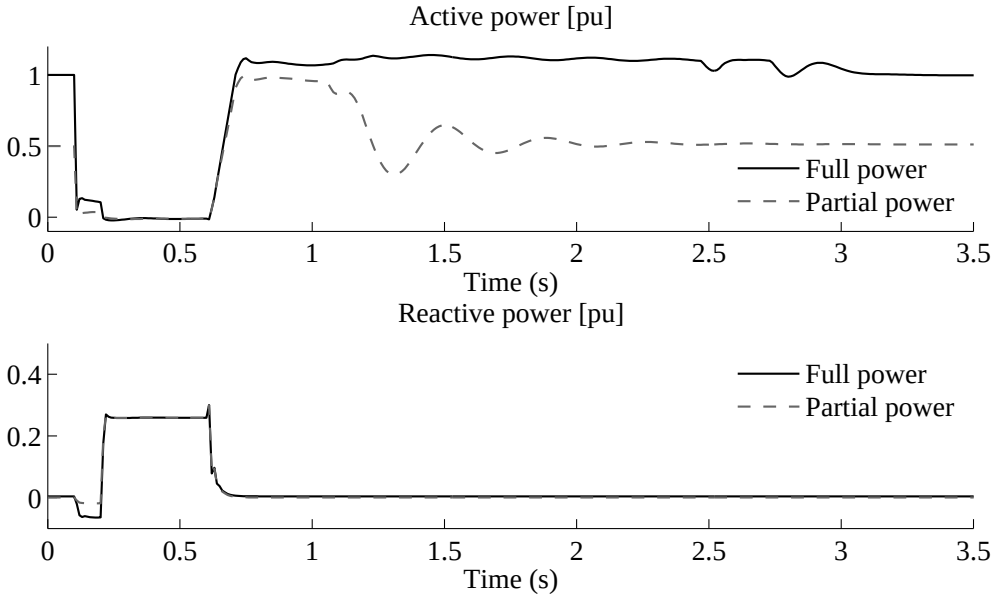

Figure 7.5. Fault response of a DFIG wind turbine at two different operating points: full load and partial load.

This finding emphasizes that the dominant source of non-linearity in an aggregated model of wind turbines for a short-term stability study can be attributed to speed controller saturation due to the reference torque or current limitations. Consequently, it is not proven that non-linearity originates only in the aerodynamic model and the MPT characteristic. This, in turn, invalidates the application of compound representation in this case. Thus, it is recommended to employ a cluster representation instead.

7.4 Adopting Horns Rev wind speed measurement data into model simulation

The operating points among the turbines in an actual wind farm are not concentrated into two values as it was assumed earlier. Instead, power outputs among the wind turbines are normally distributed more evenly. The distribution of the power is mainly influenced by the wake effect characteristics of the wind farm, which will be discussed in the next section.

One of such measurements has been reported in [125] taking the Horns Rev wind farm as the object of the investigation. The report presents wind speed measurement

for 10 wind turbines in the wind farm, which are located in a row. Each turbine size is 2 MW, with a rotor diameter of 80 meter. The distance between two adjacent turbines in a row is equivalent to 7 times rotor diameter or approximately 560 meters.

Fig. 7.6 shows incoming wind speed on each turbine for two different free wind speeds, which are 8.5 m/s and 12 m/s. The wind direction is parallel to the row, with a deviation of around $\pm 3^{\circ}$. The first turbine is located in the uppermost wind stream followed by the second turbine and so forth. In other words, the first turbine fully overshadows the second turbine and so on. The wind pattern indicates that there is a significant speed drop between the first and the second turbine, whereas the speed drop is less noticeable for the rest of the turbines in the row.

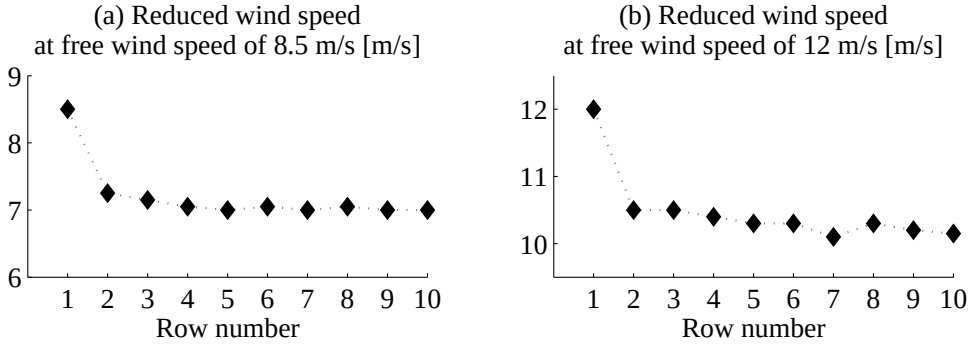

Figure 7.6. Reduced wind speed in a wind turbine row at two different free wind speed: (a) 8.5 m/s (b) 12 m/s.

In the following, the validity of the single equivalent unit representation of a wind farm is examined by adopting the measured space distribution of wind speed among wind turbines in rows in Horns Rev wind farm into a wind farm model consisting of 50 x 2MW wind turbines. The total installed capacity of the wind farm model is 100 MW. The layout of the wind farm model is given in Fig. 7.7. Wind farm cable impedances are neglected in the investigation. Wind speed direction is assumed to be 90° in the investigation, meaning that the wind stream passes 10 turbine rows, which consist of 5 wind turbines each.

By using input wind speed provided in Fig. 7.6, the corresponding output power of wind turbines in each row can be calculated as presented in Fig. 7.8. Note that the turbine power output profile produced by the simulation, has a pattern similar to the power measurement data of Horns Rev wind farm as reported in [126]. This means that steady state characteristics of the power curve used in the model has similarities with the ones in the actual turbines.

The results of the simulation are presented in Fig. 7.9. Note that a fast speed control is employed in the model. As a consequence, a high overshoot in power can be seen immediately after fault clearing. If a slow response speed control would have been used in the model, there would have been a much smaller overshoot present in the power response.

Due to relatively close operating points among the turbines, although the saturation region is reached, the aggregated model does not lose its accuracy. Again, these results reinforce confidence in using a single equivalent unit to resemble a wind farm for short-term voltage stability studies.

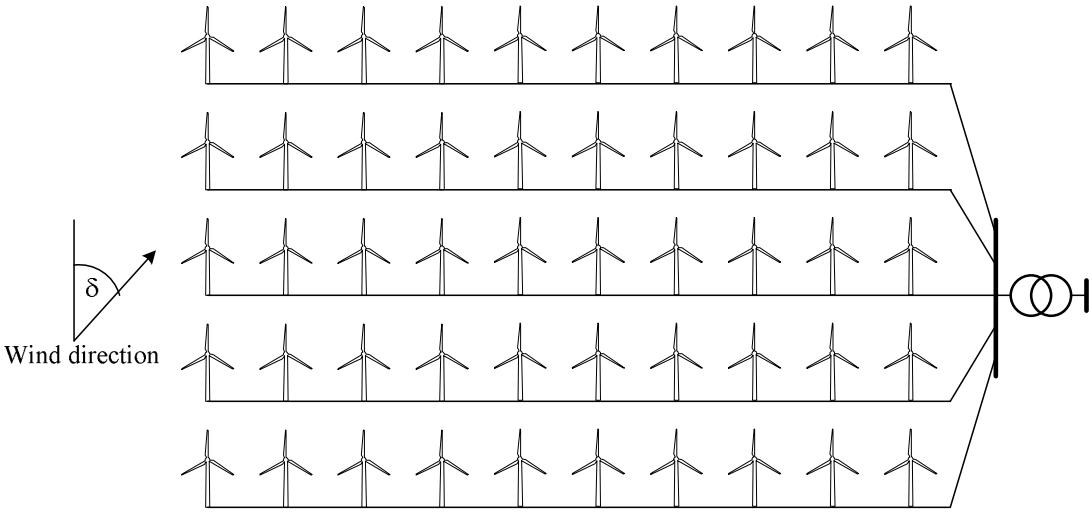

Figure 7.7. Wind farm model layout.

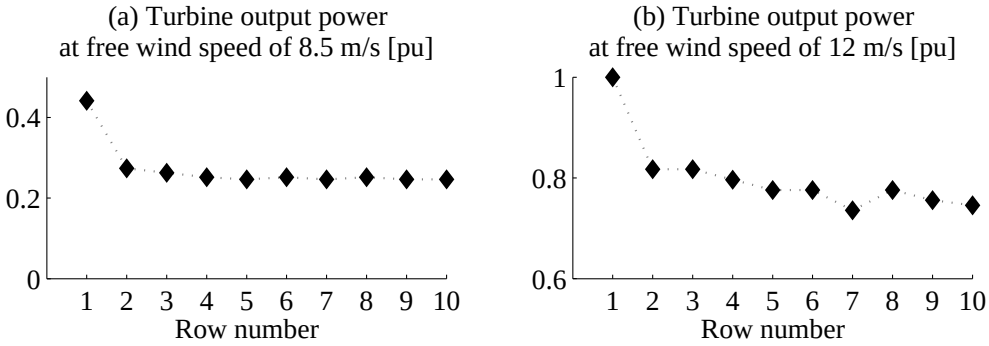

Figure 7.8. Wind turbine output power.

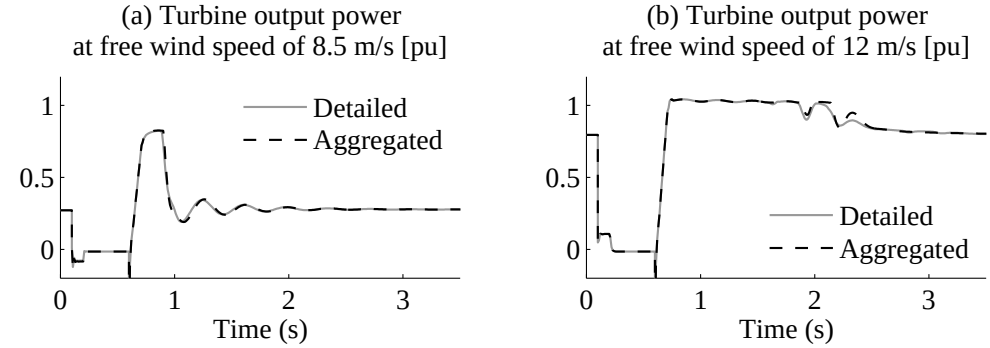

Figure 7.9. Fault response of a wind farm aggregated model consisting of DFIG wind turbine with fast speed control.

7.5 Wake effect and wind speed time delay

In a large wind farm, the time aspect of wind transport is an important consideration. For example, a wind farm with 8 rows of wind turbine and 80 meters of rotor diameter for each wind turbine, and 7 rotor diameters of distance each adjacent row has a length of nearly 4 km. At a wind speed of 12 m/s, it takes more than 5 minutes for the wind

to travel across the wind farm. At a wind speed of 8 m/s, the travel time for the wind can be more than 8 minutes. These time scales are highly relevant for a medium- and long-term system stability investigation. As a consequence, a realistic model of wind transport is a prerequisite when a wind gust effect needs to be involved in such a study.

Any change in upstream wind speed will have effects on a downstream turbine after a certain time delay due to the wind speed transport. The delay is a function of distance and wind speed. The transport time of wind speed passing between two successive turbine rows can be roughly estimated using [127]:

$$t_{delay} = \frac{\ell}{\bar{v}_w} \tag{7.1}$$

where ℓ is the distance between the two successive turbine rows and $\bar{v}_w$ is the average wind speed passing the first wind turbine.

Power extraction on wind flow passing a turbine creates a wind speed deficit in the area behind the turbine. This phenomenon is commonly called the wake effect. As a consequence, wind turbines that are located downstream obtain less wind speed than those that are upstream. The deficit in wind velocity due to the wake effect depends on several factors, such as the distance behind the turbine, turbine efficiency and turbine rotor size. Wind speed in the wake at a distance x behind the turbine rotor can be calculated by using [122]

$$v_w(x) = v_0 \left[1 - \left(\frac{R}{k_w x + R} \right)^2 \left(1 - \sqrt{1 - C_T} \right) \right] \tag{7.2}$$

where v_0 is the incoming free-stream wind speed, C_T is the turbine thrust coefficient, which has a typical curve as given in Fig. 7.10, k is the wake decay constant, and R is the turbine rotor radius.

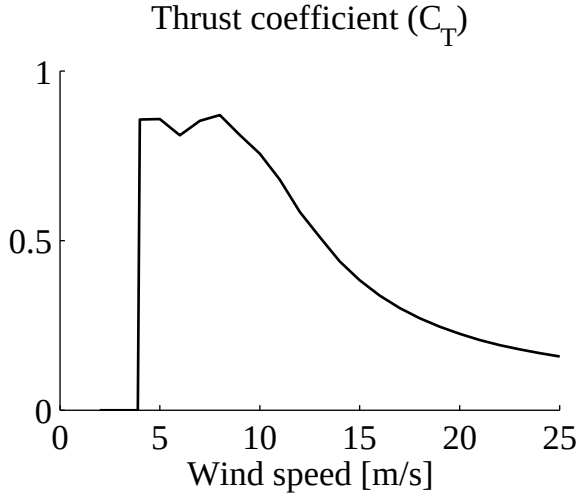

Figure 7.10. Exemplary thrust coefficient of a wind turbine used in the model.

The wind gust responses of a wind farm model that incorporates time delays and wake effects are simulated using the wind farm layout shown in Fig. 7.7 with a wind direction of 0°. As shown in Fig. 7.11, the wind speed changed from 9/m to 13/ms

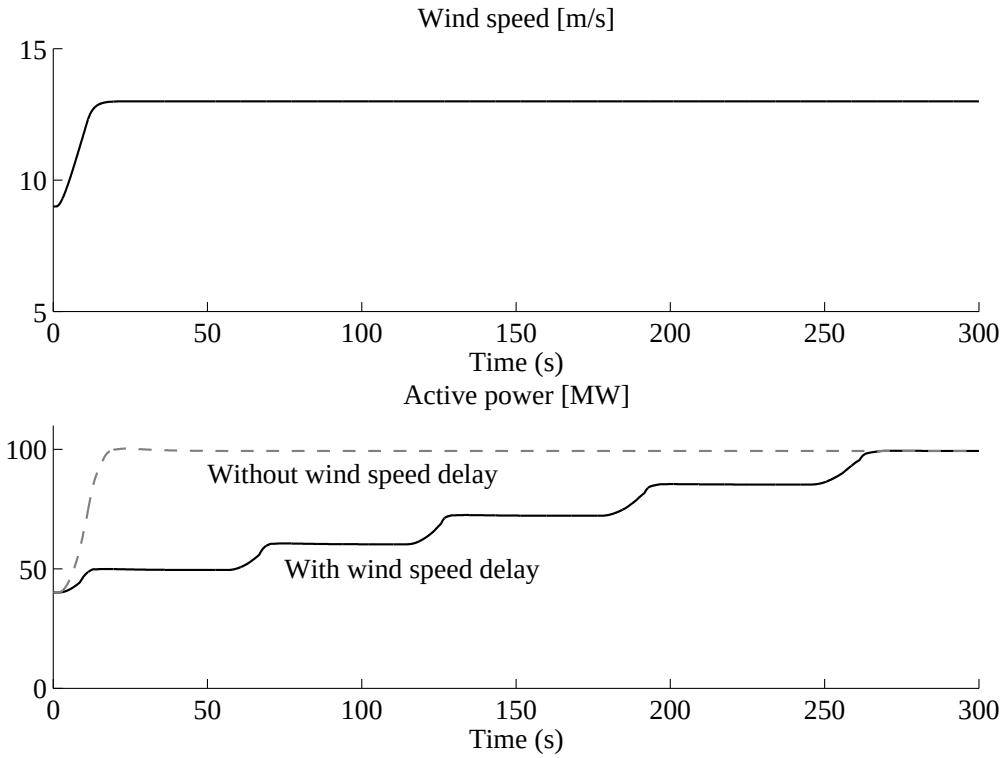

Figure 7.11. Wind gust response of a large wind farm taking into account the wake effect and wind speed delay between wind turbine rows.

within 4 seconds raising wind farm output power with a settling time of more than 4 minutes. Consequently, it can be concluded that the increase in power response due to a relatively fast change in wind speed in a large wind farm is very slow. In contrast, if a wind speed delay is neglected, the model will predict a quick increase in the wind farm power output. This finding leads to the conclusion that if the wake effect and wind speed time delay are to be considered in the aggregated model, then the single equivalent unit representation is inadequate. In other words, the wind farm is more suitably represented using a cluster representation.

Modeling detailed wind transport phenomena in a wind farm, however, is beyond the of scope of this thesis. Therefore, it is recommended that realistic modeling of phenomena is implemented in a separate tool. The output of this model, in the form of wind speed time series data for each wind turbine row can then be used in the aggregated wind turbine model.

7.6 Conclusion

In most cases of short-term stability studies, a wind farm consisting of DFIG wind turbines can be sufficiently represented by a single equivalent unit. Accuracy of a single equivalent unit becomes relatively poor only in the case of a fast speed controller and large power output discrepancies among wind turbines in a wind farm. In such a case, the wind farm can be suitably represented using the cluster method. In all cases investigated in this chapter, the advantage of using the compound representation is

not convincing. Despite increased complexity, the compound model cannot overcome model inaccuracy associated with the non-linearity of the speed controller. The wind farm should be modeled using the cluster representation if wind gust effects are included in a medium- and long-term stability study.

Chapter 8

Full Converter Wind Turbine

This chapter describes detailed models of various FCWT components, controls and FRT schemes. The importance of these components and controls in characterizing FCWT model responses is examined. Finally, a proposed model of an FCWT for power system stability studies is presented.

8.1 Introduction

More stringent grid codes currently require wind turbines to have high immunity against grid faults. In addition, wind turbines that are able to provide more reactive power support are increasingly preferred. These features can be found in a full converter wind turbine (FCWT) concept. For these reasons, FCWTs are increasingly penetrating the market.

Compared to other alternatives, the FCWT concept offers several advantages. First, decoupling between the grid and the generator minimizes the effects of a grid fault from propagating to the generator, and therefore provides better fault response. Second, the full size generator-side converter facilitates a large operating speed range for the turbine, which improves wind turbine power performance. Third, the full size grid-side converter gives more space for the wind turbine to provide reactive power into the grid, particularly during a grid fault.

Nevertheless, this concept poses some disadvantages. One of the disadvantages concerns converter losses. Since the entire output power passes the converter, the electrical losses due to the converter are higher than in a DFIG wind turbine [101]. Another concern is related to the high investment cost of the full converter although this cost trend is decreasing.

A conceptual schematic of an FCWT is given in Fig.Fig. 8.1. The turbine concept consists of a generator which is interfaced directly to the grid via a back-to-back converter. The generator can be made of a synchronous generator, with or without a gearbox, or an induction generator with a gearbox. The converter is typically made of IGBTs with an operating voltage of 690 V [74]. A prototype of a converter for a multi-megawatt wind turbine up to 5 MW equipped with IGCTs operating at medium-voltage has been developed [128]. The grid-side converter, which mainly acts as a current-regulated, voltage-fed inverter, is able to provide reactive power support

to the grid.

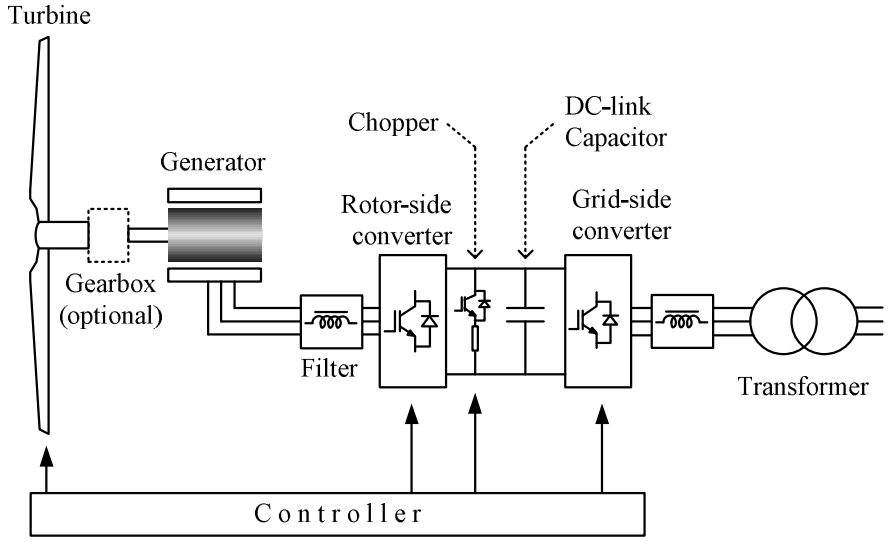

Figure 8.1. Schematic diagram of full converter wind turbine.

Various types of generators can be employed in an FCWT including a permanent magnet synchronous generator (PMSG), an electrically exited synchronous generator and an induction generator.

8.2 Full Power Converter Wind Turbine with PMSG

A permanent magnet synchronous generator does not require separate rotor excitation since the excitation is provided by the permanent magnets. Consequently, no rotor winding is needed. This substantially reduces excitation losses as well as increases the torque density of the generator [129]. The generator requires less maintenance due to the absence of rotor slip rings. This feature is very beneficial for offshore applications. Among wind turbine manufacturers which adopt this topology in their products are GE (2.5 and 3 MW series), Clipper, WinWind Multibrid and Vensys [130, 131, 132].

8.2.1 PMSG model

In the PMSG model, the flux is assumed to be sinusoidally distributed along the air gap and no damping winding is considered. The mathematical equations are constructed by aligning the d-component of machine vectors to the rotor flux. Voltage equations of the machine have the following form

$$v_{sd}^r = R_s i_{sd}^r - \omega_r \psi_{sq}^r + \frac{d\psi_{sd}^r}{dt} \tag{8.1}$$

$$v_{sq}^r = R_s i_{sq}^r + \omega_r \psi_{sd}^r + \frac{d\psi_{sq}^r}{dt} \tag{8.2}$$

with the stator flux components obtained from

$$\psi_{sd}^r = X_{sd} i_{sd}^r + \psi_{pm}^r \tag{8.3}$$
$$\psi_{sq}^r = X_{sq} i_{sq}^r \tag{8.4}$$

where v_{sd}^r and v_{sq}^r are the d and q components of the terminal voltage vector, respectively; i_{sd}^r and i_{sq}^r are the d and q components of the stator currents, respectively; R_s is the stator resistance; X_{sd} and X_{sq} are the q and q components of the stator reactances, respectively, and ψ_{pm}^r is the permanent magnet flux linkage. Superscript r indicates that the corresponding variable refers to the rotor flux reference frame.

The electromagnetic torque of PMSG can be expressed as

$$T_e = i_{sq}^r (i_{sd}^r (X_{sd} - X_{sq}) + \psi_{pm}^r). \tag{8.5}$$

For a non-salient pole machine, the stator inductances X_{sd} and X_{sq} can be assumed to be equal. Consequently, the d-component of the stator current i_{sd}^r does not influence the electromagnetic torque.

8.2.2 Generator-side controller

Typically, the generator-side converter regulates generator speed and power [133, 134, 7]. Alternately, the converter can be employed to control dc-link voltage [13, 135]. In this study, the first control method is chosen. In parallel with one of these two controller alternatives, the converter can be used to control the reactive power exchange with the generator. Fig. 8.2 provides a block diagram of the controller.

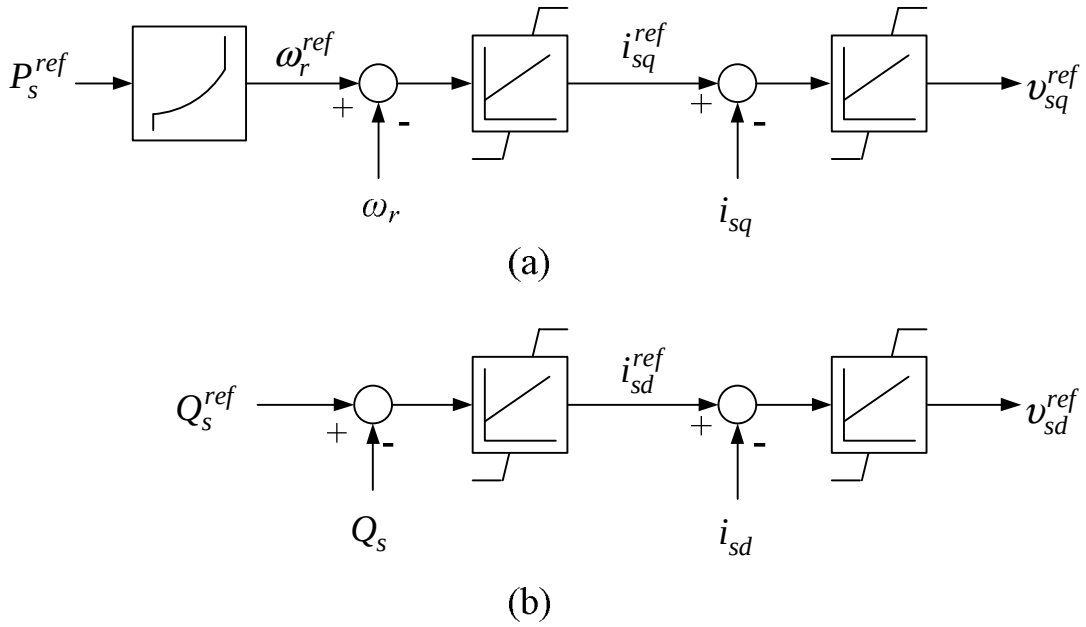

Figure 8.2. Permanent magnet synchronous generator-side converter control block diagram.

The controller is realized using the vector control method, in which the d-axis is aligned to the rotating stator flux. Using this control method, various control strategies can be implemented as described in the following [135].

Full torque control

In the full torque control strategy, the d-component of the stator current is always set to zero. For the purpose of discerning the underlying control mechanism, a simplified representation of a round pole PMSG as given in Fig. 8.3 is utilized. This representation is constructed by assuming that the stator resistance can be ignored. The internal voltage source behind an impedance is given as the sole function of the permanent magnet flux and rotor speed.

$$\vec{E} = j\omega_r \vec{\psi}_{pm} \tag{8.6}$$

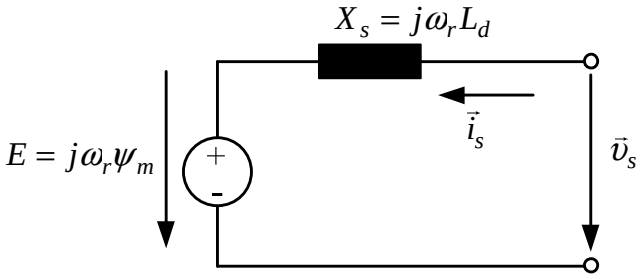

Figure 8.3. Single phase equivalent circuit a simplified round pole PMSG.

A phasor diagram of this control strategy can be illustrated as shown in Fig. 8.4.a.

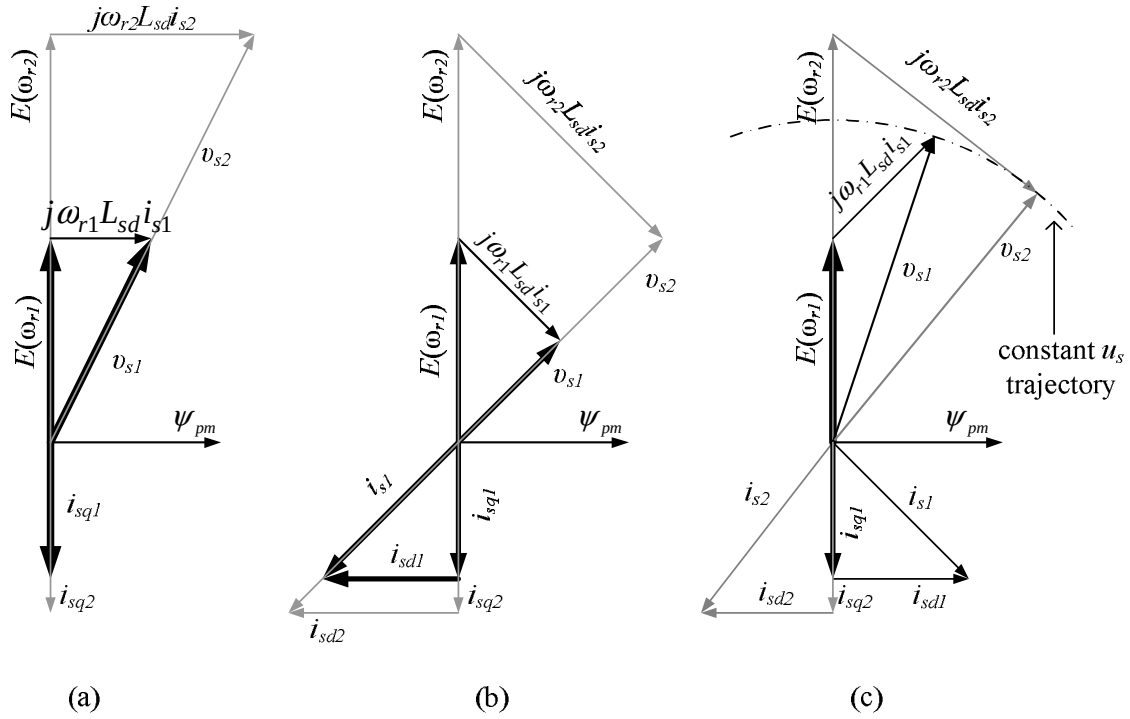

Figure 8.4. Phasor diagrams of different generator-side converter control strategies: (a) pure torque control, (b) constant reactive power, (c) constant stator voltage. A low speed operating point is indicated by black vectors and a high speed operating point is indicated by grey vectors.

The notations in the figure are as follows:

v_{s1},v_{s2}	the stator voltage vector at low and high speed, respectively
i_{s1},i_{s2}	the stator current vector at low and high speed, respectively
i_{sd1},i_{sd2}	the d-component of the stator current at low and high speed, respectively
i_{sq1},i_{sq2}	the q-component of the stator current at low and high speed, respectively
ω_{r1},ω_{r2}	the rotor speed at low and high speed, respectively
$E(\omega_{r1})$,$E(\omega_{r2})$	the back emf as function of rotor speed at low and high speed, respectively
L_{sd}	the d-component of the stator inductance
ψ_{pm}	the permanent magnet flux vector

Unity power factor

In a unity power factor strategy, the q-component of the stator current is regulated to achieve zero reactive power flow at the stator terminal. Fig. 8.4.b shows a phasor diagram of this strategy.

Constant stator voltage

The purpose of a constant stator voltage strategy is to maintain constant stator voltage by controlling the converter reactive power exchange between the generator and the converter. Fig. 8.4.c. provides a phasor diagram representation of this strategy.

Fig. 8.5 illustrates a comparison of the different control methods using dynamic simulations. The generator parameters used in the simulations are given in Table 8.1. In the simulations, the initial wind speed was 7 m/s. At t=1 wind speed increased to the rated value (12 m/s) within 4 seconds. This resulted in an increase in generator speed from 0.78 pu to 1 pu. As seen in the figure, the stator voltage in the pure torque control strategy jumped from 1.1 pu to 1.45 pu, however stator current can be maintained well below 1 pu. In the constant stator voltage strategy, the stator voltage is maintained at a constant level at the expense of high stator current. The constant reactive power strategy gives a compromised result in comparison with the other strategies.

8.2.3 Converter losses

The converter losses can be distinguished into two parts, i.e. conduction losses and switching losses. The losses model can be approximated using a polynomial expression [101]

$$P_{cl} = pi_g^2 + qi_g \tag{8.7}$$

where i_g is the generator current. The constant p is a constant determined by the internal resistance of the valves, and q is dependent on the constant voltage drop across

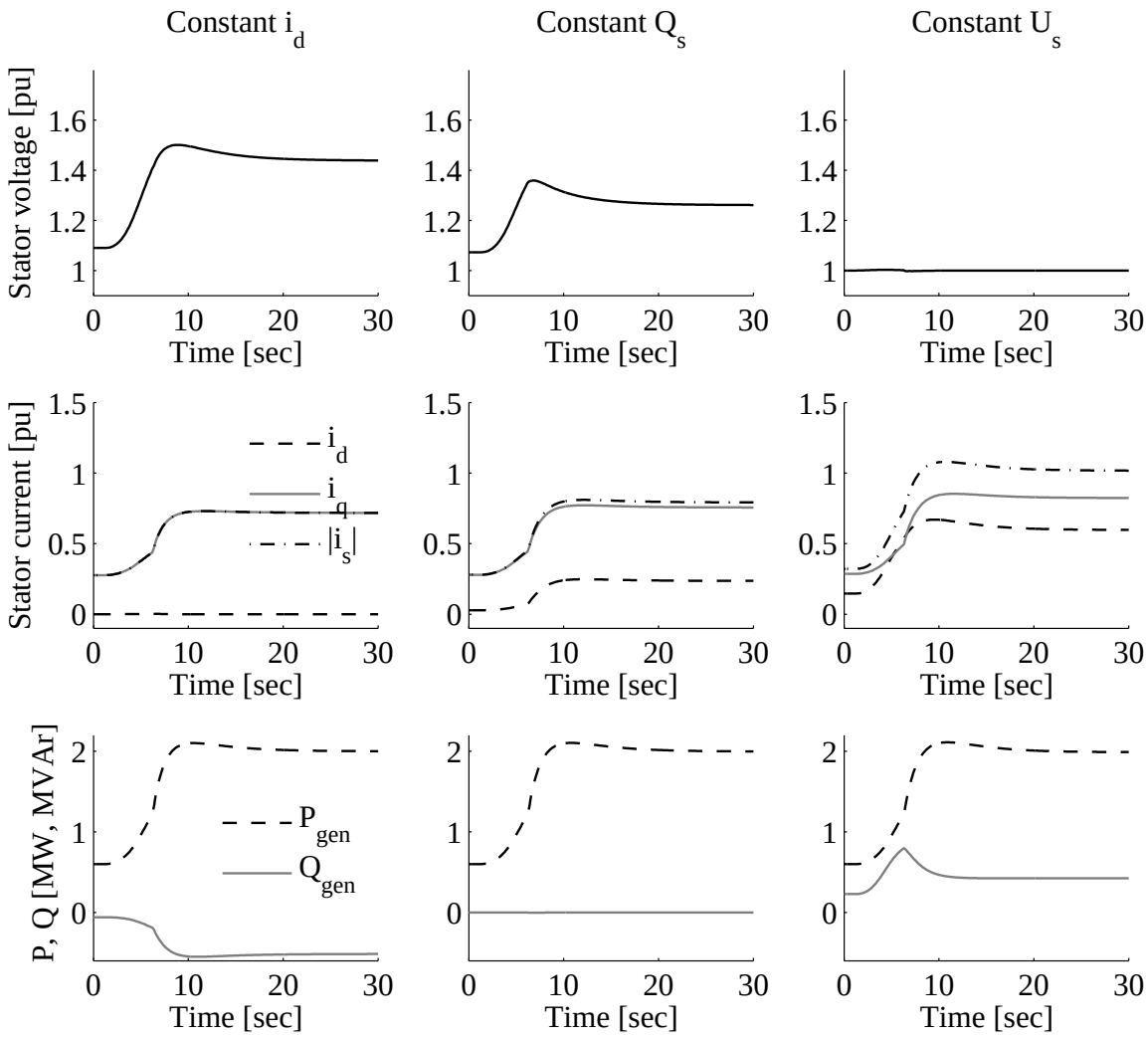

Figure 8.5. Comparison of different generator-side converter control strategies.

the valves. The converter losses normally account for 2 percent of the total input power at full power operating conditions [101].

8.2.4 Dc-link and grid-side controller

Fig. 8.6 shows a single line diagram of the dc-link and grid-side converter circuit. The grid-side converter equations expressed in the dq-components aligned with the grid voltage vector can be written as

$$v_{gd} = R_g i_{gd} + L_g \frac{di_{gd}}{dt} - \omega_e L_g i_{gq} + v_{cd} \tag{8.8}$$

$$v_{gq} = R_g i_{gq} + L_g \frac{di_{gq}}{dt} + \omega_e L_g i_{gd} + v_{cq} \tag{8.9}$$

where R_g and L_g are the grid filter resistance and reactance, respectively, i_{gd} and i_{gq}

Table 8.1. PMSG Parameters.

Parameters	Values	Units
Rated power	2	MW
Rated voltage	0.69	kV
Base frequency	50	Hz
R_s	0.01	pu
X_{sd}	0.8	pu
X_{sq}	0.5	pu
Permanent magnet flux	1.4	pu
Total inertia constant ($H_g + H_t$)	3	s

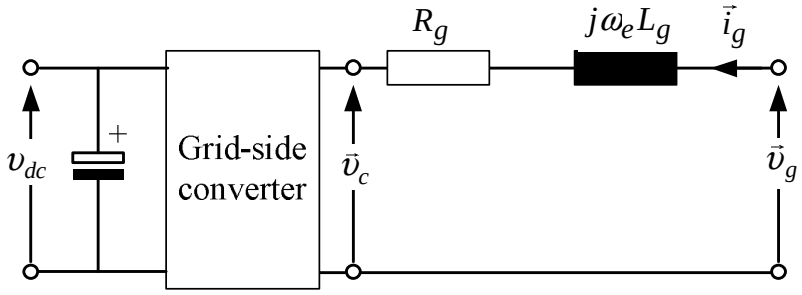

Figure 8.6. Single line diagram of dc-link and grid-side converter.

denote the grid current vector components, v_{gd} and v_{gq} denote the grid voltage vector components, v_{cd} and v_{cq} denote the converter voltage vector components.

Normally, the grid-side converter is assigned to maintain the dc-link voltage level and reactive power injection into the grid [133, 134, 7]. Otherwise the grid-side converter can also be used to control the active power of the wind turbine [13, 135]. An independent control of active power or the dc-link voltage on one side, and reactive power on the other side, can be realized using a vector control aligned with the grid voltage vector.

The dynamics of the dc-link can be expressed as

$$\frac{dv_{dc}}{dt} = \frac{P_{gen} - P_c}{Cv_{dc}} \tag{8.10}$$

where P_{gen} and P_c are the generator and grid-side converter active power, respectively; C is the dc-link capacitance. A block diagram of a grid-side converter is shown in Fig. 8.7.

8.2.5 Drive train

The drive train model of an FCWT supplied with a gearbox is identical to that of other types of wind turbines. However, a full power converter topology provides the potential to apply a gearless drive-train, which results in an increase in shaft stiffness. It should be noted, however, that elimination of the gearbox will not reduce torsional oscillations caused by turbine blades and the wind turbine mechanical shaft. This is particularly

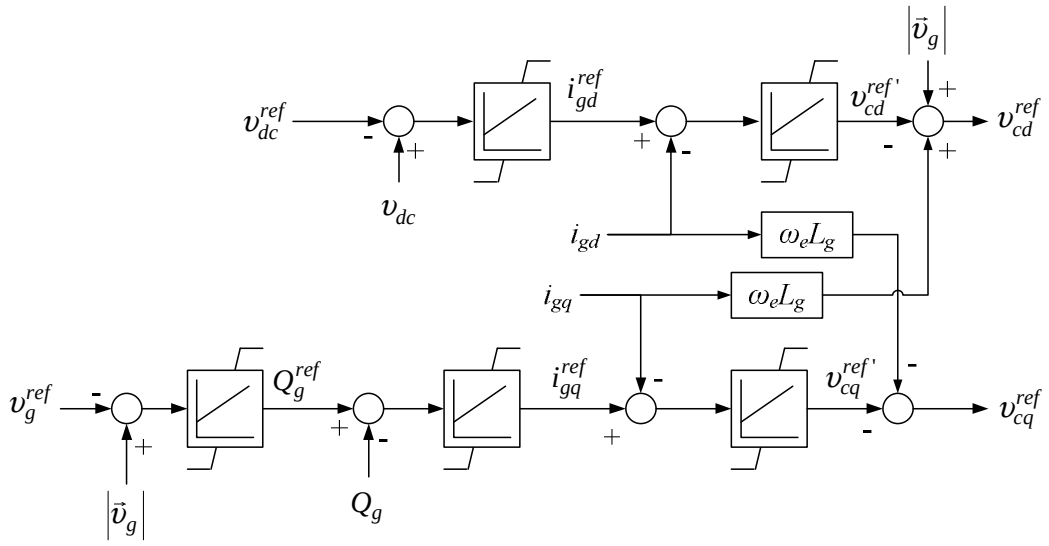

Figure 8.7. Block diagram of the grid-side converter control.

relevant if the contribution of blade flexibility (edgewise blade bending) in the torsional oscillations is considered to be significant, such as reported in [52, 54, 55, 58].

Such a gearless drive train constitutes a low-speed generator. This type of generator requires a large number of poles and a larger rotor diameter. Electrically excited and permanent magnet synchronous generators are commonly employed for this type of configuration.

8.2.6 Aerodynamic model and pitch controller

The aerodynamic model is in fact the same as those in wind turbines with doubly fed-induction generators as described in section 5.2.5. The main purpose of the pitch controller is to limit generator speed and power output at rated value.

8.3 Full Converter Wind Turbine with Synchronous Generator

A synchronous generator with a radial air gap field and salient poles is commonly used for an FCWT. The wind turbine company Enercon is one of wind turbine manufactures that uses this generator topology in their wind turbine products [136].

The stator voltage equations of a synchronous generator represented in the rotor flux reference frame can be written as follows [137].

$$v_{sd}^r = R_s i_{sd}^r - \omega_r \psi_{sq}^r + \frac{d\psi_{sd}^r}{dt} \tag{8.11}$$

$$v_{sq}^r = R_s i_{sq}^r - \omega_r \psi_{sd}^r + \frac{d\psi_{sq}^r}{dt} \tag{8.12}$$

R_s denotes the stator resistance, ψ denotes the flux linkage, ω is the speed variable, v denotes the voltage and i denotes the machine current. Subscript s and r indicate the

stator and rotor quantities, respectively, d and q are the d-axis and q-axis components of a vector, respectively.

The rotor voltage equations are given by

$$v^r_{fd} = R_{fd} i^r_{fd} + \frac{d\psi^r_{fd}}{dt} \tag{8.13}$$

$$0 = R_{kd} i^r_{kd} + \frac{d\psi^r_{kd}}{dt} \tag{8.14}$$

$$0 = R_{kq} i^r_{kq} + \frac{d\psi^r_{kq}}{dt} \tag{8.15}$$

All electrical quantities are seen from the stator, and the currents are positive when entering the machine. The stator flux linkage equations are given as follows

$$\psi^r_{sd} = X_{sd} i^r_{sd} + X_{md}(i^r_{fd} + i^r_{kd}) \tag{8.16}$$

$$\psi^r_{sq} = X_{sq} i^r_{sq} + X_{mq} i^r_{kq} \tag{8.17}$$

$$\psi^r_{fd} = X_{fd} i^r_{fd} + X_{md}(i^r_{sd} + i^r_{kd}) \tag{8.18}$$

$$\psi^r_{kd} = X_{kd} i^r_{kd} + X_{md}(i^r_{sd} + i^r_{fd}) \tag{8.19}$$

$$\psi^r_{kq} = X_{kq} i^r_{kq} + X_{md} i^r_{sq} \tag{8.20}$$

where X is the reactance, subscripts f and k denote the variable associated with the machine field and damping windings, respectively.

A generator-side converter can be constructed in several configurations. One of the options is to use a diode rectifier. This option offers fewer converter losses, however it lacks generator power controllability. Controllability can be improved by adding a booster controller which regulates dc-link voltage by controlling the dc-link current [13]. As the rectifier cannot supply reactive power to the generator, generator excitation must be fully supplied through rotor excitation.

Another option is to use a self-commutated PWM converter for the generator-side converter. This option provides both active and reactive control capability over the generator.

8.4 Full Converter Wind Turbine with Induction Generator

Application of squirrel cage induction generators in FCWTs is not very common. Since rotor excitation is absent in a squirrel cage induction generator, machine excitation must be provided entirely by the stator. This leads to high reactive power consumption, which is one of the biggest tradeoffs in using an induction generator in an FCWT. Consequently, this topology requires an overated generator-side converter. However, lower cost, robust design and the low maintenance requirements of induction generators are among the attractive factors of utilizing this topology in wind turbine applications. This topology is used by Siemens-Bonus wind turbine manufacturer [138]

A model of an induction generator was described in section 3.2, therefore it will not be further explained here.

Induction generator control can be realized either by using a constant volts/hertz method or a vector control method [81]. The volts/hertz method is comparatively simple and widely used in induction machine control applications. However, this method has the disadvantage of slow response. In contrast, a vector control method is able to perform fast control dynamics. In this thesis, only the generator vector control method of induction is discussed.

Typically, the generator vector control is aligned with the rotor flux reference frame [139]. A block diagram of the controller is shown in Fig. 8.8.

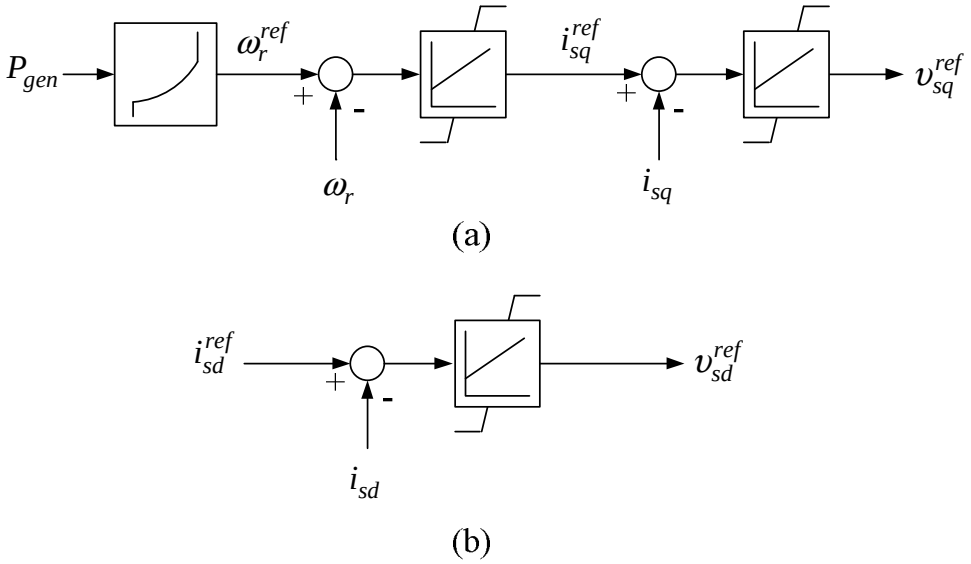

Figure 8.8. Cage induction generator-side converter control block diagram.

8.5 Fault Ride-Through Schemes

In this section, responses and measures to be taken by an FCWT when subjected to a grid fault are described. A fault that occurs on the grid near the wind turbine will cause a severe voltage dip on the grid-side converter terminal. The maximum amount of active power that can be transferred to the grid is proportional to the retained voltage on the grid-side converter terminal. Accordingly, the power transfer through the grid-side converter is immediately reduced. On the other hand, the power transfer from the rotor-side converter cannot be reduced quickly. As a consequence, the energy from the generator accumulates in the dc-link capacitor resulting in a rapid increase in dc-link voltage.

The maximum dc-link voltage for an FCWT may vary between 10 to 25 percent above the dc-link rated voltage [134, 7, 140]. In this report, a maximum dc-link capacitor voltage of 1.15 pu is considered to be reasonable. It should be noted that overly excessive dc-link voltage will destroy the capacitor and the converters. Therefore, before this happens, preventive action must be taken. A number of FRT schemes for an FCWT are proposed in [134, 7, 141, 142]. These alternatives include (1) an overdimensioned dc-link capacitor, (2) reducing power transfer from the generator into the dc-link converter, (3) employing a dc-link chopper/braking resistor to dissipate energy

in the dc-link capacitor, and (4) application of a serial compensator to reduce voltage drop on the grid-side converter terminal. The latter alternative, however, will not be discussed in this chapter since it is not specific for this topology.

8.5.1 Over-dimensioned dc-link capacitor

By employing a larger dc-link capacitor, more energy can be stored in the dc-link during a fault, thus reducing the risk of dc-link over-voltage. The required size of the capacitor is influenced by voltage dip magnitude and duration. The relation between maximum dc-link voltage, input/output power flow and dc-link capacitor size can be written as

$$\int (P_{gen} - P_c)\, dt = \frac{1}{2} C (v_{dc,max}^2 - v_{dc,rated}^2) \tag{8.21}$$

where $v_{dc,max}$ and $v_{dc,rated}$ are the maximum and rated dc-link voltage, respectively, C is the dc-link capacitance. P_{gen} and P_c are the generator and the grid-side converter power, respectively. For constant input power during a grid fault, the expression can be written as

$$P_{rated} \int \left(1 - F_o \frac{v_g(t)}{v_{dc,rated}}\right) dt = \frac{1}{2} C (v_{dc,max}^2 - v_{dc,rated}^2) \tag{8.22}$$

where v_g is the grid voltage and F_o is the over-rated factor of the grid-side converter.

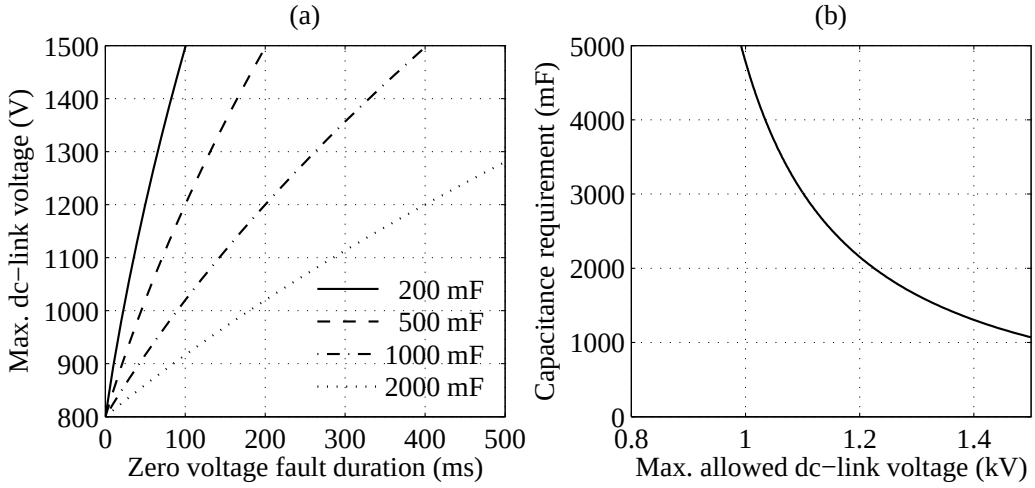

Figure 8.9. (a) Relation between dc-link capacitance value, zero voltage dip duration and the maximum dc-link voltage for 2 MW wind turbine, (b) Capacitance and maximum dc-link voltage requirement for 2 MW wind turbine with 11 percent overrated grid-side converter to fulfill FRT requirement stated in Svenska Kraftnät grid code.

Fig. 8.9.a illustrates the maximum dc-link voltage limit requirement as a function of zero voltage fault duration for different capacitance values for a 2 MW wind turbine with an 800 V dc-link voltage rating.

Fig. 8.9.b shows a more specific example of a relation between maximum allowed dc-link voltage and the capacitance requirement for a 2 MW wind turbine with an 800 V

dc-link voltage rating to ride-through the voltage profile stated in the Svenska Kraftnät grid code (see Fig. 2.4) with an 11 percent overrated grid-side converter ($F_o = 1.11$). It can be observed from the figure and the equation that the capacitance requirement is inversely quadratic with the maximum allowed dc-voltage.

Based on [143], the typical capacitor value for a 2 MW wind turbine can be calculated to be within 70 to 400 mF (55 to 270 μF per horsepower). Consequently, the capacitance requirement as illustrated in Fig. 8.9.b is considerably high. Even at 50 percent over-voltage, the capacitance requirement is still three times larger than the typical value considering that dc-link over-voltage is normally less than 20 percent.

8.5.2 Reduced generator power

By reducing the power inflow from the generator, the dc-link voltage increase can be reduced. This strategy can be realized in two different ways, i.e. (1) by reducing the aerodynamic torque by pitching the turbine blades, and (2) by reducing the generator electromagnetic torque by means of a generator-side converter.

Blade pitching

As suggested in [56], a pitch rate of 5-10°/s is typical for normal operation. During an emergency situation, a pitch rate of 10-20°/s is possible. A 10°/s pitch rate is used for a MW class GE wind turbine model as reported in [12].

However, even with a very fast pitch rate, a generator power reduction cannot be realized quickly. As seen in Fig. 8.10, with a pitch rate of 15°/s, it takes almost 2 seconds to reduce the generator power by 50 percent. As a consequence of power imbalance, the dc-link voltage rises excessively. Therefore, reducing the generator power solely by using a pitch controller is not sufficient to mitigate a dc-link overvoltage.

Electromagnetic torque reduction

Quick generator power reduction can be brought about by means of the generator-side converter. In a simple way, the generator-side converter can be deactivated once the dc-link voltage limit is violated [7]. The converter deactivation is identical to setting the generator power to zero. Another strategy is presented in [12] where the generator power reduction can be realized as a function of the converter terminal voltage. The new reference value for the generator power is defined by

$$P_{gen}^{\prime ref} = F_P P_{gen}^{ref} \tag{8.23}$$

where P_{gen}^{ref} is the reference power at normal operation and F_P is a factor that is given as a function of the grid-converter terminal voltage as shown in Fig. 8.11.

Fig. 8.12 shows the response of an FCWT subjected to an 0.8 pu voltage dip that lasts for 500 ms. The generator power quickly follows the power reference, which was set to 0.2 pu. As seen in the figure, this strategy is able to maintain the dc-link voltage below 1.2 pu. At the same time, the grid-side converter is able to continuously inject active power of 0.2 pu into the grid during the fault. Clearly, this strategy is beneficial since it can maximize power injection into the grid for a given residual voltage while reducing the risk of rotor overspeed.

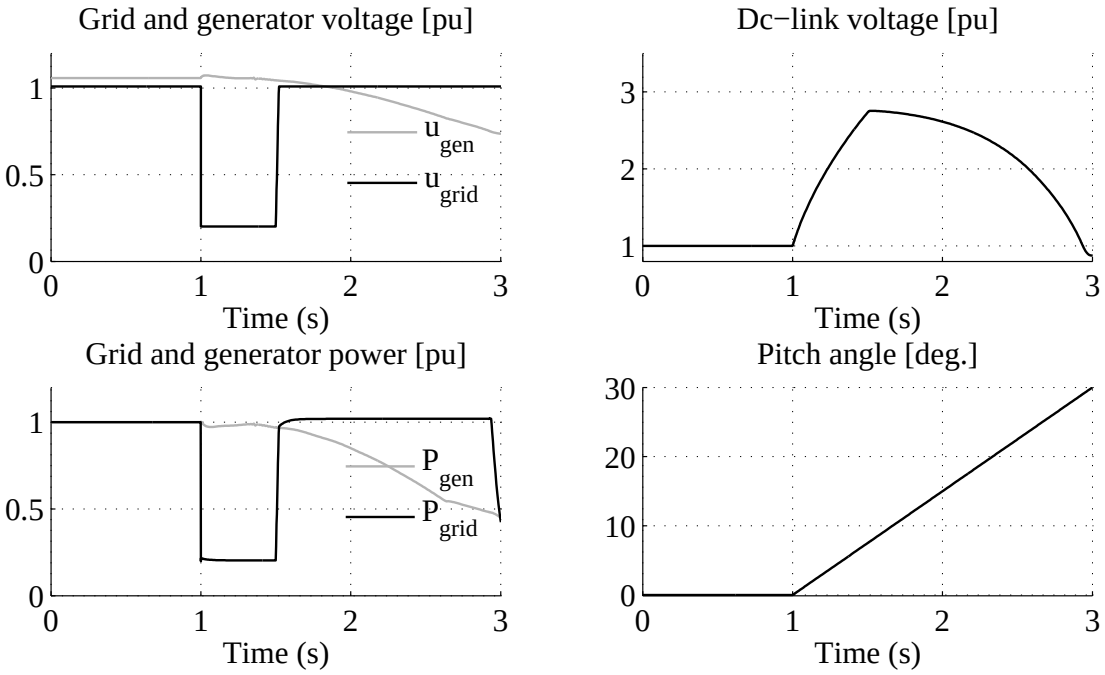

Figure 8.10. Fault response of wind turbine with full power converter using blade pitching strategy.

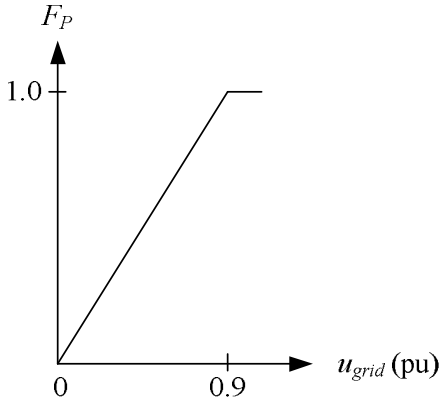

Figure 8.11. Power level factor used during grid fault.

After fault clearance, the dc-link voltage builds-up due to a power imbalance between the generator and the grid-side converter, as observed. By slightly overdimensioning the grid-side converter, this dc-link voltage build-up can be avoided.

Since the wind turbine drive train is modeled as a two-mass model, torsional oscillation can be observed clearly on generator speed and power. This oscillation is also reflected on the power output of the grid-side converter.

8.5.3 DC-link braking resistor

The excess of energy during a grid fault can be dissipated in a dc-link braking resistor as briefly introduced in section 5.2.3. The amount of power burned in the resistor is controlled by an electronic switch device (IGBT). The dc-link braking resistor can be

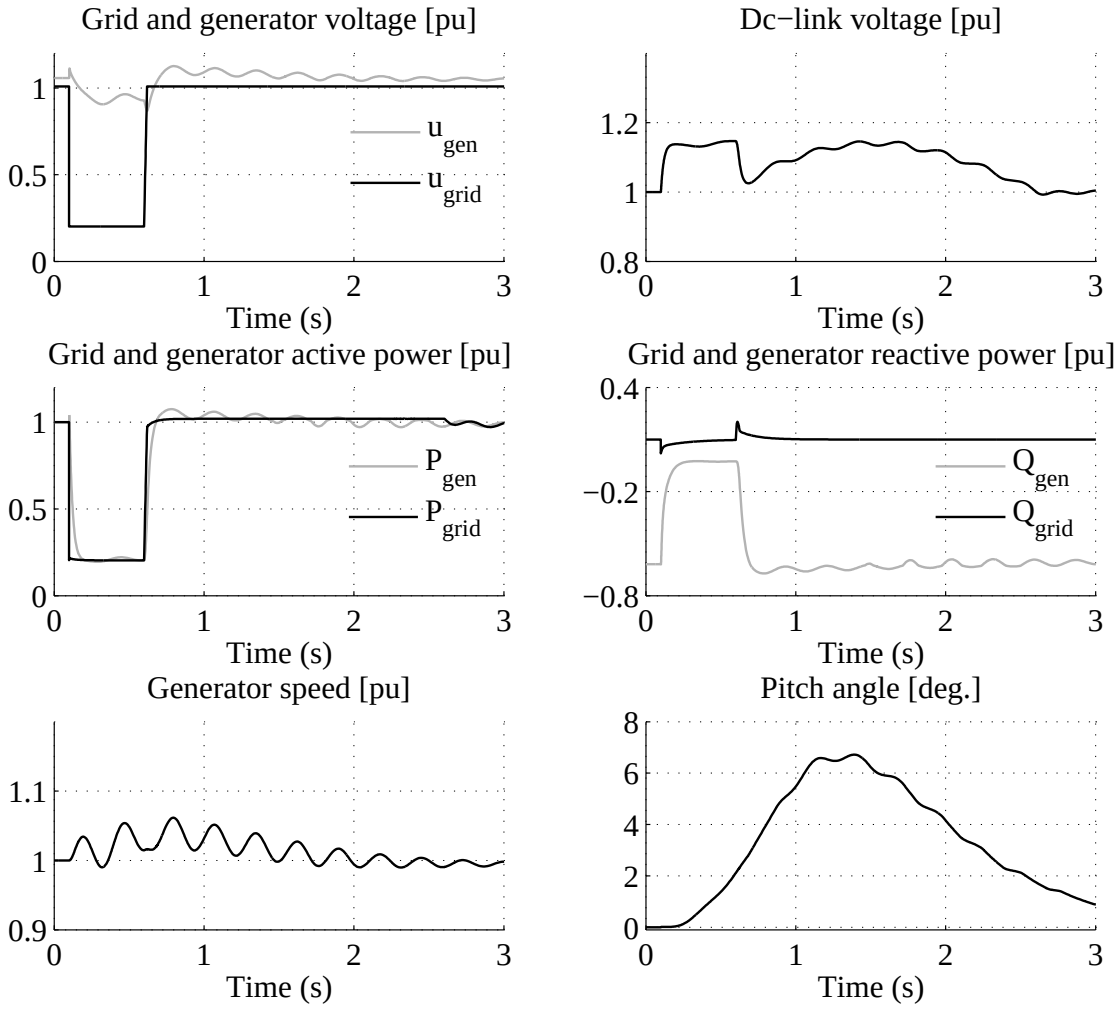

Figure 8.12. Fault response of wind turbine with full power converter using electromagnetic torque reduction strategy.

dimensioned to fully handle the entire energy dissipation during fault. Enercon is one of wind turbine companies that implements this strategy [144]. Alternately, the resistor can be designed to only handle partial power. Obviously, to be able to ride-through a severe fault, the latter option must be combined with other measures.

Full power braking resistor

The design of a full power braking resistor is dictated by voltage dip magnitude and duration. Fig. 8.13 shows the response of an FCWT using a full power braking resistor. The fault was simulated as a voltage dip of 80 percent for 500 ms. As shown in the figure, the generator terminal is virtually unaffected by the grid fault. In other words, no fault dynamic occurs on the generator-side converter. Moreover, the generator power can be constantly maintained. Therefore, continuous active power exchange with the grid can be realized during the fault. The amount of the grid power exchange is proportional to the grid-side rating and the retained grid voltage, which are 1 pu and 0.2 pu, respectively, in this case. When the fault is cleared, the generator can be

quickly restored to the rated value without causing significant transients. It is worth noting that the dc-link voltage decay is somewhat slow due to the limited rating of the grid-side converter. In terms of transient performance, this can be considered as the most advantageous option for an FRT strategy.

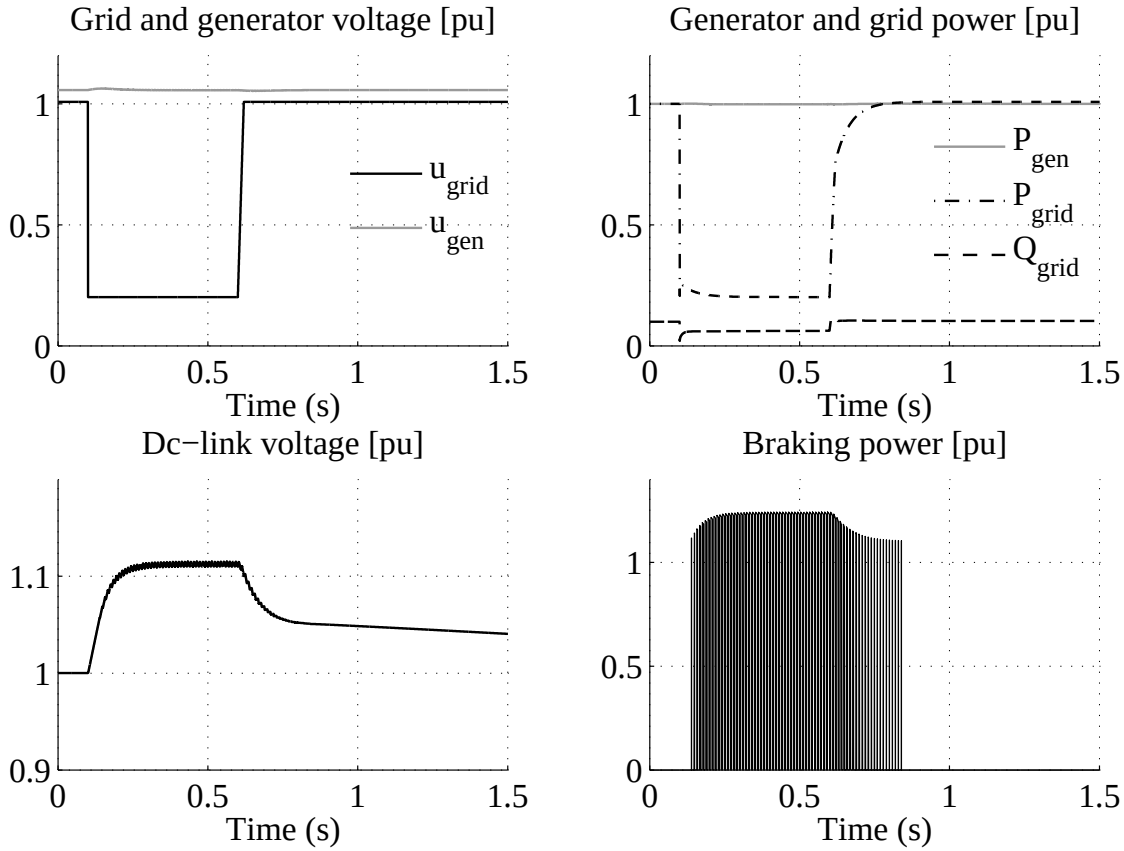

Figure 8.13. Fault response of wind turbine with full power converter using full power braking resistor.

Partial power braking resistor

For the case of a partial power braking resistor, the chopper switch must be turned-off and the generator-side converter must be deactivated once the resistor reaches its heat limit.

Alternately, a partial power braking resistor with limited capability of dissipating energy can be used in combination with other measures, such as a power inflow reduction from the generator. A simplified model of a braking resistor with limited energy capacity is reported in [12]. This model, however, does not include energy dissipation of the resistor and thereby the model is not valid for repetitive events.

In this report, energy dissipation of braking resistor is modeled in such a way that it permits the model to be used more realistically in long and severe contingencies. In order to include a heat capacity limit on the braking resistor, the energy balance of the resistor first needs to be identified. The total energy converted by the resistor is given by

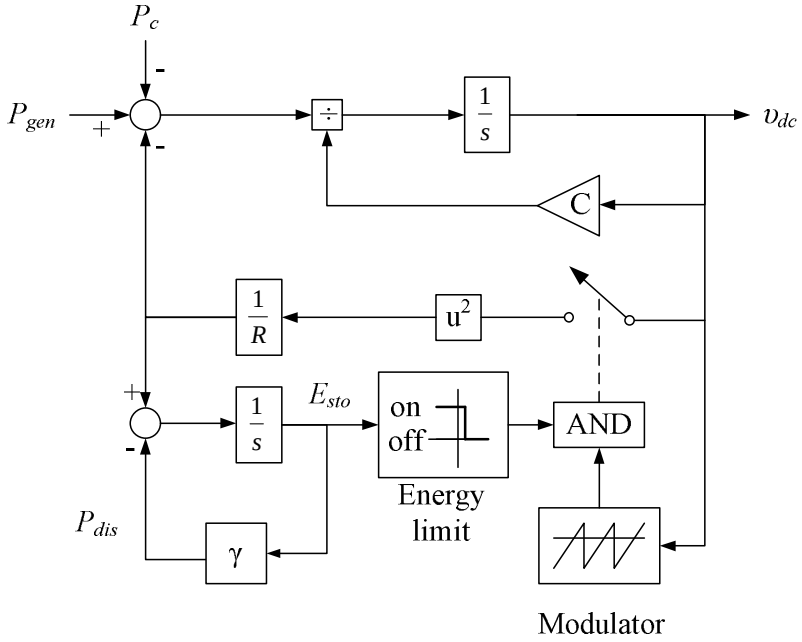

Figure 8.14. Block diagram of dc-link braking resistor.

$$P_{sto} = P_{in} - P_{dis} \tag{8.24}$$

where P_{sto} is the heat power stored in the resistor, P_{in} is the electrical power converted by the resistor, P_{dis} is the heat power dissipated from the resistor. By assuming a constant ambient temperature and assuming that the initial resistor temperature is the same as the ambient temperature, the stored energy in the resistor can be expressed as

$$E_{sto} = \int P_{sto}\, dt = Cm\,(T_R - T_a) \tag{8.25}$$

where, C is the specific heat of the resistor, m is the mass of the resistor, T_R is the resistor temperature and T_a is the ambient temperature. The dissipated energy can be written as

$$P_{dis} = h_c A\,(T_R - T_a) \tag{8.26}$$

where, h_c is the heat transfer coefficient and A is the surface area of the resistor. Thus, the energy balance equation can be simplified into

$$E_{sto} = \int P_{in} - \gamma E_{sto}\, dt \tag{8.27}$$

where γ is defined by

$$\gamma = \frac{hA}{Cm} \tag{8.28}$$

One way of controlling the braking resistor is to employ a hysteresis control method [145]. Alternately, the braking resistor can be controlled using a pulse width modulation method [146]. A schematic diagram of a braking resistor that includes an energy dissipation model is presented in Fig. 8.14.

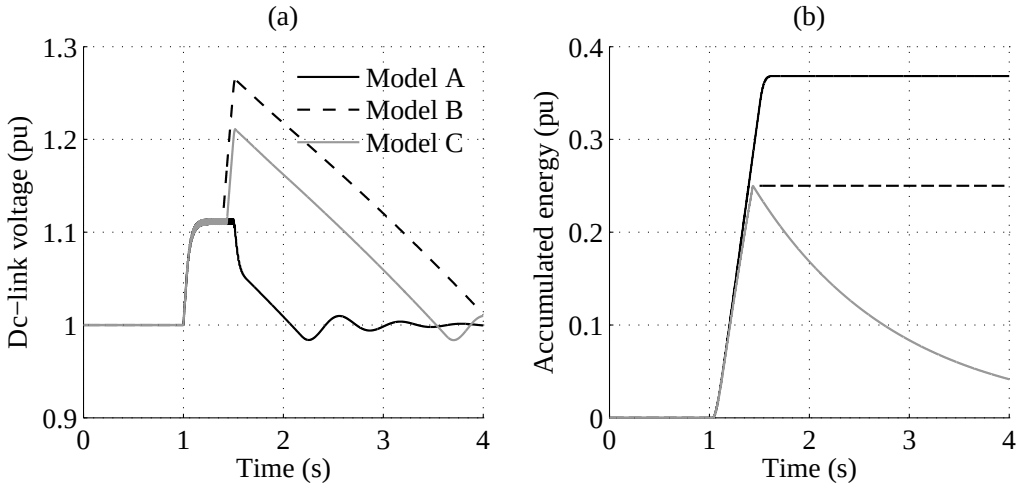

Figure 8.15. Fault response of different braking resistor models: (1) without energy limitation (Model A), (2) with energy limitation (Model B), and (3) with energy limitation and dissipation (Model C).

Fig. 8.15 shows the responses of different braking resistor models. An ideal braking resistor without energy limitation is denoted Model A in the figure. In the model with energy limitation, denoted Models B and C in the figure, the resistor cannot fully dissipate excessive energy in the dc-link capacitor. This results in an excessive increase in dc-link voltage. However, Model C provides less conservative results than Model B.

8.5.4 Control mode alteration

As reported in [147, 148, 142], the immunity of an FCWT against grid faults can be improved by swapping the converter functions, meaning that the grid-side converter acts as the master control, while the generator-side converter acts as the slave control. Accordingly, the main objective of a grid-side converter operation is to maximize active power injection into the grid for a given grid voltage level, while the generator-side converter is responsible for maintaining a constant dc-link voltage during a fault.

A comparison between the conventional control and the proposed control is shown in Fig. 8.16. Initially, the wind turbine operates using a conventional control mode where the grid-side converter is the slave control and the generator-side converter is the master control. A voltage dip occurs at t=0.1 s for 500 ms. As the severe voltage dip is detected, the control mode is altered, in which the grid-side converter is assigned as the master control, while the generator-side converter becomes the slave control. As a result, the grid-side converter active current reference is set to the maximum value. At the same time, the generator-side converter reduces generator power to keep the dc-link voltage at a predefined value. The reduction in generator power results in rotor acceleration. Rotor over-speed can be avoided owing to actions of the pitch controller, which reduces aerodynamic torque.

When the fault is cleared, the control mode is switched back to normal. In order to be successfully implemented, this strategy requires quick transition between control modes.

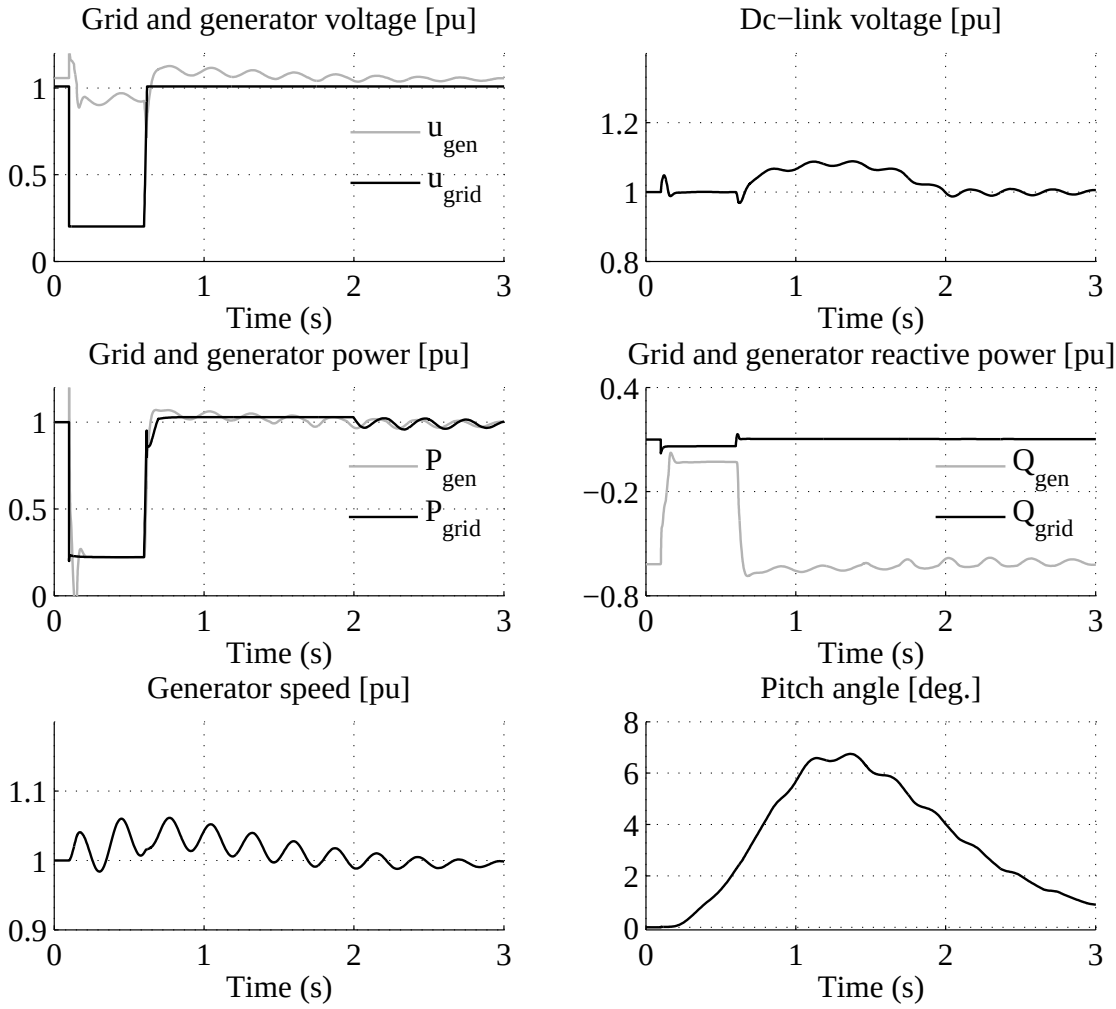

Figure 8.16. Fault response of wind turbine with full power converter using control mode alteration.

8.5.5 Combined strategy

As each FRT option has its own limitation, it is usually implemented in combination with other options. Different FRT strategy combinations for an FCWT are described in the following.

Combined strategy 1

In [7], the FRT strategy includes a coordinated control between the grid-side and generator-side converters. Once the dc-link voltage exceeds the limit, the generator-side converter is blocked. In this situation, the grid-side converter is responsible for reducing the dc-link voltage to its rated value. After the dc-link voltage returns to its rated value, the grid-side converter maintains a zero power exchange with the grid regardless of grid voltage. In this strategy, the pitch control role is to limit generator speed around nominal value. Fewer components due to the absence of a dc-link chopper is the benefit of this strategy. The disadvantage of using this strategy is, whenever the dc-link protection is activated, the power injection during fault becomes zero regardless

of the grid voltage level.

Combined strategy 2

In [134], the combination strategy includes the use of a dc-link chopper together with a pitch controller. According to this strategy, first, the braking resistor acts upon the dc-link voltage build-up. If the fault occurs for a short period, all excess energy can simply be diverted to the braking resistor. When the fault lasts for a longer period, which may risk the resistor because of its limited thermal capability, the pitch controller must be activated to reduce aerodynamic torque and hence generator power. Once the fault is cleared, the pitch angle returns to its pre-fault value. At the same time, the dc-link chopper maintains the power balance of the dc-link voltage.

The action response of this combined strategy is dictated by the blade pitch angle response, which is considerably slower than the dynamics of the dc-link. This eventually requires a braking resistor with large heat capacity.

Combined strategy 3

In [12], the FRT strategy is performed by combining the actions of the braking-resistor and the generator control. Similar to the previous strategy, for a short fault duration, the excess of power on the dc-link is dissipated entirely in the braking resistor. The dissipated power in the braking resistor decreases when the accumulated energy in the braking resistor reaches its maximum limit. Consequently, generator power must be reduced to maintain the energy balance in the dc-link.

Combined strategy 4

In [135], the FRT strategy mainly incorporates control mode alteration and a dc-link chopper. The pitch controller is only activated in the event of generator overspeed.

8.6 Model Representation for Power System Stability Studies

There are different views of representing an FCWT in power system studies. Some of the disputed aspects of modeling an FCWT for system stability studies are discussed in the following.

8.6.1 Power system interface

An FCWT can reasonably be represented as a current source due to the fact that current controller response is faster than the transient dynamics of the power system. However, one objection is that this representation may be problematic for simulating faults close to the converter terminal because the active and reactive currents cannot be distinguished from each other [13]. Accordingly, a voltage source representation of an FCWT is suggested. However, the worst case fault scenario for a wind farm in a power system stability study is typically applied to the PCC rather than to the

terminal of the converter. Consequently, the grid fault will never been too close to the converter terminal since there is a relatively high impedance between the PCC and the converter terminal due the presence of low and medium transformers. Therefore, the representation of a wind turbine as a current source can be justified.

8.6.2 DC-link and grid-side model

A constant dc-link voltage by assuming a very large dc-link capacitance and an ideal dc-link voltage controller is suggested in [13]. Grid power is assumed to be a direct function of generator power, taking into account constant converter losses.

As a dc-link capacitor is normally designed for a much shorter time constant than the fault duration stated in grid-codes, it can be assumed that the dc-link capacity is zero. This means that during a grid fault, the power transfer through the grid-side converter is limited as a direct function of grid voltage. The excessive power from the generator must be diverted by other means. This can be done by converting this excessive power into inertial energy in the form of turbine rotor rotation. Alternately, this excessive power can be dissipated in the braking resistor.

8.6.3 Drive-train model

According to in [149], drive train oscillations can be omitted for two reasons. First, the oscillations among wind turbines in a large wind farm are subjected to statistical filtering. Second, the damping from the converter is assumed to eliminate these oscillations. In contrast, it is suggested in [13] to use a two-mass drive train model in order to reflect torsional oscillations in a wind turbine drive train. This argument is supported by the simulation results discussed in the previous section where torsional oscillations are clearly observed in the grid-side power output.

8.6.4 Generator and generator-side converter model

In [149], the generator and its converter are simply represented as an algebraic expression that is subjected to power limitation during a fault event. A similar approach is also reported in [12]. By contrast, in [13] the generator is represented as a full machine representation with the stator transient omitted. The same approach is also adopted in [7], whereas it is recognized that generator excitation is not entirely influential in stability studies.

A detailed generator representation obviously provides more accurate results of generator response during a fault. However, a detailed generator representation does not improve the grid response accuracy of an FCWT model. Moreover, grid-side responses of a wind turbine do not differentiate the type of generator, as described below.

Fig. 8.17 shows the fault responses of an FCWT with a permanent magnet synchronous generator (left-hand column) and an induction generator (right-hand column). The two figures in the first row show that the stator voltage responses of the two generators are characterized by generator type. The active power and speed responses of the two generators are similar. In the two configurations, shaft torsional oscillations are visible in generator voltage, active power, reactive power and speed.

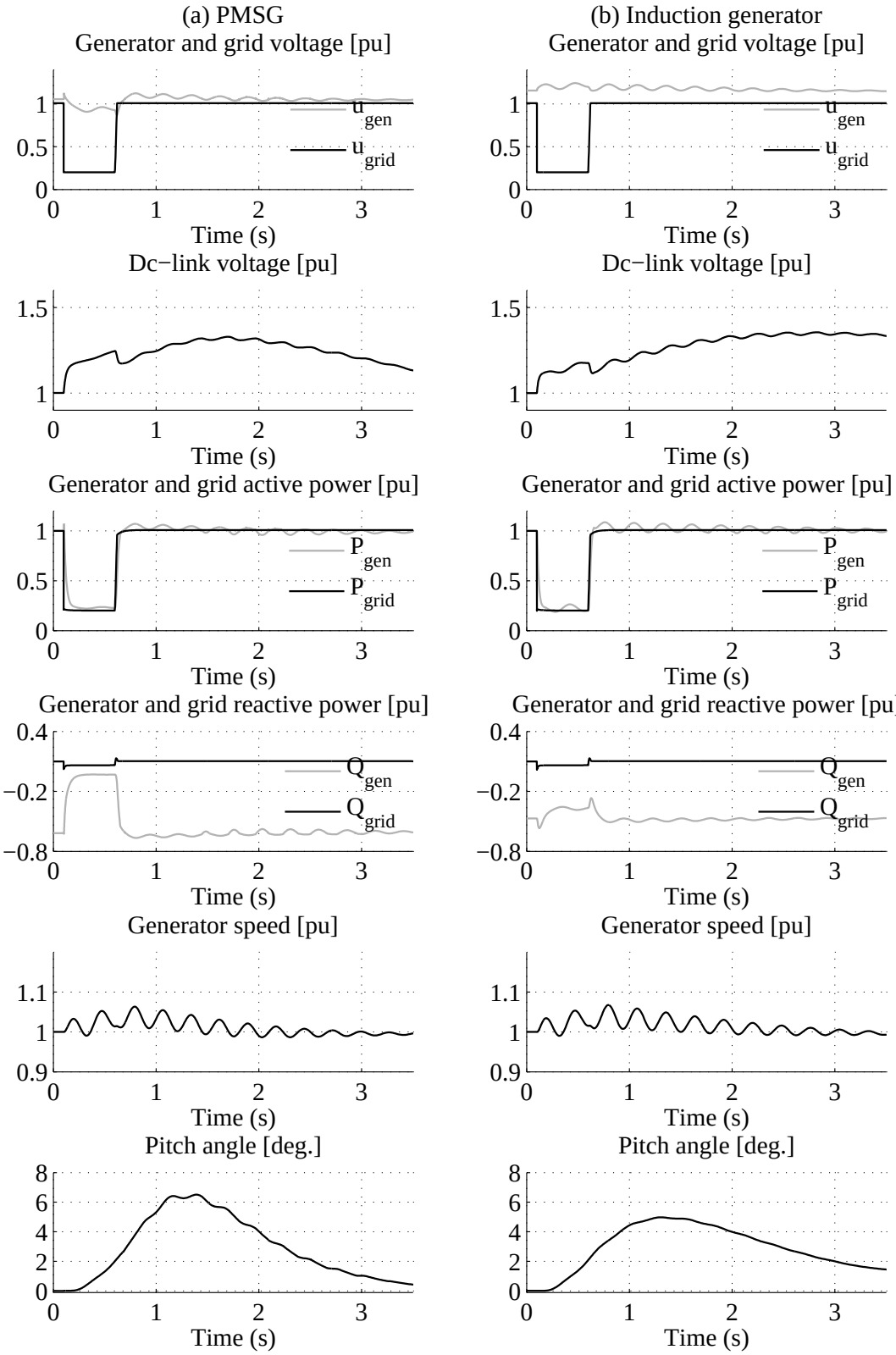

Figure 8.17. Fault response of FCWT at full power operating condition with different generator types: permanent magnet generator (left-hand column) and induction generator (right-hand column).

The similarity in the dc-link voltage response is also noticeable. This similarity indicates that the FRT controller performances of the two generators are comparable in reducing active power during a grid fault. A noticeable difference is observed in the reactive power responses of the generators. However, the grid-side reactive power response is decoupled from the generator reactive power response. In fact, active and reactive power responses of the grid-side converter in the two configurations are the same.

It is worth noting that the similarity of the grid-side response is partially caused by controller saturation. In this case, the flat response of the grid power following a fault is due to the current limitation on the grid-side converter.

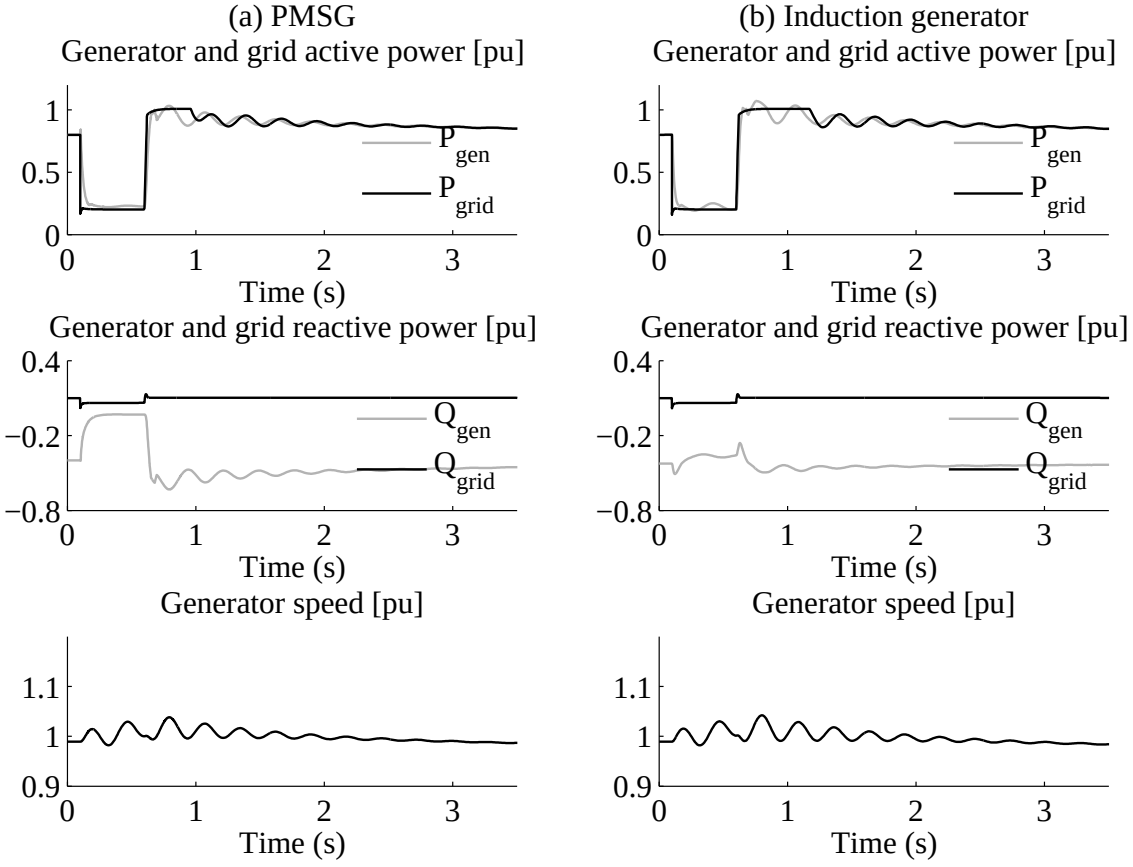

Figure 8.18. Fault response of FCWT at partial power operating condition with different generator types: permanent magnet generator (left column) and induction generator (right column).

Partial load response

As explained earlier, the grid response of a wind turbine during a full power operation is characterized by the saturation of the grid-side converter current controller. As a consequence, none of the generator dynamics can be observed on the grid-side converter output. Therefore, this section focuses on the responses of the wind turbine at partial load.

As seen in Fig. 8.18, the generator active power response is reflected on the grid-side converter output, whereas the reactive power of the generator and the grid-side converters remain decoupled. A slight difference was noticed on the power response following the fault where the turbine equipped with an induction generator experienced slightly longer grid-current saturation due to slightly higher accumulated generator power during the fault. However, in general, it can be concluded that the response of the wind turbines with different generator types at partial power operating conditions are similar.

Results also indicate that the generator active power control characterizes the active power response of the wind turbine. Consequently, the active power control of the generator must not be excluded from the model.

However, this condition is not valid if a full power braking resistor is used in the FRT scheme. This is because the generator is virtually unaffected by the grid fault, and thereby the generator can constantly supply active power to the dc-link while the grid-side converter is possible to maximize current injection into the grid. The grid response is exclusively characterized by the grid-side controller performance as shown in Fig. 8.19.

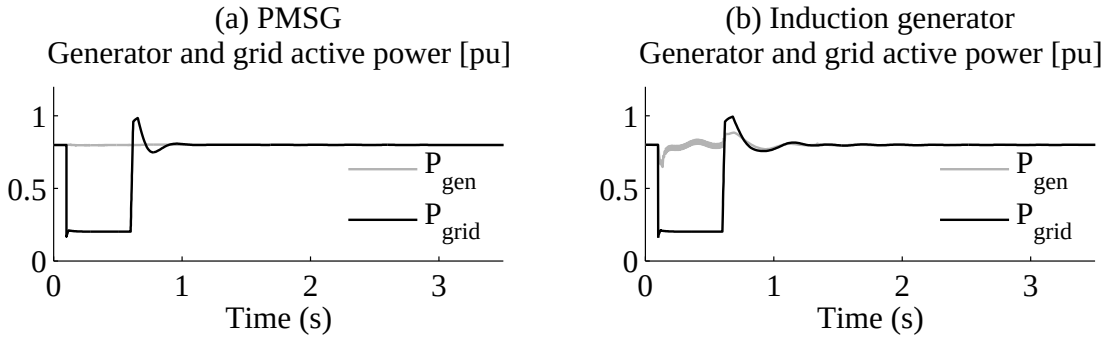

Figure 8.19. FRT response of FCWTs at partial power using a full power braking resistor equipped with a permanent magnet generator and an induction generator.

8.6.5 Proposed FCWT model

The following principles were used in developing the proposed model for an FCWT for stability studies:

1. There is no significant need for a detailed model of the generator electrical part.
2. Only generator active power or speed control needs to be incorporated into the model.
3. Generator-side and grid-side converter reactive power responses are totally separate.

Based on the fact that the detailed generator model has no influence on grid-side response in the proposed FCWT model, the generator is sufficiently modeled as a controlled electromagnetic torque or active power source with a time lag. Thus,

this representation is independent of the selected generator type. The generator-side controller is represented by a PI-controller that solely controls the active power or electromagnetic torque of the generator. The generator reactive power controller can be omitted by assuming that reactive power responses on both converter sides are fully decoupled. Using this representation means that generator losses are neglected. A block diagram of the proposed generator and generator-side converter control models is presented in Fig. 8.20.

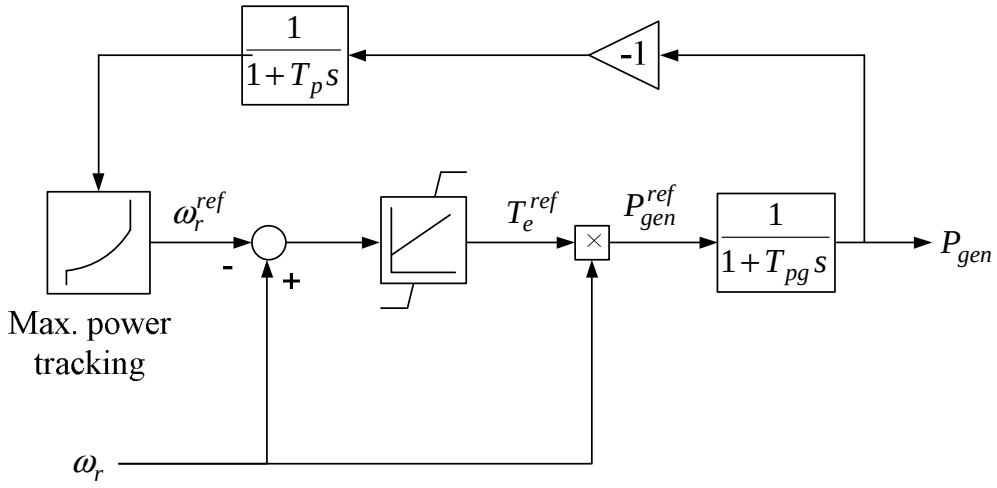

Figure 8.20. Simplified model of generator and its control.

Given that the dc-link capacitor is not too small, the dc-link model in detailed representation can be used in the proposed FCWT model, as shown in Fig. 8.21. It has been found that in order to avoid numerical problems in simulation, the dc-link capacitor size must be no less than 0.02 pu if a 10 ms simulation time-step is to be used. In this case, the base value for dc-link capacitance is defined by $C_{base} = (2P_{base})/v^2_{dc,base}$. The braking resistor can be modeled as a power source the values of which are proportional to the overvoltage in the dc-link (indicated by constant K_{BR} in Fig. 8.21). The dc-link voltage controller is modeled as a PI controller that regulates grid power injection. Simple time lags are introduced in the model for the purpose of modeling voltage and current controller time delays.

A two-mass drive train model is used in the proposed FCWT model for two reasons. First, the two-mass model provides more accurate drive train dynamic responses. Second, the two-mass model does not substantially reduce simulation efficiency. The aerodynamic and pitch controller are modeled as in the detailed model.

8.7 Model Benchmark

The network test system used in the benchmark simulations is given in Fig. 8.22. The wind turbine generator shown in the test system represents a single wind turbine equivalent of an aggregated model of a large wind farm consisting of 50x2 MW wind turbines. Internal wind farm cable impedances are neglected, while the wind turbine and platform transformers are lumped together into a single transformer. The lumped

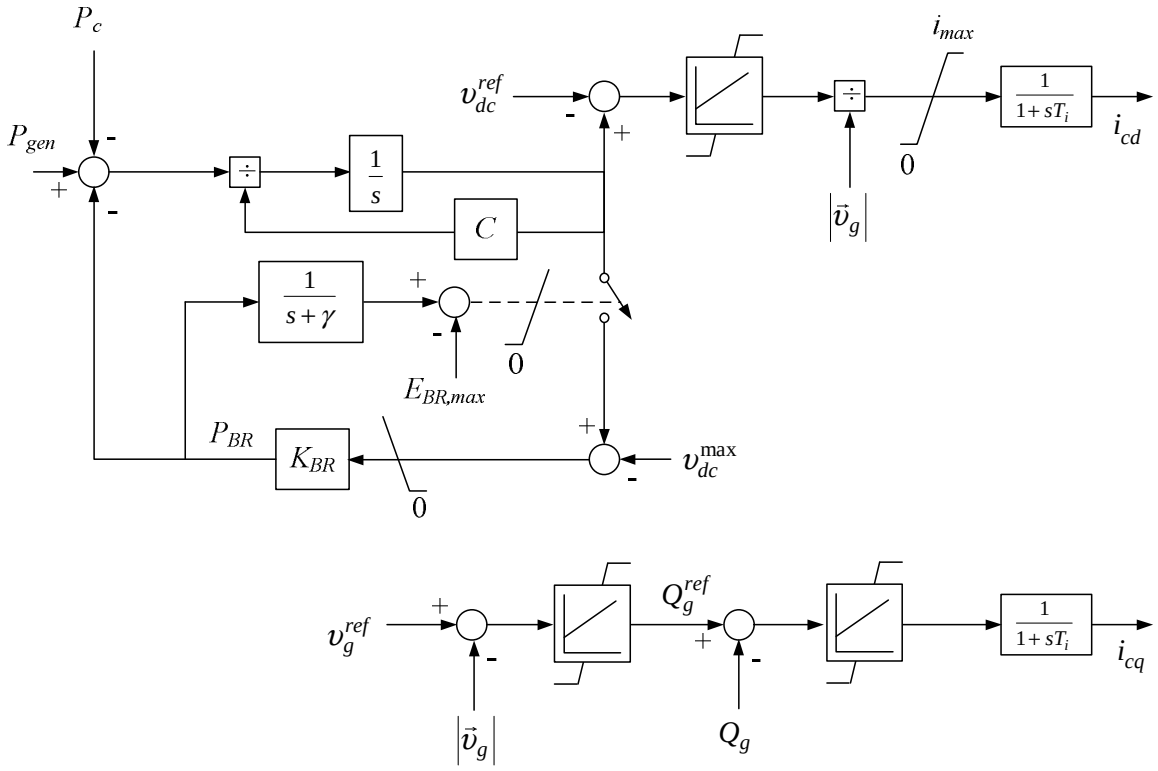

Figure 8.21. Simplified model of dc-link and grid-side converter.

transformer is rated 150 MVA. Each transmission line has an impedance of $0.04 + j0.4$ pu at a 100 MVA base.

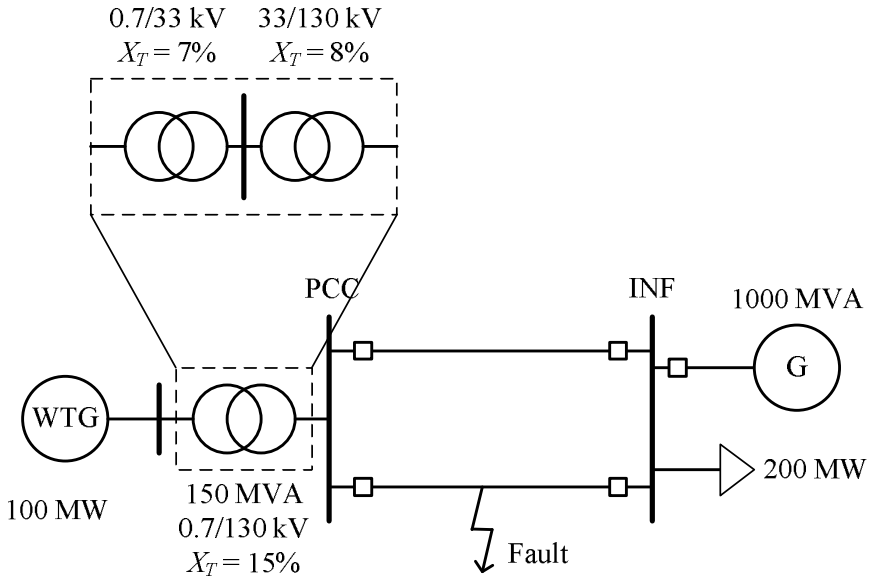

Figure 8.22. Test grid.

Fig. 8.23 shows a comparison of the results of the detailed model implemented in Matlab/Simulink and the proposed FCWT model implemented in PSS/E with a

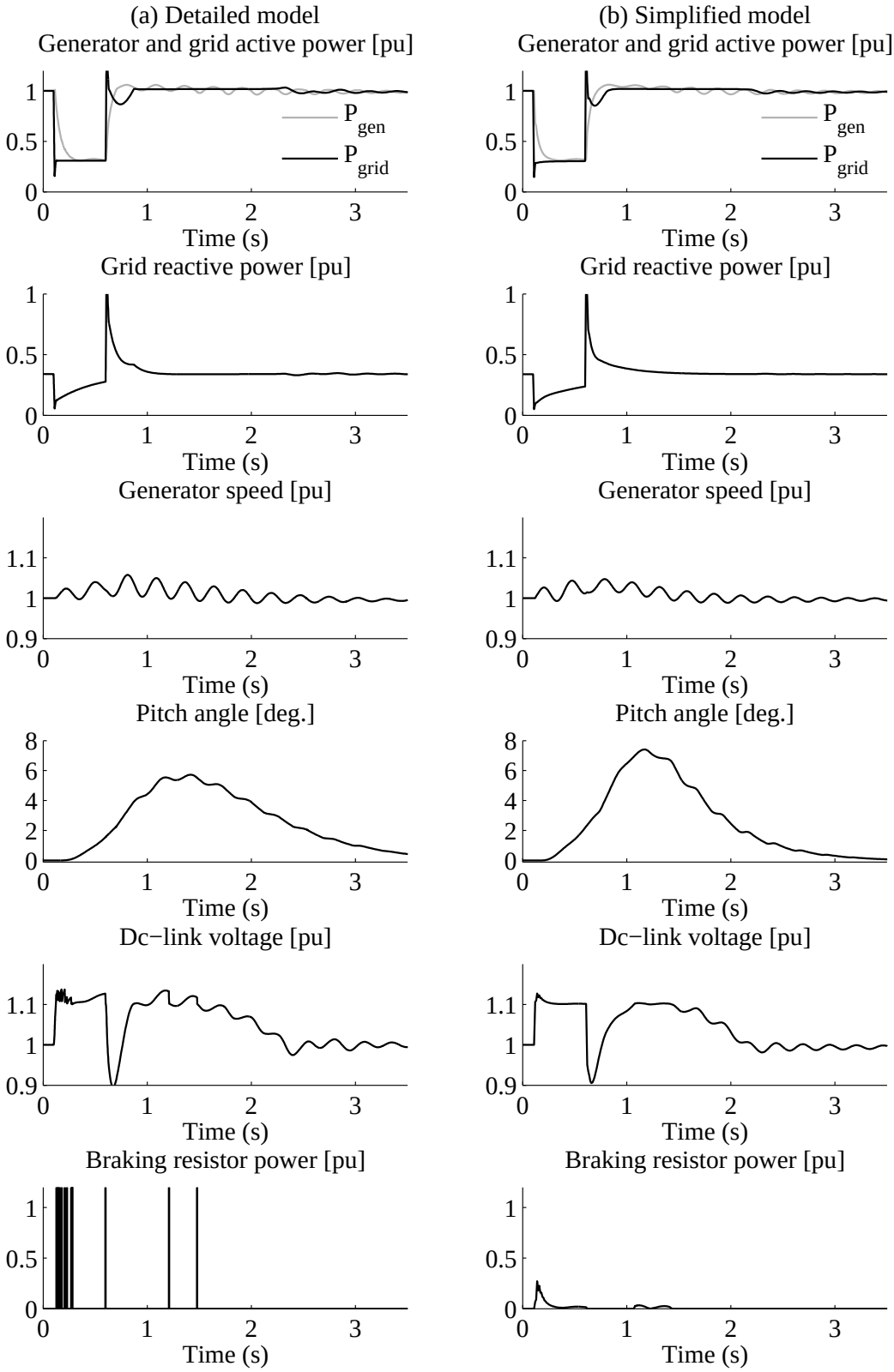

Figure 8.23. Comparison between detailed and proposed FCWT model of FCWT with partial braking resistor.

simulation time step of 10 ms. A partial dynamic braking resistor is used in these models.

The active power exchange at the grid-side converter directly follows grid voltage. During the fault, the generator-side converter receives a signal to reduce the generator power. The power reduction is proportional to the magnitude of the grid voltage. Due to the delay between the measurement and the converter action, the generator power cannot be reduced instantaneously. Consequently, imbalance power is accumulated in the dc-link, which leads to an excessive increase in dc-link voltage. When the dc-link voltage reaches the maximum limit, the dynamic braking resistor is activated, and in this way, a dc-link over-voltage is avoided.

The reduced electric power leads to rotor acceleration. The pitch control maintains the generator speed within an allowable range. The fast reduction of the generator power triggers torsional oscillations on the drive train, which are also observed in the active power and the dc-link voltage. However, the oscillations are well-damped and disappear after 3 seconds. A constant reactive power injection is employed in this model. Overshoots in active and reactive power are observed during the fault clearing, which can be attributed to the grid voltage response. In general, the results show that the simplified model is able to simulate the behavior of the wind turbine adequately.

Fig. 8.24 shows a comparison of the results of the detailed and the simplified models using a full power dynamic braking resistor. Again, the simplified model shows its ability to simulate the wind turbine response accurately. Unlike the previous simulation, no generator transient is observed in these simulations. As was explained earlier, the generator responses are isolated from the grid disturbance due to the action of the full power braking resistor.

8.8 Aggregated Model

In this section, the responses of two different representations of a wind farm consisting of FCWTs are compared. In the first representation, the wind farm is modeled as a cluster representation. It is assumed that the wind turbines in the wind farm can be divided into two clusters with an equal number of wind turbines each. Wind turbines in the first cluster generate full power while those in the second cluster produce 0.5 pu of power. This combination gives a total power production of 75 MW. In the second representation, the wind farm is modeled as a single equivalent wind turbine generating 75 MW of power output.

As shown in Fig. 8.25, following the fault, the active power level of the aggregated model is higher than that of the detailed model. This can be explained as follows: The deviation of the generator speed of the wind turbines at full power operation is considerably large during the fault. This causes the pitch controller to increase the pitch angle, which leads to a large aerodynamic power curtailment (see Fig. 8.26). In contrast, this situation is not encountered in the aggregated model since the aerodynamic power of the aggregated model is almost constant during the investigation.

The maximum error in active power level response is around 10 to 15%, which occurs during the first 300 ms after fault clearing. This figure is relatively small for a stability study. Despite the mismatch in the active power level, the reactive power response of the aggregated model matches very well with the detailed model. This

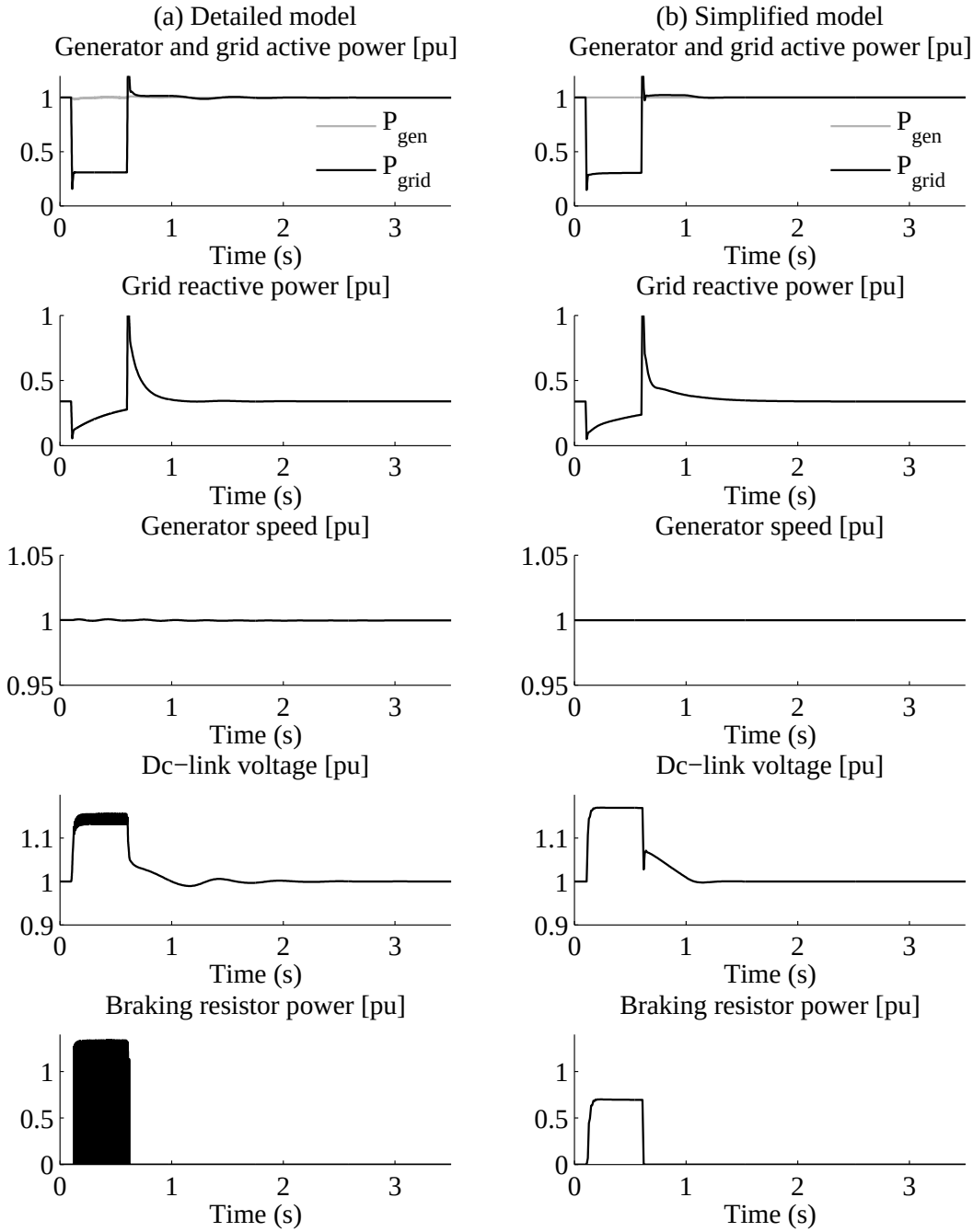

Figure 8.24. Comparison between detailed and simplified model of FCWT with full power braking resistor.

mismatch in active power response is hardly noticed in an FCWT provided with a full power dynamic braking resistor, as shown in Fig. 8.27.

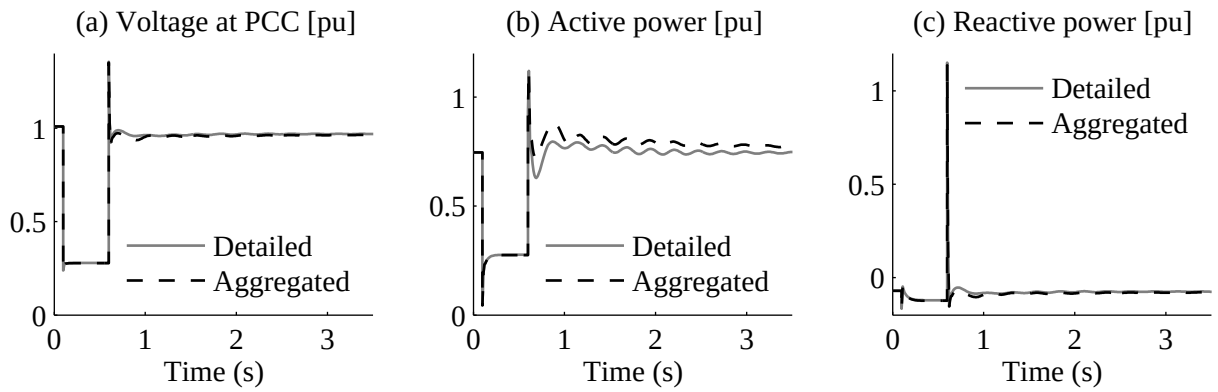

Figure 8.25. Comparison between aggregated and individual model of wind turbines with partial power braking resistor.

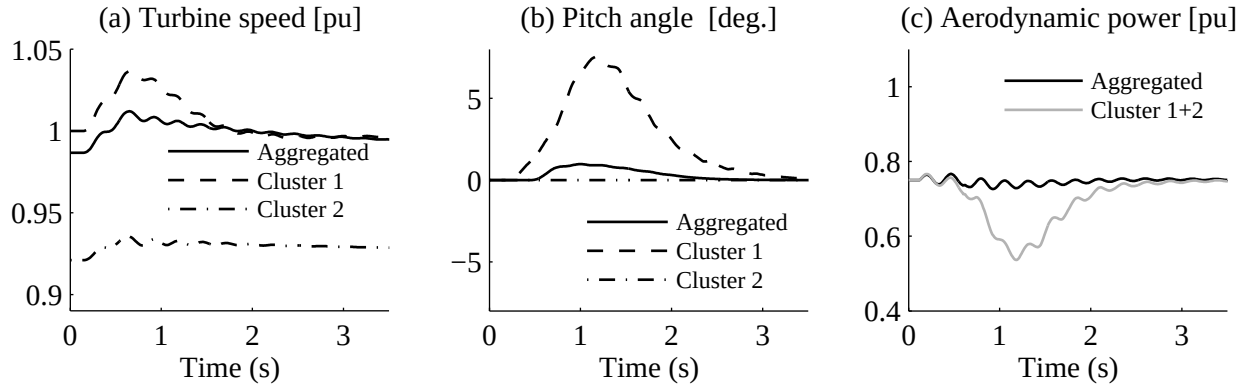

Figure 8.26. Effect of aerodynamic power curtailment on the response of aggregated and individual models of wind turbines with partial power braking resistor.

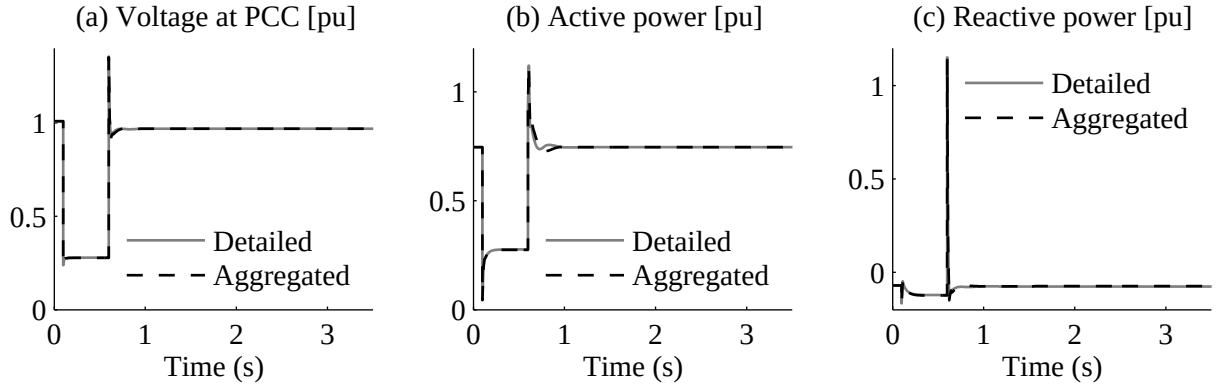

Figure 8.27. Comparison between aggregated and individual model of wind turbines provided with full power braking resistor.

8.9 Conclusion

Various FRT strategies of an FCWT were discussed and evaluated. It was found that fault responses of an FCWT equipped with a full power braking resistor were characterized by the grid-side converter response. In the case of an FCWT equipped with a partial power braking resistor, the responses were governed by the generator power controller. It is concluded that the FRT scheme of an FCWT with a full power braking resistor provides the best dynamic performance compared to the other alternatives.

It was found that torsional oscillations in the drive train, which are excited during a grid fault, were transformed to the grid. Therefore, it was necessary to include a two-mass drive train model in an FCWT model for stability studies.

The influence of the generator model was found to be insignificant in an FCWT model. Furthermore, the grid-side response did not differentiate between generator types used in an FCWT model. In fact, the generator response was dictated by the generator controller dynamics. Therefore, the generator controller must be modeled correctly.

The response of an FCWT at full load was highly influenced by the saturation limit of the grid-side converter. In contrast, during a partial load operation, the response of the wind turbine was characterized by the performance of the generator controller.

A simplified model of an FCWT for stability studies was proposed and implemented in the simulation tool PSS/E with a 10 ms simulation time step. It was found that the responses of the proposed simplified FCWT model match very well with those of the detailed FCWT model implemented in Matlab/Simulink.

A single unit equivalent model was able to sufficiently predict the response of a wind farm consisting of FCWTs during a grid fault. However, the single unit equivalent model of a wind farm gave more accurate results for FCWTs with full power braking resistors.

Chapter 9

Dynamic Reactive Power Compensation for an Offshore Wind Farm

Different influencing factors in designing dynamic reactive power compensation for an offshore wind farm consisting of FCWTs are presented in this chapter.

9.1 Introduction

In [60], an improvement of fault critical clearing time for a wind farm consisting of fixed-speed wind turbines using static shunt capacitors is reported. It is found that the amount of reactive power compensation depends on the fault location, fault duration and wind farm power output. The latter factor may cause difficulties in correctly designing the size of the compensation device. If the static shunt capacitor is switched on due to a fault during low wind power generation, there is a risk of over-voltage following voltage recovery due to over compensation. In such a case, utilization of a static shunt capacitor for voltage recovery is not suitable. Alternatively, the compensation should be performed using a dynamic compensation device, such as an SVC or a STATCOM.

Fault recovery of a wind farm consisting of fixed-speed induction generators by means of a STATCOM is demonstrated in [150]. In another study, the STATCOM is combined with mechanically switched capacitors [151]. A similar study that considers network strength is discussed in [152]. An SVC application for an offshore wind farm consisting of fixed-speed wind turbines is presented in [153]. In the aforementioned papers, however, the FRT capability of individual wind turbines is not modeled.

In this chapter, the influence of dynamic reactive power compensation on the transient stability of a wind farm is investigated. Two different dynamic compensation devices are used; namely an SVC and a STATCOM. The influence of device location is also evaluated.

In order to perform the investigation, a wind farm model is used. The layout of the wind farm is shown in Fig. 9.1. The wind farm consists of 150x2MW fixed-speed wind turbines. It should be noted that, unlike onshore wind farms, the charging current of offshore wind cables is considerably high. For this reason, the characteristics of the sea

Table 9.1: Network parameters.

Parameters	Values	Unit
Transformer 0.69/30 kV		
Rating	320	MVA
Impedance	0.06	pu
Transformer 30/150 kV		
Rating	320	MVA
Impedance	0.06	pu
Sea cable on 100 MVA base		
Resistance	0.005	pu
Reactance	0.015	pu
Admittance	0.08	pu
Overhead lines on 100 MVA base		
Resistance	0.01	pu
Reactance	0.10	pu

cable must be taken into account in the investigation. The wind farm is modeled as a single equivalent unit of a wind turbine. The wind turbine generator is modeled as a third-order model and the drive train is modeled as a two-mass model. The simulations are performed using the simulation tool PSS/E with the standard simulation time step of 10 ms.

The transient event is introduced by applying a fault on one of the transmission lines close to the PCC. The network parameters and wind turbine data are given in Table 9.1 and 9.2, respectively. A dynamic reactive power compensation device is designed to maintain voltage at the wind turbine terminal in such way that voltage recovers within the allowable level after the fault, thereby avoiding wind farm disconnection.

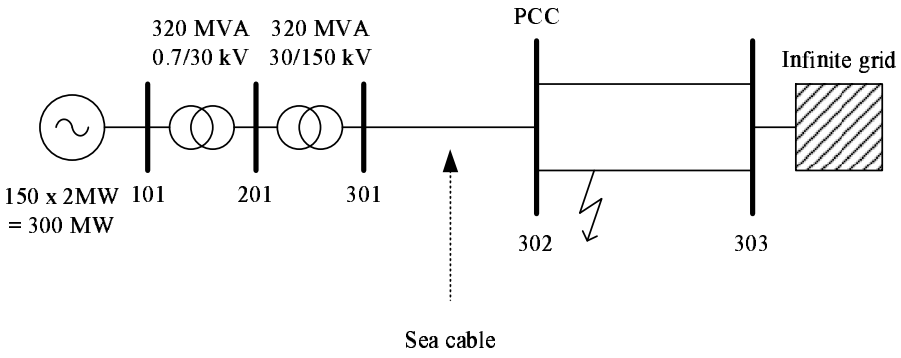

Figure 9.1. Offshore wind farm network.

Table 9.2: Wind turbine data.

Parameters	Values	Unit
Number of turbines	150	units
Generator parameters		
Rating	2	MVA
Voltage	690	V
Rs	0.00539	pu
X_{ls}	0.09062	pu
X_m	3.31065	pu
Rr	0.007616	pu
X_{lr}	0.100718	pu
H_g	0.53273	s
Turbine parameters		
Rotor inertia	5.8	s
Shaft stiffness	0.5603	

9.2 Effect of Device Type Selection

In this section, the performance of SVC and STATCOM devices for offshore wind farm reactive power compensation is compared. In addition, a fast mechanically switched capacitor is included in the comparison. All the dynamic reactive power compensation devices are rated at 170 MVAr and located at the offshore platform (bus 201).

Models of SVC and STATCOM devices in PSS/E are shown in Fig. 9.2 and Fig. 9.3, respectively.

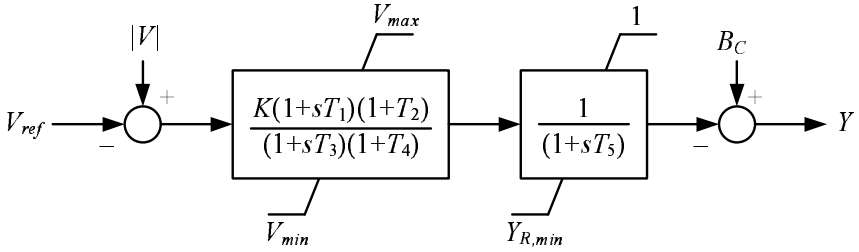

Figure 9.2. Model of SVC in PSS/E (CSVGN1).

Fig. 9.4 shows the response of the wind farm subject to a grid fault close to the PCC provided with three different types of dynamic reactive power compensators. It can clearly be seen that the STATCOM outperforms the SVC and the mechanically switched capacitor. Less than 1 second after fault clearing, the STATCOM is able to recover voltage at the PCC close to the nominal value, while the SVC takes almost 3 seconds to stabilize the voltage. In contrast, despite a 200 ms switching response time (including pick-up time and switching time), the mechanically switched capacitor fails to maintain voltage stability at the PCC, which eventually leads to a voltage collapse.

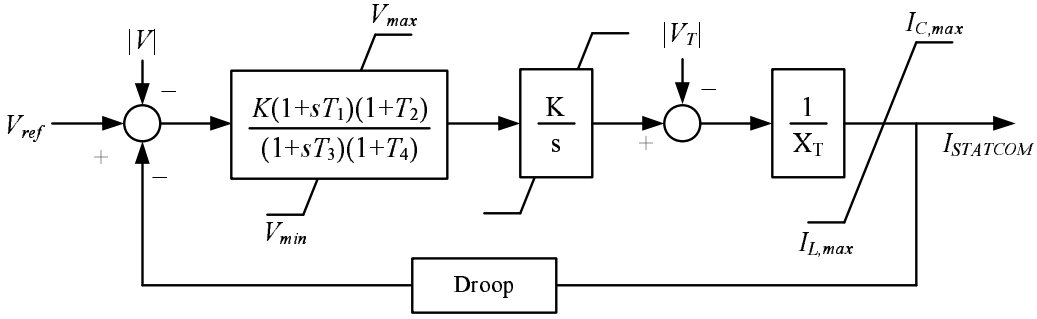

Figure 9.3. Model of STATCOM in PSS/E (CSTCON).

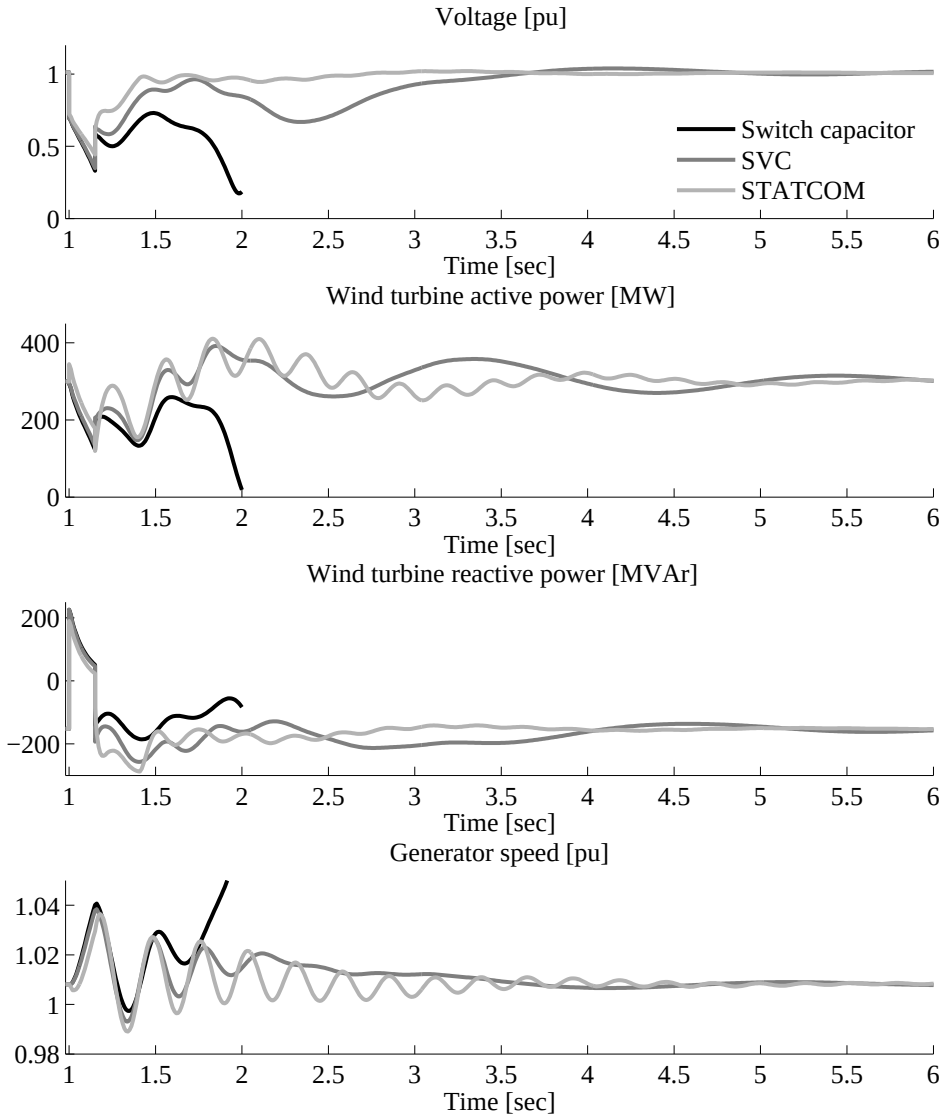

Figure 9.4. Response of wind turbine with different dynamic reactive power compensation.

9.3 Effect of Device Location

A dynamic reactive power compensation device can be located either on the offshore platform or on the onshore substation. A comparison of required device rating for the two locations is presented in Table 9.3. The results show that relocating the compensation device from the offshore platform to the onshore substation requires an increase in the size of the device by 35% for the SVC, and 52% for the STATCOM.

Besides the advantage of a smaller device size, locating the device on the offshore platform skips the use of a step-up transformer, since the device can be connected at the medium voltage-side of the offshore transformer. On the other hand, an offshore location reduces the accessibility of the device and thereby maintenance becomes more expensive.

Table 9.3: FACTS device size (MVAr) for different locations.

Location	STATCOM	SVC
Onshore (Bus 302)	160	230
Offshore (Bus 201)	105	170

9.4 Effect of Network Strength

The influence of network strength is studied. In the base case, the short circuit capacity is 2000 MVA, while the grid strength is reduced to 1330 MVA in the weak network case. The result of the simulation is presented in Table 9.4.

The results show that the size of the dynamic reactive compensator is not inversely proportional to network strength. As shown in the results, a 30% reduction in network strength corresponds to an increase in the device dimension by 90%.

Table 9.4: FACTS device size (MVAr) for different network short circuit capacities at bus 302.

Short circuit capacity	STATCOM	SVC
2000 MVA	160	230
1330 MVA	285	440

9.5 Influence of Wind Turbine Fault Ride-Through Capability

In this case, FRT capability based on active stall mechanism is implemented in the turbines. Accordingly, the mechanical input power of the turbines is reduced in the event of a grid fault. The results are presented in Table 9.5.

The results clearly show that the FRT capability of the turbines significantly reduces the requirements for the dynamic reactive power compensator. As can be seen from the table, the size of the STATCOM device can be minimized to half of the initial

requirement where the FRT capability is not included, while for the SVC device, the reduction is even more dramatic, where the new requirement is only 43% of the initial requirement.

Table 9.5: FACTS device size (MVAr) for wind turbine with and without FRT capability.

Short circuit capacity	STATCOM	SVC
Without FRT	160	230
With FRT	80	100

9.6 Conclusion

The requirements for a dynamic reactive power compensation device to maintain short-term voltage stability in an offshore wind farm consisting of fixed-speed wind turbines depends on several factors, such as the device type, location, network strength and wind turbine FRT capability. It was found that the exclusion of wind turbine FRT capability may lead to over-pessimistic estimation of the dynamic reactive power compensation requirements.

Chapter 10

Conclusions and Future Work

10.1 Conclusions

The aim of this work was to propose generic models of wind power generation for power system stability studies with an emphasis on short-term voltage stability analyses. Three types of wind power generation concepts were investigated; a fixed-speed wind turbine (FSWT) with a squirrel cage induction generator, a doubly fed induction generator (DFIG) wind turbine and a variable speed full converter wind turbine (FCWT).

Model validations of FSWT models

A fixed-speed wind turbine model and an aggregated model of a wind farm consisting of fixed-speed wind turbines were validated against field measurement data. Validation results suggest that a combination of a third-order induction generator model and a two-mass drive-train model are sufficient to predict electromechanical responses of a generator to symmetrical grid faults.

Fault ride-through schemes

Various fault ride-through (FRT) schemes for different wind turbine concepts were investigated. The three wind turbine concepts were able to stay connected during severe grid faults with appropriate FRT schemes. Large reactive power absorption by an FSWT generator during fault recovery remained unresolved, even if dynamic reactive power compensation is introduced. Large reactive power absorption may occur in a DFIG wind turbine only if the rotor converter fails to be reactivated before the fault is cleared. The study concluded that there was no reactive power problem associated with grid faults for an FCWT.

Models for stability studies

Several findings regarding generic models for the three wind turbine concepts for power system stability studies can be summarized as follows:

Fixed-speed wind turbine: A generalized model that can be used for different studies should include at least a two-mass drive train model and a third-order induction generator model with stator transient neglected. Only for a significantly large frequency

deviation, a modified fifth-order model needs to be used to provide more accurate responses.

DFIG wind turbine: In the proposed model, the electrical part of the generator was constructed from a set of algebraic equations, while the controller was modeled as a combination of PI controllers and time lags. Simple expressions were derived to solve the generator equations. It was found that fault responses of different FRT schemes were similar and thereby a unified representation of a FRT scheme was used in the model. The rotor current limiters were found to have an essential role in characterizing the response of the DFIG wind turbine model during a grid fault. A direct solution method for initialization of a DFIG wind turbine model was proposed. This method makes the model easy to implement in power system simulation tools. The study found that active power control schemes in a DFIG wind turbine can be differentiated into two main types.

Full power converter wind turbine: The generator was sufficiently modeled as a controlled electromagnetic torque with a time lag. The generator speed control by the generator-side converter must be represented, while the reactive control capability can be omitted. The dc-link capacitor and the dc-link voltage control were modeled in detail. The dc-link braking resistor was modeled as a negative power source controlled via a P-controller. If the dc-link capacitor is smaller than 0.02 pu, the dc-link model must be omitted from the model meaning that the grid-side converter power output is equivalent to the generator power output. The grid-side converter was modeled as a controlled current source. By adjusting the energy limit of the dc-link braking resistor, the model can resemble different FRT schemes of an FCWT. It was found that the drive train oscillations affect the grid-side converter output power.

For all wind turbine concepts, the aerodynamic model should be represented as a $C_p(\lambda, \beta)$ lookup-table. This representation allows wind turbine operation with large speed variations and active stall or pitch control implementations.

The computational efficiency of the models was verified by the ability of the models to run in a simulation with a 10 ms integration time step using modified Euler solver. Since no iteration is involved, the models can be conveniently implemented in a power system stability simulation tool. The accuracy of the models has been demonstrated by head-to-head comparisons against detailed models subjected to various disturbances. The comparisons showed that responses of the proposed generic models match very well with those of the detailed models.

The wind turbine models proposed in this thesis can be seen as a contribution to the ongoing discourse on standardized models of wind power generation for power system stability studies. The generic models provide more opportunities for transmission system operators and wind farm developers to confidently perform system planning studies without being dependent on proprietary models and being restricted by non-disclosure agreements with manufactures.

Wind farm aggregated model

Aggregated models of wind farms consisting of large number of wind turbines were studied. It was found that a single equivalent unit representation of a wind farm is sufficient for most short-term voltage stability investigations. In case of a wind farm consisting of DFIG wind turbines or FCWTs, non-linearities due to MPT character-

istics and saturation of electrical controllers play no important role in characterizing wind farm responses provided that the active power control response is slow. This condition remains true even if power output discrepancies among the wind turbines in the wind farm are large. For a medium-term study, which may include wind transport phenomena, a cluster representation of a wind farm provides a more realistic prediction.

Dynamic reactive power compensation

Different influencing factors in designing dynamic reactive power compensation for an offshore wind farm consisting of fixed-speed wind turbines were investigated. The study found that FRT capability of the individual turbines in the wind farm utilizing an active stall control significantly reduces the requirement for the dynamic reactive power compensation. In the presented case, the reduction of the dynamic reactive power compensation requirement was more than 50% in comparison to the case when the wind turbines in the wind farm are not equipped with FRT.

10.2 Future Work

The following prospective topics, which are relevant to the current work, are proposed for future work:

- More works need to be done to validate DFIG wind turbine and FCWT models presented in this thesis against field measurements data. The validations should comprise different operating conditions and fault types.

- It is interesting to simulate different wind turbine products available in the market using the proposed generic models. In some cases, it may need to derive and modify model parameters provided by manufacturers to adapt with the generic model representations.

- Technical and economic evaluations of various FRT schemes for wind farms. A study is needed to find the best FRT scheme options for different types of wind turbines and different grid requirements.

- More stringent grid codes have pushed wind turbines to include features similar to those of conventional generators. This approach minimizes the negative impacts of wind turbines on the grid performance. On the other hand, the advancement of FACTS technology enables grid reinforcement in a cost effective way. It is therefore important to evaluate grid reinforcement by utilizing FACTS devices in comparison with improving wind turbine capability.

- Application of an HVDC for a large offshore wind farm is an interesting subject. A study is needed to investigate the influence of an HVDC on an increased stability of the wind farm and its potential to reduce wind turbine requirements.

- Investigation of impacts of different wind turbine concepts and capabilities on the stability of the Nordic power system.

- Proposing a generalized approach for defining criteria for grid connections of wind farms taking into account characteristics and nature of the corresponding power system.

Bibliography

[1] "World wind energy association (WWEA) press release: Wind turbines generate more than 1 percent of the global electricity," Feb. 2008, available online: http://www.wwindea.org, accessed March 12, 2008.

[2] "IEA wind energy annual report 2007," International Energy Agency (IEA), Tech. Rep., Jul. 2008.

[3] H. Holttinen and J.Pedersen, "The effect of large scale wind power on a thermal system operation," in *Proc. of 4th International Workshop on Large-scale Integration of Wind Power and Transmission Networks for Offshore Wind Farms*, Billund, Denmark, Oct. 2003, p. 7.

[4] H. Li and Z. Chen, "Overview of different wind generator systems and their comparions," *IET Renewable Power Generation*, vol. 2, no. 2, pp. 123–138, 2008.

[5] *General Specification V80 - 1.8 MW 60 Hz OptiSlip® - Wind Turbine*, Vestas, May 2002.

[6] A. Hansen and L. Hansen, "Market penetration of wind turbine concepts over the years," in *Proc. European Wind Energy Conference and Exhibition 2007 (EWEC 2007)*, Milan, Italy, May 2007.

[7] V. Akhmatov, "Analysis of dynamic behavior of electric power system with large amount of wind power," Ph.D. dissertation, Technical University of Denmark, 2003.

[8] I. Erlich, J. Kretschmann, J. Fortmann, S. Mueller-Engelhardt, and H. Wrede, "Modeling of wind turbines based on doubly-fed induction generators for power system stability studies," *IEEE Transactions on Power Systems*, vol. 22, no. 3, pp. 909 – 919, Aug. 2007.

[9] P. Ledesma and J. Usaola, "Doubly fed induction generator model for transient stability analysis," *IEEE Transactions on Energy Conversion*, vol. 20, no. 2, pp. 388 – 397, Jun. 2005.

[10] Y. Lei, A. Mullane, and G. Lightbody, "Modelling of the wind turbine with a doubly fed induction generator for grid integration studies," *IEEE Transactions on Energy Conversion*, vol. 21, no. 1, pp. 257 – 264, Mar. 2006.

[11] N. Miller, J. Sanchez-Gasca, W. Price, and R. Delmerico, "Dynamic modeling of GE 1.5 and 3.6 MW wind turbine-generators for stability simulations," in *Proceeding of Power Engineering Society General Meeting*, vol. 3, Jul. 2003, pp. 1977 – 1983.

[12] K. Clark, N. Miller, W. Price, and J. Sanchez-Gasca, "Modeling of GE wind turbine-generators for grid studies," General Electric International, Inc.," Technical Report, Jan. 2008.

[13] S. Achilles and M. Pöller, "Direct drive synchronous machine models for stability assessment of wind farms," in *Proc. of 4th International Workshop on Large-scale Integration of Wind Power and Transmission Networks for Offshore Wind Farms*, Billund, Denmark, Oct. 2003.

[14] P. Kundur, J. Paserba, V. Ajjarapu, G. Andersson, A. Bose, C. Canizares, N. Hatziargyriou, D. Hill, A. Stankovic, C. Taylor, T. V. Cutsem, and V. Vittal, "Definition and classification of power system stability IEEE/CIGRE joint task force on stability terms and definitions," *Power Systems, IEEE Transactions on*, vol. 19, no. 3, pp. 1387 – 1401, Aug. 2004.

[15] O. Samuelsson and S. Lindahl, "On speed stability," *IEEE Transaction on Power Systems*, vol. 20, no. 2, pp. 1179 – 1180, May 2005.

[16] E. Cate, K. Hemmaplardh, J. Manke, and D. Gelopulos, "Time frame notion and time response of the models in transient, mid-term and long-term stability programs," *IEEE Transactions on Power Apparatus and Systems*, vol. PAS-103, no. 1, pp. 143 – 151, Jan. 1984.

[17] C. Taylor, *Power System Voltage Stability*. McGraw-Hill, Inc., 1994.

[18] H. Snel and J. Schepers, "Engineering moles for dynamic inflow phenomena," *Journal of Wind Engineering and Industrial Aerodynamics*, vol. 39, pp. 267 – 281, 1992.

[19] M. Hansen, A. Hansen, T. Larsen, S. Øye, P. Sørensen, and P. Fuglsang, "Control design for a pitch-regulated, variable speed wind turbine," Risø National Laboratory, Roskilde, Denmark, Technical report, Jan. 2005.

[20] M. Crow and J. Chen, "The multirate method for simulation of power system dynamics," *IEEE Transactions on Power Systems*, vol. 9, no. 3, pp. 1684 – 1690, Aug. 1994.

[21] M. Pöller and M. Schmieg, "The efficient simulation of multiple time scale systems," in *International Conference on Power Systems Transients (IPST) 1997*, 1997.

[22] ——, "Exploiting multiple time scale properties for fast simulation algorithms," in *Proc. 13th Power Systems Computation Conference*, 1999.

[23] S. Pekarek, O. Wasynczuk, E. Walters, J. Jatskevich, C. Lucas, N. Wu, and P. Lamm, "An efficient multirate simulation technique for power-electronic-based systems," *IEEE Transactions on Power Systems*, vol. 19, no. 1, pp. 399 – 409, Feb. 2004.

[24] F. de Mello, J. Feltes, T. Laskowski, and L. Oppel, "Simulating fast and slow dynamic effects in power systems," *IEEE Computer Applications in Power*, vol. 5, no. 3, pp. 33 – 38, Jul. 1992.

[25] J. Vernotte, P. Panciatici, B. Meyer, J. Antoine, J. Deuse, and M. Stubbe, "High fidelity simulation of power system dynamics," *IEEE Computer Applications in Power*, vol. 8, no. 1, pp. 37 – 41, Jan. 1995.

[26] M. Behnke, A. Ellis, Y. Kazachkov, T. McCoy, E. Muljadi, W. Price, and J. Sanchez-Gasca, "Development and validation of WECC variable speed wind turbine dynamic models for grid integration studies," in *Presented at AWEA's 2007 Windpower Conference*, Los Angeles, California, Jun. 2007.

[27] J. Toal, H. Urdal, J. Horne, Y. Coughlan, C. Brozio, B. Punton, A. Brown, and W. Wiechowski, "Building confidence in computer models of wind turbine generators from a utility perspective," in *Proc. Nordic Wind Power Conference (NWPC)*, Roskilde, Denmark, Nov. 2007.

[28] J. Feltes and L. Lima, "Validation of dynamic model parameters for stability analysis: industry need, current practices and future trends," in *IEEE 2003 Power Engineering Society General Meeting*, vol. 3, Jul. 2003.

[29] Y. Coughlan, P. Smith, A. Mullane, and M. O'Malley, "Wind turbine modelling for power system stability analysis - a system operator perspective," *IEEE Transactions on Power Systems*, vol. 22, no. 3, pp. 929 – 936, Aug. 2007.

[30] S. Seman, J. Niiranen, and A. Arkkio, "Ride-through analysis of doubly fed induction wind-power generator under unsymmetrical network disturbance," *IEEE Transaction on Power Systems*, vol. 21, no. 4, pp. 1782 – 1789, Nov. 2006.

[31] J. Ausin and D. Gevers, "Fault ride-through capability test unit for wind turbines," *Wind Energy*, vol. 11, no. 1, pp. 3 – 12, Jan. 2008.

[32] T. Thiringer, A. Petersson, and T. Petru, "Grid disturbance response of wind turbines equipped with induction generator and doubly-fed induction generator," in *IEEE Power Engineering Society General Meeting*, vol. 3, Jul. 2003.

[33] A. Perdana, S. Uski, O. Carlson, and B. Lemström, "Validation of aggragated model of wind farm with fixed-speed wind turbines against measurement," in *Proc. of Nordic Wind Power Conference 2006*, Espoo, Finland, May 2006.

[34] M. Martins, A. Perdana, P. Ledesma, E. Agneholm, and O. Carlson, "Validation of fixed speed wind turbine dynamic models with measured data," *Renewable Energy*, vol. 32, no. 8, pp. 1301–1316, Jul. 2007.

[35] A. Perdana, S. Uski-Joutsenvuo, O. Carlson, and B. Lemström, "Comparison of an aggregated model of a wind farm consisting of fixed-speed wind turbines with field measurement," *Wind Energy*, vol. 11, no. 1, pp. 13 – 27, 2008.

[36] P. Nielsen, G. Andersen, K. Hagemann, K. Skaug, and J. Bech, "A performance oriented wind turbine model for grid stability studies," in *2007 European Conference on Power Electronics and Applications*, Sep. 2007, pp. 1–10.

[37] "Dynamic modelling of wind generation in Ireland," ESB National Grid, Ireland, Progress and Status Report, Jun. 2005.

[38] V. Akhmatov, "Variable-speed wind turbines with doubly fed induction generators, part ii: Power system stability," *Wind Engineering*, vol. 26, no. 3, pp. 171 – 188, 2002.

[39] P. Kundur, *Power System Stability and Control*. New York: Elsevier, 1984.

[40] F. Iov, A. Hansen, N. Cutululis, and P. Sørensen, "A survey of interconnection requirements for wind power," in *Proc. Nordic Wind Power Conference (NWPC)*, Roskilde, Denmark, Nov. 2007.

[41] *Affärsverket svenska kraftnäts föreskrifter och allmänna råd om driftsäkerhetsteknisk utformning av produktionsanläggningar*, Svenska Kraftnät, Sweden, Oct. 2005.

[42] *Wind turbines connected to grids with voltages above 100 kV. Technical regulation for the properties and the regulation of wind turbines*, Elkraft System and Eltra, Denmark, Dec. 2004, availabe online: http://www.energinet.dk/en, accessed March 12, 2008.

[43] *EirGrid Grid Code Version 3.0*, EirGrid, Ireland, Sep. 2007, available online: http://www.eirgrid.com, accessed March 12, 2008.

[44] "Review of requirements for wind turbine generators under system fault conditions," EirGrid, Ireland, Technical Report, Mar. 2004, available online: http://www.eirgrid.com, accessed March 12, 2008.

[45] *PSS/E-29 Program Application Guide: Volume I*, Siemens PTI Ltd, 2002.

[46] *Advanced User's Manual DigSILENT Powerfactory version 12.1*, DigSILENT GmbH, Gomaringen, Germany, 2001.

[47] H. Antia, *Numerical methods for scientists and engineers*, 2nd ed. Basel, Switzerland: Birkhäuser Verlag, 2002.

[48] *Siemens Power Generation*, Available online: http://www.powergeneration.siemens.com, accessed June 2008, Siemens A.G.

[49] *General Specification V82 - 1.65 MW MK II NM 82 1650 Vers. 2*, Vestas, Jan. 2006.

[50] T. Thiringer and J. Luomi, "Comparison of reduced-order dynamic models of induction machines," *IEEE Transactions on Power Systems*, vol. 16, no. 1, pp. 119 – 126, Feb. 2001.

[51] A. Hansen, P. Sørensen, F. Blaabjerg, and J. Becho, "Dynamic modelling of wind farm grid interaction," *Wind Engineering*, vol. 26, no. 4, pp. 191–208, 2002.

[52] O. Wasynczuk, D. Man, and J. Sullivan, "Dynamic behavior of a class of wind turbine generators during random wind fluctuations," *IEEE Transactions on Power System apparatus and Systems*, vol. PAS-100, no. 6, pp. 2837 – 2845, Jun. 1981.

[53] E. Hinrichsen and P. Nolan, "Dynamics and stability of wind turbine generators," *IEEE Transactions on Power Apparatus and Systems*, vol. PAS-101, no. 8, pp. 2640 – 2648, Aug. 1982.

[54] O. Anaya-Lara, G. Ramtharan, E. Bossanyi, and N. Jenkins, "Assessment of structural dynamics for model validation of induction generator-based wind turbines," in *Proc. European Wind Energy Conference and Exhibition 2006 (EWEC 2006)*, Athens, Greece, Mar. 2006.

[55] G. Ramtharan, N. Jenkins, O. Anaya-Lara, and E. Bossanyi, "Influence of rotor structural dynamics representations on the electrical transient performance of fsig and DFIG wind turbines," *Wind Energy*, vol. 10, no. 4, pp. 293 – 301, Jul. 2007.

[56] S. Heier, *Gid Integration of Wind Energy Conversion Systems*. England: John Wiley & Sons, 1998.

[57] A. G. Rodriguez, M. B. Paydn, and C. I. Mitchell, "PSCAD based simulation of the connection of a wind generator to the network," in *Proc. of IEEE Porto Power Tech Proceedings*, vol. 4, Sept. 2001, p. 6.

[58] T. DJ, A. Gentile, K. JM, and P. EM., "Fixed-speed wind generator and wind-park modeling for transient stability studies," *IEEE Transaction on Power Systems*, vol. 19, no. 4, pp. 1911–1917, 2004.

[59] V. Akhmatov, H. Knudsen, and A. Nielsen, "Advanced simulation of windmills in the electrical power supply," *Electrical Power and Energy System*, vol. 22, no. 6, pp. 421 – 434, 2000.

[60] S. Salman and A. Teo, "Improvement of fault clearing time of wind farm using reactive power compensation," in *IEEE Porto Power Tech Proceedings 2001*, vol. 2, Sep. 2001, p. 6.

[61] ——, "Windmill modeling consideration and factors influencing the stability of a grid-connected wind power-based embedded generator," *Power Systems, IEEE Transactions on*, vol. 18, no. 2, pp. 793–802, May 2003.

[62] J. K. Pedersen, K. O. Helgelsen-Pedersen, N. K. Poulsen, V. Akhmatov, and A. H. Nielsen, "Contribution to a dynamic wind turbine model validation from a wind farm islanding experiment," *Electric Power Systems Research*, vol. 64, no. 1, pp. 41 – 51, Jan. 2003.

[63] T. Burton, D. Sharpe, and N. Jenkins, *Hanbook of Wind Energy.* England: John Wiley & Sons, 2001.

[64] N. Miller, W. Price, and J. Sanchez-Gasca, "Dynamic modeling of ge 1.5 and 3.6 wind turbine-generators," General Electric Company," Technical Report, Oct. 2003.

[65] C. Jauch, P. Sørensen, and B. B. Jensen, "Simulation model of a transient fault controller for an active-stall wind turbine," *Wind Engineering*, vol. 29, no. 1, pp. 33–47, 2005.

[66] A. Causebrook, D. Atkinson, and A. Jack, "Fault ride-through of large wind farms sing series dynamic braking resistors," *IEEE Transactions on Power Systems*, vol. 22, no. 3, pp. 966–975, Aug. 2007.

[67] L. Gertmar, H. Christensen, E. Nielsen, and L. Wraae, "New method and hardware for grid-connection of wind turbines and parks," in *Proc. Nordic Wind Power Conference (NWPC)*, Espoo, Finland, May 2006.

[68] *PSS/E-29 Program Application Guide: Volume II*, Siemens PTI Ltd, 2002.

[69] D. Ruiz-Vega, T. I. A. Olivares, D. O. Salinas, "An approach to the initialization of dynamic induction motor models," *Power Systems, IEEE Transactions on*, vol. 17, no. 3, pp. 747–751, Aug. 2002.

[70] A. Perdana, "Wind turbine models for power system stability studies," Technical Report, Chalmers University of Technology, Gothenburg, Sweden, 2006.

[71] P. Nørgaard and H. Holttinen, "A multi-turbine power curve approach," in *Proc. of Nordic Wind Power Conference*, Gothenburg, Sweden, Mar. 2004.

[72] V. Akhmatov, "An aggregate model of a grid-connected, large-scale, offshore wind farm for power stability investigations - importance of windmill mechanical system," *Electrical Power and Energy Systems*, vol. 24, pp. 709 – 717, 2002.

[73] L. Fernandez, J. Saenz, and F. Jurado, "Dynamic models of wind farms with fixed-speed wind turbines," *Renewable Energy*, vol. 31, pp. 1203 – 1230, 2006.

[74] A. Hansen, F. Iov, F. Blaabjerg, and L. Hansen, "Review of contemporary wind turbine concepts and their market penetration," *Wind Engineering*, vol. 28, no. 3, pp. 247 – 263, 2004.

[75] J. Rodriguez-Amenedo, S. Arnalte, and J. Burgos, "Design criteria of variable speed wind turbines with doubly fed induction generator," in *Proceedings of the European Wind Energy Conference*, Copenhagen, Denmark, Jul. 2001, pp. 1116–1119.

[76] D. Aguglia, P. Viarouge, R. Wamkeue, and J. Cros, "Selection of gearbox ratio and power converters ratings for wind turbines equipped with doubly-fed induction generators," in *Proc. of IEEE International Electric Machines and Drives Conference (IEMDC)*, vol. 1, May 2007, pp. 447 – 452.

[77] R. Pena, J. Clare, and G. Asher, "Doubly fed induction generator using back-to-bak PWM converters and its application to variable speed wind-energy generation," *IEE Proc. Electric Power Application*, vol. 143, no. 3, pp. 231 – 241, May 1996.

[78] A. Tapia, G. Tapia, J. Ostolaza, , and J. Sáenz, "Modeling and control of a wind turbine driven doubly fed induction generator," *IEEE Transactions on Energy Conversion*, vol. 18, no. 2, pp. 194 – 204, Jun. 2003.

[79] B. Chowdhury and S. Chellapilla, "Double-fed induction generator control for variable speed wind power generation," *Electric Power Systems Research*, vol. 76, no. 9, pp. 786 – 800, Jun. 2006.

[80] N. Mohan, T. Undeland, and W. Robbins, *Power electronics. Converters, applications and design*, 3rd ed. John Wiley & Sons, Inc., 2003.

[81] B. Bose, *Power electronics and ac drives.* Englewood Cliffs, New Jersey: Prentice-Hall, 1986.

[82] L. Chang, R. Doraiswami, T. Boutot, and H. Kojabadi, "Development of a wind turbine simulator for wind energy conversion systems," in *Canadian Conference on Electrical and Computer Engineering*, vol. 1, Mar. 2000, pp. 550 – 554.

[83] S. Bolik, "Modelling and analysis of variable speed wind turbines with induction generator during grid fault," PhD Thesis, Aalborg University, Aalborg, Denmark, Oct. 2004.

[84] A. Hansen and G. Michalke, "Voltage grid support of DFIG wind turbines during grid faults," in *Proc. European Wind Energy Conference and Exhibition 2007 (EWEC 2007)*, Milan, Italy, May. 2007.

[85] E. Tremblay, A. Chandra, and P. Lagace, "Grid-side converter control of DFIG wind turbines to enhance power quality of distribution network," in *IEEE Power Engineering Society General Meeting*, Jun. 2006, p. 6.

[86] V. Akhmatov, "Modelling of variable speed wind turbines with doubly-fed induction generators in short-term stability investigations," in *Proc. of International Workshop on Transmission networks for Offshore Wind Farms*, Stockholm, Sweden, Apr. 2002.

[87] S. Seman, "Transient performance analysis of wind-power induction generators," Doctoral Dissertation, Helsinki University of Technology, Espoo, Finland, Nov. 2006.

[88] M. Nunes, J. Lopes, H. Zurn, U. Bezerra, and R. Almeida, "Influence of the variable-speed wind generators in transient stability margin of the conventional generators integrated in electrical grids," *IEEE Transactions on Energy Conversion*, vol. 19, no. 4, pp. 692–701, Dec. 2004.

[89] L. Shi, Z. Xu, J. Hao, and Y. Ni, "Modelling analysis of transient stability simulation with high penetration of grid-connected wind farms of DFIG type," *Wind Energy*, vol. 10, no. 4, pp. 303–320, Mar. 2007.

[90] J. Niiranen, "Voltage dip ride-through of a doubly fed generator equipped with an active crowbar," in *Proc. of Nordic Wind Power Conference 2004*, Gothenburg, Sweden, Mar. 2004.

[91] J. Morren and S. de Haan, "Short-circuit current of wind turbines with doubly fed induction generator," *Energy Conversion, IEEE Transaction on*, vol. 22, no. 1, pp. 174 – 180, Mar. 2007.

[92] I. Erlich, M. Wilch, and C. Feltes, "Reactive power generation by DFIG based wind farms with AC grid connection," in *Proc. 2007 European Conference on Power Electronics and Applications*, Aalborg, Denmark, Sept. 2007, pp. 1–10.

[93] F. Koch, F. Shewarega, and I. Erlich, "Alternative models of the doubly-fed induction machine of power system dynamic analysis," in *Proc. International Conference on New and Renewable Energy Technologies for Sustainable Development*, Evora, Portugal, June-July 2004.

[94] I. Erlich and Shewarega, "Modeling of wind turbines equipped with doubly-fed induction machines for power system stability studies," in *Proc. IEEE PES Power Systems Conference and Exposition (PSCE)*, Nov. 2006.

[95] F. Hughes, O. Anaya-Lara, N. Jenkins, and G. Strbac, "Control of DFIG-based wind generation for power network support," *IEEE Transactions on Power Systems*, vol. 20, no. 4, pp. 1958–1966, Nov. 2005.

[96] O. Anaya-Lara, F. Hughes, N. Jenkins, and G. Strbac, "Rotor flux magnitude and angle control strategy for doubly fed induction generators," *Wind Energy*, vol. 9, no. 5, pp. 479–495, Sep./Oct. 2006.

[97] L. Morel, H. Godfroid, A. Mirzaian, and J. Kauffmann, "Double-fed induction machine: converter optimisation and field oriented control without position sensor," in *IEE Proceedings Electric Power Applications*, vol. 145, no. 4, Jul. 1998, pp. 360 – 368.

[98] R. Datta and V. Ranganathan, "Decoupled control of active and reactive power for a grid-connected doubly-fed wound rotor induction machine without position sensors," in *Conference Record of the IEEE Industry Applications Conference. Thirty-Fourth IAS Annual Meeting.*, vol. 4, Oct. 1999, pp. 2623 – 2630.

[99] M. Yamamoto and O. Motoyoshi, "Active and reactive power control for doubly-fed wound rotor induction generator," *IEEE Transactions on Power Electronics*, vol. 6, no. 4, pp. 624 – 629, Oct. 1991.

[100] L. Xu and W. Cheng, "Torque and reactive power control of a doubly fed induction machine by position sensorless scheme," *IEEE Transactions on Industry Applications*, vol. 31, no. 3, pp. 636 – 642, Jun. 1995.

[101] A. Petersson, "Analysis, modeling and control of doubly-fed induction generators for wind turbines," Ph.D. dissertation, Chalmers University of Technology, 2005.

[102] J. Ekanayake, L. Holdsworth, X. Wu, and N. Jenkins, "Dynamic modeling of doubly fed induction generator wind turbines," *Power Systems, IEEE Transaction on*, vol. 18, no. 2, pp. 803 – 809, May 2003.

[103] J. Ekanayake, L. Holdsworth, and N. Jenkins, "Comparison of 5th order and 3rd order machine models for doubly fed induction generator (DFIG) wind turbines," *Electric Power Systems Research*, vol. 67, pp. 207 – 215, 2003.

[104] L. Holdsworth, X. Wu, J. Ekanayake, and N. Jenkins, "Direct solution method for initalising doubly-fed induction wind turbines in power system dynamic models," in *IEEE Proc. of Generation, Transmission and Distribution*, vol. 150, no. 3, May 2003, pp. 334 – 342.

[105] B. Rabelo and W. Hofmann, "Control of an optimized power flow in wind power plants with doubly-fed induction generators," in *Proceeding of Power Electronics Specialist Conference (PESC)*, vol. 4, Jun. 2003, pp. 1563 – 1568.

[106] M. Poller, "Doubly-fed induction machine models for stability assessment of wind farms," in *Proceeding of Power Tech Conference*, vol. 3, Jun. 2003.

[107] A. Perdana, O. Carlson, and J. Persson, "Dynamic response of grid-connected wind turbine with DFIG," in *Proc. of IEEE Nordic Workshop on Power and Industrial Electronics*, Trondheim, Norway, Jun. 2004.

[108] L. Feddersen, "Circuit arrangement and methods for use in a wind energy installation," Vestas Wind System A/S," US Patent No. 7,102,247, Sep. 2006.

[109] R. Kemsley, G. Pannell, and C. Barbier, "Cost-effective improvements in DFIG performance under fault conditions for offshore applications," Econnect Ventures Ltd.," Technical Report, 2007.

[110] G. Marques, "Numerical simulation method for the slip power recovery system," in *Proceedings of IEE Electric Power Applications*, vol. 146, no. 1, Jan. 1999, pp. 17 – 24.

[111] M. Bollen, *Understanding Power Quality Problems: voltage sags and interuptions*. NJ, USA: IEEE Press, 2002.

[112] A. Perdana and O. Carlson, "Comparison of control schemes of wind turbines with doubly-fed induction generator," in *Proc. of Nordic Wind Power Conference 2007*, Roskilde, Denmark, Nov. 2007.

[113] W. Leithead, S. de la Salle, and D. Reardon, "Role and objectives of control for wind turbines," in *IEE Proceedings Generation, Transmission and Distribution*, vol. 138, no. 2, Mar. 1991, pp. 135 – 148.

[114] W. Leithead, S. de la Salle, D. Reardon, and M. Grimble, "Wind turbine modelling and control," in *International Conference on Control 1991 (Control '91)*, vol. 1, Mar. 1991, pp. 1 – 6.

[115] T. van Engelen and E. van der Hooft, "Dynamic inflow compensation for pitch controlled wind turbines," in *Proc. of European Energy Conference*, London, Nov. 2004.

[116] E. van der Hooft and T. van Engelen, "Estimated wind speed feed forwatd control," in *Proc. European Wind Energy Conference and Exhibition*, London, UK, Nov. 2004.

[117] D. Leith and W. E. Leithead, "Implementation of wind turbine controllers," *International Journal of Control*, vol. 66, no. 3, pp. 349–380, Feb. 1997.

[118] A. Hansen, G. Michalke, P. Sorensen, T. Lund, and F. Iov, "Co-ordinated voltage control of DFIG wind turbines in uninterrupted operation during grid faults," *Wind Energy*, vol. 10, no. 1, pp. 51 – 68, Feb. 2007.

[119] A. Hansen and G. Michalke, "Fault ride-through capability of DFIG wind turbines," *Renewable Energy*, vol. 32, no. 9, pp. 1594 – 1610, Jul. 2007.

[120] I. Erlich, K. Rensch, and Shewarega, "Impact of large wind power generation on frequency stability," in *IEEE Power Engineering Society General Meeting 2006.*, Jun. 2006.

[121] J. Slootweg, H. Polinder, and W. Kling, "Initialization of wind turbine models in power system dynamics simulations," in *Proc. 2001 IEEE Porto Power Tech Conference*, Porto, Portugal, Sep. 2001.

[122] K. Rudion, "Aggregated modelling of wind farms," Doctoral Dissertation, Otto-von-Guericke-Universität Magdeburg, Magdeburg, Germany, Feb. 2008.

[123] L. Fernandez and F. Jurado, "Aggregated dynamic model for wind farms with doubly fed induction generator wind turbines," *Renewable Energy*, vol. 33, pp. 129 – 140, 2007.

[124] M. Poller and S. Achilles, "Aggregated wind park models for analyzing power system dynamics," in *Proc. of 4th International Workshop on Large-scale Integration of Wind Power and Transmission Networks for Offshore Wind Farms*, Billund, Denmark, Oct. 2003.

[125] S. Frandsen, R. Barthelmia, O. Rathmann, H. Jørgensen, J. Badger, K. Hansen, S. Ott, P. Rethore, S. Larsen, and L. Jensen, "Summary report: the shadow effect of large wind farms: measurements, data analysis and modelling," Risø National Laboratory, Technical University of Denmark, Roskilde, Denmark, Technical report, Oct. 2007.

[126] M. Mechali, R. Barthelmie, S. Frandsen, L. Jensen, and P. Réthoré, "Wake effects at horns rev and their influence on energy production," in *Proc. European Wind Energy Conference and Exhibition 2006 (EWEC 2006)*, Athens, Greece, Feb. 2006, p. 10.

[127] M. Magnusson and A.-S. Smedman, "Air flow behind wind turbines," *Journal of wind engineering and indutrial aerodynamics*, vol. 89, pp. 169–189, 1999.

[128] A. Faulstich, J. Stinke, and F. Wittwer, "Medium voltage converter for permanent magnet wind power generators up to 5 MW," in *Proc. of European Conference on Power Electronics and Applications*, Dresden, Germany, Sep. 2005, p. 9.

[129] J. Gieras and M. Wing, *Permanent Magnet Motor Technology: Design and Applications*. CRC Press, 2002.

[130] *Wind turbine generator system of the GE Wind Energy 2.x series*, GE Wind Energy, Salzbergen, Germany, Jan. 2004.

[131] M. Lilja and I. Rissanen, "Multibrid low speed synchronous generator with frequency converter," in *Proc. of Nordic Wind Power Conference 2004*, Gothenburg, Sweden, Mar. 2004.

[132] S. Jöckel, A Herrmann and J. Rinck, "High energy production plus built-in reliability - the new Vensys 70/77 gearless wind turbines in the 1.5 MW class," in *Proc. European Wind Energy Conference and Exhibition 2006 (EWEC 2006)*, Athens, Greece, Mar. 2006.

[133] M. Chinchilla, S. Arnaltes, and J. Burgos, "Control of permanent-magnet generators applied to variable-speed wind energy systems connected to the grid," *IEEE Transactions on Energy Conversion*, vol. 21, no. 1, pp. 130–135, Mar. 2006.

[134] J. Conroy and R. Watson, "Low-voltage ride-through of a full converter wind turbine with permanent magnet generator," *IET Renewable Power Generation*, vol. 1, no. 3, pp. 182–189, Sep. 2007.

[135] G. Michalke, A. Hansen, and T. Hartkopf, "Control strategy of a variable speed wind turbine with multipole permanent magnet synchronous generator," in *Proc. European Wind Energy Conference and Exhibition 2007 (EWEC 2007)*, Milan, Italy, May. 2007.

[136] S. Heier, *Gid Integration of Wind Energy Conversion Systems*, 2nd ed. England: John Wiley & Sons, 2006.

[137] P. Krause, O. Wasynczuk, and S. Sudhoff, *Analysis of electric machinery and drive systems*. New York: Wiley-Interscience, 2002.

[138] N. Ullah, A. Larsson, A. Petersson, and D. Karlsson, "Detailed modeling for large scale wind power installations - a real project case study," in *Third International Conference on Electric Utility Deregulation and Restructuring and Power Technologies (DRPT) 2008.*, Apr. 2008, pp. 46–56.

[139] R. Pena, R. Cardenas, R. Blasco, G. Asher, and J. Clare, "A cage induction generator using back to back PWM converters for variable speed grid connected wind energy system," in *The 27th Annual Conference of the IEEE Industrial Electronics Society*, vol. 2, Nov. 2001, pp. 1376–1381.

[140] A. Abedini and A. Nasiri, "PMSG wind turbine performance analysis during short-circuit faults," in *Proc. of IEEE Canada Electrical Power Conference*, Canada, 2007, pp. 160–165.

[141] R. Ottersten, A. Petersson, and K. Pietilainen, "Voltage sag response of PWM rectifiers for variable-speed wind turbines," in *Proc. of IEEE Nordic Workshop on Power and Industrial Electronics*, Trondheim, Norway, Jun. 2004.

[142] G. Michalke, A. Hansen, and T. Hartkopf, "Fault ride-through and voltage support of permanent magnet synchronous generator wind turbines," in *Proc. Nordic Wind Power Conference (NWPC)*, Roskilde, Denmark, Nov. 2007.

[143] T. Bellei, R. O'Leary, and E. Camm, "Evaluating capacitor-switching devices for preventing nuisance tripping of adjustable-speed drives due to voltage magnification," *IEEE Transactions on Power Delivery*, vol. 11, no. 3, pp. 1373 – 1378, Jul. 1996.

[144] B. Buchholz, Z. Styczynski, and W. Winter, "Dynamic simulation of renewable energy sources and requirements on fault ride through behavior," in *Proc. of IEEE Power Engineering Society General Meeting, 2006.*, Jun. 2006, p. 7.

[145] N. Laverdure, D. Roye, S. Bacha, and R. Belhomme, "Mitigation of voltage dips effects on wind generators," in *Proc. European Wind Energy Conference and Exhibition 2004 (EWEC 2004)*, London, UK, Nov. 2004.

[146] J. F. Jr, "Brake control apparatus and method," Westinghouse Electric Corp.," US Patent No. 4,352,049, Sep. 1982.

[147] J. Morren, "Grid support by power electronic converters of distributed generation units," Ph.D. dissertation, TU Delft, Netherland, Nov. 2006.

[148] E. Robles, U. Aguirre, J. L. Villate, I. Gabiola, and S. A. naniz, "Analysis of control strategies of a full converter in a direct drive wind turbine," in *Proc. European Wind Energy Conference and Exhibition 2006 (EWEC 2006)*, Athens, Greece, Feb. 2006.

[149] M. Behnke and E. Muljadi, "Reduced order dynamic model for variable-speed wind turbine with synchronous generator and full power conversion topology," in *International Conference on Future Power Systems,*, Nov. 2005, p. 6.

[150] V. Akhmatov and K. Søbrink, "Static synchronous compensator (STATCOM) for dynamic reactive-compensation of wind turbines," *Wind Engineering*, vol. 30, no. 1, pp. 43 – 54, 2006.

[151] M. Aten, J. Martinez, and P. Cartwright, "Fault recovery of a Wind Farm with Fixed Speed Induction Generators using a STATCOM," *Wind Engineering*, vol. 29, no. 4, pp. 365 – 375, 2005.

[152] S. Foster, L. Xu, and B. Fox, "Grid integration of wind farms using SVC and STATCOM," in *Proc. of the 41st International Universities Power Engineering Conference 2006 (UPEC '06)*, vol. 1, Sep. 2006, pp. 157 – 161.

[153] R. Grunbaum, P.Halvarsson, D. Larsson, and P. Jones, "Conditioning of power grids serving offshore wind farms based on asynchronous generators," in *Second International Conference on Power Electronics, Machines and Drives, 2004 (PEMD 2004)*, vol. 1, Mar.-Apr. 2004, pp. 34 – 39.

Appendix A

Wind Turbine and Network Parameters

A.1 Alsvik Wind Turbine Parameters

Table A.1: Wind turbine parameters.

Parameter	Value	Units
Hub height	30	m
Rotor diameter	23.2	m
Rotor rated speed	42	r.p.m.
Gearbox ratio	23.75	
Turbine inertia constant (H_t)	2.6	s
Generator inertia constant (H_g)	0.22	s
Stiffness constant (K)	141.0	p.u.
Mutual damping (when applied) (D)	3.0	p.u.

Table A.2: Generator parameters.

Parameter	Value	Units
Rated power	210	kVA
Rated voltage	415	V
Stator resistance (R_s)	0.0121	p.u.
Stator leakage inductance (X_s)	0.0742	p.u.
Mutual inductance (X_m)	2.7626	p.u.
Rotor resistance (R_r)	0.0080	p.u.
Rotor leakage inductance (X_r)	0.1761	p.u.

Table A.3: Compensating capacitor parameters.

Parameter	Value	Units
Grid rated voltage	400	V
Capacitor bank susceptance (B)	0.11	p.u.

A.2 Olos Wind Farm Parameters

Table A.4: Generator parameters.

Parameters	Values	Units
Power rating (P_n)	600	kW
Voltage rating	690	V
Stator resistance (R_1)	0.0642	pu
Stator reactance (X_1)	0.0067	pu
Magnetizing reactance (X_m)	2.79	pu
Rotor resistance (R'_2)	0.0799	pu
Rotor reactance (X'_2)	0.0920	pu

Table A.5: Mechanical shaft parameters.

Parameters	Values	Units
Turbine inertia (J_t)	210	kgm2
Generator inertia (J_g)	16	kgm2
High speed shaft and gearbox inertia (estimated)	8	kgm2
Spring constant (k)	7965	Nm/rad
Gear ratio (gr)	55	

Table A.6: No-load reactive power compensator.

Parameters	Values	Units
High-speed mode	162.5	kVAr
Low-speed mode	62.5	kVAr

Table A.7: Transformer data.

Parameters	Values	Units
Winding voltage	21/0.69	kV
Winding connection	Dyn11	
Power rating (S_n)	800	kVA
Short-circuit impedance (Z_k)	4.8	%
Short-circuit power (P_k)	6730	W
Power at no-load (P_o)	934	W

Table A.8: Rising cable to the generator.

Parameters	Values & Units
Impedance (Z)	0.0138Ω/7.8°

Table A.9: Grid data (21 kV side of the wind turbine step-up transformer.)

Parameters	Values & Units
Impedance (Z_k)	$8.27\Omega/60°$

Table A.10: Line from wind farm to the substation.

Parameters	Values & Units
Impedance (Z)	$4.08\Omega\angle 25°$

A.3 DFIG Parameters

Table A.11: Generator parameters.

Parameters	Values	Units
Power rating (P_n)	2	MW
Voltage rating	690	V
Stator resistance (R_s)	0.0130	pu
Stator leakage reactance (X_{ls})	0.0770	pu
Magnetizing reactance (X_m)	2.98	pu
Rotor resistance (R_r)	0.0162	pu
Rotor reactance (X_{lr})	0.0770	pu

Table A.12: Turbine and drive-train parameters.

Parameter	Value	Units
Rotor diameter	40	m
Gearbox ratio	90	
Turbine inertia constant (H_t)	4.3	s
Generator inertia constant (H_g)	0.9	s
Stiffness constant (K_s)	2.0	p.u.
Mutual damping (D)	1.5	p.u.

Appendix B

List of Symbols and Abbreviations

Symbols

Unless specified, the quantities are in per unit of the corresponding system.

A	Braking resistor surface area [cm^2]
C	Dc-link capacitance
C_p	Aerodynamic coefficient of performance
C_T	Turbine thrust coefficient
D_m	Shaft mutual damping coefficient
E_c	Stored energy in capacitor
E_{sto}	Stored energy in braking resistor
F_o	Over-rated factor of grid side converter
F_p	Power level factor
h	Integration time step size [s]
h_c	Braking resistor heat transfer coefficient
H_g, H_t	Generator and turbine inertia constants [s]
i_a, i_b, i_c	a, b, c phase currents
i_{gd}, i_{gq}	d, q components of grid current vector
$\vec{i}_s$, $\vec{i}_r$, $\vec{i}_c$, $\vec{i}_r$	Stator, rotor, converter and grid current vectors
i_s, i_r, i_c, i_r	Stator, rotor, converter and grid current magnitudes
i_{fd}, i_{fq}	d, q components of field winding current vector
i_{kd}, i_{kq}	d, q components of damper winding current vector

i_{rd}, i_{rq}	d, q components of rotor current vector
i_{sd}, i_{sq}	d, q components of stator current vector
i_{sf}	Stator current magnitude injected into grid
$\vec{i}_{sf}$	Stator current vector injected into grid
$\vec{i}_{ms}$	Magnetizing current vector
j	Imaginary operator, $\sqrt{-1}$
J_g, J_t, J_b, J_h	Generator, turbine, blade and hub inertias [kg.m^2]
K_1	Shaft stiffness constant between hub and blade
K_2	Shaft stiffness constant between generator and hub
K_s	Shaft stiffness constant between low- and high-speed shafts
k	Ratio between magnetizing and rotor reactances (X_m/X_r)
k_w	Wake decay constant
L_s, L_r, L_m	Rotor, stator and magnetizing inductances
L_{sl}, L_{rl}	Stator and rotor leakage inductances
L_{sd}, L_{sq}	d, q components of stator inductance
m	Braking resistor mass [gram]
P, Q	Active and reactive powers
P_{cl}	Converter losses
P_{mec}	Mechanical power
P_{rated}	Rated power of wind turbine
P_{gen}, P_s, P_r, P_c	Generator, stator, rotor and grid-side converter powers
P_{in}, P_{sto}, P_{dis}	Total, stored and dissipated power of a braking resistor
Q_{gen}, Q_s, Q_r, Q_c	Generator, stator, rotor and grid-side converter reactive powers
R	Turbine rotor radius [m]
R_g, L_g	Grid filter resistance and inductance
R_s, R_r	Stator and rotor resistances
R_{fd}, R_{fq}	d, q components of field winding resistance
R_{kd}, R_{kq}	d, q components of damper winding resistance

$R_{cb,max}$	Maximum crowbar resistance
s	Generator slip
S_b or S_{base}	Generator power base value
S_e	Equivalent generator rating in model aggregation
$\vec{S}$	Complex apparent power $(P + jQ)$
t_{delay}	Wind transport time delay [s]
T_e, T_m	Electromagnetic and mechanical torque
T_a, T_R	Ambient and braking resistor temperatures [°C]
T_o	Transient open-circuit time constant [s]
v_a, v_b, v_c	a, b, c phase voltages
v_{p-p}	Phase voltage magnitude
$\vec{v_e'}$	Thevenin voltage source vector
v_{dc}	Dc-link voltage magnitude
$v_{dc,max}$	Maximum dc-link voltage magnitude
$v_{dc,rated}$	Nominal/rated dc-link voltage magnitude
v_{cd}, v_{cq}	d, q components of grid-side converter voltage vector
v_{gd}, v_{gq}	d, q components of grid voltage vector
v_{rd}, v_{rq}	d, q components of rotor voltage vector
v_{sd}, v_{sq}	d, q components of stator voltage vector
$\vec{v}_s$, $\vec{v}_r$, $\vec{v}_c$, $\vec{v}_g$	Stator, rotor, converter and grid voltage vectors
v_s, v_r, v_c, v_g	Stator, rotor, converter and grid voltage magnitudes
$v_{r,max}$	Maximum allowable rotor converter voltage magnitude
v_w	Wind speed [m/s]
$\bar{v}_w$	Average wind speed [m/s]
v_0	Incoming free-stream wind speed [m/s]
x	Distance behind wind turbine rotor [m]
X_m	Magnetizing/mutual reactance
X_{md}, X_{mq}	d, q components of mutual reactance

X'_r	Rotor transient reactance
X_s, X_r	Stator and rotor reactances
X'	Stator transient reactance
X_{fd}, X_{fq}	d, q components of field winding reactance
X_{kd}, X_{kq}	d, q components of damping winding reactance
X_{sd}, X_{sq}	d, q components of stator reactance
β	Pitch angle, in the context of $C_p(\lambda, \beta)$ [°]
λ	Tip speed ratio, in the context of $C_p(\lambda, \beta)$
ω_e, ω_r	Synchronous and rotor rotating speed
ℓ	Distance between two successive wind turbine rows [m]
$\vec{\psi}_s$, $\vec{\psi}_r$	Stator and rotor flux vectors
ψ_{sd}, ψ_{sq}	d, q components of stator flux vector
ψ_{rd}, ψ_{rq}	d, q components of rotor flux vector
ψ_{pm}	Permanent magnet flux magnitude
σ	Leakage factor
θ_t, θ_r, $\Delta\theta$	Turbine, generator and shaft twist angles [rad.]

Superscripts

s	stator flux-oriented reference frame
r	rotor flux-oriented reference frame
ref	reference

Abbreviations

DFIG	Doubly Fed Induction Generator
FCWT	Full Converter Wind Turbine
FRT	Fault Ride-Through
FSWT	Fixed-Speed Wind Turbine
GTO	Gate Turn-Off Thyristor
IGBT	Insulated-Gate Bipolar Transistor

MPT	Maximum Power Tracking
OLTC	On-Load Tap Changer
PMSG	Permanent Magnet Synchronous Generator
PI	Proportional+Integral
PWM	Pulse-Width Modulation
STATCOM	Static Compensator
SVC	Static VAR Compensator
TSO	Transmission System Operator